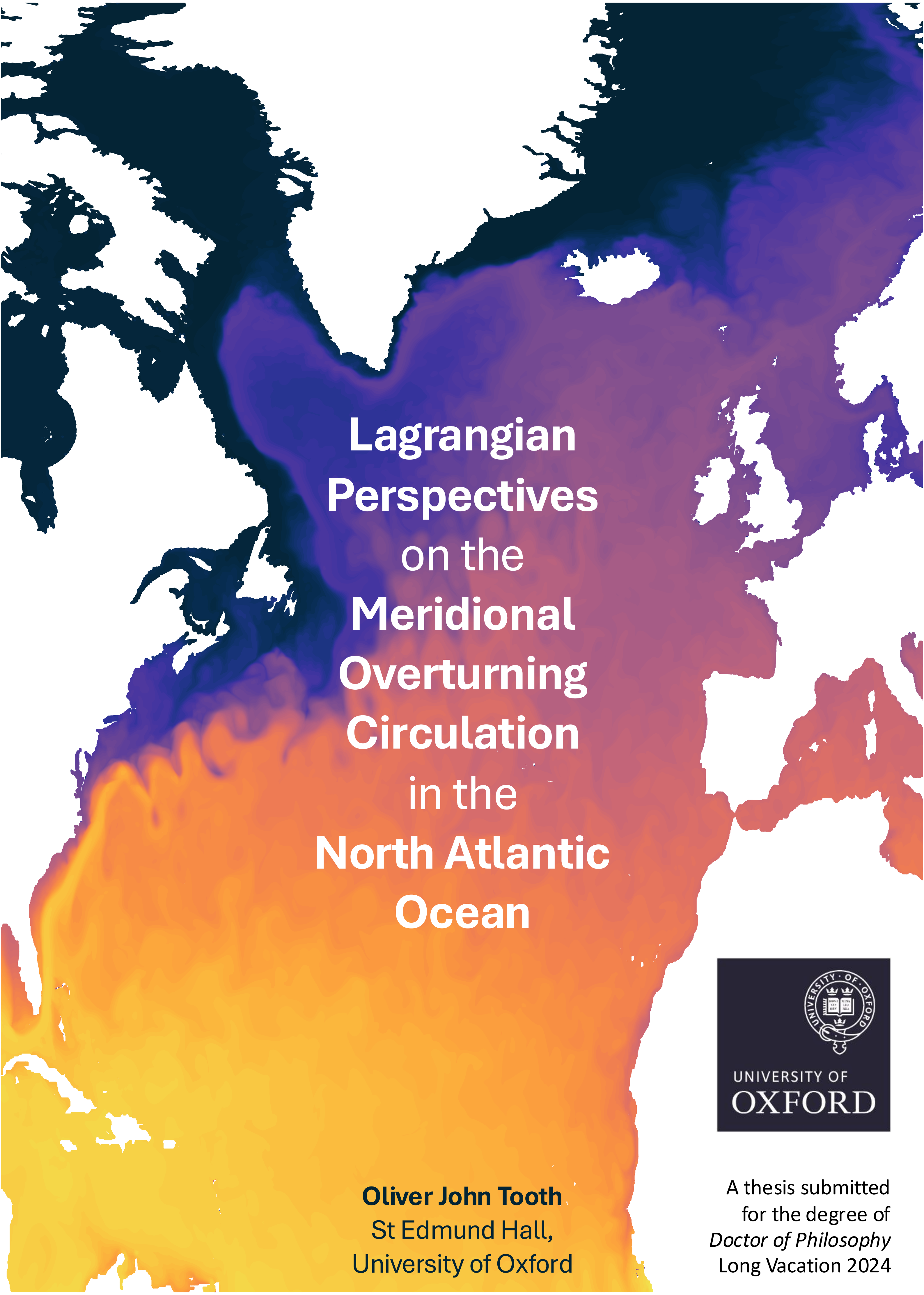

Lagrangian Perspectives on the Meridional Overturning Circulation in the North Atlantic Ocean

UNIVERSITY OF
OXFORD

Oliver John Tooth
St Edmund Hall,
University of Oxford

A thesis submitted
for the degree of
Doctor of Philosophy
Long Vacation 2024

For my great-grandfather, Stanley Ralphs,
whose kindness and courage were as boundless as the sea

Acknowledgements

First and foremost, I would like to thank Helen Johnson and Chris Wilson for being the most supportive and empowering mentors over the past four years. Since our earliest online meetings during the COVID-19 pandemic, you have constantly inspired me to be a more inquisitive and resilient scientist. I am particularly grateful to Helen for always fostering my independence and encouraging me to forge collaborations with the wider AMOC community. I very much hope that our research partnership will continue to flourish in the years to come.

Next, I would like to thank my wonderful family for being my greatest champions and always encouraging me to pursue my passions. I would not be here without the unwavering support of my parents, particularly during the COVID-19 lockdown, for which I am eternally grateful. I am also thankful to my sister for pioneering the route to university; your hard work and dedication will never cease to inspire me.

I would also like to extend a huge thank you to the members of the SNAP-DRAGON research program for welcoming me into the world of AMOC science. In particular, I am grateful to Gwyn Evans for our endless conversations on the philosophy of life and overturning. Thank you also to Ale Sanchez-Franks and Nora Fried for introducing me to OSNAP observations and the intricacies of the Irminger Sea. For broadening my overturning horizons to the subtropical North Atlantic and being the most enthusiastic collaborators, I am very grateful to Bill Johns and Nick Foukal. I am also immensely appreciative of the guidance provided by Adam Blaker in helping me navigate through the obstacle course of ocean general circulation models.

Finally, I would like to express my heartfelt thanks and deepest gratitude to Ellie, who has been a constant source of laughter and positivity over the past four years. Without your endless support and sacrifices behind the scenes, this thesis would simply not have been possible.

Abstract

The Atlantic Meridional Overturning Circulation (AMOC) plays a critical role in the global climate system through the redistribution of heat, freshwater and carbon. However, the distribution of the strength and variability of overturning across the individual circulation pathways of the North Atlantic Subtropical Gyre (STG), Subpolar Gyre (SPG) and the Nordic Seas overflows remains poorly understood. In this thesis, we investigate the detailed nature of the North Atlantic overturning circulation by introducing a novel Lagrangian framework to analyse ocean general circulation models.

We show that dense water formation along the longest SPG pathways sourced from the central and southern branches of the North Atlantic Current (NAC) accounts for more than half of the time-mean strength of the eastern subpolar AMOC in an eddy-permitting ocean model. In contrast, the strong seasonality of subpolar overturning is explained by water parcels circulating rapidly in the upper Irminger and Central Iceland Basins, whose along-stream transformation depends on their month of arrival into the eastern SPG. Looking beyond seasonal timescales, we demonstrate that the amount of dense water formed along the path of the SPG in models can be skilfully predicted, based solely on the volume transport of light waters flowing northward in the branches of the NAC, which is closely related to the strength of the SPG circulation. Finally, we present the first Lagrangian decomposition of the time-mean meridional heat transport and overturning in the subtropical North Atlantic. We show that the substantial heat transport of the STG cannot be meaningfully distinguished from that of the AMOC, since water cooled within the gyre subsequently flows northward at intermediate depths to feed regions of dense water formation at subpolar latitudes.

Overall, our findings highlight the fundamental roles of geometry and connectivity in governing the strength and variability of the AMOC in the North Atlantic Ocean.

Authorship

I am grateful to each of the following co-authors who have contributed towards the research documented throughout this thesis.

Chapter 2 (*Oliver J. Tooth, Helen L, Johnson, Chris Wilson*) - Tooth et al. (2023a)
Myself, HLJ and CW conceived the research question. I designed the Lagrangian experiments, performed the Eulerian and Lagrangian analyses, and wrote the manuscript upon which this Chapter is based. Both co-authors assisted in editing and revising the manuscript. HLJ and CW supervised the study throughout.

Chapter 3 (*Oliver J. Tooth, Helen L, Johnson, Chris Wilson, Daffyd G. Evans*) - Tooth et al. (2023b)
I conceived the research question, planned the study, performed the Eulerian and Lagrangian analyses, and wrote the manuscript upon which this Chapter is based. All co-authors assisted in editing and revising the manuscript. HLJ and CW supervised the study throughout.

Chapter 4 (*Oliver J. Tooth, Helen L. Johnson, Chris Wilson*) - in preparation
I conceived the research question, designed and performed the Lagrangian experiments and analyses, and wrote the Chapter. CW provided technical support in setting-up the Lagrangian experiments on the JASMIN High Performance Computing system. Both co-authors provided feedback on the initial manuscript draft. HLJ and CW supervised the study throughout.

Chapter 5 (*Oliver J. Tooth, Nicholas P. Foukal, William E. Johns, Helen L, Johnson, Chris Wilson*) - Tooth et al. (2024)
Myself, WEJ and NPF conceived the research question. I planned the study, designed the Lagrangian experiments, performed the Lagrangian and Eulerian analyses and wrote the manuscript upon which this Chapter is based. All co-authors assisted in editing and revising the manuscript, including providing input on the analyses. HLJ and CW supervised the study throughout.

Contents

Appendices

List of Abbreviations

AABW	Antarctic Bottom Water
AAIW	Antarctic Intermediate Water
AMOC	Atlantic Meridional Overturning Circulation
DSOW	Denmark Strait Overflow Water
DWF	Dense Water Formation
EGC	East Greenland Current
ISOW	Iceland Scotland Overflow Water
ISIW	Irminger Sea Intermediate Water
LSW	Labrador Sea Water
NEADW	North East Atlantic Deep Water
NADW	North Atlantic Deep Water
OGCM	Ocean General Circulation Model
OSNAP	Overturning in the Subpolar North Atlantic Program
SPG	Subpolar Gyre
SPMW	Subpolar Mode Water
SPNA	Subpolar North Atlantic
STG	Subtropical Gyre
STMW	Subtropical Mode Water
STUW	Subtropical Underwater
WGC	West Greenland Current

1

Introduction

1.1 The Atlantic Meridional Overturning Circulation

Ocean circulation plays a fundamental role in moderating the global climate and sustaining ecosystems through the redistribution of heat, carbon, nutrients and freshwater. One key feature of the large-scale ocean circulation is the Atlantic Meridional Overturning Circulation, which is forced by the action of the winds and the fluxes of heat and freshwater at the sea surface (e.g., Cronin & Sprintall, 2001; Ferrari & Wunsch, 2009; Stewart et al., 2014). At high latitudes, the upper ocean is cooled by intense heat loss to the overlying atmosphere to form dense water masses which ventilate the deep ocean. The formation and sinking of dense water result in two meridional overturning circulation cells, emanating from the North Atlantic and the coastal margins around Antarctica (see review by Buckley & Marshall, 2016). The upper meridional overturning cell represents the circulation North Atlantic Deep Water (NADW), which flows southward in the 1000-3000 m depth range. The abyssal ocean is ventilated through the formation of denser Antarctic Bottom Water (AABW), which flows northward in the lower meridional overturning cell. In addition to the buoyancy forcing induced by differential heating and cooling at the sea surface, meridional overturning cells are sustained through adiabatic upwelling of deep waters and diapycnal mixing throughout the ocean interior (Johnson et al., 2019; Kuhlbrodt et al., 2007). In the case of the upper meridional overturning cell, the circulation of dense NADW is closed via adiabatic upwelling along isopycnals in the Southern Ocean (e.g., Gnanadesikan, 1999; Marshall & Speer, 2012; Toggweiler & Samuels, 1995) and via diabatic upwelling in both the Southern Ocean and the Indo-Pacific basin (Rousselet et al., 2020, 2021). In this thesis, we investigate the detailed nature of the circulation pathways comprising the upper meridional overturning cell, which we herein refer to as the Atlantic Meridional Overturning Circulation (AMOC) (Fig. 1.1).

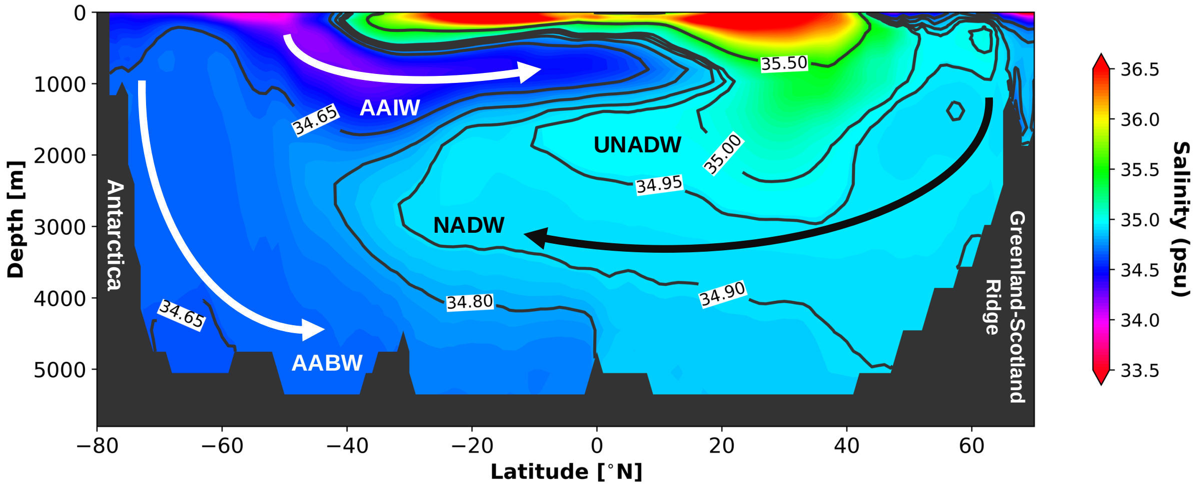

Figure 1.1: Time-mean (1990-2024) Atlantic Ocean meridional salinity section at 59°-14°W calculated using EN.4.2.2 objective ocean analyses (Good et al., 2013) is shown as a function of depth. The locations of the major Atlantic water masses are shown and are defined as follows: **AABW** = Antarctic Bottom Water, **AAIW** = Antarctic Intermediate Water, **NADW** = North Atlantic Deep Water, **UNADW** = Upper North Atlantic Deep Water.

1.2 Origins and Phenomenology of the Atlantic Meridional Overturning Circulation

The earliest conceptual models of the AMOC were formulated based on hydrographic measurements collected during the late 19th and early 20th centuries (see review by Richardson, 2008) and consisted of two quasi-symmetric circulation cells occupying the upper 2000 m on either side of the equator (Lenz, 1845; Schott, 1902; Speiss, 1928). Later expeditions revised this model by recognising the inter-hemispheric nature of the overturning circulation in the Atlantic Ocean (Brennecke, 1921) and included a deeper-reaching overturning cell sourced from the Southern Ocean (Merz, 1925). A greater understanding of the vertical water mass structure followed and the 2-dimensional depiction of the overturning circulation was extended to become a three layer structure comprising Antarctic Intermediate Water, NADW and AABW flowing at intermediate, deep and abyssal depths, respectively (Defant, 1941; Wüst, 1935, 1949) (Fig. 1.1). Although Wüst (1957) was the first to highlight the role of Deep Western Boundary Currents (DWBC) as conduits for the meridional exchange of dense waters, their significance was quantified by Henry Stommel, who developed the first 3-dimensional model of the AMOC through the linear superposition of a wind-driven upper layer and a full-depth meridional overturning cell (Richardson, 2008; Stommel, 1957, 1958).

Arguably, the most impactful contribution to our present-day description of the AMOC originates from the works of Broecker and Peng (1982) and Broecker (1991), who first conceptualised the AMOC as a "Great Ocean Conveyor Belt" connecting each of the global ocean basins through a continuous and coherent 3-dimensional circulation. While subsequent AMOC depictions have favoured greater accuracy in depicting circulation pathways and quantifying inter-basin exchanges (e.g., Gordon, 1986, 1991; Schmitz Jr, 1996; Talley, 2013) over the simplicity of Broecker (1991)'s conveyor-belt representation, its popular appeal reflects its ability to capture the most fundamental features of the AMOC (Richardson, 2008). In particular, the conveyor-belt model presented in Figure 1.2 illustrates six of the defining features of the AMOC as a physical phenomenon, namely:

1. Warm, saline waters flow northward in the upper 1000 m of the North Atlantic Ocean via a system of wind and buoyancy forced ocean currents.

2. Upon reaching the subpolar North Atlantic (SPNA) and the Nordic Seas, waters are transferred from the AMOC's upper to lower limb by forming

dense NADW through intense surface buoyancy (heat) loss and diapycnal mixing.

3. NADW is exported southward in the lower limb via the DWBC and dispersive interior pathways.
4. NADW recirculates at depth around the Southern, Pacific and Indian Oceans until it is eventually returned to the surface through wind-driven upwelling or vertical mixing.
5. Waters returned to the upper limb are imported into the South Atlantic via the Agulhas leakage ("warm route") or Drake Passage ("cold route") and thereby close the overturning cell.
6. The large temperature contrast between the warm northward flowing upper limb and cold southward return flow in the lower limb is responsible for the net northward heat transport throughout the Atlantic Ocean.

The large scale and long advective timescales of the AMOC present oceanographers with the practically impossible task of quantifying the state of the AMOC from limited in-situ observations and finite numerical model simulations. The challenge of defining a diagnostic measure of the AMOC which adequately reflects the physical phenomenon characterised by the features above will therefore be an important topic of discussion throughout this thesis.

1.3 Role of the Atlantic Meridional Overturning Circulation in the climate system

1.3.1 Redistribution of Heat & Biogeochemical Tracers by the Atlantic Meridional Overturning Circulation

The Atlantic Ocean is unique amongst the global ocean basins since heat is transported northward in both hemispheres owing to the large temperature contrast between the opposing flows in the upper and lower limbs of the AMOC.

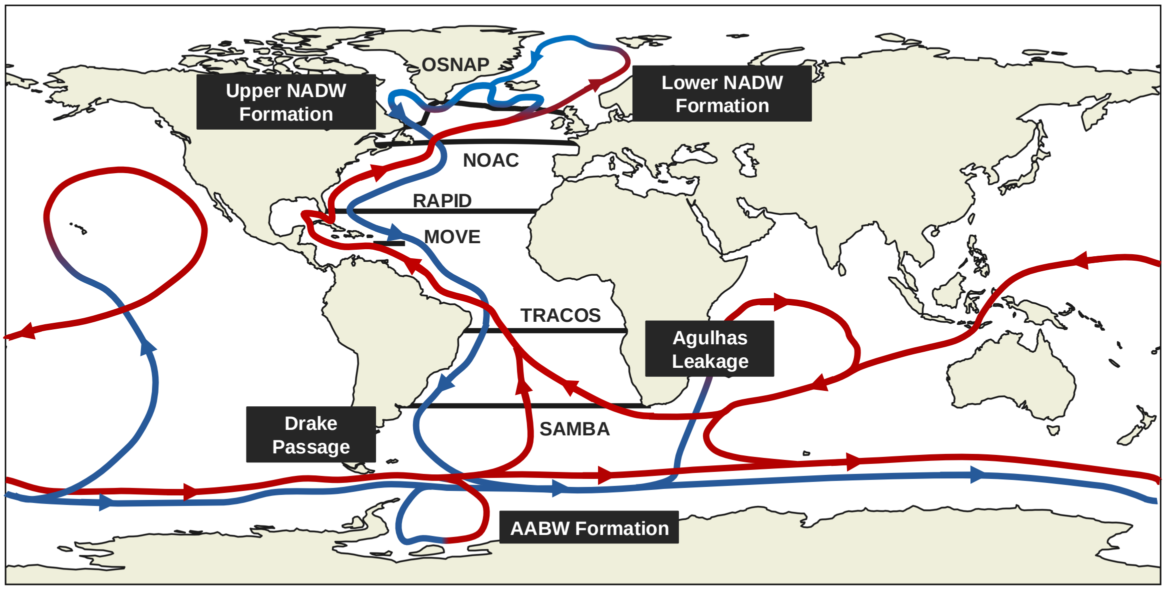

Figure 1.2: Schematic depicting the Atlantic Meridional Overturning Circulation (AMOC) in the form of a revised 'Great Ocean Conveyor Belt' following Broecker (1991) and Stokstad (2007). The pathways shown in red represent the flow of warm and light near-surface waters, whereas the pathways shown in blue represent the flow of cold, dense waters circulating at depth. In addition to the upper NADW formation taking place in the SPNA shown in Broecker (1991), we also include the formation of lower NADW in the Nordic Seas and the formation of AABW along the Antarctic continental margins (feeding the lower meridional overturning cell). The "warm" (Agulhas Leakage) and "cold" (Drake Passage) routes for near-surface waters to feed the AMOC upper limb in the South Atlantic are also shown. The solid black lines represent the locations of major ocean observing arrays in the Atlantic Ocean.

The meridional heat transport by the ocean peaks in the subtropical North Atlantic, where it accounts for 20-30% of the total atmosphere-ocean heat transport (Czaja & Marshall, 2006; Held, 2001; Trenberth & Caron, 2001; Wunsch, 2005). The northward heat transport across the equator, although weaker than in the subtropics, plays a central role in determining the mean position of the Intertropical Convergence Zone (ITCZ) in the northern hemisphere. The positioning of the ITCZ north of the equator is due to Bjerknes compensation (Bjerknes, 1964), which necessitates that a net southward atmospheric heat transport be established across the equator to balance the net northward heat transport by the ocean (Frierson et al., 2013; Kang et al., 2008; Marshall et al., 2014). A further consequence of this net northward ocean heat transport is that annually averaged surface air temperatures over the northern hemisphere are typically 1°-2°C warmer compared with the southern hemisphere (Feulner et al., 2013; Lockyer, 1906; Marshall et al., 2014).

The sinking of dense NADW and its southward export at depth in the lower limb of the AMOC also makes the SPNA a critical region for the sequestration of biogeochemical tracers into the deep ocean. The strong uptake of dissolved inorganic carbon (DIC; Takahashi et al., 2009; Zunino et al., 2015), dissolved oxygen (Atamanchuk et al., 2020; Koelling et al., 2017, 2022) and anthropogenic carbon (C_{ant}; Pérez et al., 2013; Sabine et al., 2004) at subpolar latitudes results from the cooling-driven transformation of surface water masses via air-sea exchange (termed the solubility pump). This is possible since the solubility of O_2 and CO_2 increases in colder water (Sabine & Tanhua, 2010; Volk & Hoffert, 2013; Yashayaev & Clarke, 2008). Meanwhile, the sequestration of dissolved organic carbon (DOC; Hansell et al., 2009) is governed by the biological pump, which mediates the transfer of organic matter into the deep ocean (de Vries et al., 2012; Lampitt et al., 2010; Martin et al., 2011; Sanders et al., 2014). By isolating oxygen and carbon enriched NADW from the atmosphere for many centuries in the lower limb, the AMOC ensures that the ocean maintains a long memory of biogeochemical anomalies introduced at the sea surface (Frajka-Williams et al., 2019).

In addition to its fundamental role in the global carbon cycle (e.g., Williams & Follows, 2011), the AMOC contributes to the high biological productivity of the SPNA through its associated meridional nutrient transport (Martin et al., 2011; Moore et al., 2018; Sarmiento et al., 2004; Schmittner, 2005). The AMOC provides a northward advective flux of nutrients from the subsurface of the subtropics along shoaling isopycnals which outcrop in the Subpolar Gyre (SPG) (Williams et al., 2006, 2011) in what Pelegrí and Csanady (1991) termed the North Atlantic nutrient stream. Since the high concentration of nutrients transported via the nutrient stream are ultimately sourced from waters of Sub-Antarctic origin (Palter et al., 2008; Sarmiento et al., 2004), North Atlantic primary production is intrinsically linked to the AMOC's inter-hemispheric connectivity (see review by Pelegrí et al., 2019).

1.3.2 The Atlantic Meridional Overturning Circulation in Past, Present & Future Climates

Both paleoclimate and instrumental records suggest that historical changes in the strength of the AMOC and its associated northward heat transport have moderated global climate variability on decadal to millennial timescales (e.g., Lynch-Stieglitz, 2017; Zhang et al., 2019). Over the coming century, the response of the AMOC to the increasing concentrations of greenhouse gases will also affect the trajectory of global warming through the uptake of excess heat and carbon (Boé et al., 2009; Buckley & Marshall, 2016). Here, we briefly review the role of the AMOC in shaping the past, present and future states of the Earth's climate, drawing particular attention to societally relevant impacts, such as the AMOC's influence on rainfall patterns, sea level and extreme weather events (e.g., Bellomo et al., 2021; Jackson et al., 2015; Volkov et al., 2023; Zhang et al., 2019).

Paleoclimate records offer compelling evidence that the global climate system has oscillated between markedly different states over the last glacial cycle (see review by Lynch-Stieglitz, 2017). In particular, paleoclimate data collected from Greenland ice cores (Andersen et al., 2004) show a fluctuating northern hemisphere climate over the last 120,000 years, characterised by colder stadial periods and warmer inter-stadial periods (Alley et al., 1999; Broecker et al., 1985; Lynch-Stieglitz, 2017). Throughout the second half of the last glacial cycle, these abrupt climate oscillations, referred to as Dansgaard-Oeschger events (Grootes et al., 1993; Voelker, 2002), were punctuated by Heinrich events, in which large volumes of freshwater were fluxed into the North Atlantic Ocean by iceberg discharges (Andrews, 1998; Bond et al., 1992). The prevailing paradigm is that the abrupt climate signature associated with Heinrich events is due to a shutdown and reorganisation of the AMOC in response to the freshening-induced cessation of NADW formation in the SPNA (Elliot et al., 2002; Keigwin & Lehman, 1994; Rahmstorf, 2002). In particular, paleoclimate studies propose that the dramatic reduction in ocean heat transport due to the shutdown of the AMOC results in an abrupt cooling of the northern hemisphere and a corresponding warming of the southern hemisphere (Buizert & Schmittner, 2015; Henry et al., 2016) consistent with a southward shift in the tropical atmospheric circulation (Alley, 2007). A reversal of this bipolar see-saw pattern (Alley & Clark, 1999; Broecker, 1998) has also been identified during anomalously strong AMOC states with widespread northern hemisphere warming compensated by southern hemisphere cooling (Gulev et al., 2021).

Looking to the present-day, instrumental records highlight the important role of the AMOC in regional and global climate variability through its relationship with North Atlantic Sea Surface Temperature (SST) variations on interannual to multi-decadal timescales (Delworth & Mann, 2000; Knight et al., 2005; Kushnir, 1994). This has been further demonstrated in numerical modelling studies, which show that an increase in northward heat transport associated with an intensification of the AMOC leads to a delayed increase in upper ocean heat content and hence SSTs in the SPNA (Delworth et al., 1993; Kim et al., 2018b, 2020; Zhang, 2008; Zhang et al., 2007). Alternative, albeit disputed (e.g., Zhang et al., 2013, 2016), hypotheses for the mechanism underlying North Atlantic SST variability on multi-decadal timescales include external radiative forcing (e.g., Bellomo et al., 2018; Booth et al., 2012) and stochastic atmospheric forcing (e.g., Cane et al., 2017; Clement et al., 2015).

The large-scale signature of observed low-frequency SST variability over the North Atlantic Ocean is encapsulated in a coherent mode of climate variability termed Atlantic Multi-decadal Variability (AMV; Delworth & Mann, 2000; Kerr, 2000; Kushnir, 1994; Sutton et al., 2018; Zhang, 2017). Positive phases of the AMV are associated with a dipole pattern of positive SST anomalies over the North Atlantic and considerably weaker negative SST anomalies over the South Atlantic, and thus resemble the bipolar see-saw response to AMOC changes inferred from paleoclimate records (Delworth & Mann, 2000).

The basin-scale warming and cooling of the upper North Atlantic Ocean characterised by the AMV has wide ranging climate impacts with important economic and societal implications (see review by Zhang et al., 2019). On a regional scale, positive phases of the AMV are associated with warmer and wetter summers over northern and western Europe (Knight et al., 2006; Sutton & Hodson, 2005), drier summers over southern Europe (Ruprich-Robert et al., 2017; Sutton & Dong, 2012) and North America (Enfield et al., 2001; Kushnir et al., 2010; Ruprich-Robert et al., 2018) and reduced Arctic sea ice extent (Årthun et al., 2012; Yeager et al., 2015; Zhang, 2015).

On a hemispheric scale, observations and numerical models also show a strong correlation between the AMV and the position of the ITCZ on multi-decadal timescales (Folland et al., 1986; Knight et al., 2006; Zhang & Delworth, 2006). During a positive phase of the AMV, the ITCZ shifts northward, favouring the development of Atlantic hurricanes (Sutton & Hodson, 2007; Yan et al., 2017; Zhang & Delworth, 2006) and enhancing rainy season rainfall over northeast Brazil (Folland et al., 2001) and summer monsoon rainfall over the Sahel (Folland et al., 1986; Martin et al., 2014; Zhang & Delworth, 2006).

Finally, global-scale impacts of the AMV have been identified through the modulation of other modes of atmospheric variability. For example, observational analyses suggest that the leading mode of the SST variability in the North Pacific, Pacific Decadal Variability (PDV; Deser et al., 2012), lags the AMV index by approximately a decade (Zhang & Delworth, 2007). Positive phases of the AMV have also been shown to influence tropical Pacific climate variability by inducing an equatorial Pacific SST pattern characteristic of the La Nina (cold) phase of the El Nino Southern Oscillation (ENSO; Kang et al., 2014; Levine et al., 2017).

As the concentration of greenhouse gases continues to increase over the 21st century, the AMOC will play a critical role in modulating the effective heat capacity of the ocean by governing the rate at which additional heat can be sequestered into the deep ocean (Kostov et al., 2014). This is compounded by the fact that the AMOC will also respond dynamically to anthropogenic forcing (Broecker, 1997). According to the Intergovernmental Panel on Climate Change Sixth Assessment Report (AR6), the AMOC will *very likely* decline over the 21st century irrespective of the shared socio-economic pathway or greenhouse gas emissions scenario considered (Fox-Kemper et al., 2021). The Sixth Coupled Model Intercomparison Project (CMIP6) projected decline in the AMOC over the 21stcentury ranges from 24% (4-46%) to 39% (17-55%) for 2.6°C and 8.5°C of global warming, respectively. However, the large spread in future AMOC projections amongst CMIP-class models has led to significant uncertainty in the magnitude of any future AMOC decline (Bellomo et al., 2021; Weijer et al., 2020). Furthermore, there is growing evidence that an anthropogenically forced historic AMOC decline (Caesar et al., 2018, 2021; Thornalley et al., 2018) may have been partially obscured by a compensating strengthening in the AMOC due to increasing anthropogenic aerosol forcing in coupled climate models (Hassan et al., 2021; Menary et al., 2020a; Robson et al., 2022).

The prospect of an abrupt collapse in the AMOC in response to anthropogenic forcing originates from conceptual models, such as box models, which highlighted the possibility that the AMOC could transition between two stable states (e.g., Gnanadesikan, 1999; Johnson et al., 2007; Rahmstorf & Willebrand, 1995; Stommel, 1961). Although direct observations of the AMOC are too short to corroborate the proposed bistability of the AMOC, it has frequently been invoked to explain the abrupt paleoclimate shifts coinciding with the extreme freshwater forcing recorded during Heinrich events (Lynch-Stieglitz, 2017). However, since no state-of-the-art coupled climate models included in CMIP6 simulate bistable AMOC behaviour before 2100, an abrupt collapse of the AMOC during the 21stcentury is considered a low probability, high impact event (Fox-Kemper et al., 2021).

The impacts of an abrupt AMOC collapse have been explored extensively in idealised coupled climate model experiments, in which the AMOC is artificially shutdown by introducing large freshwater inputs (hosing) to the surface of the SPNA (e.g., Jackson et al., 2023a). In response to an AMOC collapse, these experiments show substantially cooler and drier conditions over Europe and North America (Bellomo et al., 2023; Jackson et al., 2015; Vellinga & Wood, 2002, 2008), a southward shift in the ITCZ (Stouffer et al., 2006; Vellinga & Wood, 2002), a poleward shift and strengthening of the mid-latitude jet (Bellomo et al., 2021; Brayshaw et al., 2009), and an intensification of the Walker circulation (Orihuela-Pinto et al., 2022). The overall colder and drier European climate associated with a collapsed AMOC has profound implications for agriculture as crop yields decrease due to the marked reduction in projected vegetation productivity (Ritchie et al., 2020).

A further robust impact of future AMOC collapse or more gradual weakening is its substantial contribution to North Atlantic sea-level rise (Chen et al., 2019; Hu et al., 2009). This is because a weakened AMOC transports less heat northward in the subtropical North Atlantic, thereby accelerating upper ocean warming and local thermosteric sea-level rise along the western boundary (Volkov et al., 2023; Yin et al., 2010). The east coast of North America is especially vulnerable to sea-level rise owing to its high population density (Strauss et al., 2012), with coastal communities projected to be exposed to an increasing severity and frequency of coastal flood events in the decades to come (Ezer & Atkinson, 2014; Wdowinski et al., 2016).

1.4 Measures of the Atlantic Meridional Overturning Circulation

In recognition of the societal importance of the AMOC within the global climate system and the substantial uncertainty over its future trajectory, significant efforts have been made to monitor the state of the overturning circulation in recent decades. In this Section, we review the most widely used approaches to diagnose the strength of the AMOC using both in-situ observations and numerical model simulations.

1.4.1 Eulerian Measures of the Atlantic Meridional Overturning Circulation

1.4.1.1 Eulerian Overturning in Depth Coordinates

By far the most commonly used measure of the AMOC is the Eulerian meridional overturning stream function (e.g., Döös & Webb, 1994; Döös et al., 2012; Groeskamp et al., 2014). Traditionally, the meridional overturning stream function has been diagnosed in depth coordinates, which represents the zonally integrated and vertically accumulated meridional volume transport across a given latitude and above a given depth horizon (e.g., Bryan, 1986; Bryan & Cox, 1968; Manabe & Stouffer, 1988) (see Fig. 1.3a). However, the meridional overturning stream function can be defined mathematically for any given vertical coordinate ζ (e.g., density, temperature, salinity, oxygen etc.) as follows (Hirschi et al., 2020):

$$\psi(\phi, \zeta, t) = \int_{x_w}^{x_e} \int_{z(x,\phi,\zeta)}^{\eta} v(x, \phi, z', t)\ dz'\ dx \tag{1.1}$$

where the meridional velocity $v(x, \phi, z, t)$ is first accumulated vertically from the sea surface η to a specified depth $z(x, \phi, \zeta)$ (decreasing downward) before being integrated zonally between the western (x_w) and eastern (x_e) boundaries of the basin (Danabasoglu et al., 2014; Döös et al., 2008; Zika et al., 2012). In the case of the traditional meridional overturning stream function in depth coordinates, $\psi_z(\phi, z, t)$, the depth $z(x, \phi, \zeta)$ denotes a geopotential level (i.e., $\zeta = z$). However, this can be modified to be the depth of any given seawater property; for example, $\psi_{\sigma_\theta}(\phi, \sigma_\theta, t)$ is the meridional overturning stream function in potential density coordinates, where potential density is referenced to the sea surface.

To further simplify the 2-dimensional meridional overturning stream function in depth coordinates, the AMOC strength at each latitude has been traditionally defined as the maximum of $\psi_z(\phi, z, t)$ over the depth of the water column as follows:

$$MOC_z(\phi, t) = max_z\Big[\psi_z(\phi, z, t)\Big] \tag{1.2}$$

Physically, this represents the net volume transport, typically expressed in terms of Sverdrups (1 Sv $\equiv$ 1x10^6 m^3 s^{-1}), flowing northward which is balanced by a southward return flow at depth. As such, the depth at which the stream function reaches its maximum constitutes the interface between the upper and lower limbs of the AMOC at a given latitude. This ability to interpret both $\psi_z(\phi, z, t)$ and $MOC_z(\phi, t)$ geometrically, in addition to allowing us to identify regions of upwelling and downwelling at high latitudes, is a major advantage of the meridional overturning stream function in depth coordinates.

In addition to calculating the strength of vertical overturning, observations and numerical models are often used to quantify the societally-relevant meridional transports of heat and freshwater. The Meridional Heat Transport (MHT) by the ocean across a given latitude is calculated by zonally and vertically integrating the product of the meridional velocity $v(x, \phi, z, t)$ and the potential temperature $\theta(x, \phi, z, t)$ (Bryan, 1982; Johns et al., 2011; Johns et al., 2023b):

$$Q(\phi, t) = \int_{-H(x,\phi)}^{\eta} \int_{x_w}^{x_e} \rho_0 C_p v(x, \phi, z, t)\theta(x, \phi, z, t) \; dx \; dz \tag{1.3}$$

where ρ_0 is a reference seawater density, C_p is the specific heat capacity of seawater and $H(x, \phi)$ is the depth of the seafloor.

We can also define the Meridional Freshwater Transport (MFT) by the ocean across a given latitude as:

$$F_W(\phi, t) = \int_{-H(x,\phi)}^{\eta} \int_{x_w}^{x_e} v(x, \phi, z, t)\Big(\frac{S_0 - S(x, \phi, z, t)}{S_0}\Big) \; dx \; dz \tag{1.4}$$

where S is the seawater salinity and S_0 is a reference salinity. Recent studies have strongly criticised this calculation of MFT owing to its dependence on an arbitrary reference salinity, and instead favour the use of ocean salt transport due to its lack of ambiguity (e.g., Schauer & Losch, 2019).

Heat and freshwater transports are traditionally separated into vertical "overturning" and horizontal "gyre" components related to the zonal mean circulation and deviations from the zonal mean, respectively (e.g., Böning & Herrmann, 1994; Bryan, 1982; Bryden & Imawaki, 2001; Johns et al., 2011; Marsh et al., 2008; McDonagh et al., 2015; Msadek et al., 2013). Although this simple geometric decomposition into basin-wide vertical and horizontal circulation cells does conform to the traditional view of overturning as a closed circulation in depth coordinates, there is considerable debate regarding the degree of association between horizontal circulation and the Subtropical Gyre (STG). In order for the horizontal component of MHT to be equivalent to the heat transported by the STG, all recirculating water masses must, by construction, return along constant depth surfaces. However, observations suggest that water masses flowing northward in the upper Florida Current typically return southward at greater depths and densities (Spall, 1992; Talley, 2003) owing to cooling and subduction by Ekman pumping along-stream. Thus, it is possible that a substantial fraction of the STG heat transport will instead project onto the vertical component typically associated with overturning (Berglund et al., 2021). The extent to which subtropical MHT can be partitioned into physically meaningful components associated with the flow structures of the AMOC and STG therefore remains an important open question.

1.4.1.2 Diagnosing the Eulerian Overturning in Depth Coordinates from Observations

The decision of observational oceanographers to diagnose the AMOC strength in depth coordinates was principally informed by the hydrography of the subtropical North Atlantic, given that strong thermal stratification ensures warm and saline water flowing northward is vertically separated from cold and fresh NADW returning southward (Kanzow et al., 2007). Prior to the early 2000s, diagnosing the strength of the AMOC from in-situ observations relied upon the collection of vertical profiles of seawater properties along a line of constant latitude to form a hydrographic section (e.g., Bryden & Hall, 1980; Roemmich & Wunsch, 1985). However, reliably inferring long-term AMOC changes from individual "snapshots" captured by hydrographic sections is a major challenge due to the aliasing of high-frequency intra-annual variability (Frajka-Williams et al., 2019; Kanzow et al., 2007; Wunsch & Heimbach, 2006).

In recognition of the need for high-frequency measurements of seawater properties in order to improve confidence in observations of AMOC variability, trans-basin ocean observing systems were introduced. The Rapid Climate Change Meridional Overturning Circulation and Heat Flux Array (herein referred to at the RAPID arrray) was deployed in 2004 to provide the first continuous estimates of the AMOC strength and structure, as well as heat and freshwater transports across 26.5°N (Cunningham et al., 2007). The observing system consists of moored instruments measuring seawater properties along the western and eastern boundaries of the basin to calculate the geostrophic transport of the Mid-Ocean region

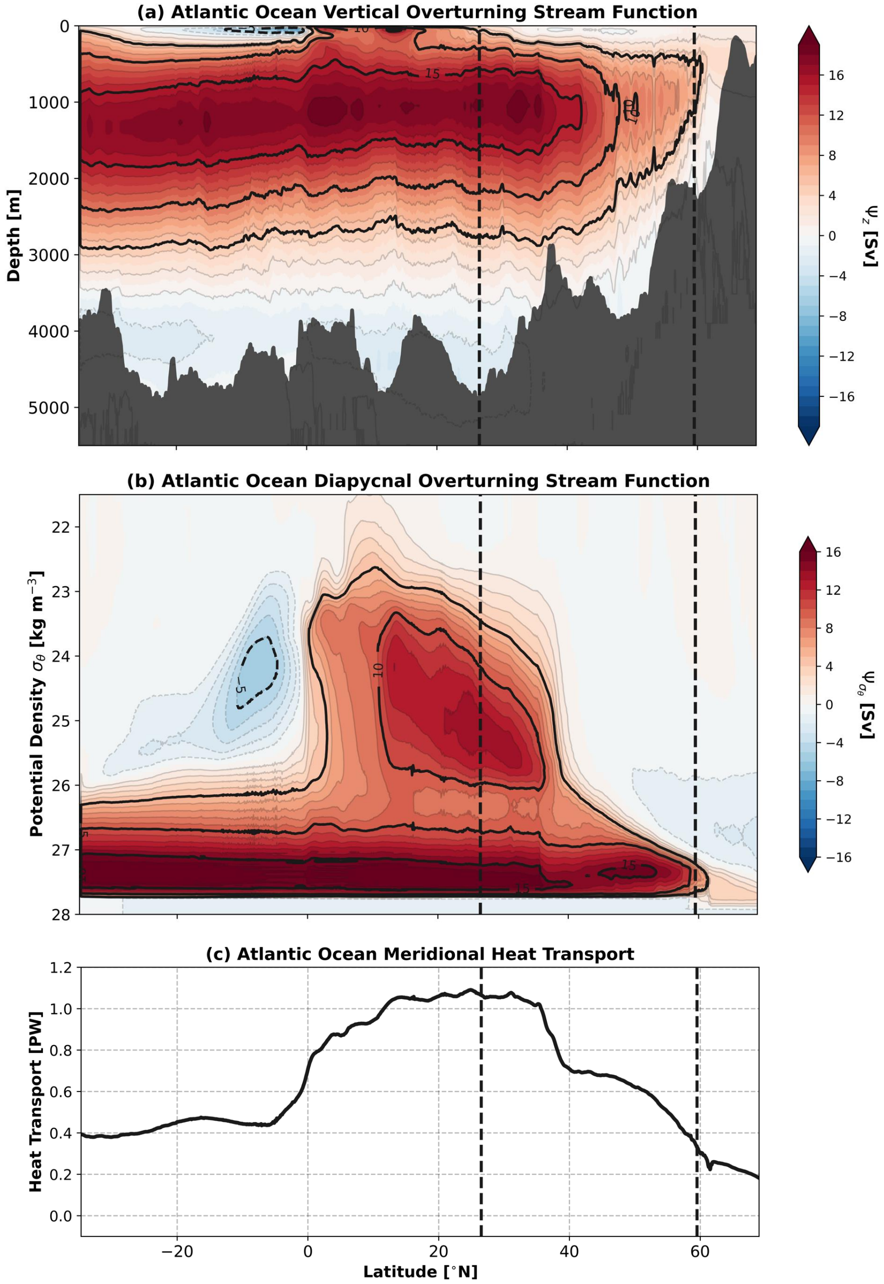

Figure 1.3: (a) Time-mean (1990-2015) Atlantic Ocean Eulerian meridional overturning stream function in latitude-depth coordinates. (b) Time-mean (1990-2015) Atlantic Ocean Eulerian overturning stream function in latitude-density coordinates, where potential density is referenced to the sea surface. Positive streamlines (red shading) indicate a clockwise circulation, whereas negative streamlines (blue shading) indicate anti-clockwise circulation. (c) Time-mean (1990-2015) Atlantic Ocean meridional heat transport as a function of latitude. All diagnostics are calculated using the ORCA0083-N06 ocean sea-ice hindcast (Table 1.1), which simulates the historical period from 1958-2015. Black dashed lines indicate the latitudes of the RAPID (26.5°N) and OSNAP (59°N) observing arrays.

(Baehr et al., 2004; Hirschi et al., 2003), acoustic Doppler current profilers (ADCPs) directly measuring the transport of the western boundary current, a submarine cable providing electromagnetic estimates of the Florida Current transport (Meinen et al., 2010; Shoosmith et al., 2005), and satellite-derived surface Ekman transports (McCarthy et al., 2015a). Estimates of the AMOC strength in depth coordinates are made at 10 day intervals by combining these transport components with a spatially-uniform compensation transport, constructed to ensure conservation of mass across the section (Kanzow et al., 2007).

Over the entire 17-year period of available RAPID observations (2004-2020), the average strength of the AMOC at 26.5°N is 16.9 ± 1.2 Sv and is dominated by large seasonal to interannual variability (Johns et al., 2023b). The average MHT across 26.5°N is 1.20 ± 0.12 PW between 2004-2020 (Johns et al., 2023b) and the time-mean MFT is 0.43 ± 0.02 Sv between 2004-2018 (Li et al., 2021b). Both the MHT and MFT across the RAPID array exhibit a very high correlation with the AMOC strength (Johns et al., 2023b; Li et al., 2021b; McDonagh et al., 2015), underscoring the dominant role of the overturning circulation in the redistribution of heat and freshwater.

Following the success of the RAPID program, several contemporaneous ocean observing systems have since been deployed throughout the Atlantic Ocean (see Fig. 1.2, Frajka-Williams et al., 2023). These include the South Atlantic MOC Basin-wide Array (SAMBA) at 34.5°S (Kersalé et al., 2020; Meinen et al., 2013), Meridional Overturning Variability Experiment (MOVE) at 16°N (Kanzow et al., 2006; Send et al., 2011), TRopical Atlantic Circulation & Overturning at 11°S (TRACOS; Herrford et al., 2021; Tuchen et al., 2022) and the North Atlantic Changes array (NOAC) at 47°N (Rhein et al., 2019; Wett et al., 2023).

1.4.1.3 Eulerian Overturning in Density Coordinates

Analysis of biennial hydrographic sections extending from Greenland to Portugal by the OVIDE program highlighted one of the major shortcomings of the traditional meridional overturning stream function in depth coordinates when implemented at subpolar latitudes (Lherminier et al., 2007; Lherminier et al., 2010). In contrast to the subtropics, where warm and saline northward flow is separated vertically from the cold and fresh southward return flow at depth, the weaker vertical stratification in the SPNA means that the upper and lower limbs of the AMOC reside at similar depths, but on opposite sides of the basin. This arises because warmer, lighter waters flowing northward in the eastern SPNA become colder and denser while circulating cyclonically around the SPG. As a result, the total shallow-to-deep conversion captured by the meridional overturning stream function in depth coordinates significantly underestimates the total light-to-dense conversion taking place in the SPNA (Buckley et al., 2023; Zhang & Thomas, 2021). In order to obtain a more accurate 2-dimensional depiction of the complex, 3-dimensional flow field, the meridional overturning stream function in density coordinates, $\psi_{\sigma_\theta}(\phi, \sigma_\theta, t)$ (see Fig. 1.3b), is now widely used to calculate the AMOC strength at subpolar latitudes (e.g., Lherminier et al., 2010; Lozier et al., 2019).

The latest addition to the family of trans-basin ocean observing systems is the Overturning in the Subpolar North Atlantic Program (OSNAP), which has continuously measured the volume, heat and freshwater transports across the subpolar basin since 2014 (Li et al., 2017; Lozier et al., 2017). The OSNAP trans-basin observing system consists of two sections: OSNAP West, which extends from the southeastern Labrador Shelf to the southwest coast of Greenland, and OSNAP East, which extends from the southeast coast of Greenland to the Scottish Shelf. Moored instruments, measuring seawater properties and velocities, are located along the boundaries of each of the four major basins of the SPNA, namely, the Rockall Trough, Iceland Basin, Irminger Basin, and Labrador Sea. Data from the OSNAP observing system is also supplemented by satellite-derived surface Ekman transports and data from Argo floats, satellite altimetry and climatological seawater properties in order to calculate transport metrics (Fu et al., 2023).

Over the 6-years of available OSNAP observations, the average strength of the AMOC across the full observing array is 16.7 ± 0.6 Sv. Historically, numerical modelling studies have identified dense water formation in the Labrador Sea interior as a major contributor to the subpolar AMOC and its decadal to multi-decadal variability (Böning et al., 2006; Li & Lozier, 2018; Menary et al., 2015; Yeager & Danabasoglu, 2014). However, OSNAP observations have broadened this long-standing paradigm (Fu et al., 2023; Li et al., 2021a; Lozier et al., 2019) to recognise the significant role played by both the eastern and western basins, given that the mean strength and interannual variability of the subpolar AMOC is dominated by dense water formation north of OSNAP East (16.3 ± 0.6 Sv) rather than OSNAP West (3.0 ± 0.5 Sv). This is consistent with the earlier observations of Pickart and Spall (2007), which showed a weak diapycnal overturning in spite of strong water mass transformation in the Labrador Sea. As a consequence of the close relationship between heat loss and dense water formation, the total MHT is also dominated by OSNAP East (0.42 ± 0.01 PW), which explains 85% of the time-mean total MHT (0.50 ± 0.01 PW) between 2014-2020 (Lozier, 2023). This is in contrast to the partitioning of the time-mean MFT between the two OSNAP sections, since OSNAP West (-0.17 ± 0.01 Sv) and OSNAP East (-0.18 ± 0.01 Sv) contribute approximately equally to the total southward transport of freshwater.

1.4.1.4 Eulerian Overturning in Thermohaline Coordinates

The contradiction between the relatively weak diapycnal overturning recorded along the OSNAP West array and the strong wintertime cooling experienced by water masses within the Labrador Sea highlights an important limitation of the meridional overturning stream function in density coordinates. Specifically, when warm and salty water masses circulate around the Labrador Sea they are both cooled and freshened along-stream, such that the densification due to heat loss is almost entirely offset by freshening-induced lightening due to exchange with fresh coastal current waters (Bebieva & Lozier, 2023; Zou et al., 2020b, 2024). As a result of this density compensation, the total light-to-dense conversion captured by the meridional overturning stream function in density coordinates is approximately six times weaker than the amount of warm-to-cold and saline-to-fresh conversion taking place north of OSNAP West (Lozier, 2023).

The inability of the meridional overturning stream function formulated in density coordinates to capture water mass changes taking place along isopycnals has motivated the use of meridional overturning stream functions in potential temperature, $\psi_\theta(\phi, \theta, t)$, and salinity, $\psi_S(\phi, S, t)$, coordinates to diagnose the diathermal and diahaline contributions to overturning (e.g., Buckley et al., 2023; Zou et al., 2020b). A further advantage of calculating the meridional overturning stream functions in potential temperature and salinity coordinates is that they are intrinsically related to the MHT and MFT. For example, the MHT (Fig. 1.3c) can be expressed succinctly in terms of the volume transport in temperature layers as follows:

$$Q(\phi, t) = \rho_0 C_p \int_{\theta_H}^{\theta_\eta} \psi_\theta(\phi, \theta, t)\ d\theta \tag{1.5}$$

where θ_η and θ_H represent the potential temperatures at the sea surface and the sea floor, respectively (Boccaletti et al., 2005; Czaja & Marshall, 2006; Ferrari & Ferreira, 2011). A disadvantage of visualising the AMOC in either the ϕ-θ or ϕ-S plane is that potential temperature and salinity do not always increase monotonically with depth and thus interpreting streamlines geometrically can be challenging. Previous studies have attempted to overcome this challenge by re-projecting the meridional overturning stream function in tracer coordinates into depth coordinates by plotting the values of the stream function at the zonal-mean depths of the iso-surfaces at each latitude (Foukal & Chafik, 2024; McIntosh & McDougall, 1996; Rousselet et al., 2020; Xu et al., 2018b).

Other studies have dispensed with geographical coordinates all together in favour of combining temperature and salinity coordinates to form a thermohaline stream function (Cuny et al., 2002; Döös et al., 2012; Marsh et al., 2005; Zika et al., 2012). The thermohaline stream function, defined as the integral of volume transport in the θ-S plane, represents the transformation of water masses across temperature and salinity surfaces without differentiating between flow occurring along or across isopycnals (Döös et al., 2012; Zika et al., 2012). Many of the advantages of using the thermohaline stream function to quantify the strength of the AMOC are outlined in Zika et al. (2012), including the ability to easily calculate advective transports of heat and freshwater alongside the typical transit times of the global thermohaline circulation. An obvious drawback of the thermohaline stream function is the absence of any geographical information to relate diathermal and diahaline transformation of water masses to where they occur in the global ocean. It is possible to determine the geographical pathway of a water mass following a given streamline from one basin to the next (Zika et al., 2012); however, there remains inherent ambiguity when similar thermohaline properties are found in several ocean basins.

1.4.1.5 Eulerian Overturning & the Water Mass Transformation Framework

A major advantage of quantifying the strength of the AMOC in tracer (i.e., density, temperature or salinity) rather than traditional depth coordinates is that it can be directly related to air-sea buoyancy fluxes and mixing through the water mass transformation framework (Evans et al., 2023; Marsh, 2000; Speer & Tziperman, 1992; Walin, 1982; Xu et al., 2018b; Zou et al., 2024). Introduced by Walin (1982), the water mass transformation framework connects the rate of change of volume below a given tracer surface to the net volume flux across the surface and the divergence of volume transport at the boundaries of the specified geographical domain (Buckley et al., 2023).

Since, on sufficiently long timescales, the total water mass transformation north of a given latitude must be balanced by southward export in the lower limb rather than through the accumulation of volume (Buckley et al., 2023; Desbruyères et al., 2019), the strength of the AMOC in density coordinates can be estimated directly from diapycnal volume fluxes. Given that surface buoyancy fluxes dominate diapycnal transformation, many observational and numerical modelling studies have used the surface-forced water mass transformation due to the fluxes of heat and freshwater at the sea surface as an indicator of AMOC strength (e.g., Desbruyères et al., 2019; Grist et al., 2009; Josey et al., 2009; Marsh, 2000; Megann et al., 2021; Petit et al., 2020). However, an important caveat of this approach is that it neglects the contribution of diapycnal mixing, which plays a critical role in the formation of NADW and, hence, the composition of the lower limb in the SPNA (Evans et al., 2023; Jackson & Petit, 2023; Stendardo et al., 2024; Zou et al., 2024).

1.4.2 Lagrangian Measures of the Atlantic Meridional Overturning Circulation

The Lagrangian perspective of fluid dynamics, where fluid motion is measured by following an individual parcel through space and time, provided the basis for the earliest measurements of ocean circulation (Bower et al., 2019). Although many early records of ocean currents resulted from measurements of opportunity (Richardson, 2019), coordinated Lagrangian measurements now constitute a key component of the global ocean observing system, including those made by surface drifters (Lumpkin et al., 2017) and subsurface Argo profiling floats (Wong et al., 2020). To complement the necessarily limited number of Lagrangian observations (Bower et al., 2019), the calculation of virtual water parcel trajectories using the Eulerian velocity fields of Ocean General Circulation Models (OGCMs) began in the 1990s (e.g., Blanke & Raynaud, 1997; Döös, 1995; Drijfhout et al., 1996). This Lagrangian approach to understanding the kinematics of the ocean circulation is similar to the use of Eulerian passive tracers. However, there is an important distinction between the two methodologies; Lagrangian trajectories represent the pathways of water parcels passively advected by the resolved model velocity field, whereas passive tracer experiments include an explicit diffusion term (e.g., Döös et al., 2013).

1.4.2.1 Lagrangian Particle Tracking

Throughout this thesis, we evaluate the trajectories of virtual water parcels using the Lagrangian particle tracking tool TRACMASS, which was first introduced by Döös (1995). TRACMASS, alongside its close relative Ariane (Blanke & Delecluse, 1993), belongs to the inaugural family of Lagrangian particle tracking tools, which determine water parcel trajectories using analytical streamtube methods. To define a streamtube, let us consider an incompressible (Boussinesq) and thus non-divergent flow field output by a typical OGCM. We can define a streamtube as a collection of streamlines which form an impermeable tube, since there can be no flow normal to a streamline. It can be further shown that, in order to obey mass conservation, the mass flux, or equivalently, the volume flux must remain constant along the streamtube, thereby ensuring volume transport is conserved along-stream. By modelling each water parcel trajectory as an individual streamtube with a prescribed initial volume transport, Döös (1995) and Blanke and Raynaud (1997) developed analytical methods to quantify the volume transport pathways comprising a steady, incompressible flow field.

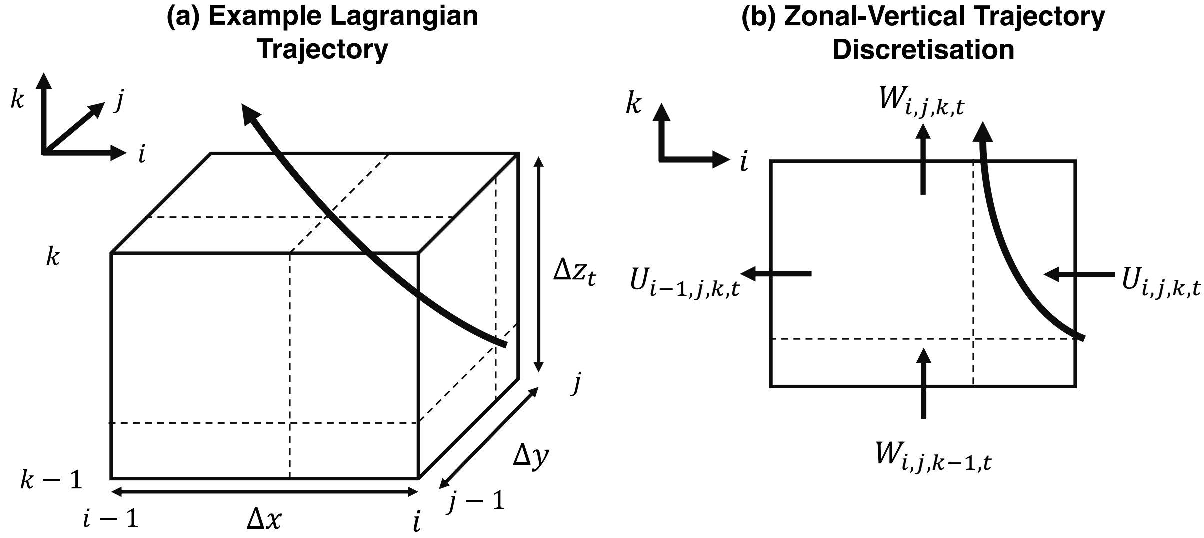

Figure 1.4: (a,b) Schematics illustrating an example Lagrangian water parcel trajectory path through a numerical model grid cell calculated using an analytical streamtube method.

To calculate the Lagrangian trajectory of a given water parcel through a steady 3-dimensional velocity field, the trajectory path through each numerical model grid cell is determined analytically by solving for the streamlines between the grid cell faces (see Fig. 1.4) (Blanke & Raynaud, 1997; Döös et al., 2013, 2017). This is achieved using the discrete form of the continuity equation applied to a given model grid cell:

$$U_{i,j,k,t} - U_{i-1,j,k,t} + V_{i,j,k,t} - V_{i,j-1,j,t} + W_{i,j,k,t} - W_{i,j,k-1,t} = 0 \tag{1.6}$$

where U and V, representing the volume transports in the zonal (x) and meridional (y) directions, are defined as follows:

$$U_{i,j,k,t} = u_{i,j,k,t}\ \Delta y_{i,j}\ \Delta z_{i,j,k,t} \quad V_{i,j,k,t} = v_{i,j,k,t}\ \Delta x_{i,j}\ \Delta z_{i,j,k,t} \tag{1.7}$$

where u and v are the zonal and meridional velocities at the grid cell face (i, j, k), Δx and Δy are the zonal and meridional grid cell spacings and Δz is the time-evolving vertical level thickness. The vertical (z) volume transports through the upper ($W_{i,j,k,t}$) and lower ($W_{i,j,k-1,t}$) grid cell faces (see Fig. 1.4b) are determined using continuity rather than using the resolved model vertical velocities (Döös et al., 2017).

Inside a grid cell, the velocity components of a water parcel ($u = u(x)$, $v = v(y)$, $w = w(z)$) are calculated by linearly interpolating between the velocity values defined at opposing grid cell faces (Döös et al., 2013). For example, the local zonal velocity $u(x)$ is given by:

$$u(x) = u_{i-1,j,k} + \Big(\frac{x - x_{i-1}}{\Delta x}\Big)(u_{i,j,k} - u_{i-1,j,k}) \tag{1.8}$$

An analytical expression for the water parcel displacement in each coordinate direction is then obtained following Blanke and Raynaud (1997), which describes the trajectory path through the grid cell. To identify the location where the water parcel exits the grid cell, the transit times taken to reach each opposing grid cell face are calculated (t_x, t_y, t_z). The shortest of the three possible transit times (t_{min}) determines both which grid cell face the water parcel will cross to enter the adjacent grid cell and its final displacements along the remaining two coordinate axes (i.e., $y_{out} = y(t_{min})$ and $z_{out} = z(t_{min})$ when exiting via a zonal grid cell face).

Since the initial application to steady-state velocity fields output by OGCMs (Blanke & Raynaud, 1997; Döös, 1995; Drijfhout et al., 1996), the analytical integration scheme described above has been extended to time-evolving flow fields (e.g., Döös et al., 2013, 2017). The stepwise-stationary scheme assumes that the flow is steady between successive time-mean velocity fields output by an OGCM (Döös et al., 2017). When Lagrangian trajectories are evaluated offline using existing OGCM output this is typically implemented in one of two ways. The simplest approach is to assume that the velocity field is piece-wise stationary and changes discretely at a time-step equivalent to the interval between two successive velocity fields output by the model (Blanke & Raynaud, 1997; Blanke et al., 1999). The alternative approach is to linearly interpolate between the velocity fields output by the OGCM to generate a larger number of shorter intermediate time-steps (Döös et al., 2017).

There are three major advantages of evaluating water parcels trajectories using analytical streamtube methods over discrete time-stepping schemes (e.g., OceanParcels; Delandmeter & Van Sebille, 2019). Firstly, analytical schemes are, by definition, more accurate than numerical integration schemes, which include both truncation errors and errors resulting from the interpolation of the velocity field along the trajectory path. Second, analytical schemes are more computationally efficient than numerical schemes since we only need to calculate trajectory positions on model grid cell faces (see review by Van Sebille et al., 2018). Finally, streamtube-based methods respect the inherent three-dimensional non-divergence of the flow field calculated using a Boussinesq OGCM, thereby enabling Lagrangian trajectories to be interpreted as volume transport pathways (Van Sebille et al., 2018). An additional benefit of this self-consistency is that trajectories can be advected both forward and backward in time and therefore allow us to determine both the evolution and the origins of water parcels (Blanke & Raynaud, 1997).

1.4.2.2 Lagrangian Overturning Stream Functions

Since Lagrangian trajectories evaluated using analytical streamtube methods represent the pathways of water parcels whose volume transport is conserved along-stream, there is a long-history of using trajectories to quantify the water mass exchanges between ocean basins (Blanke & Raynaud, 1997; Blanke et al., 1999; Döös, 1995). Such connectivity analyses are now routinely performed by summing the volume transports associated with the subset of all water parcel trajectories, evaluated either forward or backward-in-time, which transit between two specified regions (Van Sebille et al., 2018).

A natural extension to quantifying the Lagrangian connectivity between two regions is to assess how such connectivity is achieved. To do this, Blanke et al. (1999) introduced the concept of the Lagrangian stream function as a means to project the 3-dimensional volume transport pathways of a given water mass into a two-dimensional representation of the flow field. Let us consider a region of the North Atlantic Ocean bounded by two zonal trans-basin sections to the north and south and continental land masses to the east and west. Water parcels are initialised along both the northern and southern boundaries, sampling the total volume transport directed into the region, before being passively advected until they exit the region via either boundary. The volume transport V_n conveyed along a water parcel trajectory, indexed by n, is recorded on each crossing of a model grid cell face, resulting in a 3-dimensional volume transport field representing its flow through the domain. Since each water parcel trajectory entering a model grid cell must subsequently exit, the volume transport field associated with the water parcel is non-divergent by construction and thus satisfies the following condition:

$$V^{\lambda}_{i,j,k,n} - V^{\lambda}_{i-1,j,k,n} + V^{\phi}_{i,j,k,n} - V^{\phi}_{i,j-1,k,n} + V^{z}_{i,j,k,n} - V^{z}_{i,j,k-1,n} = 0 \tag{1.9}$$

where V^{λ}, V^{ϕ}, V^{z} are the volume transport due to the water parcel crossing zonal (i, λ), meridional (j, ϕ) and vertical (k, z) model grid cell faces, respectively. By summing the 3-dimensional volume transport fields associated with all water parcel trajectories and integrating along a chosen coordinate axes (i.e., zonal, meridional or vertical), a two-dimensional non-divergent volume transport field is obtained, which can be represented using a stream function.

Returning to our North Atlantic example, we choose to construct a Lagrangian meridional overturning stream function ($F^{\phi z}$) by vertically accumulating (downwards; the direction of increasing k) the 2-dimensional volume transport field obtained by integrating zonally over the total water parcel volume transport field (see Fig. 1.5a-b) as follows (Döös et al., 2008; Kjellsson & Döös, 2012):

$$F^{\phi z}_{j,k} = \sum_{k'=1}^{k} \sum_{i} \sum_{n} V^{\phi}_{i,j,k',n} \tag{1.10}$$

Importantly, as discussed by Döös et al. (2013) and Berglund et al. (2017), the indices i, j, k do not need to correspond to the discrete coordinates of the numerical model grid. For example the vertical index k is often replaced with a discrete potential temperature θ, absolute salinity S or potential density σ_θ index to form a Lagrangian meridional overturning stream function in latitude-tracer coordinates (Berglund et al., 2021, 2022, 2023).

The total Lagrangian stream function, constructed from all of the water parcel trajectories entering a given region, has been shown to converge towards the time-mean Eulerian stream function (over the duration water parcels are advected) provided that a sufficient number of water parcels are initialised (Döös et al., 2008; Kjellsson & Döös, 2012). According to Döös et al. (2008), a sufficient "Lagrangian resolution" is achieved when the Lagrangian stream function is independent of the number of water parcel trajectories initialised. In practice, this equates to prescribing a sufficiently small volume transport per water parcel, since the volume transport associated with each water parcel is inversely proportional to the total number of trajectories initialised (Döös, 1995; Döös et al., 2013).

The advantage of calculating the Lagrangian stream function for a given flow field is that it can be partitioned into partial Lagrangian stream functions, reflecting the contributions of specific collections of trajectories, which share common water mass properties (Blanke et al., 1999; Döös et al., 2008). This ability to decompose the time-mean flow field into separate circulation pathways has led many studies to employ Lagrangian stream functions in order to investigate the structure and connectivity of the AMOC. In the South Atlantic, Lagrangian stream functions have been used extensively to assess the sources of the upper limb of the AMOC, including quantifying the contributions of cold (Drake Passage) and warm (Agulhas leakage) water pathways (Berglund et al., 2021; Drijfhout et al., 2003; Durgadoo et al., 2013, 2017; Rühs et al., 2019; Schmidt et al., 2021;

Speich et al., 2001, 2002). In the North Atlantic, there has naturally been a greater focus on identifying the mean flow pathways responsible for transforming water masses between the upper and lower limbs of the AMOC. In particular, Thomas et al. (2015) and Lique and Thomas (2018) decomposed the Lagrangian meridional overturning stream function in latitude-depth coordinates according to the locations where dense NADW is subducted from the surface mixed layer in both historical and future climate simulations. Meanwhile, Berglund et al. (2023) used Lagrangian meridional overturning stream functions in latitude-depth and latitude-tracer coordinates to quantify the exchanges of heat and salt along the inter-gyre boundary and highlight the importance of subsurface mixing in forming Subpolar Mode Water (SPMW), the precursor to NADW.

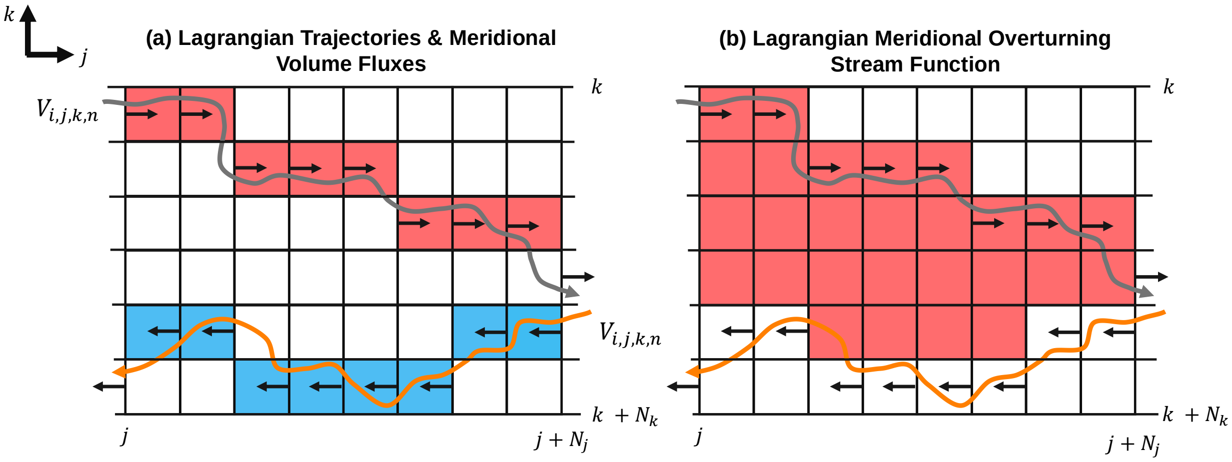

Figure 1.5: Schematics illustrating the construction of a Lagrangian overturning stream function using the volume transports associated with two idealised water parcel trajectories. The shallow trajectory, shown in grey, is initialised along the southern boundary before flowing northward in the AMOC upper limb until reaching the northern boundary. The deep trajectory, shown in orange, is initialised along the northern boundary before flowing southward in the AMOC lower limb until reaching the southern boundary. (a) The fixed volume transports $V_{i,j,k,n}$ conveyed along each trajectory are recorded on crossing each meridional grid cell face (j, k) to form a 2-dimensional volume transport field in the latitude-depth (ϕ-z) plane (red shading depicts northward transport, blue shading depicts southward transport). (b) The Lagrangian meridional overturning stream function in latitude-depth coordinates ($F_{j,k}^{\phi z}$) is then obtained by calculating the cumulative sum of the meridional volume transport field from the sea surface ($k = 1$) to the sea floor ($k + N_k$).

Given that the convergence between Lagrangian and Eulerian stream functions strictly only applies to steady flow fields, there have, understandably, been far fewer studies dedicated to investigating the nature of AMOC variability using the Lagrangian framework. However, extending the use of Lagrangian stream functions beyond the decomposition of more familiar Eulerian diagnostics may bring some notable advantages. In particular, since Lagrangian overturning stream functions are calculated using water parcel trajectories whose transit times range from days to decades, there is an opportunity to use large collections of Lagrangian overturning stream functions calculated from many successive water parcel initialisations to investigate the detailed nature of water mass transformation variability following the flow. Furthermore, this would allow us to identify the dominant pathways and advective timescales of variability, which is not possible using traditional Eulerian overturning stream functions calculated from individual "snapshots" of the flow field.

1.5 Pathways of the Atlantic Meridional Overturning Circulation in the North Atlantic Ocean

Throughout this thesis, our analyses focus on the circulation pathways and dynamics of the North Atlantic Ocean, spanning the latitudinal range 5°N - 65°N. In this Section, we provide a state-of-the-science summary of the water masses and circulation pathways constituting the North Atlantic Meridional Overturning Circulation (Fig. 1.6).

Traditionally, the large-scale circulation of the North Atlantic Ocean has been characterised by the complex interplay between the AMOC and the primarily wind-driven STG and SPG circulations. The anticyclonic STG takes a classically asymmetric form with an intense, narrow western boundary current flowing northward, which is compensated by a broad and diffuse southward return flow throughout the ocean interior. In contrast, the cyclonic SPG circulation is more zonally symmetric owing to the strong topographic steering of currents in the presence of weaker stratification (Talley et al., 2011). In order for a large-scale overturning circulation to exist, the subtropical and subpolar gyres are connected through the northward flowing North Atlantic Current (upper limb) and the southward flowing DWBC (lower limb).

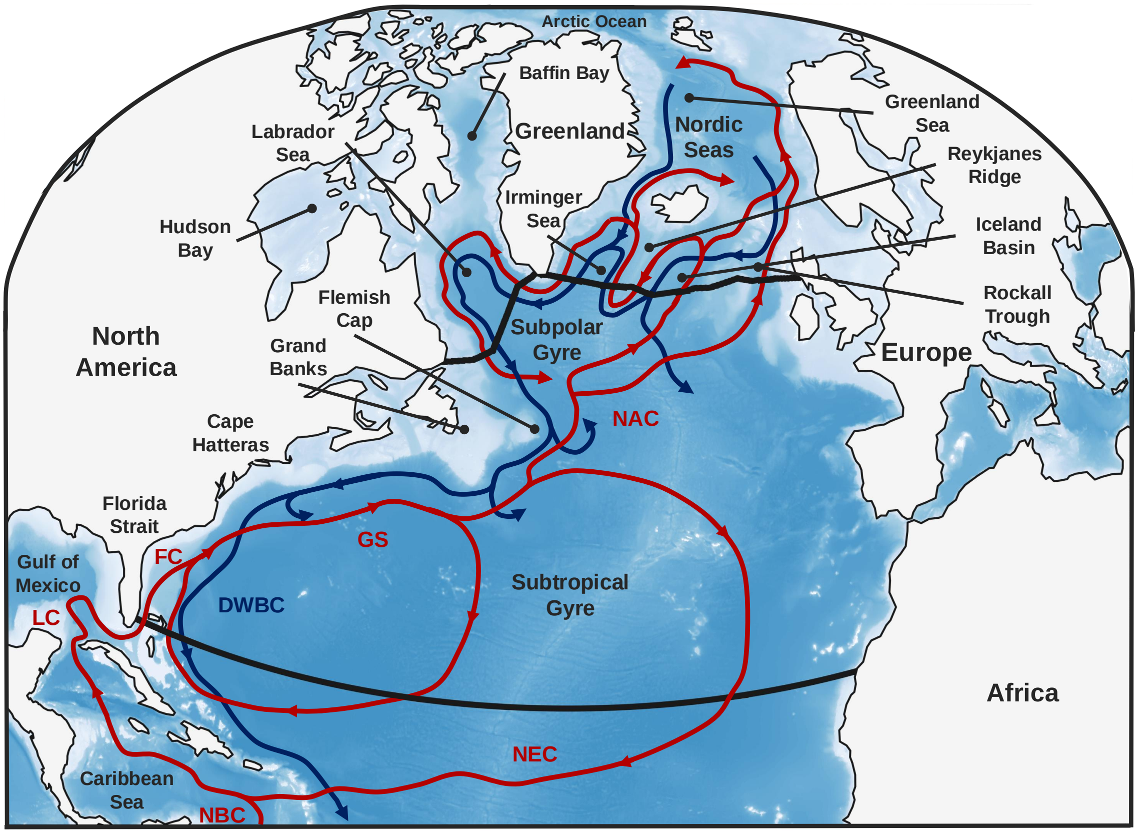

Figure 1.6: Schematic of the circulation pathways which constitute the Atlantic Meridional Overturning Circulation in the North Atlantic Ocean. The pathways of upper limb waters flowing in the upper 1000 m of the North Atlantic are shown in red and are defined as follows: **NEC** = North Equatorial Current, **NBC** = North Brazil Current, **LC** = Loop Current, **FC** = Florida Current, **GS** = Gulf Stream, **NAC** = North Atlantic Current. The Deep Western Boundary Current (**DWBC**), alongside dispersive interior pathways, returns dense lower limb waters southward.

At the southern boundary of the STG, upper limb waters, originating from the Drake Passage (∼40%) and the Agulhas leakage (∼60%; Rodrigues et al., 2010; Rühs et al., 2019), arrive via the North Brazil Current and diffuse interior pathways (Fratantoni et al., 2000; Halliwell et al., 2003). On reaching the subtropics, these intermediate waters combine with Subtropical Underwater (STUW) recirculating in the southern limb of the STG. STUW, also known as salinity maximum water, forms in the westward flowing North Equatorial Current when high salinity surface waters are subducted below warmer and fresher tropical waters (Talley et al., 2011; Worthington, 1976). Upper limb waters then flow northwestward through the Caribbean Sea and the Yucatan Channel into the Gulf of Mexico (Candela et al., 2003; Johns et al., 2002; Rousset & Beal, 2010). Here they contribute to the strongly eddying Loop Current before being exported northward through the Straits of Florida via the Florida Current (Lumpkin & Johnson, 2013; Molinari & Morrison, 1988). Interestingly, although both hydrographic (Schmitz et al., 1993; Schmitz & McCartney, 1993; Schmitz & Richardson, 1991) and nutrient (Palter et al., 2008) analyses suggest that tropical-origin waters make an important contribution to the total Florida Current transport, little is known about how these specific waters evolve downstream and hence contribute to the AMOC at subtropical latitudes.

North of the Florida Straits, upper limb waters transported in the Florida Current combine with recirculating STG waters flowing northward in the Antilles Current to form a western intensified boundary current, widely known as the Gulf Stream. On separating from the coast of North America near Cape Hatteras (Schmitz Jr, 1996), the Gulf Stream transitions from a narrow western boundary current into a highly turbulent and strongly meandering current transporting a core of warm and saline water into the central North Atlantic (e.g., Lillibridge & Mariano, 2013; Rossby, 1996). The separated Gulf Stream transport intensifies downstream, steadily increasing from $\sim$30 Sv at the Florida Straits to $>$140 Sv at 65°W (Hogg, 1992; Hogg & Johns, 1995). Due to its growing instability, the separated Gulf Stream loses water on both its northern and southern flanks via large eddy-driven recirculation features known as the Northern (Hogg, 1992; Hogg et al., 1986) and Southern (Worthington, 1976) Recirculation Gyres, respectively.

Upon reaching the Grand Banks of Newfoundland near 50°W, the remaining Gulf Stream waters bifurcate into two branches (Johns et al., 1995; Mann, 1967). Near-surface waters in the upper branch are overwhelmingly recirculated within the STG (Berglund et al., 2022; Burkholder & Lozier, 2011b), whereas subsurface waters continue to flow northward to form the North Atlantic Current (NAC) (Clarke et al., 1980; Kwon & Riser, 2005; Rossby, 1996). The absence of a direct pathway enabling near-surface subtropical waters to be advected into the SPNA has been demonstrated repeatedly using both surface drifters (Bower et al., 1985; Bower & Lozier, 1994; Brambilla & Talley, 2006; Hakkinen & Rhines, 2009; Rypina et al., 2011) and simulated water parcel (Burkholder & Lozier, 2011b; Foukal & Lozier, 2016) trajectories.

Along the path of the Gulf Stream and within the Southern Recirculation Gyre, upper limb waters are transformed by vertical convective mixing induced by wintertime surface buoyancy loss (Joyce et al., 2013). This results in the formation of a vertically homogenous water mass known as Subtropical Mode Water (STMW; Feucher et al., 2019; Hanawa & Talley, 2001; Worthington, 1958). Following formation, newly ventilated STMW, identifiable through its low potential vorticity signature, is isolated from the atmosphere by lateral subduction along isopycnals, which extend below the seasonal thermocline in spring (McCartney & Talley, 1982). These upper limb waters are then recirculated throughout the STG interior and by flowing eastward in the Azores Current (Schmitz Jr, 1996) before returning southward via the slow and diffuse Canary Current (Talley et al., 2011). STMWs are finally returned to the Florida Straits and the Antilles Current via the westward flowing North Equatorial Current, thereby completing a single loop of the anticylonic STG.

The fate of both STUW and STMW formed within the STG has been investigated extensively using passive tracers (e.g., Qu et al., 2013), simulated water parcel trajectories (e.g., Berglund et al., 2022; Blanke et al., 2002; Gary et al., 2014) and subsurface floats (e.g., Fratantoni et al., 2013; The Climode Group et al., 2009). Collectively, these Lagrangian studies suggest that upper limb waters, preconditioned in the STG, are exported northward into the SPG via subsurface Gulf Stream pathways, which shoal with distance northward along the path of the NAC (Burkholder & Lozier, 2011a; Foukal & Lozier, 2016; Gary et al., 2014; Häkkinen et al., 2011; Kwon & Riser, 2005; Kwon et al., 2015). On reaching the Grand Banks, these subtropical-origin waters exchange heat and salt with relatively colder and fresher subpolar waters (Berglund et al., 2023) at the confluence between the NAC and the Labrador Current (Fratantoni & Pickart, 2007; Jutras et al., 2023; Rossby, 1996). At around 51°N, the NAC retroflects eastward to form a broad topographically steered flow (Bower & Von Appen, 2008; Rossby, 1996, 1999), which constitutes both the southern limb of the cyclonic SPG circulation and the upper limb of the AMOC.

Once the NAC crosses the Mid-Atlantic Ridge at the Charlie Gibbs Fracture Zone, it divides into several branches feeding the eastern SPG to the northeast (Fratantoni, 2001; Krauss, 1986; Sy et al., 1992) and the Portugal Current to the south (Brambilla & Talley, 2008; Flatau et al., 2003; Schott & Brandt, 2007). Observational estimates suggest that, of the 16-20 Sv of upper limb water entering the eastern SPG via the NAC, almost 90% arrives in the Iceland Basin via the northern and central branches, while the remaining 10% arrives in the southern branch feeding the Rockall Trough (Daniault et al., 2016; Mercier et al., 2015; Sarafanov et al., 2012). The composition of upper limb waters, also known as SPMWs (McCartney & Talley, 1982), changes markedly across each of the NAC branches as the influence of subtropical-origin water increases with distance eastward. Downstream, these SPMWs are distributed between the Atlantic Water inflows to the Nordic Seas (8.4 Sv; Sarafanov et al., 2012) and the cyclonic SPG circulation (12.7 Sv; Sarafanov et al., 2012; Van Aken & Becker, 1996), which in-turn supply approximately equal volumes of NADW to the lower limb of the AMOC (Chafik & Rossby, 2019; Petit et al., 2020).

Atlantic Water flows northward across the Greenland-Scotland Ridge into the Nordic Seas via the Norwegian Atlantic Current (∼7 Sv; Hansen & Østerhus, 2000; Hansen et al., 2008; Østerhus et al., 2019) and the Northern Icelandic Irminger Current (∼1 Sv; Jónsson & Valdimarsson, 2012; Semper et al., 2022). The fate of the Atlantic Water inflow to the Nordic Seas has previously been described as a double estuary circulation comprising of both thermohaline and estuarine components (e.g., Eldevik & Nilsen, 2013; Rudels, 2010; Stigebrandt, 1981). On, average, 70% of the Atlantic Water inflow transport forms dense overflow waters (defined by a potential density greater than 27.8 kg m^{-3}) via the thermohaline circulation, while the remaining 30% is returned as cold, fresh Polar Water in the so-called estuarine circulation (Østerhus et al., 2019; Tsubouchi et al., 2021). Typically, overflow waters are formed in the Nordic Seas by one of two primary mechanisms (Brakstad et al., 2023). Firstly, dense water can be formed via progressive diapycnal transformation due to intense surface heat loss along the boundary current encircling the Nordic Seas (e.g., Eldevik et al., 2009; Isachsen et al., 2007; Mauritzen, 1996). The second mechanism is via open-ocean convection resulting from wintertime surface buoyancy loss over the interior of the weakly stratified Iceland and Greenland Seas (Marshall & Schott, 1999; Swift & Aagaard, 1981).

Approximately 3.2 Sv of the freshest, densest variety of overflow water, known as Denmark Strait Overflow Water (DSOW; Østerhus et al., 2019; Tsubouchi et al., 2021), overspills the Denmark Strait sill west of Iceland before entraining ambient SPMWs to form lower NADW (Dickson et al., 2008; Dickson & Brown, 1994; Jochumsen et al., 2012), the densest component of the AMOC lower limb. To the east, around 2.6 Sv Iceland Scotland Overflow Water (ISOW; Eldevik & Nilsen, 2013; Østerhus et al., 2019) descends from the Norwegian Sea into the Iceland Basin via the Iceland-Faroe Ridge and the Faroe Bank Channel (Beaird et al., 2013; Kanzow & Zenk, 2014; Østerhus et al., 2008), where entrainment of subtropical-origin SPMWs produces its characteristic high salinity, observed downstream (Johns et al., 2021; Yashayaev & Dickson, 2008). ISOW subsequently flows southward at depth along the eastern flank of the Mid-Atlantic Ridge (Lankhorst & Zenk, 2006), where it is partitioned between interior pathways flanking the Mid-Atlantic Ridge (Liu et al., 2024; Lozier et al., 2022; Zou et al., 2020a) and deep cyclonic pathways which form North East Atlantic Deep Water (NEADW; Daniault et al., 2016; Racapé et al., 2019); a dense water mass which combines with DSOW in the DWBC.

In the eastern SPG, the remaining SPMWs that did not cross the Greenland-Scotland Ridge circulate cyclonically around the Iceland Basin, undergoing continuous densification (Brambilla et al., 2008; Stendardo et al., 2024) through surface buoyancy loss along-stream (Petit et al., 2020). On reaching the eastern flank of the

Reykjanes Ridge, weakly stratified SPMWs are considered to be preconditioned to form upper NADW downstream (de Boisséson et al., 2012; Thierry et al., 2008). These preconditioned SPMWs subsequently flow southward in the East Reykjanes Ridge Current before retroflecting to form the northward flowing Irminger Current along the western flank of the Rekjanes Ridge (Daniault et al., 2016; de Jong et al., 2020; de Jong & de Steur, 2016). In addition to recirculating SPMWs, the Irminger Current transports SPMW sourced from a minor branch of the NAC (Chafik et al., 2022; Daniault et al., 2016; Fried et al., 2023). The Irminger Current flows cyclonically around the Irminger Sea (Krauss, 1995; Reverdin et al., 2003) before bifurcating south of Denmark Strait to feed the Northern Icelandic Irminger Current (Hansen & Østerhus, 2000; Semper et al., 2022) and the southward flowing East Greenland Current system (Våge et al., 2011).

The East Greenland Current system consists of two western boundary currents, namely, the East Greenland Coastal Current, which transports freshwater along the continental shelf (Bacon et al., 2002; Sutherland & Pickart, 2008), and the East Greenland Current (EGC) at the shelf break (Le Bras et al., 2018). The EGC transports both relatively warm and saline SPMWs sourced from the NAC and much colder and fresher Polar Water of Arctic-origin (Foukal et al., 2020; Rudels et al., 2005). On reaching Cape Farewell, the topographically-steered EGC flows northwestward as the West Greenland Current (WGC; Holliday et al., 2009), which circumnavigates the Labrador Sea along the continental shelf break. This strongly eddying "rim current" (Pacini & Pickart, 2022; Schott & Brandt, 2007; Talley et al., 2011) becomes the offshore branch of the largely barotropic Labrador Current, flowing southward along the western boundary of the Labrador Sea (Hall et al., 2013). The inshore branch of the Labrador Current, known as the Labrador Coastal Current, is fed by a combination of fresh recirculating West Greenland Coastal Current waters and Arctic-origin waters exported through the Hudson and Davis Straits (Cuny et al., 2002; Florindo-López et al., 2020; Lazier & Wright, 1993).

Away from the continental shelf break, the interior of the Labrador and Irminger Seas is filled with an intermediate water mass known as Labrador Sea

Water (LSW; Lazier, 1980; Talley & McCartney, 1982; Yashayaev et al., 2008), formed in deep winter mixed layers via open-ocean convection (Marshall & Schott, 1999; Pickart et al., 2002). Following its formation, LSW is either transported into the boundary current (Schott & Brandt, 2007) or recirculated within the central Labrador and Irminger Seas via the closed cyclonic circulation of the Irminger Gyre (Faure & Speer, 2005; Lavender et al., 2005; Sy et al., 1997). The entrainment of LSW into the boundary current takes place via eddy exchange (e.g., Georgiou et al., 2019; Spall, 2004, 2011; Straneo, 2006). The net effect of this exchange of buoyancy between the lighter boundary current and denser convective interior is that the boundary current becomes denser along-stream (Brüggemann & Katsman, 2019; Holte & Straneo, 2017; Straneo, 2006), while stratification increases in the basin interior (de Jong et al., 2014; Katsman et al., 2004; Lilly et al., 1999).

In addition to eddy fluxes, direct heat loss to the overlying atmosphere can induce boundary densification via local convective mixing (Bebieva & Lozier, 2023; Spall, 2004; Wåhlin & Johnson, 2009). In the Labrador Sea, this convection occurring within the boundary current itself has been suggested as the primary mechanism by which SPMW forms upper LSW (Pickart et al., 1997, 2002; Spall & Pickart, 2001), the lightest component of the AMOC lower limb (e.g., Rhein et al., 2011, 2017). This should be distinguished from deep LSW, which is formed by open-ocean convection in the Labrador Sea interior (Yashayaev et al., 2008) before being laterally transported into the boundary current along isopycnals (Cuny et al., 2002; Georgiou et al., 2021).

Recently, Le Bras et al. (2020) used mooring observations along OSNAP East to identify a similar mode of dense water formation in the western Irminger Sea. In particular, the authors identified two convective water masses analogous to LSW, namely, upper Irminger Sea Intermediate Water (ISIW), which is formed along the edge of the boundary current, and deep ISIW, which is formed in the Irminger Sea interior. Moreover, Le Bras et al. (2020) showed that the close proximity of upper ISIW formation to the western boundary current results in rapid export on seasonal timescales, whereas deep ISIW typically recirculates in the basin interior on interannual timescales. Similar rapid export of lower limb waters has been identified along the boundaries of the Labrador Sea in a model (MacGilchrist et al., 2020), where newly ventilated LSW is exported southward in the deep Labrador Current in only a matter of months (Brandt et al., 2007; Holte & Straneo, 2017).

At the exit of the Labrador Sea, the Labrador Current transports both upper and lower NADW varieties to be exported equatorward in the AMOC lower limb. However, given that the typical Labrador Current transport (∼30 Sv; Dengler et al., 2006; Zantopp et al., 2017) is almost twice that of the subpolar AMOC strength (∼16 Sv; Lozier et al., 2019), a robust recirculation of NADW must take place within the SPG (Mertens et al., 2014; Schott et al., 2004) via a combination of deep cyclonic pathways feeding the Labrador Sea interior (Fischer & Schott, 2002; Lavender et al., 2000) and the NAC (Breckenfelder et al., 2017; Mertens et al., 2014).

Subsurface Lagrangian floats have also been used to challenge the long-standing paradigm that the DWBC is the principal conduit for the remaining NADW to be exported to the subtropical North Atlantic (Stommel, 1958). The majority of NADW exported from the Labrador Sea is detrained from the DWBC on reaching the Grand Banks before continuing equatorward via highly dispersive interior pathways (Bower et al., 2011; Bower et al., 2009; Fischer & Schott, 2002), consistent with results from passive tracer experiments (e.g., Lozier, 1999; Rhein et al., 2002; Rhein et al., 2015). The dominant role of interior pathways in transporting NADW across the inter-gyre boundary is similarly reproduced by simulated water parcel trajectories (Gary et al., 2011; Lozier et al., 2013; Petit et al., 2023a; Zou & Lozier, 2016) and is explained by deep eddy-driven recirculation gyres (Lozier, 1999; Lozier et al., 1997). On reaching 26.5°N, most of the interior NADW is returned to the DWBC (Bower et al., 2009), which crosses the RAPID array below 1000 m offshore of the Bahamas. This marks the completion of the North Atlantic Overturning Circulation which, on average, transforms ∼17 Sv of warm, light water in the upper 1000 m into cold, dense NADW returning southward at depth.

1.6 Variability of the Atlantic Meridional Overturning Circulation in the North Atlantic Ocean

We have seen in Section 1.3 that changes in the strength of the AMOC have wide-reaching climate impacts with significant socio-economic implications. In this Section, we discuss the nature of North Atlantic overturning variability as recorded in observations and simulated in OGCMs. Although the strength of the AMOC in the North Atlantic Ocean exhibits a rich spectrum of variability extending from daily to centennial timescales, we draw particular attention to the mechanisms governing seasonal to multi-decadal AMOC variability. We note that, while the focus of this thesis is on the processes and circulation pathways local to the North Atlantic, on multi-centennial timescales, coupled climate models suggest a significant role for the Southern Ocean in forcing AMOC variability through the generation of upper ocean thermohaline anomalies (Delworth & Zeng, 2012; Martin et al., 2015).

Since the strength of the AMOC at a given latitude is typically diagnosed by calculating either the vertical or diapycnal overturning stream function, any process which acts to modify the depth or density dependent meridional velocity field can induce variability in the overturning strength. The two most important drivers of AMOC variability are momentum and buoyancy forcing at the sea surface, due to changes in wind stress and the fluxes of heat and freshwater, respectively (Biastoch et al., 2008; Delworth et al., 1993; Häkkinen, 1999). As discussed in Jackson et al. (2022), we can partition the effects of wind stress forcing on the meridional velocity field and, hence, the AMOC into separate ageostrophic and geostrophic components. Ageostrophic wind-driven AMOC anomalies result from local changes in meridional Ekman transport induced by anomalous zonal wind stress (Baehr et al., 2004; Jayne & Marotzke, 2001; Wunsch & Heimbach, 2009). Meanwhile, geostrophic wind-driven AMOC anomalies are owed to changes in zonal density gradients due to the heaving of isopycnals in response to anomalous wind stress curl (Chidichimo et al., 2010; Kanzow et al., 2010; Zhao & Johns, 2014b) or to boundary wave adjustment to wind forcing changes (Hermanson et al., 2014; Kanzow et al., 2010).

In contrast to the adiabatic generation of AMOC anomalies by the winds, buoyancy forcing induces geostrophic overturning anomalies diabatically through surface-forced water mass transformation (Biastoch et al., 2008; Kim et al., 2024; Yeager et al., 2021). Following their generation, density anomalies are communicated equatorward along the western boundary, where they modify the meridional geostrophic flow according to the thermal wind relation (Waldman et al., 2021). The extent to which AMOC variability is driven by wind or buoyancy forcing strongly depends on both the location and timescale of the variability in question (e.g., Bryden, 2021; Jackson et al., 2022; Larson et al., 2020; Polo et al., 2014; Yeager & Danabasoglu, 2014). Thus, we next focus on the mechanisms responsible for seasonal and interannual to multi-decadal overturning variability at both subtropical and subpolar latitudes.

1.6.1 Seasonal Variability in the North Atlantic Meridional Overturning Circulation

Both observations and numerical models show that AMOC variability is most pronounced on monthly to seasonal timescales, with fluctuations on the order of the time-mean AMOC strength recorded at both subtropical and subpolar latitudes (Johns et al., 2023b; Lozier et al., 2019; Moat et al., 2020, ∼17 Sv).

In the subtropical North Atlantic, high-frequency overturning variability is principally driven by local wind forcing (e.g., Blaker et al., 2015; Duchez et al., 2016; Roberts et al., 2013; Zhao & Johns, 2014a, 2014b). Indeed, Roberts et al. (2013) were able to reproduce between 70-80% of the observed AMOC variability at the RAPID array along 26.5°N by forcing an ocean model with observed winds. The remaining overturning variability (20-30%) is associated with intrinsic ocean variability (Germe et al., 2022; Hirschi et al., 2013; Thomas & Zhai, 2013), which is unrelated to the external forcing by momentum and buoyancy fluxes at the sea surface. Instead, this internal AMOC variability emerges from the chaotic mesoscale ocean eddy field (Biastoch et al., 2008; Grégorio et al., 2015; Hirschi et al., 2013; Thomas & Zhai, 2013).

On monthly timescales, subtropical overturning and, by extension, MHT variability reflects the local ageostrophic response to fluctuations in zonal wind stress, in which meridional Ekman transport anomalies are balanced by a depth-independent geostrophic return flow in the ocean interior (e.g., Jayne & Marotzke, 2001; Moat et al., 2020; Wunsch & Heimbach, 2006). On longer seasonal timescales, Kanzow et al. (2010) showed that a substantial fraction of subtropical AMOC variability results from the geostrophic response of the upper-ocean to seasonal wind forcing. The seasonal cycle of subtropical overturning measured at the RAPID array is characterised by a minimum in spring and a maximum between autumn and early winter (Kanzow et al., 2010; Mielke et al., 2013), with an amplitude of 2.0 ± 0.1 Sv (Moat et al., 2020). By relating the geostrophic transport in the upper 1000 m to the density difference between the eastern and western boundaries at 26.5°N, Kanzow et al. (2010) demonstrated that seasonal geostrophic transport anomalies result from isopycnal heaving along the eastern boundary in response to seasonal changes in local wind stress curl, consistent with the earlier studies of Köhl (2005) and Chidichimo et al. (2010). Thus, the seasonal cycle of vertical overturning in the subtropical North Atlantic reflects a combination of local Ekman and wind-forced Rossby wave dynamics (Kanzow et al., 2010; Zhao & Johns, 2014a).

In the SPNA, similarly large overturning variability has been observed on monthly to seasonal timescales at the OSNAP array (Fu et al., 2023; Li et al., 2021b; Lozier et al., 2019). According to Fu et al. (2023), seasonal variability accounts for 40% of the monthly diapycnal overturning variability measured across the full OSNAP array, with OSNAP East making the dominant contribution. The observed seasonal cycle in subpolar overturning is characterised by a maximum in spring (21.1 ± 1.2 Sv) and a minimum in winter (12.3 ± 1.2 Sv) and is, therefore, in antiphase with the seasonal cycle of vertical overturning in the subtropics. The strength of seasonal diapycnal overturning variability recorded at OSNAP East

(6.2 Sv peak-to-trough amplitude in Fu et al., 2023) is slightly larger than reported in Mercier et al. (2015), who observed a seasonal cycle of diapycnal overturning with an amplitude of approximately 4 Sv along the OVIDE section extending from Greenland to Portugal. However, we note that the observations used in the studies above do not overlap (OSNAP East: 2014-2020; OVIDE: 1993-2010). Moreover, Mercier et al. (2024) recently showed that the amplitude of seasonal overturning variability at OVIDE is sensitive to the choice of objective analysis used to provide gridded temperature and salinity measurements.

In contrast to the subtropical North Atlantic, observations and ocean reanalyses suggest that both wind and buoyancy forcing play an important role in generating seasonal overturning variability at subpolar latitudes (Fu et al., 2023; Holte & Straneo, 2017; Wang et al., 2021). However, this may also be a consequence of using density-coordinates rather than depth-coordinates to calculate the strength of subpolar overturning, given that both changes in the meridional velocity field and the heaving of isopycnals can project onto the diapycnal overturning stream function (e.g., Wang et al., 2021).

Using the 6-years of available OSNAP observations, Fu et al. (2023) argued that seasonality of subpolar overturning reflects both a delayed response to wintertime dense water formation and the seasonal cycle of southward Ekman transport. This followed a number of earlier studies which highlighted the close relationship between seasonal overturning variability and the export of seasonal western boundary density anomalies (e.g., Le Bras et al., 2020; Straneo, 2006; Wang et al., 2021). In particular, Holte and Straneo (2017) used Argo float data to suggest that the delayed springtime overturning maxima in the western SPG results from the time taken for wintertime dense water formation in the Labrador Sea interior to be communicated into the encircling boundary current. Similarly, in the eastern SPG, Li et al. (2021a) observed strong seasonality in the layer thickness of upper NADW exported in the western boundary current of the Irminger Sea. The delayed response of the subpolar overturning circulation to seasonal buoyancy forcing does not, however, account for the wintertime seasonal *minimum* in diapycnal overturning at OSNAP. Fu et al. (2023) instead propose that this is due to an increase in the southward Ekman transport across the OSNAP East array during winter, which acts to reduce the northward volume transport of the upper limb.

There is also evidence which challenges the emerging consensus that wintertime dense water formation drives the seasonal subpolar overturning variability. For example, several studies, including Fu et al. (2023), have shown that the seasonal cycle of surface buoyancy-driven transformation in the eastern SPG far exceeds the overturning seasonality measured at OSNAP East (Petit et al., 2020; Xu et al., 2018a). This difference implies that only a small fraction of the dense waters formed each winter are efficiently exported across the OSNAP East array on seasonal timescales. Meanwhile, the remaining seasonal water mass transformation must be balanced by volume changes within isopycnal layers north of OSNAP East (Petit et al., 2020). Indeed, Le Bras et al. (2020) recently showed that only convected water masses formed close to the EGC can be exported on seasonal (1-3 months) timescales, whereas the remainder recirculate within the Irminger Sea on interannual timescales. As a result of the wide range of export timescales convolved in the western boundary currents of the Labrador and Irminger Seas, Li et al. (2021a) conclude that there is no discernable relationship between subpolar overturning variability and western boundary density changes recorded along the OSNAP array. It, therefore, remains an open question to what extent the overturning seasonality measured in the SPNA can be attributed to seasonal dense water formation, as is often inferred using lagged correlations.

1.6.2 Interannual to Multi-Decadal Variability in the North Atlantic Meridional Overturning Circulation

On interannual to multi-decadal timescales, variations in the strength of the AMOC at both subtropical and subpolar latitudes are dominated by wind and buoyancy forcing associated with the North Atlantic Oscillation (NAO) (e.g., Biastoch et al., 2008; Danabasoglu et al., 2016; Eden & Willebrand, 2001; Yeager, 2020; Yeager & Danabasoglu, 2014), which is the dominant mode of atmospheric variability in the North Atlantic sector (Hurrell, 1995; Marshall et al., 2001). The ocean response to NAO forcing can be understood as a combination of a fast ageostrophic response and a delayed geostrophic response (Eden & Willebrand, 2001; Khatri et al., 2022; Lohmann et al., 2009). During a positive phase of the NAO, the fast response results from the anomalous meridional Ekman transport induced by the intensification of both the subtropical easterlies and the subpolar westerlies (Khatri et al., 2022). Thus, since these Ekman transport anomalies are divergent between subtropical and subpolar latitudes (Jackson et al., 2022), NAO-forced overturning variability is not meridionally coherent on interannual timescales (Balan Sarojini et al., 2011; Bingham et al., 2007). In the subtropics, Zhao and Johns (2014b) showed that the fast Ekman response to a shift to a negative phase of the NAO played an important role in driving the $\sim$30% reduction in the AMOC strength at 26.5°N during the winter of 2009-10 (McCarthy et al., 2012).

The delayed geostrophic response to NAO forcing also differs significantly between subtropical and subpolar latitudes for two reasons: (i) the westward propagation speed of baroclinic Rossby waves induced by anomalous wind and buoyancy forcing depends strongly on latitude (e.g., Wunsch & Heimbach, 2013), and (ii) the buoyancy forcing associated with the NAO is localised over regions of deep convection within the SPNA.

In the subtropical North Atlantic, baroclinic Rossby waves propagate westward across the basin on interannual timescales (e.g., Cabanes et al., 2008; Hirschi & Marotzke, 2007), meaning that wind forcing projects strongly onto interannual AMOC variability (Biastoch et al., 2008; Böning et al., 2006; Stepanov et al., 2016). This Rossby wave adjustment to NAO-induced wind forcing can be understood as follows: anomalous wind stress curl generates isopycnal heave; the resulting density anomalies propagate towards the western boundary as baroclinic Rossby waves, thereby modifying the basin-wide density gradient and hence the strength of the upper-ocean geostrophic flow (Cabanes et al., 2008; Hirschi & Marotzke, 2007; Zhai et al., 2014; Zhao & Johns, 2014b). On longer, decadal timescales, observed AMOC variability at 26.5°N (e.g., Frajka-Williams et al., 2018) is hypothesised to result from a delayed geostrophic response to prolonged periods of surface buoyancy forcing at subpolar latitudes (Jackson et al., 2016; Robson et al., 2012). Such meridionally coherent modes of decadal AMOC variability arise because subpolar density anomalies are communicated meridionally along the western boundary via either rapid boundary wave propagation (Getzlaff et al., 2005; Johnson & Marshall, 2002) or slower advection within the DWBC (Bower et al., 2009; Marotzke & Klinger, 2000; Van Sebille et al., 2011; Zhang, 2010).

Unlike in the subtropics, the local formation of buoyancy anomalies coupled with the longer timescales taken for Rossby waves to propagate across the basin (Buckley et al., 2012; Tulloch & Marshall, 2012) means that NAO-induced wind and buoyancy forcing projects most strongly onto decadal AMOC variability at subpolar latitudes. During positive phases of the NAO, anomalous cyclonic wind stress curl over the SPNA leads to a gradual spin-up of the SPG through increased Ekman upwelling in the basin interior (Eden & Willebrand, 2001). The anomalously strong westerly winds also enhance surface heat loss over the central Labrador and western Irminger Seas, which favours increased dense water formation by strengthening deep convection (Danabasoglu et al., 2014; Yeager et al., 2021). The resulting subsurface density (buoyancy) anomalies are advected throughout the basin interior (Chafik et al., 2022; Lavender et al., 2000), where they act to further intensify the cyclonic SPG circulation by steepening the zonal dynamic height gradient across the basin (Häkkinen & Rhines, 2004; Kim et al., 2024; Roussenov et al., 2022; Yeager et al., 2021). Since there is a strong coupling between the overturning and gyre circulations at subpolar latitudes (Yeager et al., 2015), the strengthening of the SPG circulation in response to a positive phase of the NAO yields a concordant strengthening of the subpolar AMOC (Böning et al., 2006; Eden & Jung, 2001; Roussenov et al., 2022).

In addition to their redistribution throughout the SPG interior, subsurface density anomalies generated during positive phases of the NAO have also been highlighted as an important precursor to low-frequency AMOC variability further south (Ortega et al., 2017, 2021; Robson et al., 2014). On reaching the tail of the

Grand Banks, positive density anomalies advected southward in the DWBC act to increase the zonal density gradient across the basin and, therefore, strengthen the northward geostrophic flow of the upper limb according to the thermal wind relation (Biastoch et al., 2008; Chafik et al., 2023; Kostov et al., 2023; Tulloch & Marshall, 2012). Numerical models show that the increase in northward heat transport associated with such a strengthening of the AMOC also leads to a delayed increase in upper ocean heat content and SSTs in the SPNA on decadal to multi-decadal timescales (Delworth & Mann, 2000; Delworth & Zeng, 2012; Knight et al., 2006; Latif et al., 2007; Msadek & Frankignoul, 2009; Roberts et al., 2013; Williams et al., 2015). This is further supported by observations, which show a delayed warming and salinification of the upper eastern SPG in response to the intensification of the AMOC following persistent positive phases of the NAO in the early 1990s (Bersch et al., 2007; Cuny et al., 2005; Fu et al., 2020) and late 2010s (Desbruyères et al., 2021). In contrast, during negative phases of the NAO, observations indicate that anticyclonic wind stress curl anomalies and reduced heat loss induce a delayed cooling and freshening (Bryden et al., 2020; Robson et al., 2016) of the upper eastern SPG by favouring the recirculation of subpolar-origin waters (Fox et al., 2022; Holliday et al., 2020).

Since the northward propagation of upper-ocean thermohaline anomalies from the SPNA into the Nordic Seas has also been shown to yield predictable regional climate impacts (e.g., Årthun et al., 2017; Straneo & Heimbach, 2013; Yeager et al., 2015), accurately representing the dynamical memory of low frequency AMOC variability is widely considered to be an essential component of skillful decadal climate prediction (Dunstone et al., 2011; Yeager & Robson, 2017). Yet, in contrast to the large number of studies investigating the role of the AMOC in the generation of upper-ocean thermohaline anomalies (e.g., Årthun et al., 2021; Häkkinen, 1999; Kim et al., 2020; Moat et al., 2019), much less attention has been paid to their subsequent evolution, including their ability to influence dense water formation downstream (e.g., Dong & Sutton, 2005; Passos et al., 2024). On the one hand, numerous simple box models and low-resolution coupled climate models suggest that thermohaline anomalies generated by low-frequency AMOC variability can feed back onto subpolar overturning variability by impacting the strength of water mass transformation (i.e., via the salt-advection feedback) (Delworth et al., 1993; Griffies & Tziperman, 1995; Rahmstorf, 1996; Stommel, 1961). However, this is inconsistent with Fu et al. (2020), who used observations to show that the subpolar AMOC has remained stable in spite of the large-scale thermohaline variability during recent decades. If the subpolar overturning circulation is indeed strongly decoupled from upper-ocean buoyancy anomalies advected around the SPG as proposed in Fu et al. (2020), this raises several important open questions. Firstly, what physical processes are responsible for setting the amount of dense water formed along the path of the SPG? Secondly, how predictable is SPG dense water formation on interannual to decadal timescales?

1.7 Aims & thesis overview

In this thesis, we seek to develop new insights into the nature of the Meridional Overturning Circulation in the North Atlantic Ocean by introducing a novel Lagrangian framework to analyse numerical model simulations. By combining traditional Eulerian analyses with carefully formulated Lagrangian particle tracking experiments, we will address each of the following research questions:

1. How is the time-mean strength of the AMOC partitioned amongst the individual circulation pathways of the eastern SPNA? (Chapter 2)

2. What is the detailed nature of the overturning pathways in the eastern SPNA, including the geography and advective timescales of diapycnal water mass transformation? (Chapter 2)

3. Which circulation pathways are responsible for seasonal overturning variability in the eastern SPG? (Chapter 3)

4. What are the physical mechanisms underpinning seasonal overturning variability in the eastern SPG in both the Eulerian and Lagrangian frames of reference? (Chapter 3)

5. To what extent do upper limb buoyancy anomalies advected along the path of the SPG influence the strength of the subpolar overturning circulation? (Chapter 4)

6. How predictable are interannual to decadal variations in the amount of dense water formed along the path of the SPG? (Chapter 4)

7. What contribution does the STG make to the time-mean meridional overturning and heat transport at 26.5°N? (Chapter 5)

8. To what extent do the Eulerian vertical and horizontal heat transport components reflect the contributions made by the STG and the large-scale AMOC to the total meridional heat transport in the subtropical North Atlantic? (Chapter 5)

1.8 Software & Data availability

The Lagrangian trajectory data generated as part of this thesis have been made available in publicly accessible repositories where possible (see Table 1.2). The code used to undertake the Lagrangian analyses presented in the following Chapters has been consolidated to create the open-source Lagrangian Trajectories Toolbox (https://github.com/oj-tooth/lt-toolbox).

Table 1.1: List of numerical models used in this thesis.

	ORCA025-GJM189	ORCA0083-GO8p7	ORCA0083-N06
Chapter(s)	2, 3	4	5
Ocean General Circulation Model	NEMO v3.5 (ORCA025)	NEMO v4.0.4 (eORCA12)	NEMO v3.6 (ORCA12)
Ocean Resolution	1/4°	1/12°	1/12°
Vertical Levels	75	75	75
Sea Ice Model	LIM v2	CICE v4	LIM v2
Run Length	1958-2015	1958-2021	1958-2015
Initial Conditions	Levitus climatology (Levitus et al., 1998) and PHC2.1 (Steele et al., 2001)	EN.4.2.2 (1995-2014) climatology (Good et al., 2013)	Levitus climatology (Levitus et al., 1998), PHC2.1 (Steele et al., 2001) and MEDATLAS (Jourdan et al., 1998)
Forcing	DFS 5.2	JRA55-do	DFS5.2
References	Jean-Marc Molines (2021)	Megann et al. (2022)	Moat et al. (2016)

Table 1.2: List of Lagrangian trajectory datasets used in this thesis.

Chapter(s)	**Description**
2 & 3	ORCA025-GJM189 Lagrangian Trajectories https://doi.org/doi/10.5281/zenodo.6573899
5	ORCA0083-N06 Lagrangian Trajectory Crossings of 26.5°N https://doi.org/10.5281/zenodo.10069800

2

Lagrangian overturning pathways in the eastern subpolar North Atlantic

We saw in Section 1.3 that the subpolar North Atlantic Ocean (SPNA) plays a critical role in the global climate system through the formation of dense NADW that feeds the lower limb of the AMOC. In this Chapter, we diagnose the contribution of individual circulation pathways to the time-mean strength of the subpolar AMOC and determine the dominant advective timescales of water mass transformation in the eastern SPNA.

2.1 Introduction

Both numerical modelling studies (e.g., Menary et al., 2020b; Petit et al., 2023b; Yeager et al., 2021; Zhang & Thomas, 2021) and recent observations made along the OSNAP observing array (e.g., Fu et al., 2023; Li et al., 2021a; Lozier et al., 2019) show that water mass transformation east of Greenland (north of OSNAP East, see Fig.2.1a) dominates both the mean strength and seasonal to interannual variability of the subpolar overturning circulation. Therefore, in this opening Chapter, we focus on the circulation pathways responsible for the time-mean strength of the AMOC in the eastern SPNA.

Observational studies exploring the sources of NADW feeding the AMOC lower limb in the eastern SPNA have revealed that dense water formation is distributed approximately equally between the Iceland and Irminger Basins and the Nordic Seas (Bringedal et al., 2018; Chafik & Rossby, 2019; Petit et al., 2020). In the eastern SPG, upper NADW formation is characterised by the progressive densification of SPMWs circulating cyclonically in the Iceland and Irminger Basins (Brambilla & Talley, 2008; de Boisséson et al., 2010; Petit et al., 2020; Stendardo et al., 2024). This surface buoyancy-driven transformation along the horizontal boundary currents of the eastern SPG has been characterised as a form of "lateral subduction" by Chafik and Rossby (2019), and is estimated to be responsible for around 40% of time-mean diapycnal overturning at OSNAP East (Hirschi et al., 2020; Zhang & Thomas, 2021). Away from the SPG boundaries, upper NADW with a similar composition to deep LSW (Pickart et al., 2003) is also formed by deep convection in the Irminger Sea interior (de Jong et al., 2012; Piron et al., 2016).

Collectively, these two modes of dense water formation occurring south of the Greenland-Scotland Ridge dominate the variability of the subpolar AMOC on monthly to decadal (Desbruyères et al., 2019; Petit et al., 2020) timescales. This is contrasted by the transport of dense overflow waters returning across the Greenland-Scotland Ridge, which exhibit little variability on interannual to decadal timescales (Østerhus et al., 2019).

Although the processes governing water mass transformation in both the eastern SPG and the Nordic Seas have been subject to extensive research (e.g., Årthun, 2023; Desbruyères et al., 2019; Evans et al., 2023; Grist et al., 2009, 2016; Petit et al., 2020, 2021), what remains unaddressed is how the diapycnal overturning integrated across the OSNAP East section is distributed amongst the circulation pathways of the eastern SPG and the Nordic Seas overflows. Moreover, given that recent observations suggest that variations in upper NADW formation can imprint onto both seasonal and interannual overturning variability (Le Bras et al., 2020), there is a growing need to identify the dominant advective timescales over which dense water formation takes place within the eastern SPNA.

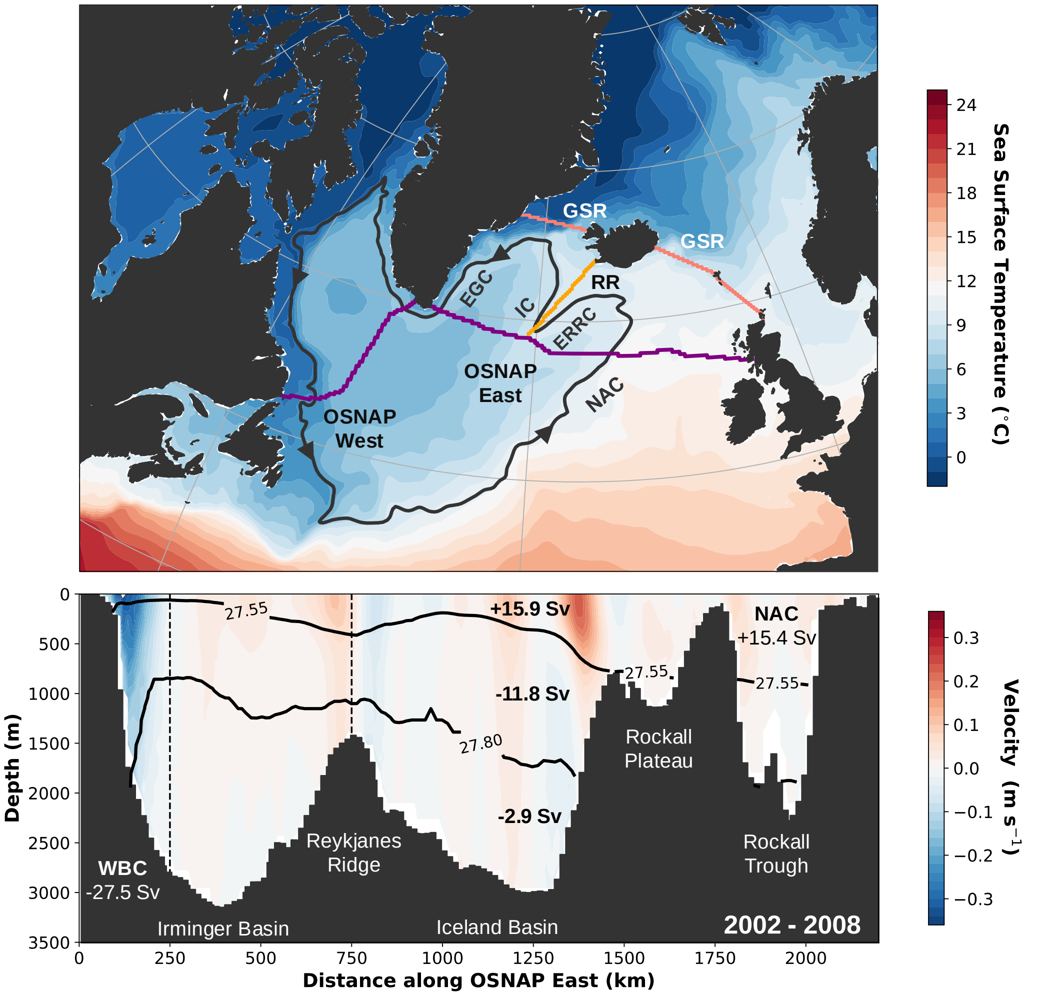

Figure 2.1: Time-mean sea surface temperature and volume transports in the SPNA in ORCA025-GJM189. (a) The location of the OSNAP observing array (purple line) superimposed on a map of mean (1976-2015) sea surface temperature and the boundary of the SPG (defined as the largest closed contour of sea surface height following Foukal & Lozier, 2018). The Reykjanes Ridge (RR, orange line) and the Greenland-Scotland Ridge (GSR, pink line) sections are used to define circulation pathways and determine the extent of water mass transformation in each of the subpolar basins in Section 2.3.3. The major currents intercepted by the OSNAP East array are identified: North Atlantic Current (NAC), East Reykjanes Ridge Current (ERRC), Irminger Current (IC), and East Greenland Current (EGC). (b) Model-derived summertime mean (JJA; 2002-2008) velocity perpendicular to OSNAP East (positive transports are northward) overlaid by σ_θ = 27.55 kg m^{-3} (the isopycnal of maximum overturning reported by Sarafanov et al., 2012) and σ_θ = 27.80 kg m^{-3} (the observed upper limit of overflow waters transformed in the Nordic Seas). Simulated net transports (bold) are included for the upper layer ($<$ 27.55 kg m^{-3}), intermediate layer ($27.55 \leq \sigma_\theta < 27.80$) and the deep layer ($\geq$ 27.80 kg m^{-3}) following Sarafanov et al. (2012). The NAC transport is defined as the net upper layer transport east of Reykjanes Ridge (dashed line at 750 km). The western boundary current (WBC) transport is defined as the net top-to-bottom transport within 250km of Greenland (dashed line).

In this Chapter, we employ Lagrangian particle tracking to investigate the structure of the time-mean overturning circulation in the eastern SPNA within an eddy-permitting ocean sea-ice hindcast simulation. We first establish the fidelity of the gyre and overturning circulations simulated in ORCA025-GJM189 through comparison with observations of the SPNA. By extending the methodology of Georgiou et al. (2020, 2021), we then formalise the concept of the Lagrangian overturning in density-coordinates and show how trajectories traced from the northward inflows across a model-defined OSNAP East section reveal the mean pathways of the overturning circulation, including their along-stream diapycnal transformation. In contrast to traditional zonally-integrated metrics, we demonstrate how the Lagrangian overturning in density-coordinates can be decomposed to quantify the contributions made by individual pathways to overturning at OSNAP East, their associated advective timescales and the extent of water mass transformation in the Iceland-Rockall and Irminger Basins.

This Chapter is organised as follows. In Section 2.2, we introduce the eddy-permitting model simulation and Lagrangian particle tracking experiments. Section 2.3.1 explores the composition of the time-mean northward transport across OSNAP East. The time-mean Lagrangian overturning in the eastern SPG is defined in density-coordinates in Section 2.3.2. In Section 2.3.3, we decompose the Lagrangian overturning in the eastern SPG by circulation pathway, quantifying the extent of water mass transformation in each basin and identifying the dominant advective timescales over which overturning takes place. Finally, in Section 2.3.4, we reproduce our findings using time-averaged velocity and hydrographic fields, before extending our analysis to investigate the overturning pathways and advective timescales of the Nordic Seas overflows. The Chapter concludes with a summary of our principal findings and a discussion of their wider implications for high-latitude AMOC variability (Section 2.4).

2.2 Methods

2.2.1 Ocean General Circulation Model

To investigate the nature of the time-mean overturning circulation in the eastern SPNA, we use output from the ORCA025-GJM189 (see Table 1.1) ocean sea-ice hindcast simulation produced by the Drakkar initiative (Bernard et al., 2006). The simulation uses a global implementation of the Nucleus for European Modelling of the Ocean (NEMO) model (Madec et al., 2013) coupled to the thermodynamic Louvain-la-Neuve Ice Model version 2 (LIM2) (Fichefet & Maqueda, 1999). The ocean is simulated using the eddy-permitting ORCA025 configuration of the NEMO v3.5 model (Madec et al., 2013), which utilises the ORCA tripolar quasi-isotropic grid with a nominal horizontal resolution of 1/4° (27.75 km at the equator, 13.8 km at 60°N) and 75 unevenly spaced z-partial-step-coordinate levels, ranging from 1 m at the surface to 200 m below 4000 m depth. Subgrid-scale parameterisations include horizontal biharmonic viscosity for momentum, Laplacian isopyncal diffusivity for tracers and the TKE turbulence closure scheme for vertical mixing (Bernard et al., 2006). While there is no explicit parametrisation of mesoscale eddy mixing in this simulation (e.g., Gent & Mcwilliams, 1990), sub-grid scale diffusion of momentum and tracers does admit the partial resolution of mesoscale eddies. A comprehensive description of the ORCA025-GJM189 configuration can be found in Jean-Marc Molines (2021).

The ORCA025-GJM189 hindcast simulates the historical period from 1958-2015 initialised from rest. Atmospheric forcing, in the form of surface heat, freshwater, and momentum fluxes, is computed using the CORE bulk formulae (Large et al., 1994; Large & Yeager, 2004) and the Drakkar Forcing Set 5.2 (Dussin et al., 2016), which combines surface fluxes from the ERA40 (Uppala et al., 2005) and ERA-Interim reanalyses (Dee et al., 2011). The initial conditions of the simulation are provided by a combination of the Levitus climatological hydrography (Levitus et al., 1998) and Polar Science Center Hydrographic Climatology (Steele et al., 2001) in the Arctic. A relaxation of sea surface salinity towards the Levitus climatological hydrography with a piston velocity of 167 mm day^{-1}, equivalent to a 60 day decay time for 10 m of water depth (Jean-Marc Molines, 2021), is included to minimise model drift. In the absence of a dedicated spinup period, we discard the first 18 years of the simulation to allow for the initial adjustment of the model. The depth of the surface mixed layer (MLD) is diagnosed using a potential density criterion, as in MacGilchrist et al. (2020): $\Delta\sigma_{\theta}$ = 0.01 kg m^{-3}, where $\Delta\sigma_{\theta}$ is the difference in potential density from the sea surface. We additionally construct stationary velocity and hydrographic fields by averaging 5-day mean model outputs from 1976-2015. To preserve the spatial signature of wintertime convection when calculating the time-mean MLDs, we elect to average the 5-day mean MLDs across all months between 1976-2015 rather than compute them directly from the time-mean potential density field.

We choose to place the simulated period (1976-2015) into context throughout the study by comparing transports and hydrography along the model-defined OSNAP East section (defined as in Menary et al., 2020a) with relevant observations. In agreement with previous Lagrangian studies using models based on ORCA025 (e.g., Asbjørnsen et al., 2021; de Boisséson et al., 2012; Desbruyères et al., 2013, 2015; MacGilchrist et al., 2020), we will show that the velocity and hydrographic fields of the ORCA025-GJM189 simulation can adequately reproduce the gyre and overturning circulations of the eastern SPNA.

To provide an initial impression of the model, Figure 2.1b presents the summertime mean velocity fields and volume transports across the OSNAP East section during the 2002-2008 observational period of Sarafanov et al. (2012). Upper ocean transports across the section are generally well represented within the simulation: the net transport above the 27.55 kg m^{-3} isopycnal between the Rekyjanes Ridge and Scotland is 15.4 Sv in the model compared with 15.5 ± 0.8 Sv observed by Sarafanov et al. (2012) at 59.5°N. Although the simulated top-to-bottom transport of the Irminger Sea Western Boundary Current (WBC) is 4.6 Sv weaker than observations during the summers of 2002-2008, we note the strong agreement between the mean WBC transport (31.0 Sv) in the model and the 32.0 ± 2.7 Sv reported in Sarafanov et al. (2012) for the extended period between 1978-2006. We also highlight the weaker simulated lower NADW transport ($\geq$ 27.8 kg m^{-3}) across OSNAP East (2.9 Sv) compared with the 13.3 $\pm$ 1.3 Sv observed at 59.5°N (Sarafanov et al., 2012). This absence of the densest water masses results from the excessive entrainment of ambient Atlantic waters by the Nordic Seas overflows in this simulation (MacGilchrist et al., 2020), which is a well-documented bias in current-generation OGCMs (e.g., Danabasoglu et al., 2010; Wang et al., 2015). MacGilchrist et al. (2020) also showed that the weaker than observed lower NADW transports in this simulation contribute to biases downstream, including low mid-depth stratification and excessively deep mixed layers in the central Labrador Sea.

2.2.2 Lagrangian Particle Tracking

We use the Lagrangian offline particle tracking tool TRACMASS (v7.1; Aldama-Campino et al., 2020) introduced in Section 1.4.2.1 to determine the trajectories of virtual water parcels advected by the time-evolving ORCA025-GJM189 velocity field. We evaluate water parcel trajectories using the stepwise-stationary scheme, which linearly interpolates the model velocities between successive 5-day mean velocity fields using a series of 100 intermediate time-steps (Döös et al., 2017).

We calculate purely advective trajectories except in the surface mixed layer. To reconcile the strongly time-dependent process of vertical turbulent mixing with our use of 5-day mean velocity and hydrographic fields, we choose to implement the mixed layer physics scheme of Paris et al. (2013). This ensures that otherwise smooth trajectories adequately sample the effects of vertical turbulent mixing captured in the Eulerian tracer fields. At each time-step, the parameterisation identifies the water parcels located within the surface mixed layer and introduces a random vertical displacement governed by a maximum vertical velocity of $|w| = 10$ cm s^{-1} (Georgiou et al., 2021; van Sebille et al., 2013). Unlike alternative diffusive mixing schemes (e.g., Döös, 1995), this scheme does not allow water parcels to be displaced across the base of the mixed layer and hence does not artificially contribute to dense water formation.

We perform two Lagrangian experiments to determine the structure of the time-mean subpolar AMOC at OSNAP East. In our primary Lagrangian experiment, water parcels are initialised on the first available day of each month (based on where the centre of the nearest 5-day mean window falls) between 1976-2008 and advected forward-in-time for a maximum of 7 years. In total, more than 11.2 million water parcels are initialised sampling the full-depth northward transport across OSNAP East over 396 months. During each monthly intialisation, we distribute water parcels in proportion to the volume transport through each grid cell, with a minimum of one water parcel per cell. The number of water parcels assigned to each grid cell along the model-defined OSNAP East section is determined by:

$$N_{gc} = ceil\left(\frac{V_{gc}}{V_{max}}\right) \tag{2.1}$$

where V_{gc} is the absolute northward volume transport across the grid cell face and V_{max} represents the maximum volume transport per water parcel. We choose a maximum volume transport of $V_{max} = 2.5$ mSv per parcel to generate sufficiently large monthly ensembles of virtual water parcels to calculate robust Lagrangian diagnostics (Jones et al., 2016). Water parcels are then distributed evenly across the model grid cell face to ensure adequate sampling of the local velocity field. To illustrate how this works in practice, consider the case of a 52 mSv northward transport across a grid cell face along the OSNAP East array. Here, we would distribute $ceil\left(\frac{52}{2.5}\right) = 21$ water parcels, each representing approximately 2.48 mSv, evenly across the grid cell face.

Following initialisation, water parcels are advected through the time-evolving velocity field until they meet any one of three conditions: (i) returning to the OSNAP East section, (ii) crossing the Greenland-Scotland Ridge northwards, or (iii) reaching the maximum advection time of 7 years. Our choice of a 7-year maximum water parcel advection time ensures that >99.1% of water parcels are intercepted at either OSNAP East or the Greenland-Scotland Ridge. We note that the remaining water parcels (<0.9%), terminated between OSNAP East and the Greenland-Scotland Ridge, overwhelmingly circulate at depth within the lower limb of the AMOC and thus would contribute negligibly to the time-mean overturning measured at the section. The decision to terminate water parcels on reaching the Greenland-Scotland Ridge was motivated by the results of a preliminary experiment, which highlighted that inflows to the Nordic Seas typically required multiple decades to return to OSNAP East in the form of dense overflow waters. Given that the ORCA025-GJM189 hindcast only simulates a 40 year historical period (time-mean over 1976-2015), we choose to use our primary Lagrangian experiment to investigate the structure of the time-mean overturning within the eastern SPG, south of the Greenland-Scotland Ridge.

In our second, complementary Lagrangian experiment, we extend our analysis to examine the contributions of both the eastern SPG and the Nordic Seas overflow pathways sourced from the northward inflows across the OSNAP East section to the time-mean overturning in the eastern SPNA. To do this, we replicate our primary experiment using time-averaged (stationary) velocity and tracer fields (1976-2015), whilst also significantly increasing the maximum advection time to 60 years in order to explicitly resolve the pathways of the Nordic Seas overflows. Moreover, since the stationary velocity field does not evolve through time, we require only a single initialisation of 22,657 numerical water parcels to sample the entire northward transport across the OSNAP East section. We note that fewer water parcels are released in our second Lagrangian experiment compared with the average monthly initialisation (28,372) using time-evolving fields since eddy-induced northward transports are substantially weaker across OSNAP East in the stationary velocity field.

In each of our Lagrangian experiments, we output the position and properties of water parcels at every grid-cell crossing. Since the potential temperature (°C) and salinity (PSU) are defined at the center of each grid cell, TRACMASS uses a linear interpolation scheme in time and space to determine water parcel properties from the two nearest model T-points. The potential density referenced to the sea surface is subsequently computed using the EOS-80 non-linear equation of state (Fofonoff & Millard Jr., 1983) as in our ORCA025 configuration of NEMO (Madec et al., 2013).

2.3 Results

2.3.1 Northward inflow across OSNAP East

We begin by analysing the structure of the time-mean northward inflow across OSNAP East in our primary Lagrangian experiment (1976-2008). Figure 2.2a shows the average distribution of full-depth northward transport sampled by Lagrangian water parcels flowing across the OSNAP East section. Of the 64.9 Sv of total northward transport, 21.3 Sv enters via the Irminger Basin (west of the Reykjanes Ridge), representing the combined transports of the Irminger Current and the Irminger Gyre. In comparison, Våge et al. (2011) used mean absolute geostrophic velocities from 1991–2007 to estimate northward transports of 13 ± 3 Sv and 4.2 ± 1.9 Sv ($\sim$17.2 Sv in total) for the Irminger Current and the Irminger Gyre, respectively. The larger full-depth northward transport determined from Lagrangian water parcels is explained by the absence of compensating southward transports due to recirculation features in the interior Irminger Basin (see blue bars in Figure 2.2a). Figure 2.2b highlights a sharp density contrast between the dense northward transport of the Irminger Gyre, feeding the basin interior, and the lighter, surface-intensified transport of the Irminger Current along the western Reykjanes Ridge. These differences in density reflect the contrasting origins of the two currents: the northward limb of the Irminger Gyre transports LSW formed via open-ocean deep convection into the Irminger Sea interior (Lavender et al., 2000; Våge et al., 2011), whereas the Irminger Current is fed by water sourced from the NAC, which recirculates from the southward flowing East Reykjanes Ridge Current (ERRC) (Bower et al., 2002; Koman et al., 2020).

To the east of the Reykjanes Ridge, inflow across OSNAP East occurs via the branches of the NAC. The structure and composition of the NAC shown in Figure 2.2 compares favourably with observations. Each of the NAC branches

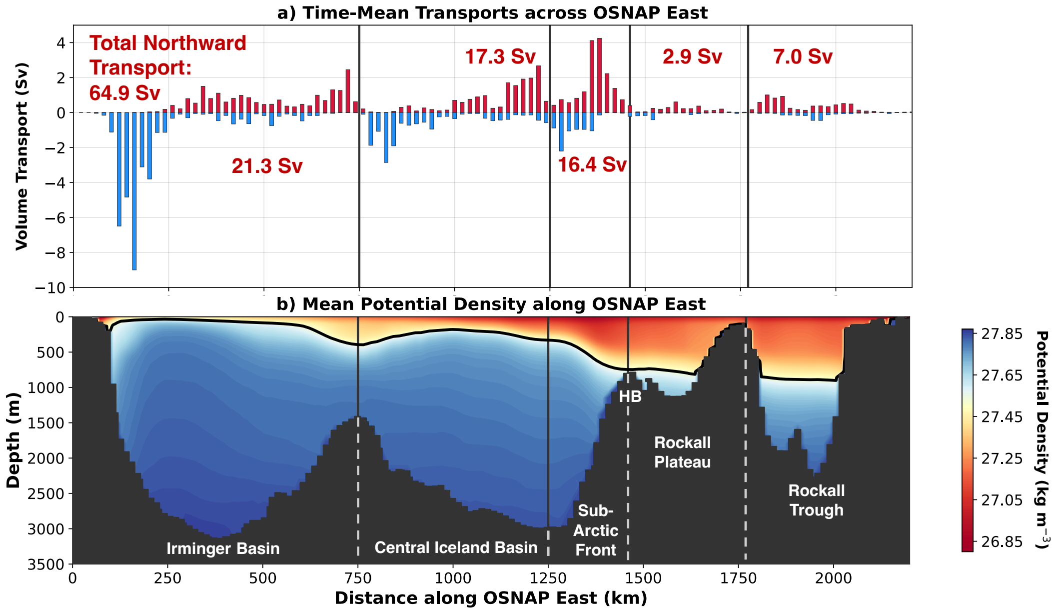

Figure 2.2: Time-mean (1976-2008) volume transports and potential density at OSNAP East. (a) Mean full-depth northward (red) and southward (blue) transports across OSNAP East summed using discrete bins (Δx = 20 km) along the section. Vertical solid lines divide the inflow across the section into five geographic regions with the corresponding total northward volume transports shown. (b) Mean potential density along OSNAP East overlaid by the 1976-2008 mean isopycnal of maximum Eulerian overturning (27.51 kg m^{-3}), denoting the interface between the upper and lower limbs of the AMOC. The location of the Hatton Bank is labelled along OSNAP East as HB.

is associated with a characteristic SPMW, formed during wintertime convection (McCartney & Talley, 1982), whose properties reflect the relative contributions of subpolar and subtropical waters (de Boisséson et al., 2012). In the central Iceland Basin, the northern NAC branch advects 17.3 Sv of relatively cold and fresh SPMW, sourced predominantly from the Labrador Sea (de Boisséson et al., 2012). To the east, the central NAC branch, transporting 16.4 Sv, is characterised by a sharp salinity front known as the Sub-Arctic Front (SAF; Bersch et al., 1999). As the oceanographic boundary of the SPG (Bersch et al., 2007), the SAF divides water of subpolar origin on the western side of the central NAC branch from subtropical-origin water to the east. The strong density-gradient across this baroclinic front produces the intensification of transport along the steep western flank of the Rockall Plateau, which resembles the quasi-permanent Hatton-Bank jet observed by Houpert et al. (2018).

East of the Hatton Bank, Figure 2.2b shows that northward flowing SPMWs become lighter as the influence of warm and saline subtropical water increases towards Scotland. The relatively weak 2.9 Sv of northward transport over the Rockall Plateau likely results from the compensating transports of the unstable southward flow observed along the western flank of the Rockall Plateau and the northward flowing Rockall Bank jet to the east (Houpert et al., 2018). The remaining 7.0 Sv of inflow transport enters the Rockall Trough via two northward flowing boundary currents representing the southernmost branch of the NAC. This mean transport agrees with the recent observations of Houpert et al. (2020), who estimated that 6.6 Sv of NAC water flows northward in the Rockall Trough (2014–2018).

2.3.2 Overturning in Density-Coordinates at OSNAP East

To evaluate the extent to which water masses are transformed north of OSNAP East, we first calculate the time-mean Eulerian overturning stream function in density-coordinates in Figure 2.3a-c. This is constructed by averaging the monthly integrated northward and southward volume transports across the OSNAP East section in discrete potential density bins ($\Delta\sigma_\theta$ = 0.01 kg m^{-3}) between 1976-2008 (Fig. 2.3a). A net volume transport distribution in density-coordinates (Fig. 2.3b) is then produced by summing the time-averaged northward and southward transport distributions in Figure 2.3a, before the mean Eulerian overturning stream function is obtained by computing the cumulative sum from the lightest to the densest isopycnal layer following Lozier et al. (2019). The strength of the time-mean AMOC at OSNAP East, given by the maximum of the time-mean overturning stream function shown in Figure 2.3c, is 15.3 Sv at σ_{MOC} = 27.51 kg m^{-3}, which is in broad agreement with the 1992-2006 average of 15.9 $\pm$ 1.9 reported by Sarafanov et al. (2012). The simulated overturning strength is weaker than both that reported in Sarafanov et al. (2012) and the 2014-2020 estimate of 16.3 $\pm$ 2.9 Sv at OSNAP East (Fu et al., 2023) because we have computed the maximum of the time-mean Eulerian overturning stream function as opposed to calculating the average of the maximum Eulerian overturning each month as done

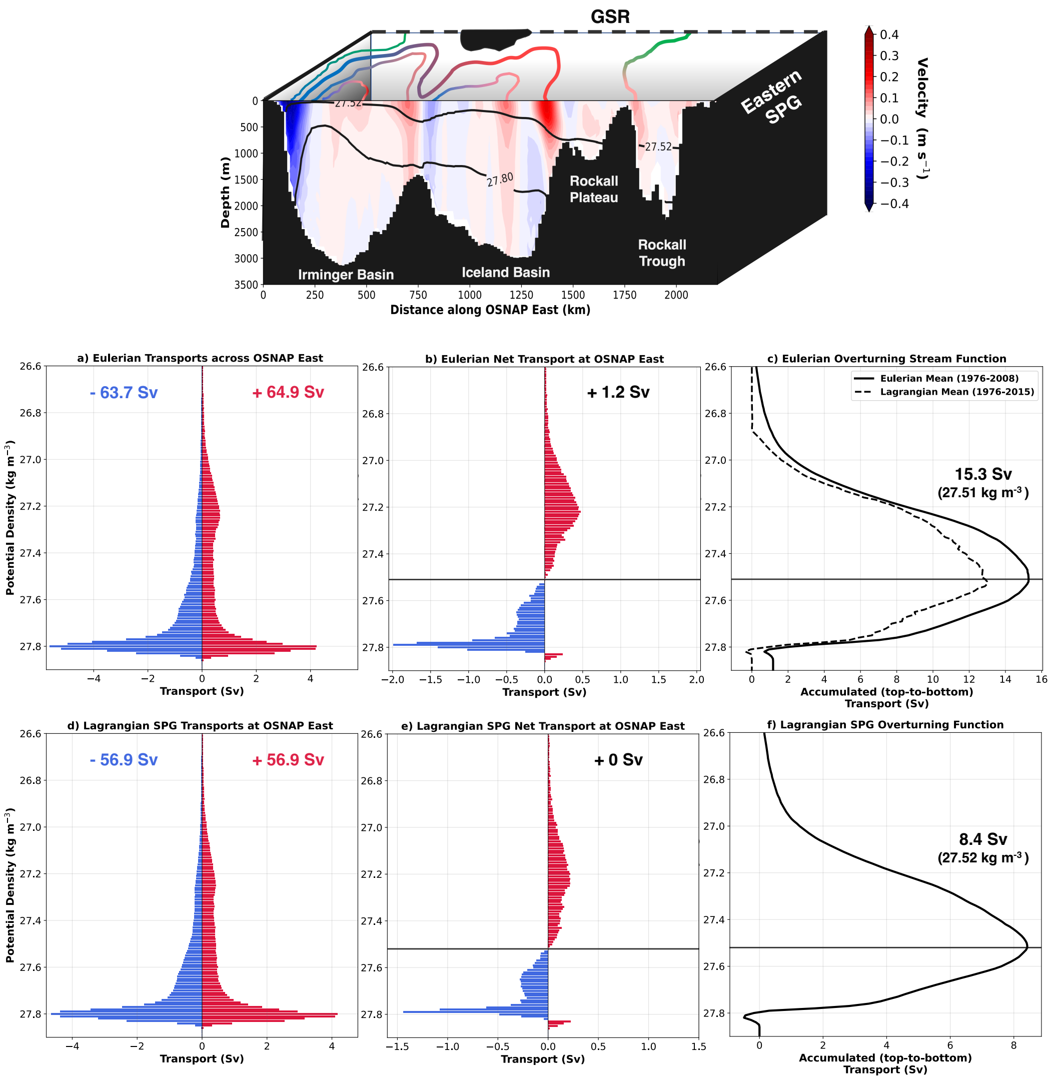

Figure 2.3: Time-mean (1976 - 2008) volume transports and overturning in potential density coordinates (σ_θ) at OSNAP East. (a) Monthly Eulerian northward (red) and southward (blue) volume transports, integrated in 0.01 kg m^{-3} potential density bins and averaged across all 396 months. (b) The net volume transport distribution across OSNAP East obtained by summing the mean northward and southward transports (a) in each potential density bin. The net throughflow to the Arctic Ocean is also shown. (c) Eulerian overturning stream function (solid line) and complementary Lagrangian overturning stream function (dashed line) computed from the eastern SPG and Nordic Seas overflow trajectories evaluated using 1976-2015 stationary velocity and hydrographic fields (see Section 2.3.4). The magnitude and isopycnal of the maximum Eulerian overturning stream function is also shown. (d) Lagrangian mean northward (red) and southward (blue) volume transport distributions of the eastern SPG determined by averaging the volume transports of water parcels which return to OSNAP East in 0.01 kg m^{-3} potential density bins. (e) Lagrangian net volume transport distribution of the eastern SPG in potential density-space. Note that no net throughflow to the Arctic Ocean is permitted. (f) Lagrangian overturning stream function of the eastern SPG with the magnitude and isopycnal of maximum Lagrangian overturning shown. The horizontal (solid) lines identify the isopycnals of maximum Eulerian (b, c; $\sigma_{MOC} = 27.51$ kg m^{-3}) and Lagrangian (e, f; $\sigma_{LMOC} = 27.52$ kg m^{-3}) overturning.

in observations. Concomitant with the absence of NADW in the densest classes, a lighter isopycnal of maximum overturning (σ_{MOC}) is simulated at OSNAP East compared with observations (27.55 kg m^{-3}; Chafik & Rossby, 2019; Li et al., 2021a; Sarafanov et al., 2012), indicating that the upper cell of the AMOC is too shallow in the model (Danabasoglu et al., 2010). The net poleward transport across the section is 1.2 Sv, which is consistent with the estimates of 1.0-1.6 Sv of throughflow to the Arctic Ocean east of Greenland used in inverse models (Lherminier et al., 2007; Lozier et al., 2019).

To complement the traditional Eulerian overturning stream function, we next define a Lagrangian measure of the diapycnal overturning at OSNAP East by extending the methodology of Georgiou et al. (2020, 2021). We use the trajectories generated in our primary Lagrangian experiment to quantify the time-mean water mass transformation taking place along the circulation pathways confined to the south of the Greenland-Scotland Ridge. To achieve this, we first extract the 9.8 million of the total 11.2 million virtual water parcels which return to OSNAP East without crossing the Greenland-Scotland Ridge and within the maximum 7 year advection period (τ_{max}) to form 396 ensembles, one for each month between 1976-2008. For each monthly ensemble initialised at time t, we sum the absolute volume transports of the $N(t)$ recirculating water parcels in discrete potential density bins as follows:

$$V(\sigma_\theta^*, t) = \sum_{n \in N(t)} V_{n,\sigma_\theta,t} \Pi(\sigma_\theta^*) \tag{2.2}$$

where $V_{n,\sigma_\theta,t}$ is the absolute volume transport conveyed by a water parcel identified with index n, which crosses the OSNAP East array with an associated potential density σ_θ. We note that, in practice, the initial position and potential density are expressed as $p = p(i, j, t)$ and $\sigma_\theta = \sigma_\theta(i, j, t)$, where i and j are the ORCA025 grid indices of the model-defined OSNAP East array. The boxcar function $\Pi(\sigma_\theta^*)$ is defined with a bin width $\Delta\sigma_\theta$ = 0.01 kg m^{-3} as follows:

$$\Pi(\sigma_\theta^*) = \begin{cases} 1 & \text{for } |\sigma_\theta^* - \sigma_\theta| \leq \frac{\Delta\sigma_\theta}{2} \\ 0 & \text{elsewhere} \end{cases}$$

where an asterisk is used to denote that σ_θ^* represents a range of σ_θ values, given by $\sigma_\theta^* \pm \Delta\sigma_\theta/2$.

We construct two separate volume transport distributions each month according to the properties of water parcels on their initial northward $V_{North}(\sigma_\theta, t)$ and final southward $V_{South}(\sigma_\theta, t + \tau_{out})$ crossings of the OSNAP East section, where τ_{out} is the water parcel termination time following initialisation. In keeping with the Eulerian calculation outlined above, the time-mean northward $\bar{V}_{North}(\sigma_\theta)$ and southward $\bar{V}_{South}(\sigma_\theta)$ Lagrangian volume transport distributions (Fig. 2.3d) are obtained by averaging the monthly transport distributions at OSNAP East. Figure 2.3d shows that, on average, 56.9 Sv (87.7%) of the 64.9 Sv total northward transport across OSNAP East recirculates within the eastern SPG, south of the Greenland-Scotland Ridge. The remaining 8.0 Sv of northward transport which crosses the Greenland-Scotland Ridge is divided between the net throughflow to the Arctic Ocean (1.2 Sv) and 6.8 Sv of residual transport which would eventually return to OSNAP East either via the dense Nordic Seas overflows or via the fresh East Greenland Coastal Current (EGCC).

Returning to the recirculating northward transport within the eastern SPG, we next calculate the time-mean Lagrangian diapycnal overturning stream function (Blanke et al., 1999), $F(\sigma_\theta^*)$, analogously to the Eulerian diapycnal overturning stream function, by taking the cumulative sum of the time-mean Lagrangian net volume transport distribution ($\bar{V}_{North}(\sigma_\theta) - \bar{V}_{South}(\sigma_\theta)$ in Fig. 2.3e) from the lightest (σ_{min}) to the densest (σ_{max}) potential density bin as follows:

$$F(\sigma_\theta^*) = \sum_{\sigma_\theta=\sigma_{min}}^{\sigma_\theta^*} \bar{V}_{North,\sigma_\theta} - \bar{V}_{South,\sigma_\theta} \tag{2.3}$$

The time-mean Lagrangian overturning stream function of the eastern SPG, presented in Figure 2.3f, reaches a maximum of 8.4 Sv at σ_{LMOC} = 27.52 kg m^{-3}, in close agreement with the isopycnal of maximum Eulerian overturning (σ_{MOC} = 27.51 kg m^{-3}).

To evaluate the performance of our Lagrangian particle tracking approach, we use our estimate of the time-mean Lagrangian overturning to construct a steady-state volume budget of the eastern SPG (Fig. 2.4), which can be validated using recent observations. For consistency, we choose to express the net volume flux from the upper to the lower limb of the AMOC between OSNAP East and the Greenland-Scotland Ridge as a percentage of the net upper limb transport recorded at the OSNAP East section. The maximum Lagrangian overturning shown in Figure 2.3f informs us that 55% (8.4 Sv) of the time-mean net transport of the upper limb across OSNAP East (15.3 Sv shown in Fig. 2.3c) is transferred into the lower limb within the Iceland-Rockall and Irminger Basins, south of the Greenland-Scotland Ridge. This corresponds closely with the studies of Chafik and Rossby (2019), Petit et al. (2020) and Sarafanov et al. (2012), who estimate that the Iceland and Irminger Basins are collectively responsible for 50% (9.6 Sv between 2012-2016), 52% (7.6 Sv between 2014-2016) and 60% (10.2 Sv between 2002-2008) of the diapycnal overturning north of OSNAP East, respectively. We therefore conclude that the Lagrangian overturning stream function accurately

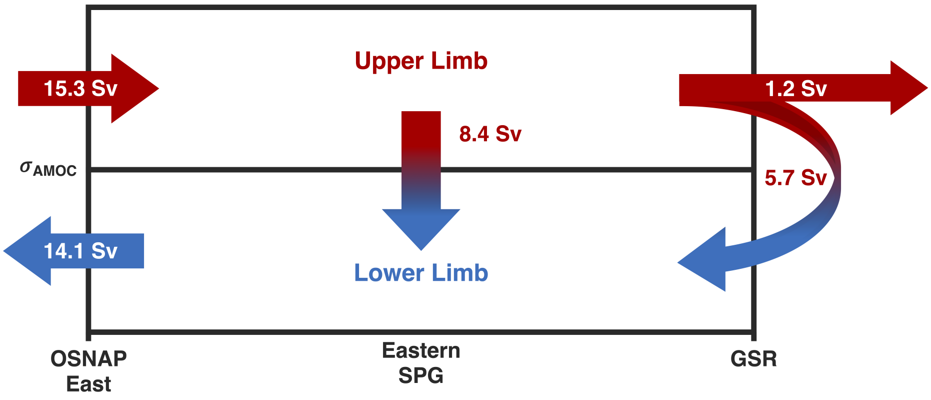

Figure 2.4: Schematic of the upper and lower limb volume budget of the eastern SPG, defined as the region north of OSNAP East and south of the Greenland-Scotland Ridge (GSR). The total upper limb volume transport flowing northward across OSNAP East (15.3 Sv) is given by the maximum of the time-mean Eulerian overturning stream function. The net northward volume transport across the Greenland-Scotland Ridge (1.2 Sv) is assumed to equal the net throughflow to the Arctic Ocean across OSNAP East. The remaining 14.1 Sv of upper limb volume transport across OSNAP East is returned southward in the lower limb. The time-mean Lagrangian overturning within the eastern SPG informs us that 8.4 Sv of the total 14.1 Sv volume flux into the lower limb occurs south of the GSR, which implies that the remaining 5.7 Sv is due to diapycnal water mass transformation taking place within the Nordic Seas and the Arctic Ocean.

depicts the contribution of dense water formation within the eastern SPG to the time-mean strength of the AMOC at OSNAP East.

2.3.3 Lagrangian overturning pathways in the eastern SPG

We next explore how the time-mean Lagrangian overturning is distributed across the major circulation pathways of the eastern SPG. To do this, we classify water parcels according to the route by which they recirculate back to the OSNAP East section. Three circulation pathways are defined geographically: water parcels which flow westward across the Reykjanes Ridge north of OSNAP East (IcRo-RR-Irm), and water parcels confined to the Iceland-Rockall (***IcRo-IcRo***) and Irminger Basins (***Irm-Irm***) respectively. We note that no water parcels with an Irminger Basin inflow return to the section east of the Reykjanes Ridge.

Figure 2.5 highlights the strong disparity between the distributions of northward transport and Lagrangian density-coordinates overturning across our three circulation pathways. We find that, while the ***IcRo-IcRo*** and ***Irm-Irm*** pathways account for 81% (46.1 Sv) of the mean northward transport recirculating within the eastern SPG, they are collectively responsible for only 25% (2.1 Sv) of the time-mean Lagrangian overturning at OSNAP East. To understand the source of this disparity, we examine the net densification of water parcels during their recirculation in the eastern SPG ($\Delta\sigma_\theta$) as a function of their inflow location along OSNAP East (Fig. 2.6). To obtain this, we first calculate the net change in potential density of recirculating water parcels between their northward and southward crossings of the OSNAP East section (i.e, $\Delta\sigma_\theta = \sigma_{South} - \sigma_{North}$) before averaging in discrete $x - z$ bins (Δz = 25 m, Δx = 25 km), where z and x correspond to the depth and distance along the OSNAP East section where a water parcel initially flows northward.

Figure 2.6 shows that along-stream densification is principally confined to water parcels flowing northward across OSNAP East in the upper limb (i.e., above the mean depth of the isopycnal of maximum Lagrangian overturning). Yet, almost

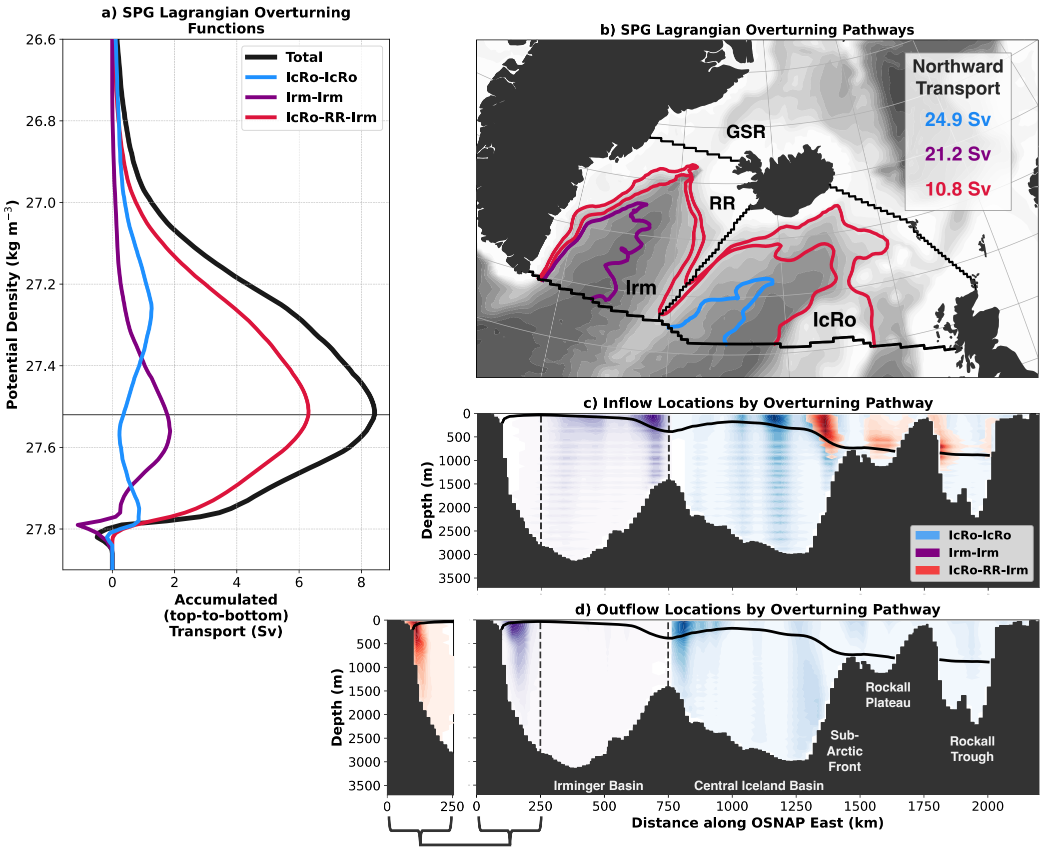

Figure 2.5: Lagrangian pathways of water parcels recirculating back to OSNAP East within the eastern SPG. (a) The total SPG Lagrangian overturning stream function decomposed by circulation pathway through the major basins: **IcRo** = Iceland-Rockall Basin, **Irm** = Irminger Basin, **RR** = Reykjanes Ridge. (b) Example trajectories illustrating each of the three categories of circulation pathways north of the section and their respective mean northward transports across OSNAP East (Sv). Shading represents ORCA025 model bathymetry contoured every 250 m. (c) Inflow and (d) Outflow locations of water parcels along OSNAP East classified by pathway. Volume transports (Sv) for each pathway are averaged in discrete $x - z$ space (Δz = 25 m, Δx = 25 km) using all 396 initialisation months before normalising by the maximum mean transport recorded across all bins (darker colour shading thus indicates where, on average, transport is strongest for each overturning pathway). For clarity, the outflow locations of the ***IcRo-RR-Irm*** and ***Irm-Irm*** pathways in the EGC are presented separately in panel d. The 1976-2008 mean isopycnal of maximum Lagrangian overturning (27.52 kg m^{-3}), denoting the interface between the upper and lower limbs of the AMOC, is shown in (c) and (d) in bold.

three-quarters (72%) of the volume transport recirculated within the Iceland-Rockall and Irminger Basins flows northward across OSNAP East in the lower limb of the AMOC, where, in the presence of weak diapycnal mixing (Waterhouse et al., 2014), water parcels overwhelmingly recirculate along isopycnals ($|\Delta\sigma_\theta| \leq 0.01$ kg m^{-3}). The central Iceland Basin represents a notable exception, however, since Figure 2.6 shows a concentrated region of negative diapycnal transport ($\Delta\sigma_\theta$ < -0.01 kg m^{-3}) below the isopycnal of maximum Lagrangian overturning. We attribute this to subpolar-origin water parcels in the lower limb of the AMOC becoming lighter on mixing with warm subtropical inflows, as previously highlighted by Berglund et al. (2023) and de Boisséson et al. (2012). Such upwelling from the ocean interior arises from divergence along the northern branch of the NAC, whereby the obduction of subpolar water into the mixed layer replenishes SPMW advected northward (Brambilla et al., 2008).

Since the ***IcRo-IcRo*** and ***Irm-Irm*** pathways represent successive stages along one continuous SPG pathway intercepted by the OSNAP East array, we choose to consider their contributions to the mean Lagrangian overturning collectively. In agreement with the observational studies of Thierry et al. (2008) and Petit et al. (2020), we find that ***IcRo-IcRo*** water parcels, sourced primarily from the northernmost NAC branch, undergo initial densification within the upper limb of the AMOC before flowing southward across OSNAP East in the ERRC (Fig. 2.5a, Fig. 2.6). Given that the ERRC retroflects south of 59°N (Daniault et al., 2016), this "preconditioned" SPMW rapidly returns northward across OSNAP East via the Irminger Current. Since Figure 2.5c shows that inflow to the Irminger Current remains concentrated within the upper limb of the AMOC, it is hence the substantial densification experienced downstream in the Irminger Basin that is responsible for the subduction of ***Irm-Irm*** water parcels into the lower limb of the AMOC. These successive transformations of SPMW manifest in the Lagrangian overturning stream functions presented in Figure 2.5a (blue and purple lines) through an increase in the isopycnal of maximum Lagrangian overturning from 27.26 kg m^{-3} (***IcRo-IcRo***) to 27.56 kg m^{-3} (***Irm-Irm***). Meanwhile, the secondary peak in Lagrangian overturning along the ***IcRo-IcRo*** pathway is explained by a small fraction of water parcels, which are transformed directly into the lower limb of the AMOC while transiting from the Rockall Trough to the ERRC.

The remaining 10.8 Sv of northward transport recirculating within the eastern SPG transits directly from the central and southern branches of the NAC to the EGC via the Reykjanes Ridge in the ***IcRo-RR-Irm*** pathway (Fig. 2.5b). Interestingly, Figure 2.5d shows a clear distinction between the southward outflow locations of the ***IcRo-RR-Irm*** and ***Irm-Irm*** pathways, with the latter concentrated further offshore within the EGC. Despite accounting for less than a fifth of the total SPG northward transport across OSNAP East, we find that the ***IcRo-RR-Irm*** pathway is responsible for three-quarters of the time-mean Lagrangian overturning within the eastern SPG (6.3 Sv at 27.52 kg m^{-3}). This is consistent with Figure 2.6, which shows that, on average, water parcels initialised within the warm, surface-intensified core of the Sub-Arctic Front and the upper 1000 m of the Rockall Trough and Plateau experience the largest diapycnal transformation during their recirculation. The ***IcRo-RR-Irm*** pathway also dominates the mean cross-Reykjanes Ridge transport of the SPG north of OSNAP East (12.4 Sv), which encouragingly resides between the observed estimates of Daniault et al. (2016) (11.3 ± 4.2 Sv north of 58.5°N during 2002-2012) and Petit et al. (2018) (13.6 ± 0.8 Sv between 59-62°N in 2015). Interestingly, Koman et al. (2020) reported a notably weaker cross-Reykjanes Ridge transport north of OSNAP East (∼6.8 Sv) compared with previous observational studies; however, this discrepancy may partly be explained by the limitations of the Argo-altimetry methodology used. The remaining 0.6 Sv of cross-Reykjanes Ridge transport is accounted for by Atlantic Water trajectories which feed the North Icelandic Irminger Current flowing northwards over the Denmark Strait (Jónsson & Valdimarsson, 2005).

2.3.3.1 Overturning pathways crossing the Reykjanes Ridge

Our finding that pathways crossing the Reykjanes Ridge directly north of 59°N are the largest contributor to the density-coordinates overturning of the eastern

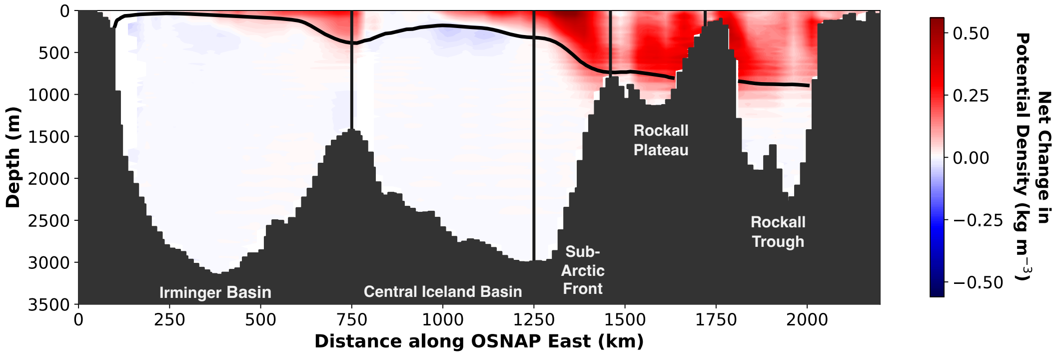

Figure 2.6: Net change in potential density of water parcels as a function of their inflow location along OSNAP East. The net change in potential density, $\Delta\sigma_\theta$ (kg m^{-3}), between northward and southward crossings of OSNAP East is computed for recirculating water parcels initialised over all 396 months before averaging in discrete $x - z$ space (Δz = 25 m, Δx = 25 km). The 1976-2008 mean isopycnal of maximum Lagrangian overturning (27.52 kg m^{-3}), denoting the interface between the upper and lower limbs of the AMOC, is shown in bold. Vertical solid lines correspond to the geographical limits of the major northward currents crossing the section.

SPG at OSNAP East is especially interesting given that the existence of substantial cross-ridge transport has historically been debated (e.g., Chafik et al., 2014; Petit et al., 2018). Here, we investigate the nature of these overturning pathways further and quantify the extent to which water parcels are transformed east and west of the Reykjanes Ridge.

To decompose the time-mean Lagrangian overturning stream function by basin, we record the potential density of each water parcel on crossing the Reykjanes Ridge in order to generate two partial Lagrangian overturning stream functions, capturing the successive diapycnal transformations of water parcels within the Iceland-Rockall and Irminger Basins:

$$F_{\textit{IcRo-RR-Irm}}(\sigma_\theta) = F_{\textit{IcRo-RR}}(\sigma_\theta) + F_{\textit{RR-Irm}}(\sigma_\theta) \tag{2.4}$$

If ***IcRo-RR-Irm*** water parcels reflected one pathway, continuously transformed along-stream, we would expect a decomposition in which the maxima of $F_{\textit{IcRo-RR}}(\sigma_\theta)$ and $F_{\textit{RR-Irm}}(\sigma_\theta)$ are equal in magnitude yet increasing in potential density, such that the maximum of $F_{\textit{IcRo-RR-Irm}}(\sigma_\theta)$ lies between them. The decomposition presented in Figure 2.7a is intriguing because the isopycnal of maximum Lagrangian overturning for the ***IcRo-RR-Irm*** pathway (27.51 kg m^{-3}) does not reside halfway between the maxima of the two constituent Lagrangian overturning stream functions (***IcRo-RR***: 27.31 kg m^{-3} and ***RR-Irm***: 27.52 kg m^{-3}). Instead, the maximum of the total Lagrangian overturning stream function is found close to the peak of overturning within the Irminger Basin. This displacement arises from the substantial water mass transformation across isopycnals denser than those at which the maximum overturning sits in the Iceland-Rockall Basin, which contributes a substantial 2.1 Sv to the maximum Lagrangian overturning at 27.52 kg m^{-3}. This additional overturning at higher densities in the Iceland-Rockall Basin also imprints onto the distribution of ***IcRo-RR-Irm*** water parcels in T-S space presented in Figure 2.7b, which suggests that two distinct overturning pathways cross the Reykjanes Ridge north of OSNAP East.

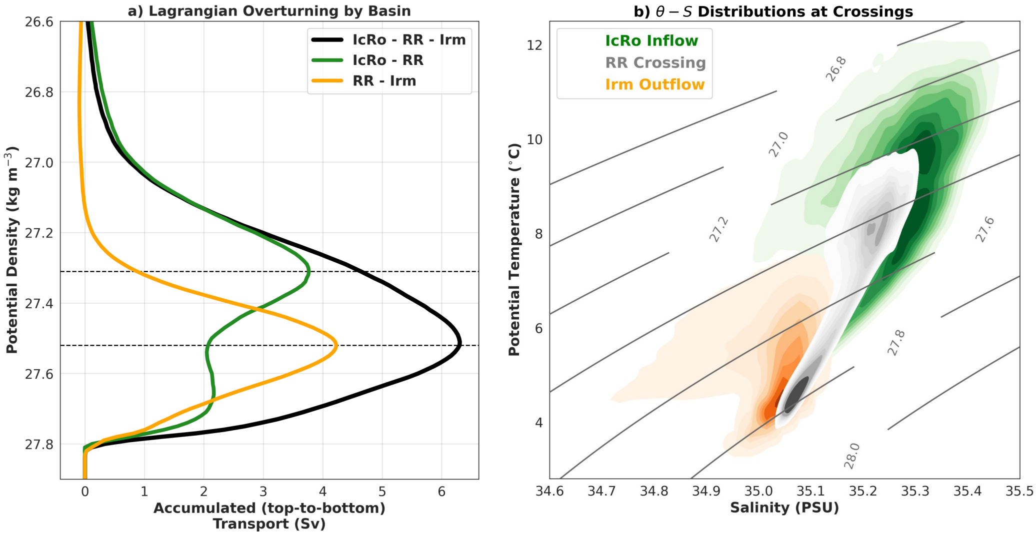

Figure 2.7: Water mass transformation along the pathways crossing the Reykjanes Ridge directly north of OSNAP East. (a) The Lagrangian Overturning Function of the ***IcRo-RR-Irm*** pathway (black line) decomposed by basin; overturning in the Iceland-Rockall basin (***IcRo-RR***) is shown in green and the Irminger basin (*RR-Irm*) in orange. Note that taking the sum of the two basin Lagrangian overturning stream functions (green and orange lines) recovers the ***IcRo-RR-Irm*** Lagrangian overturning stream function (black). (b) Density distribution of water parcel potential temperature and salinity at inflow (***IcRo***, green), on crossing the Reykjanes Ridge (***RR***, grey) and at outflow (***Irm***, orange) for the ***IcRo-RR-Irm*** pathway. Contours, corresponding to iso-proportions of the density, are plotted with an interval of 0.1, such that 10% of all water parcels are contained within the shaded region between any two contours. Overlaid potential density contours are computed using EOS80 as in the NEMO model.

The two pathways crossing the Reykjanes Ridge can be isolated by categorising water parcels according to their inflow locations along OSNAP East. Of the 10.8 Sv crossing the ridge north of 59°N, we find that 8.7 Sv is sourced from the SAF and exhibits a progressive increase in potential density along-stream, in close agreement with the evolution of SPMW described by Brambilla and Talley (2008). The SPMW advected along this ***Ic-RR-Irm*** sub-pathway is initially relatively warm (8.7 ± 2.0 °C) and salty (35.2 ± 0.1), reflecting an approximately equal mixture of subtropical and subpolar waters mixed along the SAF. Figure 2.8a illustrates how water parcels sourced from the SAF circulate cyclonically around the Iceland Basin before crossing the Reykjanes Ridge with an average potential density of 27.48 ± 0.19 kg m^{-3}. This agrees closely with the density of SPMW found along the Reykjanes Ridge in both the modelling study of de Boisséson et al. (2012) and the observations of Thierry et al. (2008) between 1990-2006. SAF water parcels undergo further densification along the northern boundary of the Irminger Basin, including subduction into the lower limb of the AMOC on the edge of the EGC. The resulting entrainment into the EGC, coupled with the pathway's intermediate density (27.62 ± 0.20 kg m^{-3}) on returning to OSNAP East, suggests that SPMWs originating from the SAF are the likely source of upper Irminger Sea Intermediate Water, recently identified by Le Bras et al. (2020).

The gradual densification exhibited along the SAF pathway is largely explained by the small median depth change of SPMW water parcels ($\Delta z \approx +55$ m), which, in the presence of sloping isopycnals, enables water masses to undergo continuous cooling and freshening during recirculation. Although this implies that density compensation occurs within the SPG (Xu et al., 2016; Zou et al., 2020a), we find that thermal changes dominate the diapycnal transformation, in agreement with estimates of the surface-forced water mass transformation due to air-sea fluxes (e.g., Desbruyères et al., 2019; Marsh, 2000). The largely horizontal ***Ic-RR-Irm*** sub-pathway accounts for 4.8 Sv of the maximum Lagrangian overturning at OSNAP East, and thus corresponds closely with the horizontal component of overturning estimated by Zhang and Thomas (2021) using OSNAP observations (5.6 Sv).

a) Example Trajectories: SAF Origin

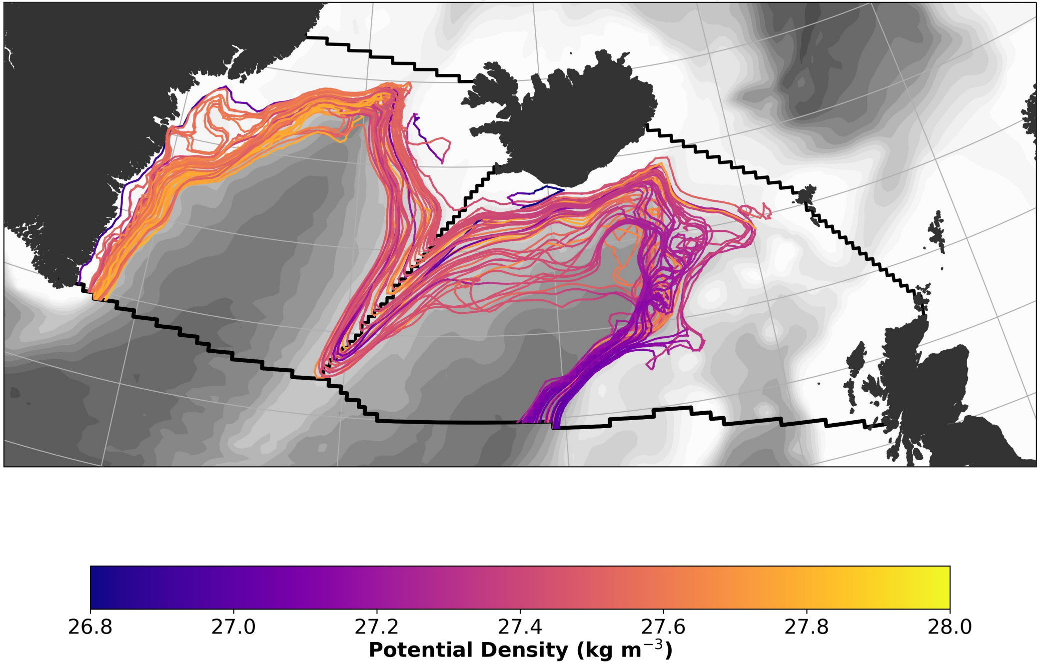

b) Example Trajectories: Rockall Origin

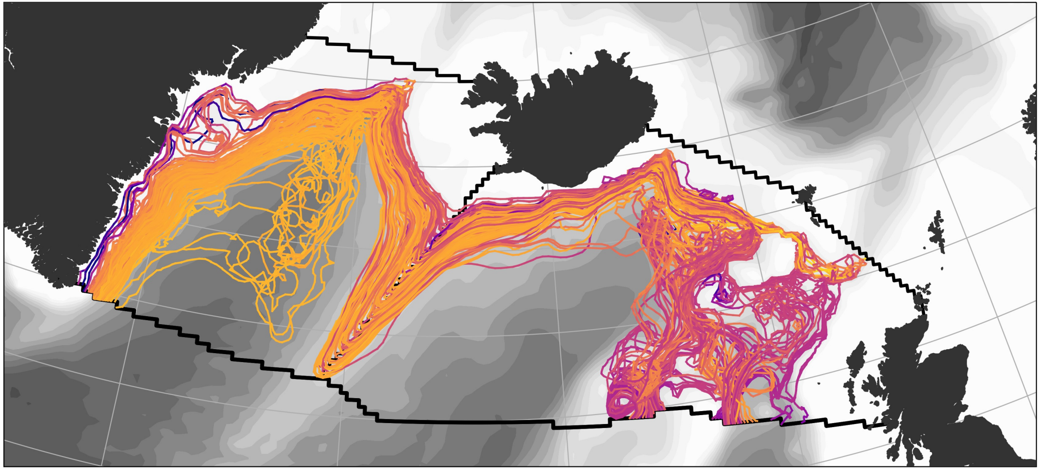

Figure 2.8: Example trajectories for the two principal overturning pathways crossing the Reykjanes Ridge north of OSNAP East. The potential density evolution along 50 randomly sampled trajectories originating from (a) the Sub-Arctic Front and (b) the Rockall Trough and Plateau is shown in colour. Trajectories are superimposed on the ORCA025 model bathymetry contoured every 250 m.

The remaining 2.1 Sv of the ***IcRo-RR-Irm*** pathway flows northward across OSNAP East at intermediate depths via the Rockall Trough and Rockall Plateau. Although the water masses transported along this ***Ro-RR-Irm*** sub-pathway are predominantly of subtropical-origin, they are found to be denser on arrival at the section compared with ***Ic-RR-Irm*** water parcels, owing to their greater salinity (35.3 ± 0.1). Figure 2.8b shows that water parcels are advected northwards feeding the 500-1000 m "entrainment zone" in the northern Iceland Basin (Dickson et al., 2002; Sarafanov, 2009) before undergoing dramatic cooling and freshening near the Faroe Bank Channel. This step-change in water properties along the Rockall pathway (Fig. 2.7b) closely resembles the formation of Icelandic Slope Water (ISW) (Holliday et al., 2009; Read, 2000; Van Aken & De Boer, 1995): ISW is a water mass formed when ISOW descending the Iceland-Faroes Ridge entrains ambient SPMW. This interpretation of the ***Ro-RR-Irm*** sub-pathway is additionally supported by the recent observations of Petit et al. (2018), who showed that ISW was the second largest contributor to the westward flow across the Reykjanes Ridge between 50°N and 63°N. After following the 1000 m bathymetric contour around the northern Iceland Basin (Fig. 2.8b), water parcels reach the Reykjanes Ridge with an average density of 27.70 ± 0.12 kg m^{-3}, consistent with their large median depth change of +380 m. In contrast to the SAF pathway, water parcels experience minimal further densification in the Irminger Basin before returning to OSNAP East via the EGC and deep interior pathways.

2.3.3.2 Timescales of Lagrangian overturning in the eastern SPG

One of the most valuable properties of the Lagrangian overturning stream function, as applied here, is that it integrates across water parcels with recirculation times ranging from days to years. We can therefore examine the temporal structure underlying the time-mean Lagrangian overturning in the eastern SPG and diagnose the dominant advective timescales over which water mass transformation takes place north of OSNAP East. Throughout our subsequent discussion, we choose to define the times taken to recover 50% ($\tau_{50\%}$) and 90% ($\tau_{90\%}$) of the maximum Lagrangian overturning as measures of the characteristic overturning timescale for each of our circulation pathways.

In Figure 2.9a we present the Lagrangian overturning of the eastern SPG as a function of the time water parcels spend north of OSNAP East, such that at any given time only the subset of all recirculating water parcels which have already returned to the section are included in the calculation. Since only water parcels which recirculate south of the Greenland-Scotland Ridge are included in this calculation, we reserve discussion of the overturning timescales associated with Nordic Seas overflows for Section 2.3.4.2. Surprisingly, we find that three-quarters of the maximum Lagrangian overturning within the eastern SPG (at 27.52 kg m^{-3}) can be explained by water parcels which spend 1.4 years or less north of OSNAP East. A further 5.6 years is required to recover the remaining 25% of the maximum Lagrangian overturning, along with the majority of SPG overturning in the highest density classes (> 27.7 kg m^{-3}).

Previous Lagrangian studies have considered the circulation and overturning timescales as equivalent (e.g., Georgiou et al., 2020, 2021). However, Figure 2.9b shows that, on average, 50% of the northward transport returns to OSNAP East in just 0.6 years, approximately half of the time taken to recover the equivalent proportion of the maximum Lagrangian overturning ($\tau_{50\%}$ = 1.0 yrs). This large disparity between the overturning and circulation timescales indicates that water recirculating along isopycnals, primarily in the lower limb (Fig. 2.6), must, on average, return to OSNAP East more quickly than water which is transformed across isopcynals. The ***Irm-Irm*** pathway is an important exception, however, given that isopycnal transport in the Irminger Gyre recirculates to OSNAP East more slowly than the adjacent Irminger Current, despite its shorter path length (not shown).

Figure 2.9b also shows that the diapycnal overturning within the eastern SPG is characterised by episodes of strong diapycnal transformation associated with the return flows of each of the major overturning pathways identified in Section 2.3.3. The rapid accumulation of Lagrangian overturning between 0.5 - 1.5 years following northward flow across OSNAP East is dominated by ***Irm-Irm*** and ***Ic-RR-Irm*** pathways. The initial pulse of overturning recovered at OSNAP East is explained by water parcels recirculating along the ***Irm-Irm*** pathway, which are advected through the Irminger Basin on seasonal timescales ($\tau_{50\%}$ = 0.5 yrs). Meanwhile, dense water formation along the ***Ic-RR-Irm*** pathway is divided evenly between water parcels recirculating on sub-annual and interannual timescales ($\tau_{50\%}$ = 1.0 yrs). As the largest contributor to the time-mean strength of the SPG Lagrangian overturning at OSNAP East, the especially narrow distribution of overturning times exhibited by ***Ic-RR-Irm*** water parcels ($\tau_{90\%}$ = 1.6 yrs) supports the conclusion of Petit et al. (2020) that surface buoyancy loss over the Irminger and Iceland Basins projects onto diapycnal overturning with minimal lag.

Once 1.5 years have elapsed following northward flow across OSNAP East, a more gradual accumulation of Lagrangian overturning is evident in Figure 2.9b, attributable to the deep ***IcRo-IcRo*** ($\tau_{90\%}$ = 2.6 yrs) and ***Ro-RR-Irm*** ($\tau_{90\%}$ = 3.4 yrs) pathways. The longer overturning timescale of both pathways is associated with the entrainment of SPMW, sourced from the Rockall Trough, into the Norwegian Seas overflow, which subsequently returns to OSNAP East at depth either via the ERRC (***IcRo-IcRo***) or the EGC (***Ro-RR-Irm***) (see Fig. 2.5d). Our finding that entrainment can contribute to deep water formation in the northern Iceland Basin on subdecadal timescales agrees with the recent observational study of Devana et al. (2021). Those authors estimated a total advection time of 1.5 - 2.5 years for upper ocean anomalies in the Iceland Basin to be entrained by ISOW and return to OSNAP East.

2.3.4 Lagrangian overturning in stationary fields

2.3.4.1 Comparing the time-mean Lagrangian overturning in the eastern SPG using time-evolving and stationary fields.

An important limitation of our primary Lagrangian experiment is our inability to explicitly resolve the overturning pathways of the Nordic Seas overflows within the relatively short 7-year advection time. To diagnose the contribution of the Nordic Seas overflow pathways to the time-mean strength of the AMOC at OSNAP East, we choose to replicate our primary Lagrangian experiment using time-averaged velocity and tracer fields (1976-2015). There are two principal advantages of using a stationary velocity field in our Lagrangian analysis. Firstly, trajectory calculations are more efficient since using a single time-averaged velocity field

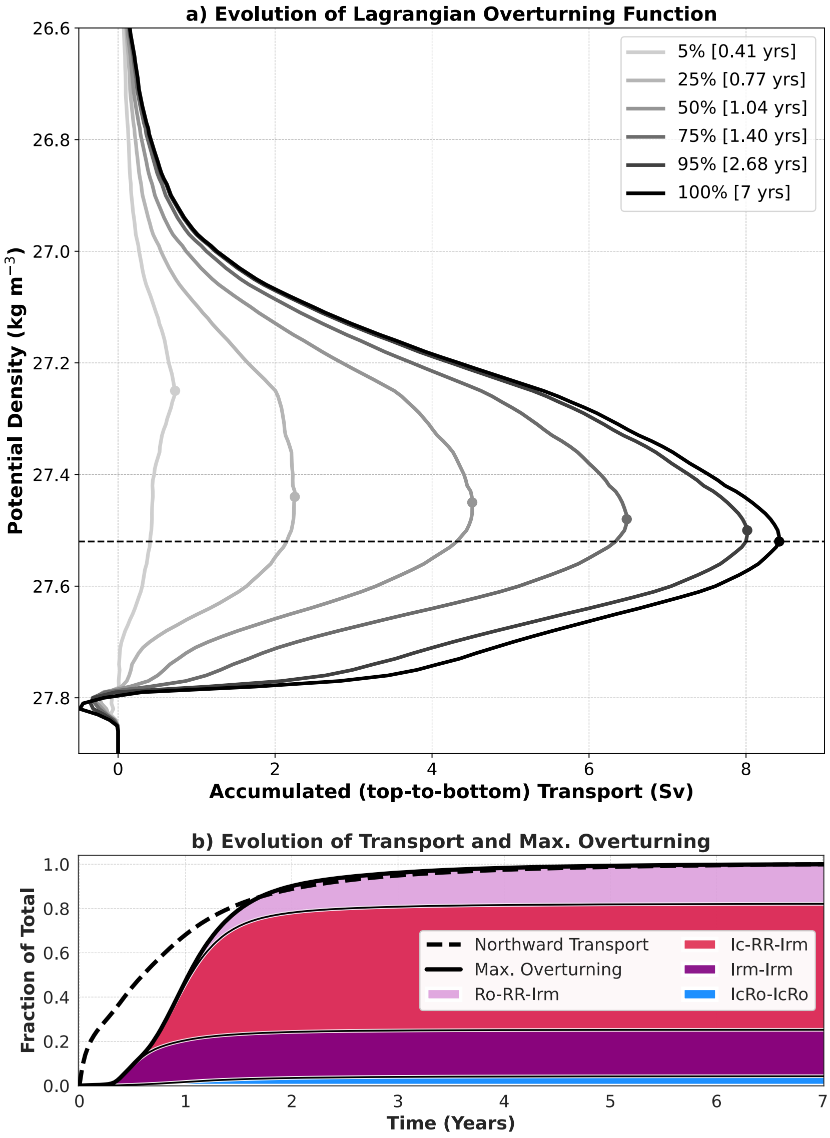

Figure 2.9: Evolution in time of Lagrangian overturning within the eastern SPG at OSNAP East. (a) Lagrangian overturning stream function evaluated as a function of time elapsed following northward flow across OSNAP East, with the maximum denoted for each profile (dots). The horizontal dashed line in (a) corresponds to the isopycnal of maximum Lagrangian overturning (27.52 kg m^{-3}) once 7 years have elapsed. (b) Normalised cumulative volume transport (black-dashed) and Lagrangian overturning (black-solid) at the 27.52 kg m^{-3} isopycnal as a function of time elapsed following northward flow across OSNAP East. The proportion of the maximum Lagrangian overturning accounted for by each of the eastern SPG circulation pathways is shaded.

eliminates the need for multiple water parcel initialisations. Secondly, since stationary velocity and tracer fields are, by definition, time-independent, their use permits an arbitrary maximum advection time. Here, we choose to advect water parcels for a maximum of 60-years, thereby exceeding the length of the historical period simulated by our ocean model hindcast by a further two decades. We begin by validating our stationary fields approach by comparing the Lagrangian overturning pathways and transports in the eastern SPG determined from both time-evolving and time-averaged fields.

To ensure consistency in our comparison of the two Lagrangian experiments, the diagnostics presented in Figure 2.10 include only the water parcels which return to OSNAP East within the eastern SPG and within 7 years of flowing northwards across the section. Figure 2.10a shows that, while the absence of time-varying transports results in a small 0.5 Sv overestimation of the maximum Lagrangian overturning at 27.52 kg m^{-3}, the time-mean Lagrangian overturning stream functions generated from stationary and time-evolving fields are in remarkably close agreement.

On partitioning the maximum Lagrangian overturning in the eastern SPG between the four circulation pathways defined in Section section 2.3.3, we encouragingly find that the composition of SPG overturning at OSNAP East is reproduced using stationary fields, including the dominance of the pathways crossing the Reykjanes Ridge. The median recirculation time and northward transport advected along the dominant ***Ic-RR-Irm*** pathway are especially well represented in stationary fields (Fig. 2.10c-d), suggesting that eddy-induced transports make only a limited contribution to the time-mean overturning along this route. In contrast, the northward transport advected along the ***IcRo-IcRo*** and ***Irm-Irm*** pathways are found to be underestimated by 10.2 Sv and 5.2 Sv, respectively, in our stationary fields experiment. We attribute this considerable underestimation to our averaging over the seasonal cycle, given that observational studies find substantial transport variations in both the Irminger and Iceland-Rockall Basins on seasonal timescales (de Jong et al., 2020; Gary et al., 2011). As a further consequence of our smoothing of seasonal variations in the velocity field of the eastern SPG, Figure 2.10d shows a notable increase in the median recirculation times of the ***IcRo-IcRo*** and ***Irm-Irm*** pathways when using stationary fields. Interestingly, the maximum overturning contribution of the ***Irm-Irm*** pathway

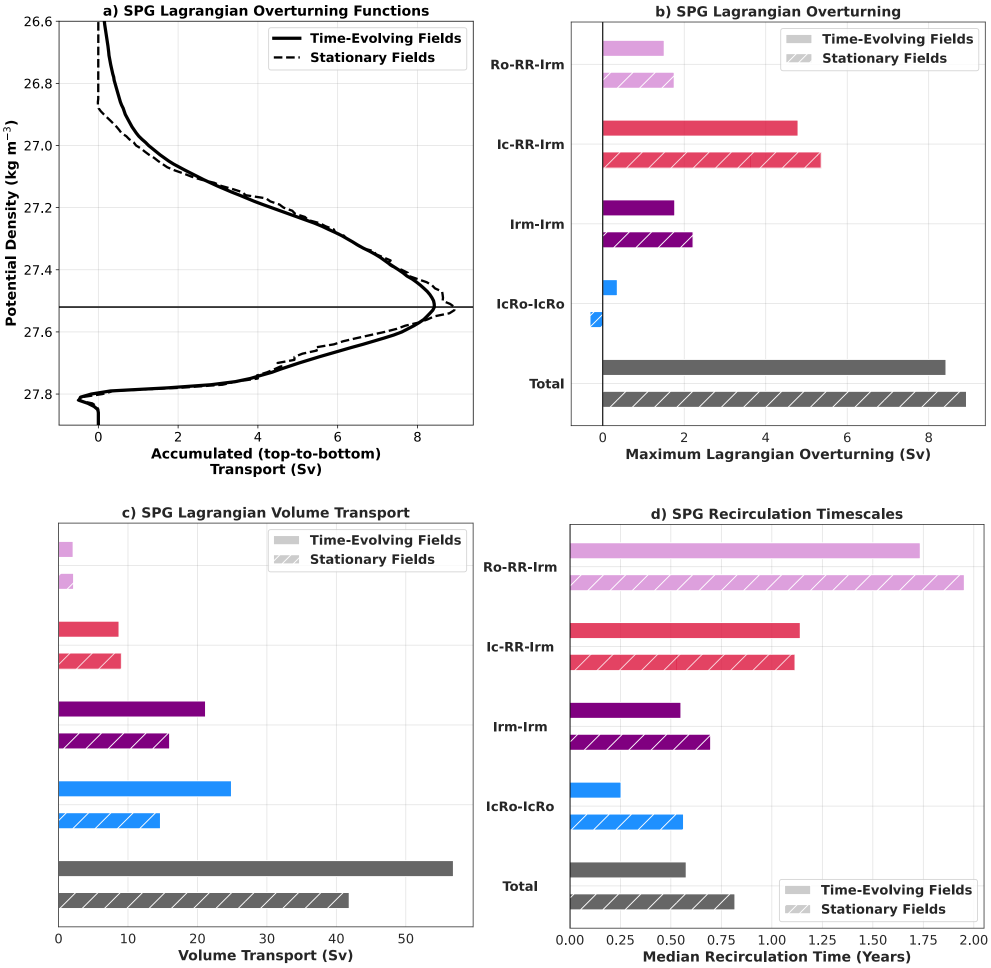

Figure 2.10: Lagrangian overturning diagnostics in the eastern SPG determined from time-evolving and stationary fields experiments. (a) Time-mean Lagrangian overturning stream functions for the eastern SPG calculated from ensembles of trajectories advected by time-evolving (solid line) and stationary (dashed line) velocity and tracer fields. The solid line at 27.52 kg m^{-3} identifies the shared isopycnal of maximum Lagrangian overturning in the eastern SPG. (b-d) The Lagrangian overturning at 27.52 kg m^{-3}, total northward transport across OSNAP East, and median recirculation time are decomposed into the circulation pathways of the eastern SPG as defined in Section section 2.3.3. Diagnostics determined from stationary velocity and tracer fields are distinguished using hatched bars.

remains in broad agreement between our two Lagrangian experiments (Fig. 2.10b), suggesting that seasonally transformed water parcels recirculating within the Irminger Basin do not contribute substantially to the time-mean strength of the AMOC at OSNAP East. In the Iceland-Rockall Basin, the obscuring of wintertime transformation from the upper to the lower limb in time-averaged fields yields a negative overturning contribution for the ***IcRo-IcRo*** pathway, corresponding to the steady obduction of water into the upper limb along the northern NAC branch (see Fig. 2.6).

In spite of the biases discussed above, we conclude that the structure of the time-mean overturning at OSNAP East is sufficiently well represented in stationary velocity and tracer fields to justify their use in investigating the pathways of the Nordic Seas overflows.

2.3.4.2 Pathways crossing the Greenland-Scotland Ridge.

We explore the nature of overturning along the pathways of the Nordic Seas overflows by considering all of the trajectories which return to OSNAP East within the maximum 60 year advection time of our second Lagrangian experiment. Over the entire duration of the experiment, 94.2% of the total northward transport initialised along OSNAP East returns to the section, allowing us to recover 13.0 Sv of the time-mean Lagrangian overturning (Fig. 2.11a). It should be noted that, since the time-mean Lagrangian overturning stream function, by definition, does not include the 1.2 Sv net throughflow to the Arctic, we would not expect the maximum Lagrangian overturning to converge towards the maximum of the Eulerian stream function shown in Figure 2.4c (15.3 Sv), irrespective of our choice of the maximum advection time.

The Nordic Seas overflows are captured within the 4.3 Sv sourced from the SAF and the Rockall Trough, which flows northward across the Greenland-Scotland Ridge before returning to OSNAP East either via the Iceland Basin or the Irminger Sea (hereafter the ***IcRo-GSR-Ic/Irm*** pathway). We note that this recirculating transport does not include a further 2.9 Sv, which flows northward across the Greenland-Scotland Ridge following initialisation but does not return to OSNAP East within the 60-year maximum advection time. On combining this outstanding transport with the recirculating transport of the ***IcRo-GSR-Ic/Irm*** pathway, we obtain an estimate of the total cross Greenland-Scotland Ridge transport of 7.2 Sv, which is in broad agreement with observations of the Atlantic inflow into the Nordic Seas (8.0 ± 0.7 Sv; Østerhus et al., 2019). Figure 2.11a shows that, water parcels transformed in the Nordic Seas within the 60-year maximum advection time collectively contribute 3.9 Sv to the time-mean strength of the AMOC at OSNAP East. The remaining 0.4 Sv of the total 4.3 Sv of recirculating transport flowing across the Greenland-Scotland Ridge returns southward across OSNAP East in the upper limb via the fresh EGCC.

Figure 2.11b presents the T-S distributions of overflow water parcels on their northward and southward crossings of both OSNAP East and the Greenland-Scotland Ridge. Concurrent with our earlier findings, the Iceland-Rockall Basin plays a critical role in preconditioning subtropical-origin waters en route to the Nordic Seas. On crossing the Greenland-Scotland Ridge, water parcels represent SPMW of intermediate density (27.37 ± 0.14 kg m^{-3}), which is distinctly lighter than that crossing the Reykjanes Ridge as observed by Brambilla and Talley (2008). On returning to the Greenland-Scotland Ridge, ***IcRo-GSR-Ic/Irm*** water parcels have, on average, been cooled to 2.2 ± 1.5 °C, yielding a potential density (27.83 ± 0.19 kg m^{-3}) within the observed range for overflow waters (Dickson & Brown, 1994). South of the ridge, the poor representation of diapycnal mixing between the overflows and ambient Atlantic waters results in excessive entrainment of ambient Atlantic waters by the overflows. This warming and salinification (Fig. 2.11b) reduces the average potential density of overflow water parcels to 27.70 ± 0.16 kg m^{-3} and thus directly imprints onto the structure of diapycnal overturning downstream, where the southward transport in the density range of the observed overflows is $\sim$11 Sv less than found in observations (Sarafanov et al., 2012).

We next distinguish between the water mass varieties that are equivalent to DSOW and ISOW in the model (albeit found at lighter densities). We define DSOW (ISOW) as ***IcRo-GSR-Ic/Irm*** water parcels which return to OSNAP East in the lower limb of the AMOC via the sills west (east) of Iceland. It should be noted that this definition excludes water parcels flowing southwards in the EGCC. Figure 2.11c shows that ISOW water parcels (1.3 Sv) predominantly originate from the surface inflows to the Rockall Trough, whereas DSOW (2.6 Sv) water parcels are sourced approximately equally from the warm, subtropical inflows to the SAF

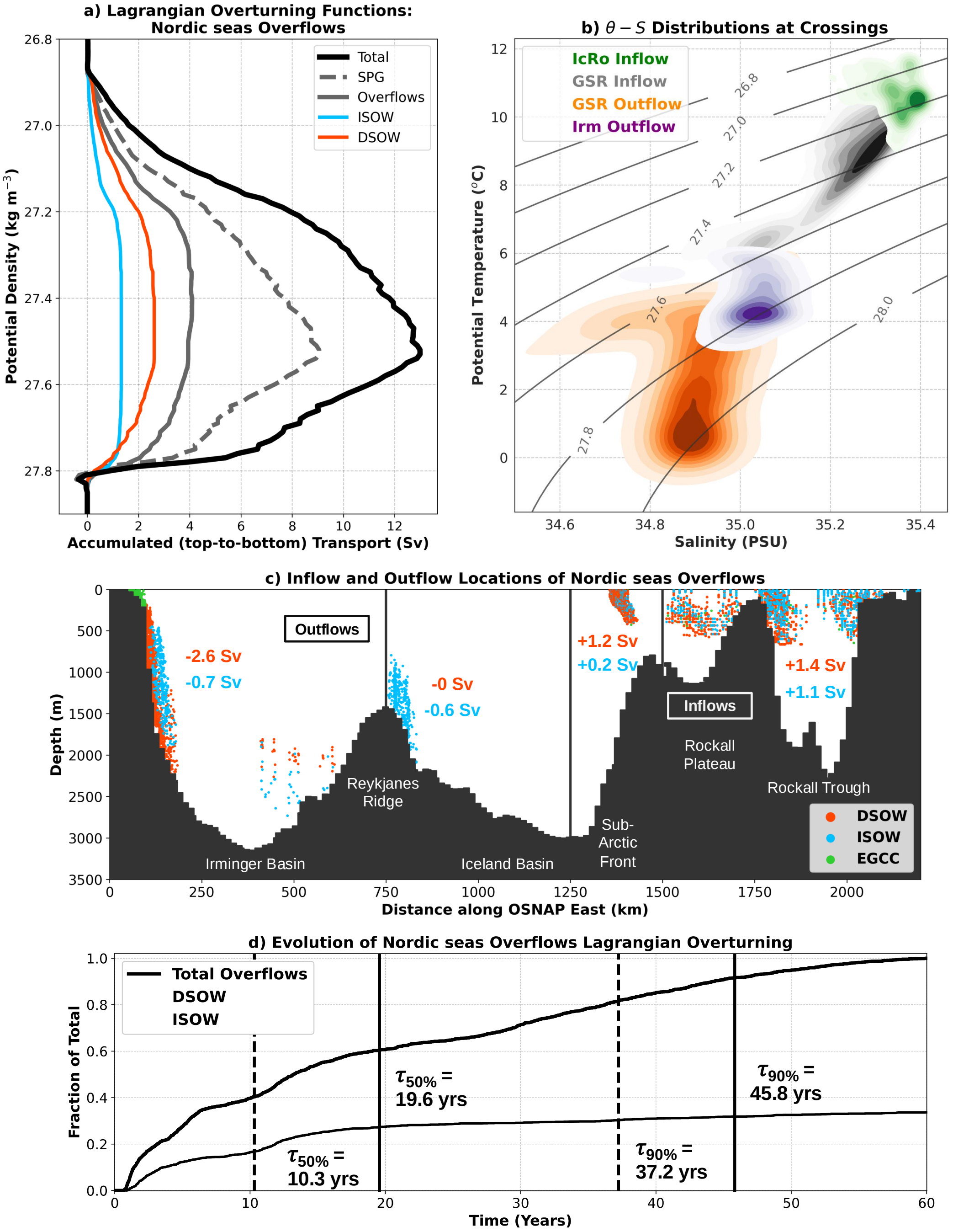
a) Lagrangian Overturning Functions: Nordic seas Overflows

b) $\theta - S$ Distributions at Crossings

c) Inflow and Outflow Locations of Nordic seas Overflows

d) Evolution of Nordic seas Overflows Lagrangian Overturning

Figure 2.11: Lagrangian overturning, transports and timescales for water parcels flowing northward across the Greenland-Scotland Ridge. (a) The total Lagrangian overturning stream function at OSNAP East determined using stationary fields decomposed into the contributions made by the eastern SPG and the Nordic Seas overflows. The Lagrangian overturning of the Nordic Seas overflows is further divided between DSOW and ISOW varieties. (b) Density distribution of water parcel potential temperature and salinity at inflow, on northward and southward crossings of the Greenland-Scotland Ridge, and on return to OSNAP East for the ***IcRo-GSR-Ic/Irm*** pathway. Contours, corresponding to iso-proportions of the density, are plotted with an interval of 0.1, such that 10% of all water parcels are contained within the shaded region between any two contours. (c) Inflow and Outflow locations of DSOW and ISOW water parcels along OSNAP East. The water parcels which return to OSNAP East via the fresh EGCC are shown in green. (d) Normalised cumulative Lagrangian overturning of the Nordic Seas overflows at the 27.52 kg m^{-3} isopycnal as a function of time elapsed following northward flow across OSNAP East.

and below 250 m over the Rockall Plateau. Since, by definition, all of the transport advected along our two overflow pathways is transformed from the upper to the lower limb of the AMOC north of OSNAP East, it follows that DSOW contributes twice as much as ISOW to the time-mean strength of Lagrangian overturning in our stationary fields experiment (Figure 2.11a). However, it remains unclear how the residual 1.7 Sv, which does not return to OSNAP East on entering the Nordic Seas, is distributed between DSOW and ISOW pathways.

On returning to OSNAP East, DSOW is transported southwards in the EGC and to a lesser extent through deep interior pathways on the western flank of the Reykjanes Ridge. Meanwhile, the export of ISOW across OSNAP East is divided almost equally between the ERRC in the western Iceland Basin and at depth in the EGC, offshore of DSOW. This distribution contrasts with recent observations, which found no substantial cross-Reykjanes Ridge transport of ISOW north of the Bight Fracture Zone (Petit et al., 2018), and hence north of OSNAP East. One likely explanation for this discrepancy, proposed in the modelling study of Xu et al. (2010), is that the simulated ISOW is too light compared with observations, and thus flows over shallower fractures in the Reykjanes Ridge north of 59°N. In reality, approximately half of the 5.3 ± 0.4 Sv of ISOW flowing southward across OSNAP East in the ERRC (2014-18) is derived from the entrainment of SPMW and Labrador Sea Water in the northern Iceland Basin (Johns et al., 2021). However, we find negligible along-stream transformation of *IcRo-IcRo* water parcels within or above the observed ISOW density range (Fig. 2.5a), suggesting that excessively entrained SPMWs are advected unrealistically by pathways crossing the Reykjanes Ridge (***Ro-RR-Irm***) within the model.

A further distinction between ISOW and DSOW varieties can be made by examining the dominant advective timescales over which overflow water parcels are overturned north of OSNAP East. Figure 2.11d shows that, while 90% of the Lagrangian overturning along the ISOW pathway can be explained by water parcels which spend 37.2 years or less north of OSNAP East, almost an additional decade ($\tau_{90\%}$ = 45.8 yrs) is required to accumulate the equivalent proportion of the Lagrangian overturning along the DSOW pathway. This difference in overturning timescales is explained by the fact that DSOW water parcels are twice as likely (82%) to enter the Arctic Ocean during their recirculation compared with ISOW water parcels (41%), and thus spend a greater amount of time north of the Greenland-Scotland Ridge (44.8 years for DSOW compared with 34.9 years for ISOW). We also find that 92% of the residual overflow transport (1.7 Sv), requiring more than 60 years to return to OSNAP East, enters the Arctic Ocean through either the Fram Strait or the Barents Sea. Our inability to recover these residual overflow water parcels within the duration of our Lagrangian experiment is hence unsurprising, given that recent chemical tracer studies estimate that Atlantic Waters can spend between 30-50 years circulating within the Arctic Ocean before returning to the Fram Strait (Stöven et al., 2016; Wefing et al., 2021).

2.4 Discussion & Conclusions

In this study, we demonstrate how Lagrangian particle tracking can be employed to partition the diapycnal overturning across a trans-basin section amongst the circulation pathways comprising the subpolar AMOC. In this first application of our Lagrangian overturning framework, we explore the structure of the time-mean overturning circulation in the eastern SPNA using an eddy-permitting ocean hindcast simulation (ORCA025-GJM189). By advecting water parcels from the northward inflows across OSNAP East using both time-evolving and stationary velocity and tracer fields, coupled with a simple parameterisation of vertical convective mixing, we quantify how water mass transformation along the circulation pathways of the eastern SPG and Nordic Seas overflows projects onto the diapycnal overturning at OSNAP East. We show how the Lagrangian overturning stream function, complementing the traditional Eulerian stream function, can be used to diagnose the extent to which water parcels are transformed in each basin and to identify the dominant advective timescales of the overturning circulation in the eastern SPNA.

In our primary Lagrangian experiment using time-evolving fields, we evaluate the trajectories of more than 11.2 million numerical water parcels initialised over 396 months between 1976-2008 to investigate the overturning pathways of the eastern SPG. Our analysis shows that 55% (8.4 Sv) of the time-mean overturning recorded at OSNAP East takes place south of the Greenland-Scotland Ridge in this model, underscoring the dominant role of the SPG in water mass transformation (Desbruyères et al., 2019; Menary et al., 2020a; Petit et al., 2020). Through a decomposition of the time-mean Lagrangian overturning stream function, we show that the SPG pathways crossing the Reykjanes Ridge north of OSNAP East make the largest contribution to mean strength of the AMOC at the section. The principal overturning pathway, accounting for 4.8 Sv of the maximum overturning, is sourced from the central NAC branch along the SAF, and undergoes continuous densification by circulating horizontally across sloping isopycnals. Moreover, since water parcels are subducted into the lower limb of the AMOC on the edge of the EGC and overturn rapidly in less than 2 years, we suggest that the SAF is the likely source of upper ISIW recently defined by Le Bras et al. (2020).

The short overturning timescales of the eastern SPG pathways are dynamically important since they govern the rate at which thermohaline anomalies can propagate advectively through the Iceland and Irminger Basins, and thus imprint onto the overturning measured at OSNAP East. The SPNA exhibits large-scale thermohaline variability on decadal timescales (Desbruyères et al., 2021; Hátún et al., 2005; Holliday, 2003; Lozier et al., 2008), forced in part by abrupt transitions in the North Atlantic Oscillation (NAO Hurrell, 1995). Following the sharp transition to a strong positive phase of the NAO in 2012, the persistence of negative wind stress curl increased the export of freshwater from the Labrador and Newfoundland shelves into the branches of the NAC (Holliday et al., 2020). According to the recent observational study of Biló et al. (2022), fresh anomalies advected in the NAC reached the Reykjanes Ridge in early 2016 before transiting to the EGC mooring positioned along OSNAP East in a further 6-11 months. This implies a total advection time of between 1.5-1.9 years for the freshening signal to propagate from the Iceland Basin to the Irminger Sea, in close agreement with our dominant overturning timescale of 1.6 years along the *Ic-RR-Irm* pathway.

Thermohaline anomalies have also been shown to propagate from the upper to the deep ocean via the entrainment of SPMW by the Iceland-Scotland overflows (Devana et al., 2021; Dickson et al., 2002; Sarafanov, 2009). In particular, Sarafanov et al. (2010) attributed the persistent salinifcation of ISOW during the late 1990s to the NAO-induced increase in subtropical throughput to the eastern SPNA. Here, we have identified a deep overturning pathway along which upper intermediate waters of subtropical-origin undergo dramatic cooling and freshening on mixing with ISOW south of the Iceland-Scotland Ridge. The resulting water mass, resembling dense ISW (Read, 2000; Van Aken & De Boer, 1995), crosses the Reykjanes Ridge north of 59°N before returning to OSNAP East via the EGC and deep interior pathways. Our conclusion that it takes 3.4 years for 90% of the overturning to occur along this pathway aligns with the recent finding of Devana et al. (2021), who showed that NAO-induced freshening of the upper ocean can propagate into the deep overflows via turbulent entrainment on subdecadal timescales.

To overcome our inability to recover the recirculating transport associated with the Nordic Seas overflows in our primary Lagrangian experiment, we conduct a supplementary experiment using time-averaged velocity and tracer fields (1976-2015) to advect numerical water parcels initialised along OSNAP East for up to 60 years. We find strong agreement between the structures of the time-mean Lagrangian overturning within the eastern SPG evaluated in our stationary and time-evolving fields experiments. However, this similarity masks significant biases introduced by time-averaging model fields, including the substantial underestimation of northward transport advected along basin interior pathways within the SPG.

Over the duration of our second Lagrangian experiment, 4.3 Sv of the total 7.2 Sv flowing northwards across the Greenland-Scotland Ridge returns to OSNAP East via either the dense Nordic Seas overflows (3.9 Sv) or the fresh EGCC (0.4 Sv). The remaining 2.9 Sv of cross-ridge transport is partitioned between the net throughflow to the Arctic Ocean (1.2 Sv) and residual transport (1.7 Sv), representing water parcels which require more than 60 years to return to OSNAP East. Crucially, even if all of this residual transport is ultimately subducted into the lower limb of the AMOC along the ***IcRo-GSR-Ic/Irm*** pathway, the contribution of the Nordic Seas overflows (3.9 Sv + 1.7 Sv = 5.6 Sv) would still remain secondary to transformation within the eastern SPG, albeit closer to the observed estimate of 5.8 ± 0.7 Sv (Østerhus et al., 2019). Although we find that both DSOW and ISOW varieties overturn on multi-decadal timescales, their final properties are strongly influenced by the excessive entrainment of ambient Atlantic waters south of the Greenland-Scotland Ridge in this simulation. In contrast to the substantial overturning variability recorded at OSNAP East (Desbruyères et al., 2019; Li et al., 2021a; Petit et al., 2020), observed overflow transports across the Greenland-Scotland Ridge exhibit only weak variability on interannual-decadal timescales (Østerhus et al., 2019). Thus, while it has been shown that thermohaline anomalies can be imported into the Nordic Seas via the Atlantic Water inflows (Asbjørnsen et al., 2021; Glessmer et al., 2014), the fact that water parcels typically integrate across multiple decades of water mass transformation before returning to OSNAP East means that such anomalies are unlikely to persist downstream to imprint onto Lagrangian overturning variability via this route.

The use of a single eddy-permitting ocean sea-ice hindcast is naturally a limitation of the present study. While the ORCA025 configuration has been validated extensively within the SPNA region (e.g., de Boisséson et al., 2010, 2012; Desbruyères et al., 2013, 2015; MacGilchrist et al., 2020), it remains an open question as to how the model's inability to fully resolve ocean turbulence occurring at the mesoscale and submesoscale might impact the faithful representation of the individual overturning pathways comprising the subpolar AMOC. Multi-decadal ocean sea-ice hindcasts are now routinely performed at eddy rich resolutions (at least 1/10° according to Hallberg, 2013), such as ORCA12 (Marzocchi et al., 2015), FLAME (Böning et al., 2006) and VIKING20 (Biastoch et al., 2021; Böning et al., 2016), and show substantial improvements in the simulated gyre and overturning circulations compared with observations. In particular, eddy-rich models have been found to more realistically represent the pathways and properties of both the NAC (Breckenfelder et al., 2017; Marzocchi et al., 2015) and the Nordic Seas overflows south of the Greenland-Scotland Ridge (Behrens et al., 2017). On the other hand, the transition to high resolution models has also introduced new biases, including overestimating the strength of both the subpolar AMOC and SPG circulation when compared with observed estimates (Hirschi et al., 2020; Jackson & Wood, 2020). To complicate this picture, simulated gyre and overturning circulations are also strongly influenced by the surface boundary conditions employed in ocean hindcasts (Biastoch et al., 2021). Therefore, while it is beyond the scope of this study, addressing the sensitivity of Lagrangian overturning pathways simulated within the SPNA to the choice of both horizontal model resolution and atmospheric forcing remains an important subject in need of further research.

This Chapter has demonstrated that the Lagrangian overturning stream function is a valuable addition to existing measures of the diapycnal overturning (e.g., Lozier et al., 2019; Marsh, 2000), owing to its unique ability to connect water mass transformation integrated at the basin-scale to the individual circulation pathways comprising the subpolar AMOC. Extending the Lagrangian overturning framework to investigate how seasonal to decadal overturning variability is manifested amongst the overturning pathways of the SPNA will be the subject of Chapters 3 & 4.

3

Seasonal overturning variability in the eastern subpolar North Atlantic

In Chapter 2, we introduced a novel Lagrangian measure of the overturning in the eastern SPNA by quantifying the total light-to-dense transformation occurring along recirculating water parcel trajectories. In this Chapter, we extend this Lagrangian overturning framework to identify the circulation pathways responsible for seasonal overturning variability at OSNAP East and characterise their advective timescales and along-stream transformations within the eastern SPG.

3.1 Introduction

Throughout the North Atlantic Ocean, observational and numerical modelling studies demonstrate that the variability of the AMOC is larger on seasonal than interannual timescales (Lozier et al., 2019; Mielke et al., 2013; Willis, 2010; Xu et al., 2014). In the eastern SPNA, both observations and ocean reanalyses show a pronounced seasonality in the AMOC (Fu et al., 2023; Jones et al., 2023; Mercier et al., 2015), which is closely related to the export of seasonal western boundary density anomalies (Le Bras et al., 2020; Wang et al., 2021). Since the formation of dense waters exported along the western boundary is principally governed by surface buoyancy loss over the Iceland and Irminger basins (Brambilla et al., 2008; Pacini et al., 2020; Petit et al., 2020), we might anticipate a seasonal cycle of overturning at OSNAP East which closely reflects the seasonality of surface buoyancy forcing within this region. However, the observed amplitude of seasonal overturning variability ($\sim$4 Sv; Fu et al., 2023; Mercier et al., 2015) is typically 5 times smaller than the magnitude of seasonal surface buoyancy-driven transformation ($\sim$20 Sv; Petit et al., 2020; Xu et al., 2018a). This difference reflects the fact that overturning variability depends upon both the transformation of water masses into the lower limb of the AMOC and the rate at which they are subsequently exported southward across the OSNAP East section. Given that we saw in Chapter 2 that water masses circulate within the eastern SPG on timescales ranging from weeks to years, it therefore remains an open question to what extent the overturning seasonality measured at OSNAP East can be attributed to seasonal dense water formation.

The recent modelling study of Wang et al. (2021) attributes the seasonality of overturning at OSNAP East to the projection of seasonal density changes in the western Irminger Sea onto the time-mean barotropic transport of the EGC. On the one hand, this is consistent with OSNAP observations, which reveal strong seasonality in the thickness of upper ISIW (the lightest component of the lower limb) exported southward in the EGC during 2014-18 (Le Bras et al., 2020; Li et al., 2021a). However, on the other hand, observations also show pronounced seasonality in the volume transport of the western boundary current (Mercier et al., 2024), which is closely correlated with the seasonality of wind stress curl over the Irminger Sea (Daniault et al., 2011a; Daniault et al., 2011b; Le Bras et al., 2018; Pacini et al., 2020). To our knowledge, no study to date has explored how such seasonal changes in both the density structure and transport of the EGC might act in combination to modulate the seasonality of overturning measured at OSNAP East.

In the traditional Eulerian overturning framework discussed above, seasonal overturning variability is proposed to depend upon the efficient export of lower limb water masses within several months of their formation upstream (Fu et al., 2023). At OSNAP East, Le Bras et al. (2020) showed that overturning seasonality is preferentially determined by variations in the formation rate of upper ISIW due to its rapid export southward within the EGC (Pacini et al., 2020). In contrast, variability in the formation rate of deep ISIW formed in the Irminger Sea interior was found to imprint onto interannual Eulerian overturning variability owing to its slower entrainment into the boundary current (Le Bras et al., 2020; Li et al., 2021a). Given the diversity of export times convolved in the western boundary current of the Irminger Sea, it is perhaps therefore unsurprising that changes in the velocity and density field of the EGC alone have been shown to account for only 10% of the monthly AMOC variability at OSNAP East (Li et al., 2021a).

One way to better understand the relationship between seasonal surface buoyancy-driven transformation and the overturning seasonality recorded at OSNAP East is to explicitly account for the diverse range of export timescales by adopting a Lagrangian frame of reference. Hence, in this Chapter, we make use of the Lagrangian particle tracking experiment detailed in Chapter 2 to explore how the seasonal overturning variability simulated at OSNAP East is distributed amongst the individual circulation pathways of the eastern SPG in an eddy-permitting ocean model.

This Chapter is structured as follows. We begin by reviewing the Lagrangian particle tracking approach, and defining both the Eulerian and Lagrangian overturning in density-space at OSNAP East in Section 3.2. Section 3.3.1 explores the seasonal Eulerian overturning variability simulated at OSNAP East and addresses the physical mechanisms responsible, including the important role of seasonal water parcel recirculation times in the upper Irminger Sea. In Section 3.3.2, we introduce a complementary Lagrangian measure of overturning variability at OSNAP East and compare the advective timescales of water parcels contributing to the time-mean strength and seasonality of Lagrangian overturning. We also decompose the seasonal cycle of Lagrangian overturning by circulation pathway, and examine the role of along-stream diathermal and diahaline transformations in driving seasonal dense water formation. The Chapter concludes with a discussion of our principal findings in Section 3.4.

3.2 Methods

3.2.1 Ocean General Circulation Model

In this study we use output from the eddy-permitting ORCA025-GJM189 ocean-sea-ice hindcast (Jean-Marc Molines, 2021) documented in Table 1.1 and Section 2.2.1. Our justification for using the ORCA025-GJM189 hindcast to investigate the physical mechanisms underpinning seasonal overturning variability in the eastern SPG is as follows. The ORCA025-GJM189 model is configured at a nominal horizontal resolution (1/4°), which is approximately four times finer than the typical resolution used in the ocean component of CMIP6 climate models (e.g., Heuzé, 2021) and is more typical of the climate models involved in the upcoming CMIP7 analysis. Thus, understanding how such eddy-permitting models represent seasonal to interannual subpolar overturning variability is crucial if we are to have confidence in their ability to project future trends in the AMOC.

As discussed in Chapter 2, there is broad agreement between the summertime upper ocean transports across the OSNAP East section in ORCA025-GJM189 and the observations of Sarafanov et al., 2010 at 59.5°N. Moreover, previous studies (e.g., de Boisséson et al., 2012) have highlighted the close agreement between the simulated water mass properties of SPMWs transformed at the surface of the eastern SPG at eddy-permitting resolution and those observed by Brambilla and Talley (2008) and Thierry et al. (2008). Model biases primarily emerge at depth in the ORCA025-GJM189 hindcast, where there is an absence of deep stratification within the eastern SPG due to excessive mixing between the Nordic Seas overflows and ambient Atlantic waters south of the Greenland-Scotland Ridge (MacGilchrist et al., 2020).

(a) Example trajectories initialised across OSNAP East

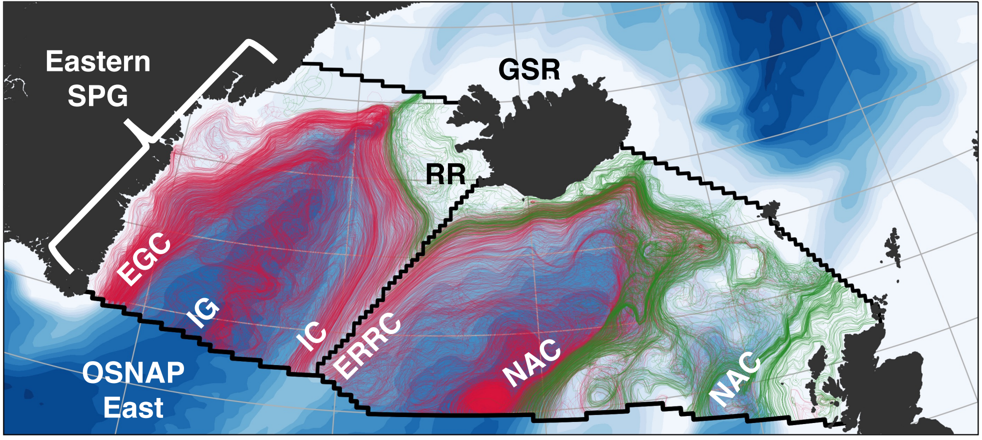

(b) Volume transport initialised across OSNAP East

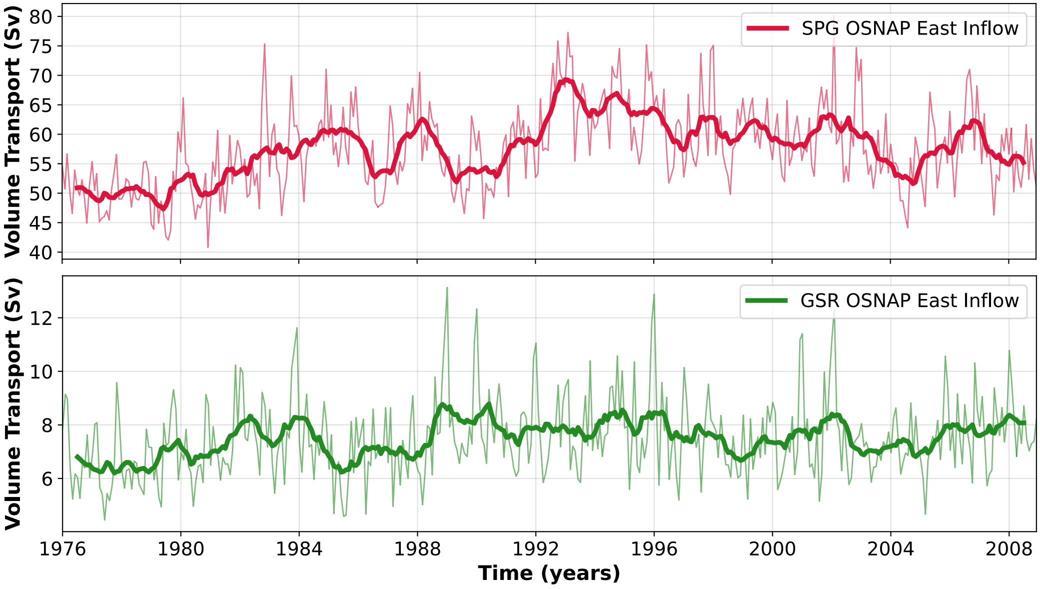

Figure 3.1: Lagrangian trajectories and volume transports across the model-defined OSNAP East section. (a) Example Lagrangian trajectories initialised on the northward inflows across OSNAP East in January 1990. Trajectories of water parcels which recirculate back to OSNAP East within the eastern SPG (south of the Greenland-Scotland Ridge) are shown in red, whereas green trajectories represent water parcels which cross the Greenland-Scotland Ridge northwards as Atlantic Water inflows to the Nordic Seas. (b) Monthly volume transports initialised on the northward inflows across OSNAP East which recirculate within the eastern SPG (red, upper panel) and those which cross the Greenland-Scotland Ridge northwards (green, lower panel). The bold lines overlaid are low pass filtered volume transports using a 12-month running mean.

3.2.2 Lagrangian Particle Tracking

To investigate the nature of seasonal overturning variability in the eastern SPG, we make use of the primary Lagrangian experiment documented in Section 2.2.2. Here, we briefly review the experimental strategy, highlighting the details which are particularly relevant for this Chapter.

Water parcels are initialised to sample the full-depth northward transport across the OSNAP East section on the earliest available day of each month (based on the centre of the nearest 5-day mean window) for a period of 33 years (1976-2008). Water parcels are removed from the experiment on meeting any one of three conditions: (i) returning to the OSNAP East section (red trajectories in Fig. 3.1a), (ii) crossing the Greenland-Scotland Ridge northwards (green trajectories in Fig. 3.1a), or (iii) reaching the maximum advection time of 7 years. Our decision to terminate water parcels on reaching the Greenland-Scotland Ridge is motivated by recent observations, which show that monthly to seasonal overturning variability at OSNAP East is dominated by surface buoyancy forcing over the Iceland and Irminger Basins rather than by variations in the overflow transport exiting the Nordic Seas (Bringedal et al., 2018; Østerhus et al., 2019; Petit et al., 2020). It should also be noted that $>$99.1% of water parcels are intercepted on crossing either OSNAP East or the Greenland-Scotland Ridge within the 7-year maximum advection time. The remaining 0.9% of water parcels almost exclusively circulate at depth within the lower limb of the AMOC north of OSNAP East and therefore do not contribute to the seasonal overturning variability.

3.2.3 Definitions of overturning in density-coordinates

We use two complementary measures of the overturning in density-coordinates at OSNAP East in this study. The Eulerian diapycnal overturning stream function, $\psi(\sigma_\theta, t)$, is calculated directly from the time-evolving velocity and potential density fields along the model-defined OSNAP East section as defined in Section 1.4.1. We denote the isopycnal at which the Eulerian overturning stream function reaches a maximum as σ_{MOC}, representing the interface between the upper and lower limbs of the AMOC at OSNAP East. The maximum Eulerian overturning (MOC), measuring the overall strength of the AMOC, therefore equates to the net northward transport within the upper limb integrated along the section. To ensure comparability between our Eulerian and Lagrangian analyses, Eulerian overturning stream functions are computed using the 5-day mean velocity and potential density fields output on the earliest available day of each month between 1976-2008.

An important consideration when calculating the Eulerian overturning stream function at OSNAP East is how to account for the variability of net throughflow to the Arctic, which is not transformed into the lower limb of the AMOC. In Lozier et al. (2019), a prescribed net throughflow of +1.6 ± 0.2 Sv is applied across the OSNAP East section to ensure a zero net meridional mass transport across the combined OSNAP East and West sections. Here, as in Menary et al. (2020a), we choose not to compensate for the variations in the net throughflow across OSNAP East since this would prevent us from investigating the transport structure of the upper limb in Section 3.3.1.2. Critically, we find no seasonal signal in the net throughflow across the OSNAP East section (see Fig. A.1) and hence its inclusion in the Eulerian overturning stream function does not impact the findings of this Chapter.

To complement the Eulerian diapycnal overturning, we additionally diagnose the strength of the overturning at OSNAP East using the Lagrangian overturning stream function introduced in Chapter 2. The Lagrangian overturning stream function, $F(\sigma_{\theta}^{*}, t)$, quantifies the total light-to-dense transformation occurring along water parcel trajectories flowing northward across OSNAP East at time t. To compute the Lagrangian overturning each month, we first subset the 9.8 million water parcels which recirculate back to OSNAP East within the eastern SPG (south of the Greenland-Scotland Ridge) into 396 ensembles of water parcel trajectories, one for each month between 1976-2008 (Fig. 3.1b). Each monthly ensemble contains $N(t)$ water parcels, which flow northward across OSNAP East at time t and return southward across the section at the later time $t + \tau_{out}$, where

τ_{out} is the water parcel termination time. A Lagrangian diapycnal overturning stream function is calculated for each monthly ensemble as follows:

$$F(\sigma_\theta^*, t) = \sum_{\sigma_\theta=\sigma_{min}}^{\sigma_\theta^*} V_{North,\sigma_\theta}(t) - V_{South,\sigma_\theta}(t + \tau_{out}) \tag{3.1}$$

where V_{North} and V_{South} represent the absolute volume transport distributions of the ensemble of water parcels in density-coordinates on their initial northward and final southward crossings of OSNAP East section, respectively. In practice, we calculate these volume transport distributions by summing the absolute volume transports of the $N(t)$ water parcels initialised each month in discrete potential density bins ($\Delta\sigma_\theta = 0.01$ kg m^{-3}) as introduced in Section 2.3.2:

$$V(\sigma_\theta^*, t) = \sum_{n \in N(t)} V_{n,\sigma_\theta,t}\Pi(\sigma_\theta^*) \tag{3.2}$$

where $V_{n,\sigma_\theta,t}$ is the absolute volume transport conveyed by a water parcel identified with index n, which crosses the OSNAP East array with an associated potential density σ_θ. The boxcar function $\Pi(\sigma_\theta^*)$ is equal to 1 if $|\sigma_\theta^* - \sigma_\theta| \leq \Delta\sigma_\theta/2$, and is otherwise 0.

Since the volume transport conveyed by each water parcel is conserved along its entire trajectory, the total northward and southward transports across OSNAP East due to recirculating water parcels are equal in the Lagrangian overturning calculation, and thus there is no net flow across the section. In keeping with its Eulerian counterpart, the strength of Lagrangian overturning (LMOC) is given by the maximum of the Lagrangian overturning stream function, which occurs at the isopycnal of maximum Lagrangian overturning σ_{LMOC}. We note that the strength and variability of the Lagrangian overturning is not sensitive to our chosen parameterisation of vertical convective mixing along water parcel trajectories in the surface mixed layer (see Fig. A.2), and therefore its inclusion does not impact the conclusions of this Chapter.

3.3 Results

3.3.1 Seasonal overturning variability: An Eulerian perspective

3.3.1.1 Seasonal Eulerian overturning at OSNAP East

We begin by exploring the time-mean strength of the diapycnal overturning at OSNAP East in ORCA025-GJM189 from the traditional Eulerian perspective. Over the duration of the study period (1976-2008), the time-mean MOC at OSNAP East is 16.6 ± 2.7 Sv in ORCA025-GJM189, corresponding closely with observed estimates of the MOC at both 59.5°N (16.6 ± 1.1 Sv in 2002-2008; Sarafanov et al., 2012) and OSNAP East (16.3 ± 2.9 Sv in 2014-2020; Fu et al., 2023). The mean isopycnal of maximum Eulerian overturning (σ_{MOC} = 27.52 kg m^{-3}) is lighter in the simulation compared with observations (27.55 kg m^{-3}), owing to the shoaling of the NADW overturning cell in response to the excessive entrainment of ambient Atlantic water by the Nordic Seas overflows in the model (MacGilchrist et al., 2020).

Figure 3.2a shows that MOC at OSNAP East exhibits variability on monthly to interannual timescales. Concordant with the previous studies of Lozier et al. (2019) and Mercier et al. (2015), we find that MOC variability at OSNAP East is most pronounced on monthly timescales (monthly SD = ±2.7 Sv), where monthly MOC values range from 7.8 Sv in October 1978 to 28.7 Sv in January 1996. The simulated MOC variability is weaker on interannual timescales (SD of annual means = ± 1.0 Sv), in agreement with previous results from ocean models and reanalyses (Wang et al., 2021; Xu et al., 2014). The gradual increase in the MOC from the 1970s to the mid-1990s (+0.1 Sv yr^{-1}, $p < 0.01$) and the subsequent decline in the MOC between 1996 and 2000 (-1.3 Sv yr^{-1}, $p < 0.01$) are well-documented trends, consistently found in both observations (Kieke et al., 2007; Mercier et al., 2015) and numerical modelling studies (Böning et al., 2006; Desbruyères et al., 2013; Xu et al., 2013).

The intra-annual variability in the MOC at OSNAP East is dominated by the strong seasonal cycle shown in Figure 3.2b. The peak-to-peak amplitude of the seasonal cycle is 4.1 Sv, in close agreement with the 4.2 Sv found by Wang et al. (2021) using a 1/12° Global Ocean Physics Reanalysis (1993-2016)

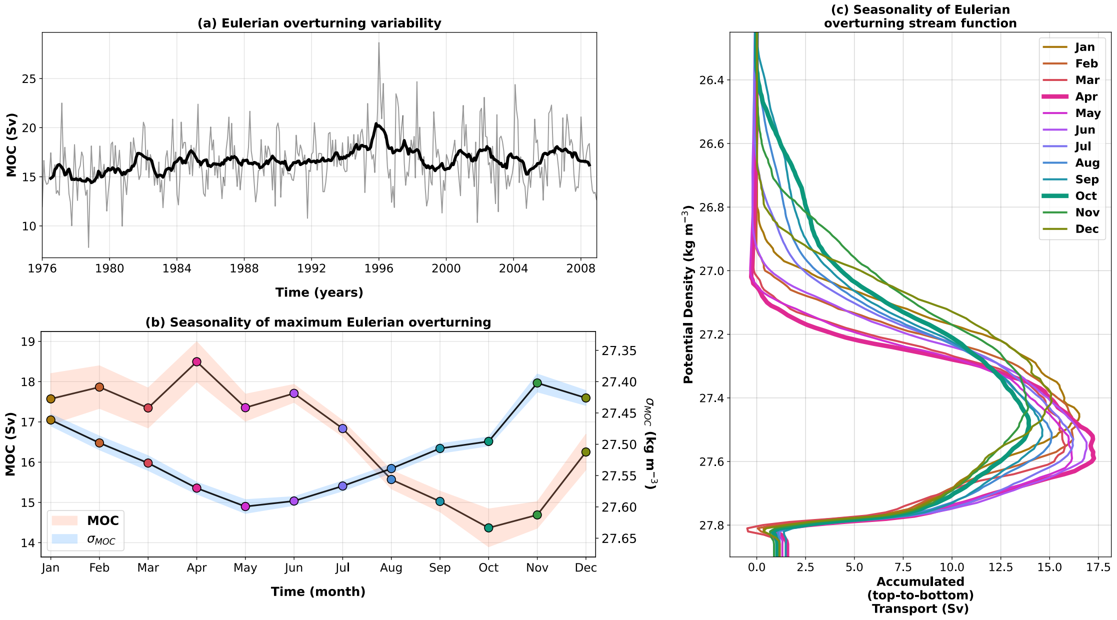

(a) Eulerian overturning variability

(b) Seasonality of maximum Eulerian overturning

(c) Seasonality of Eulerian overturning stream function

Figure 3.2: Eulerian overturning variability at the model-defined OSNAP East section. (a) Monthly maximum of the Eulerian overturning stream function in density-coordinates (first available day of each month, grey line) and 12-month running mean (black bold line) overlaid for 1976-2008. (b) Mean seasonal cycles of the maximum of the Eulerian overturning and the isopycnal of maximum overturning (σ_{MOC}) computed from monthly composites. Shading represents ±1 standard error of the monthly estimates (i.e., monthly standard deviation divided by $\sqrt{n}$ where n is the number of independent samples - equivalent to the number of years in this case). (c) Monthly composites of the Eulerian overturning stream function calculated in discrete density-coordinates (bin width is 0.01 kg m^{-3}); maximum (April) and minimum (October) months in the MOC seasonal cycle are included in bold.

and the 4.3 Sv seasonal cycle recorded along the OVIDE section (1993-2010) by Mercier et al. (2015). Figure 3.2b indicates that, on average, the MOC reaches a maximum in April (18.5 Sv) and a minimum in October (14.4 Sv). We note that, while there is strong consensus that the subpolar MOC reaches a maximum in spring (e.g., Holte & Straneo, 2017; Li et al., 2021a), the occurrence of the seasonal MOC minimum during autumn in this simulation disagrees with the findings of previous reanalysis (August; Wang et al., 2021) and observational (December; Mercier et al., 2015) studies. One possible reason for this inconsistency between studies is that the MOC seasonal cycle, when computed from monthly composites, is non-stationary, such that the timing of the seasonal extrema will be dependent upon the years chosen to compute those composites. This is particularly notable in the results of Wang et al. (2021), where the most probable timing of the minimum of the MOC seasonal cycle at OSNAP East transitions from autumn during the years overlapping our study period (1993-2008) to summer between 2009-2016.

Given that the strength of the MOC equates to the net transport above σ_{MOC}, seasonal variations in the MOC can be attributed to either changes in the meridional velocity field or to changes in the isopycnal structure at OSNAP East. To understand how the composition of the MOC upper limb evolves on seasonal timescales, Figure 3.2c presents monthly composites of the Eulerian overturning stream function evaluated at OSNAP East. We note that the maximum values of the monthly mean stream functions presented in Figure 3.2c underestimate the time-mean MOC determined from the maxima of monthly mean stream functions in Figure 3.2b. This is because the isopycnal of maximum overturning, σ_{MOC}, can vary substantially within each of the monthly composites (Lozier et al., 2019). Figure 3.2c shows that the seasonal maximum of the MOC in April occurs when upper limb waters flowing northwards across OSNAP East are relatively cold and dense (σ_{MOC} = 27.57 kg m^{-3} in Fig. 3.2b) having experienced intense surface buoyancy loss along the NAC during the previous winter (Grist et al., 2016). Conversely, the minimum of the MOC seasonal cycle in October is characterised by the arrival of warm and light upper limb waters (σ_{MOC} = 27.50 in Fig. 3.2b) at OSNAP East, which have been transformed by summertime buoyancy gain in the NAC during the months prior (Li et al., 2021a).

The seasonal cycle of Eulerian overturning at OSNAP East therefore corresponds to the expansion (a lighter upper limb coinciding with a weaker MOC in summer-autumn) and contraction (a denser upper limb coinciding with a stronger MOC in winter-spring) of the overturning stream function in density-coordinates (Fig. 3.2c), which is consistent with seasonal variations in surface buoyancy forcing over the NAC upstream.

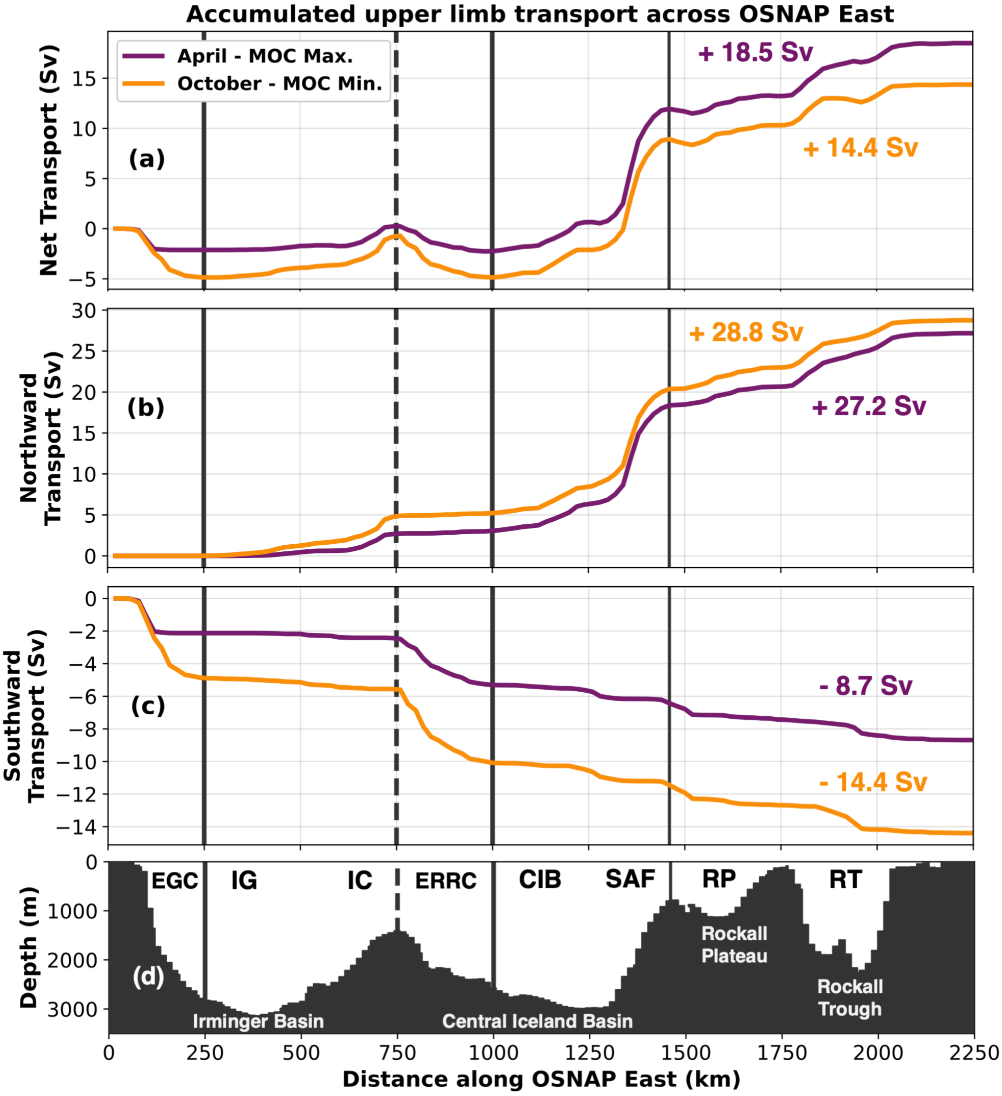

Figure 3.3: Mean Eulerian volume transport in the upper limb (i.e. above σ_{MOC}) of the MOC accumulated with distance eastward along the model-defined OSNAP East section. The net upper limb volume transport (a) is decomposed into its respective northward (b) and southward components (c). The model bathymetry along the OSNAP East array is presented in (d). The values shown in bold represent the total transports accumulated across the OSNAP East section for the maximum (April, purple) and minimum (October, orange) months of the MOC seasonal cycle. Vertical lines partition the volume transport across the section into five geographical regions corresponding to the major currents intercepted by the array: East Greenland Current (EGC), Irminger Gyre and Irminger Current (IG & IC), East Reykjanes Ridge Current (ERRC), the Central Iceland Basin and Sub-Arctic Front (CIB & SAF), and the Rockall Plateau and Rockall Trough (RP & RT).

3.3.1.2 Mechanisms of seasonal Eulerian overturning variability

To identify the mechanisms responsible for seasonal Eulerian overturning variability, we next decompose the net transport of the upper limb, determined directly from the simulated velocity and potential density fields along OSNAP East, into its constituent northward and southward components during April and October (corresponding to the extrema of the MOC seasonal cycle in Figure 3.2b). Figure 3.3 indicates that, in spite of the year-round net northward transport in the upper limb, the seasonal cycle of the MOC results from changes in the southward transport above σ_{MOC} at OSNAP East. This is highlighted in Figure 3.3c, which shows that the total southward transport in the upper limb increases significantly from -8.7 Sv in April, when the Eulerian overturning reaches its seasonal maximum, to -14.4 Sv when the MOC seasonal minimum occurs in October.

	EGC	**IG & IC**	**ERRC**	**CIB & SAF**	**RT & RP**	**Total**
Net Upper Limb Volume Transport (Sv)						
April	-2.1	2.4	-2.5	14.2	6.5	18.5
October	-4.9	4.2	-4.2	13.9	5.4	14.4

Table 3.1: Mean Eulerian net volume transport (Sv) in the upper limb of the AMOC (i.e., above σ_{MOC}) for the major currents along the OSNAP East array during April and October. The major currents are defined geographically as follows: East Greenland Current (EGC, 0 km < $x \leq 250$ km), Irminger Gyre and Irminger Current (IG & IC, 250 km < $x \leq 750$ km), East Reykjanes Ridge Current (ERRC, 750 km < $x \leq 1000$ km), Central Iceland Basin and Sub-Arctic Front (CIB & SAF, 1000 km < $x \leq 1450$ km), and Rockall Plateau and Rockall Trough (RP & RT, 1450 km < $x \leq 2300$ km). Note x corresponds to the distance from Cape Farewell on the east Greenland coast.

By further decomposing the seasonal upper limb transport according to the major currents crossing the OSNAP East array (Table 3.1), we find that the seasonal minimum of the MOC results from the combination of a 2.8 Sv strengthening of the EGC southward transport above σ_{MOC} and a 1.1 Sv weakening of the southern NAC branch feeding the Rockall Trough. This agrees with the recent results of Wang et al. (2021), who demonstrated that variations in the southward transport along the western boundary of the Irminger Sea play a prominent role in modulating the seasonal cycle of overturning at OSNAP East. Moreover, Wang et al. (2021) showed that the seasonality of the EGC upper limb transport is principally explained by seasonal density changes in the upper Irminger Sea projecting onto the mean barotropic transport of the western boundary current.

To explore this further, Figure 3.4 presents the mean potential density field along OSNAP East in April and October and the corresponding locations of σ_{MOC}. In April, we find that the erosion of stratification, owing to intense wintertime heat loss, permits deep convective mixing in the Irminger Sea interior (de Jong et al., 2012; de Jong & de Steur, 2016; Piron et al., 2016), such that σ_{MOC} (27.57 kg m^{-3} in April) outcrops at the surface (Fig. 3.4a). As a consequence, there is a reduction in the total upper limb northward transport entering the Irminger Sea across OSNAP East (Table 3.1; see IG & IC), since the majority of water flowing northward does so in the lower limb of the AMOC (de Jong et al., 2020). The equal magnitudes of the upper limb transports entering the Irminger Sea northward (IG & IC) and leaving the Iceland Basin southward via the East Reykjanes Ridge Current (ERRC) in Table 3.1 is explained by the anticyclonic recirculation of water south of the OSNAP East section. Along the western boundary, the isopycnal of maximum overturning slopes steeply with distance offshore during spring, decreasing the cross-sectional area over which southward flow can contribute to the upper limb of the AMOC at OSNAP East. Thus, since the weaker upper limb southward transport of the EGC (-2.1 Sv, Table 3.1) compensates for less of the stronger northward transport above σ_{MOC} in the NAC (20.7 Sv, Table 3.1), the MOC reaches a seasonal maximum in spring.

A contrasting density structure is found in autumn, when Figure 3.4b shows that surface heating through summer has restored the stratification in the upper Irminger Sea. This agrees closely with the recent observations of de Jong et al. (2020), who found the lowest monthly-mean density along OSNAP East during October. Since the depth of σ_{MOC} in Figure 3.4b exceeds 100 m throughout the entire Irminger Basin, there is a larger northward upper limb transport in the Irminger Gyre and the Irminger Current (4.2 Sv). However, this is more than compensated for by the vertical migration of the isopycnal of maximum overturning offshore of the East Greenland shelfbreak, which enables water flowing southward in the upper 200 m of the EGC to be included within the lighter upper limb (σ_{MOC} = 27.50 kg m^{-3} in October) as recently observed by Le Bras et al. (2020). This, in conjunction with the weaker transport of warm, saline water flowing northward in the NAC (-1.4 Sv), is therefore responsible for the MOC seasonal minimum in October.

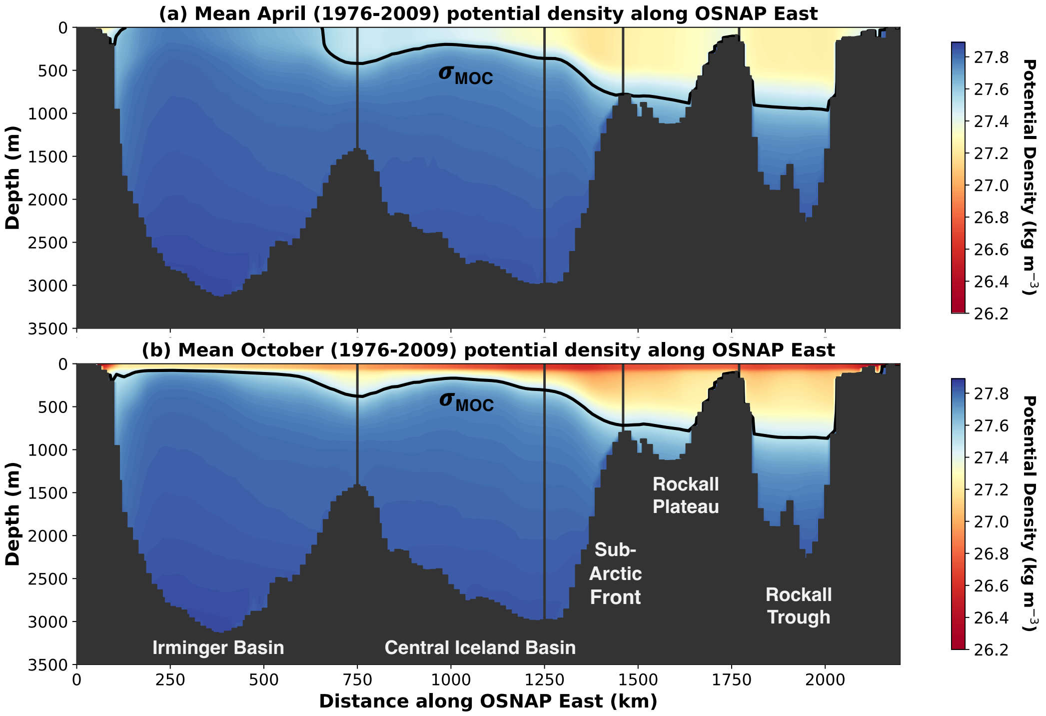

Figure 3.4: Mean potential density along the model-defined OSNAP East section in (a) April and (b) October overlaid by the corresponding mean isopycnal of maximum Eulerian overturning (April: σ_{MOC} = 27.57 kg m^{-3}, October: σ_{MOC} = 27.50 kg m^{-3}), denoting the seasonal interface between the upper and lower limbs of the AMOC.

In contrast with the conclusion of Wang et al. (2021), we do not find that the seasonal cycle of MOC can be accounted for by changes in the density structure of the western Irminger Basin alone. Rather, we propose that seasonal variations in the velocity field of the upper EGC act in conjunction with migrations of σ_{MOC} to drive the seasonality of Eulerian overturning at OSNAP East. To demonstrate this, we consider the Lagrangian trajectories of water parcels recirculating exclusively

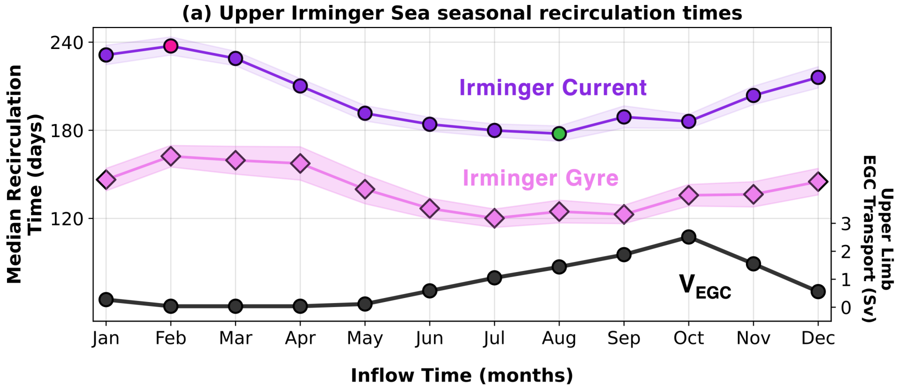

(a) Upper Irminger Sea seasonal recirculation times

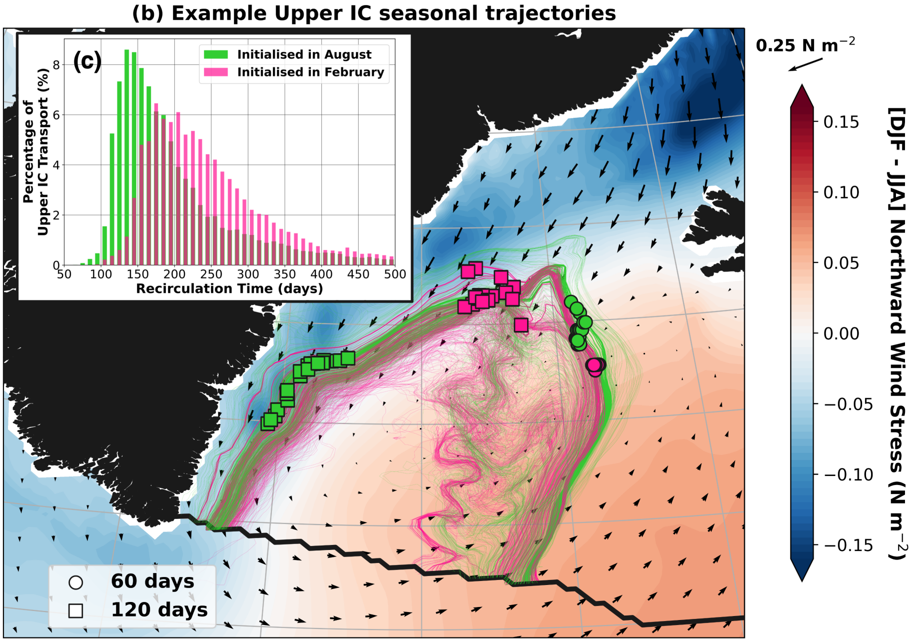

(b) Example Upper IC seasonal trajectories

Figure 3.5: (a) Seasonal cycle of median recirculation times north of the model-defined OSNAP East section for water parcels initialised in the upper 250 m of the Irminger Current (***IC***, purple) and Irminger Gyre (***IG***, pink) pathways. The total volume transport of upper Irminger Sea water parcels flowing southward in the EGC within the upper limb (i.e., above σ_{MOC}) is given by the solid black line (V_{EGC}). Note that, unlike the water parcel recirculation times (purple and pink), the EGC volume transports (black) are plotted according to the month during which they cross OSNAP East southward in the EGC. (b) Example water parcel trajectories flowing northward in the upper 250m of the Irminger Current during February (pink) and August (green) 2000. The associated median recirculation times are also coloured accordingly in a). Way point markers show the locations of water parcels remaining within the boundary current at 60- (circles) and 120-days (squares) following initialisation. Trajectories are superimposed on filled contours of the difference between the mean winter (DJF) and summer (JJA) northward component of the wind stress fields calculated between 1976-2015. The time-mean wind stress field (1976-2015) is shown by the overlying vectors included at the centre of every 4^{th} model grid cell. (c) Distributions of upper ***IC*** recirculation times determined from all of the water parcels flowing northward across OSNAP East during February (pink) and August (green) between 1976-2008 (i.e., 33 initialisations for each month).

within the upper 250 m of the Irminger Sea. Following Våge et al. (2011), and guided by the simulated time-mean current structure presented in Chapter 2 (see Fig. 1.2), we define a fixed boundary located 500 km from Cape Farewell to differentiate between the cyclonic circulation pathways of the Irminger Gyre (***IG***), recirculating within the basin interior, and the Irminger Current (***IC***), positioned on the western flank of the Reykjanes Ridge. Figure 3.5a shows a strong seasonal signal in the median amount of time water parcels spend north of OSNAP East; recirculation times are longest when water parcels flow northward across OSNAP East during winter and are shortest when they arrive at the section during summer. For the upper ***IC*** pathway, this amounts to water parcels typically spending 8 months recirculating in the Irminger Sea following initialisation in February compared with only 6 months when initialised in August (Fig. 3.5a).

Critically, it is the decrease in upper ***IG*** and ***IC*** recirculation times between February-May (Fig. 3.5a) which contributes to the seasonality of Eulerian overturning at OSNAP East. This is because the reduction in the recirculation times of water parcels crossing OSNAP East northwards in the upper ***IC*** during spring produces a convergence of water parcels flowing southward in the upper EGC during autumn. The strongest convergence occurs in October, consistent with the observed intensification of the upper EGC at OSNAP East during autumn (Le Bras et al., 2018; Pacini et al., 2020), and amounts to a -1.0 Sv anomaly in the full-depth transport of the EGC. Although the magnitude of this transport anomaly remains small compared with the typical magnitude of the EGC in this simulation (31.0 Sv), its surface-intensified nature has disproportionate consequences for the strength of the AMOC at OSNAP East. Figure 3.5a shows that the convergence of upper Irminger Sea water parcels within the EGC occurs almost exclusively within the upper limb of the AMOC. Thus, by acting in concert with the deepening of σ_{MOC} during late-summer and autumn (Fig. 3.4b), the convergence of upper ***IG*** and ***IC*** water parcels within the boundary current can explain 2.6 Sv of the 2.8 Sv increase in the upper limb EGC southward transport between April and

October, accounting for almost two-thirds of the amplitude of the MOC seasonal cycle at OSNAP East (4.2 Sv).

Previous studies have highlighted the close relationship between seasonal variations in the large-scale circulation of the Irminger Sea and wind-stress forcing acting over the basin (Daniault et al., 2011a; Daniault et al., 2011b; Le Bras et al., 2018). To determine whether local wind-stress forcing can account for the seasonality of water parcel recirculation times in the upper Irminger Sea, we next compare the character of upper ***IC*** trajectories flowing northward across OSNAP East in February and August, corresponding to the longest and shortest recirculation times, respectively. Figure 3.5b shows that the longer median recirculation times of upper ***IC*** water parcels flowing northward across OSNAP East in February is due to their slower advection along the boundary current through spring-summer. The weakening of the boundary current is explained by the springtime spin-down of the gyre circulation owing to the decrease in wind-stress curl acting over the Irminger Sea (Daniault et al., 2011b). In addition to their slower recirculation times along the boundary current, water parcels flowing northward in February are more likely to be entrained into slower circulation pathways in the basin interior, resulting in a longer tail in the distribution of recirculation times in Figure 3.5c. The shorter recirculation times exhibited by upper ***IC*** water parcels flowing northward in August results from the autumn-wintertime spin-up of the gyre during their recirculation north of OSNAP East. Figure 3.5b shows that water parcels flowing northward in August experience especially fast advection within the EGC, where the strongest north-easterly winds act along-stream. This is consistent with the study of Le Bras et al. (2018), who found that seasonal variations in the wind-stress curl, and by extension the EGC transport, are largely determined by changes in the local wind stress field acting along the East Greenland coast.

It is important to emphasise that the relationship we have determined between wind-stress forcing and seasonal Eulerian overturning variability at OSNAP East may not be applicable throughout the entire SPNA. For example, Wang et al. (2021) showed that dramatic seasonal variations in wind-stress curl over the Labrador Sea do not translate into overturning seasonality, given that northward and southward boundary current transports across OSNAP West vary synchronously and thus act to compensate one another on seasonal timescales. This suggests that the larger basin geometry of the eastern SPNA plays an integral role in enabling seasonal wind-stress forcing to project onto the seasonal overturning variability recorded at OSNAP East.

3.3.2 Seasonal overturning variability: A Lagrangian perspective

3.3.2.1 Seasonal Lagrangian overturning at OSNAP East

The Lagrangian overturning framework provides us with an alternative view of the overturning variability at OSNAP East on seasonal timescales. Whereas the Eulerian stream function integrates the meridional transports across OSNAP East in density-coordinates at a given snapshot in time, the Lagrangian overturning stream function measures the total light-to-dense transformation that the northward transport arriving at OSNAP East will go on to experience during its recirculation within the eastern SPG. As such, the meridional transports comprising the Lagrangian overturning stream function belong to a single collection of water parcels (sharing a common inflow time), whereas the Eulerian stream function includes two unrelated collections of water parcels flowing northwards and southwards, respectively. We should therefore consider the Lagrangian overturning to be a complementary measure to the Eulerian overturning at OSNAP East, which explicitly accounts for both the transformation and subsequent export of dense water masses within the eastern SPG by preserving knowledge of water parcel identity.

Figure 3.6a presents the strength of the Lagrangian overturning within the eastern SPG between 1976 and 2008, consistent with our earlier Eulerian analysis (Fig. 3.2a). The smaller magnitude of Lagrangian overturning in Figure 3.6a compared with the Eulerian overturning shown in Figure 3.2a is due to the exclusion of water parcels which are transformed north of the Greenland-Scotland Ridge from our analysis. We find that, on average, 8.9 ± 2.2 Sv of water flowing northwards across OSNAP East is transferred from the upper to the lower limb of the AMOC within the Iceland and Irminger basins. This transformation is slightly stronger than the time-mean Lagrangian overturning found in Chapter 2, because here we compute the average of the maximum Lagrangian overturning each month as opposed to taking the maximum of the time-mean Lagrangian overturning stream function as in Section 2.3.2.

In contrast with the seasonality of the Eulerian overturning at OSNAP East, the seasonal cycle of Lagrangian overturning in Figure 3.6b shows a steady increase from a minimum of 6.4 Sv in May to a maximum of 11.5 Sv in November. While the phase difference between the seasonal cycles of the MOC and the LMOC may initially appear counter-intuitive, recall that the strength of the Lagrangian overturning quantifies how much of the total northward transport flowing north across OSNAP East in any given month is transformed from the upper to the lower limb in the Iceland and Irminger basins. Interestingly, the seasonal cycle of the LMOC is closely correlated with the seasonality of both σ_{LMOC} (Fig. 3.6b: $r = -0.85$, $p < 0.01$) and σ_{MOC} (Fig. 3.2b: $r = -0.86$, $p < 0.01$), suggesting that the potential density of upper limb water parcels on flowing northward across OSNAP East is an important indicator of their future contribution to overturning seasonality north of the section. This is in marked contrast to the seasonal cycle of the Eulerian overturning, which implies that the coldest and densest upper limb waters flowing northward across OSNAP East in April lead to a maximum in the MOC.

To better understand the relationship between the composition of the upper limb and the strength of Lagrangian overturning, Figure 3.6c shows how the Lagrangian overturning stream function evolves over the duration of the mean seasonal cycle. Here, we find that the maximum of the LMOC, for water parcels flowing north in November, occurs when relatively light upper limb water parcels experience sufficient wintertime surface buoyancy loss to enter the lower limb before returning to OSNAP East. Meanwhile, denser upper limb water parcels arriving at OSNAP East in May, previously transformed by wintertime cooling,

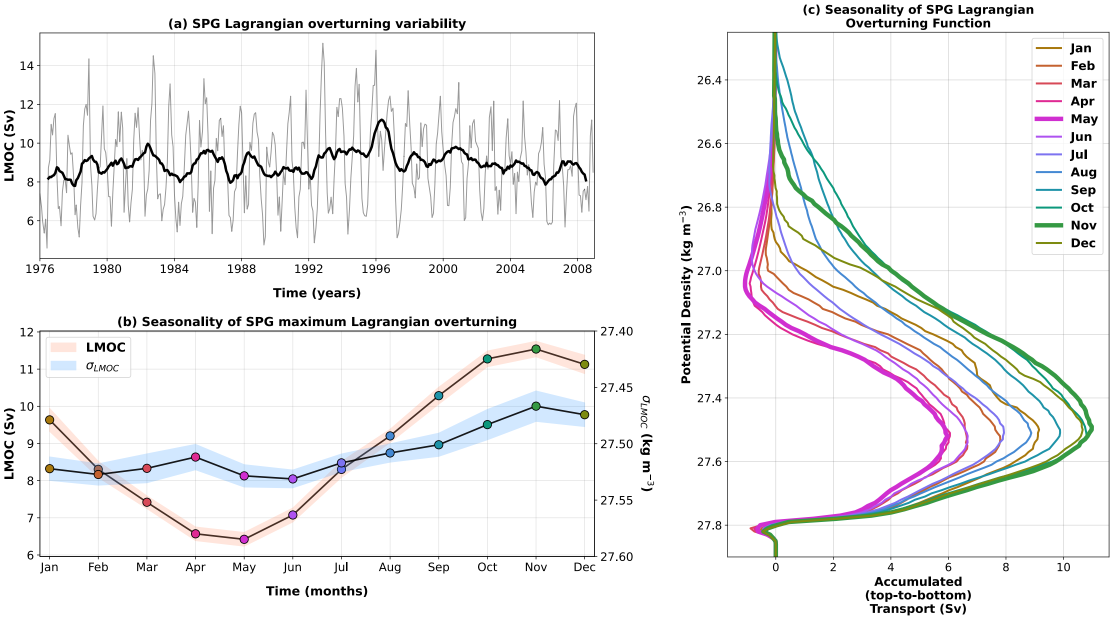

Figure 3.6: Lagrangian overturning variability of the eastern SPG at the model-defined OSNAP East section. (a) Monthly maximum Lagrangian overturning (LMOC; computed from the subset of particles initialised on the inflow across OSNAP East that recirculate south of the Greenland-Scotland Ridge, grey line) and 12-month running mean (bold black line) overlaid for 1976-2008. (b) Mean seasonal cycles of the LMOC and the isopycnal of maximum Lagrangian overturning (σ_{LMOC}) computed from monthly composites. Shading represents ±1 standard error of the monthly estimates (i.e., monthly standard deviation divided by $\sqrt{n}$ where n is the number of independent samples - equivalent to the number of years in this case). The strength of Lagrangian overturning, representing the total (volume) flux of water parcels from the upper to the lower limb, is plotted according to their common inflow time across the OSNAP East section. (c) Monthly composites of the Lagrangian overturning stream function calculated in discrete density-space (bin width is 0.01 kg m^{-3}); maximum (November) and minimum (May) months in the LMOC seasonal cycle are included in bold.

experience substantial summertime buoyancy gain north of OSNAP East to become lighter downstream. This negative diapycnal transformation is captured in the pronounced region of negative Lagrangian overturning between 26.8 - 27.2 kg m^{-3} in Figure 3.6c and results in the weakest seasonal volume flux into the lower limb.

The seasonal cycle of Lagrangian overturning at OSNAP East therefore reflects the seasonality of the surface-forced water mass transformation within the Iceland and Irminger basins. The strengthening of the LMOC for water parcels crossing OSNAP East in summer-autumn corresponds to an increasing volume flux across

σ_{LMOC}, owing to intense surface buoyancy loss along water parcel trajectories during the ensuing winter. Meanwhile, the weakening of the LMOC for water parcels crossing OSNAP East through winter-spring reflects a decreasing volume flux into the lower limb as water parcels in the upper limb gain buoyancy along their trajectories during the ensuing summer.

3.3.2.2 Timescales and origins of seasonal Lagrangian overturning

We have demonstrated that a close phase relationship exists between the seasonal cycle of Lagrangian overturning at OSNAP East and the seasonality of surface buoyancy forcing over the Iceland and Irminger basins. Since wintertime surface buoyancy loss greatly exceeds summertime buoyancy gain over the eastern SPG (Xu et al., 2018b), the time-mean LMOC is governed by the fraction of upper limb water parcels which fail to return to OSNAP East before the onset of winter and therefore experience sufficient surface buoyancy loss to be transferred into the lower limb during their recirculation. In contrast, the *seasonality* of Lagrangian overturning is determined by upper limb water parcels whose along-stream diapycnal transformation is dependent on their month of arrival across the OSNAP East section. To better distinguish between the origins and advective timescales of water parcels responsible for the time-mean strength and seasonality of Lagrangian overturning at OSNAP East, we next decompose the Lagrangian overturning stream function according to both the time water parcels spend north of OSNAP East (herein referred to as the water parcel recirculation time) and the distance from the East Greenland coast that water parcels flow northward across the section (Fig. 3.7).

Figure 3.7a presents the proportion of the mean strength of Lagrangian overturning and amplitude of the seasonal cycle (difference between November-May LMOC monthly composites) accumulated as a function of the time water parcels spend north of OSNAP East. We find that the entire LMOC seasonal cycle and 25% of the mean strength of Lagrangian overturning can be explained by water parcels which spend less than 8.5 months recirculating within the

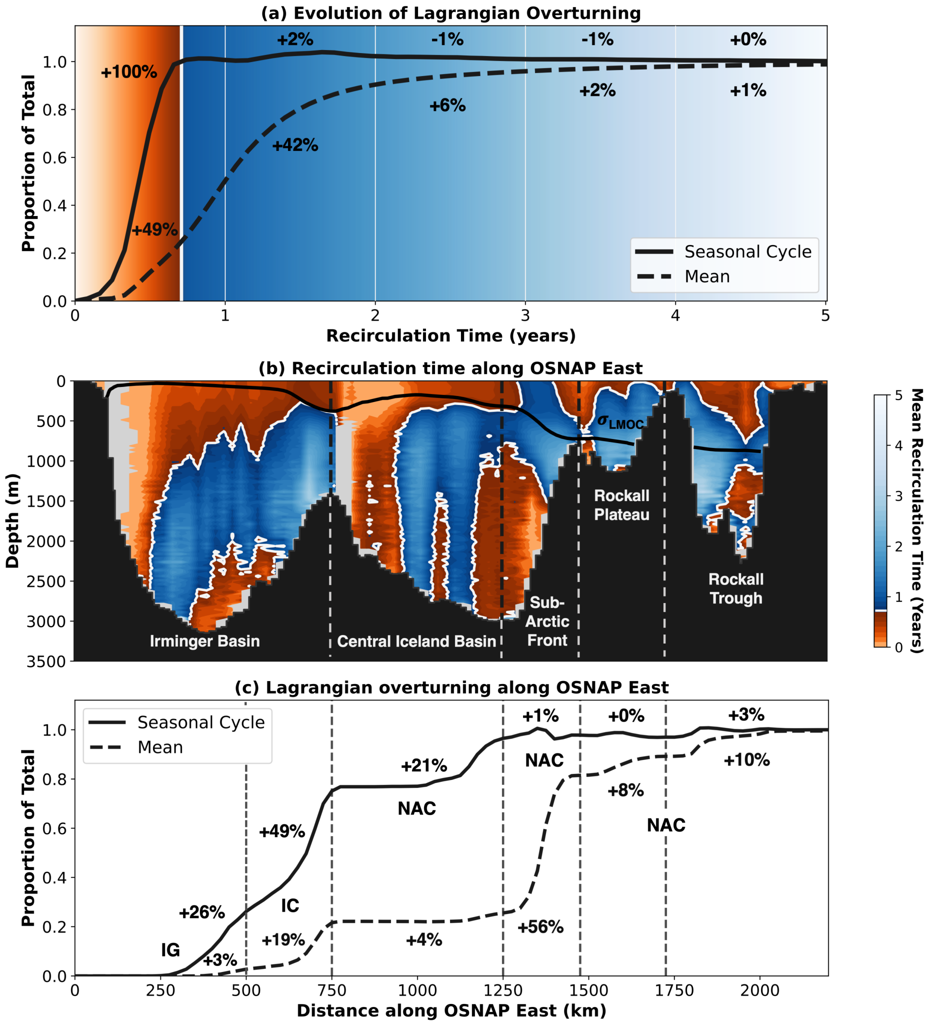

Figure 3.7: Decomposition of the mean strength and seasonality of Lagrangian overturning within the eastern SPG by recirculation time and distance along OSNAP East. (a) Normalised mean strength and seasonality (amplitude of the seasonal cycle calculated as November-May difference between LMOC monthly composites) of the Lagrangian overturning at σ_{LMOC} evaluated as a function of the time in which water parcels recirculate back to the OSNAP East section. (b) Mean recirculation time of water parcels initialised on the northward inflow across OSNAP East as a function of their initial position in $x - z$ space, where x is the distance along the OSNAP East section (km) and z is the depth (m). All 9.8 million eastern SPG water parcels initialised across 396 months (1976-2008) are binned according to their initial position, before computing the mean recirculation time for each bin (Δz = 25 m, Δx = 25 km). Grey regions coincide with the major southward currents intersected by the OSNAP East array, hence no northward flowing water parcels are initialised here. (c) Normalised mean strength and seasonality of the Lagrangian overturning at σ_{LMOC} accumulated as a function of the distance from the East Greenland coast that water parcels flow northward across OSNAP East.

eastern SPG. Interestingly, the absence of any further accumulation of seasonal Lagrangian overturning variability after 8.5 months following northward inflow across OSNAP East implies that, irrespective of its time of arrival, once a water parcel has experienced wintertime surface buoyancy loss it can no longer imprint onto the seasonal cycle of Lagrangian overturning. Thus, the remaining 75% of the mean volume flux into the lower limb is accounted for by water parcels which spend between 8.5 months and 7 years recirculating within the eastern SPG, and experience at least one winter north of OSNAP East.

To understand how the recirculation time of a water parcel is related to its inflow location along OSNAP East, we next calculate the average recirculation time of water parcels within the eastern SPG as a function of their northward crossing locations along the section. Figure 3.7b indicates that, on average, the recirculation times of the major upper ocean currents intercepted by OSNAP East are shortest in the upper ocean and generally increase with depth. This is consistent with observations in the eastern SPNA, which show that northward transport is surface intensified in the NAC branches (Holliday et al., 2018; Houpert et al., 2018, 2020) and the Irminger Current (de Jong et al., 2020; Fried & de Jong, 2022) since isopycnals in the upper ocean shoal strongly westward. We attribute the short recirculation times ($\leq$ 8.5 months) found in the lower limb in Figure 3.7b to rapidly recirculating water parcels sampling short-lived mesoscale eddies, which are only partially resolved in the model velocity field.

A prominent feature of Figure 3.7b is the transition from upper limb pathways which contribute to the seasonal cycle of the LMOC (orange, $\leq$ 8.5 months) in the Irminger and Central Iceland Basins to longer pathways (blue, > 8.5 months), sourced from the central and southern NAC branches, which dominate its mean strength. Figure 3.7c quantifies this distinction, highlighting that 74% of the time-mean LMOC is due to water parcels originating from the Sub-Arctic Front and the Rockall Trough and Plateau, whereas 96% of the seasonal cycle of Lagrangian overturning can be explained by water parcels sourced from the Irminger and Central Iceland Basins ($x \leq 1250$ km). We note that the recirculation times of water parcels flowing northward in the upper 250-m of the Central Iceland and Irminger basins also vary seasonally (see Fig. 3.5a), however this does not influence their contribution to the seasonal cycle of Lagrangian overturning.

To summarise, we have found a clear distinction between the origins and advective timescales of water parcels responsible for the mean strength and seasonality of Lagrangian overturning at OSNAP East. Seasonal overturning variability is associated with water crossing the section in the upper Irminger and Central Iceland Basins, where the rapid recirculation of water parcels in less than 8.5 months yields along-stream transformations which are dependent on their time of arrival at OSNAP East. Conversely, the time-mean LMOC is determined by water parcels, originating from the central and southern NAC branches, whose longer recirculation time (> 8.5 months) guarantees their diapycnal transformation into the lower limb through intense wintertime buoyancy loss.

3.3.3 Pathways of seasonal Lagrangian overturning

To further investigate the sources of seasonal Lagrangian overturning variability within the eastern SPG, we classify water parcels according to five cyclonic circulation pathways defined between OSNAP East and the Greenland-Scotland Ridge introduced in Chapter 2. The majority of water parcels recirculate exclusively within the Iceland-Rockall (***IcRo-IcRo***) and Irminger basins (***IG*** and ***IC***, see Fig. 3.8b for regional definitions). The remaining water parcels cross the section in the NAC and flow westward across the Reykjanes Ridge before returning to OSNAP East via the EGC, which flows southward along the western boundary of the Irminger Sea. These water parcels are subdivided into two pathways according to their inflow location along the section: the ***Ic-Irm*** pathway comprises water parcels sourced from the central NAC branch positioned along the Sub-Arctic Front, while the ***Ro-Irm*** pathway originates from the southern NAC branch feeding both the Rockall Trough and the Rockall Plateau (Fig. 3.8b).

Concordant with our earlier analysis, Figure 3.8 shows the clear distinction between the circulation pathways responsible for the seasonality of the LMOC

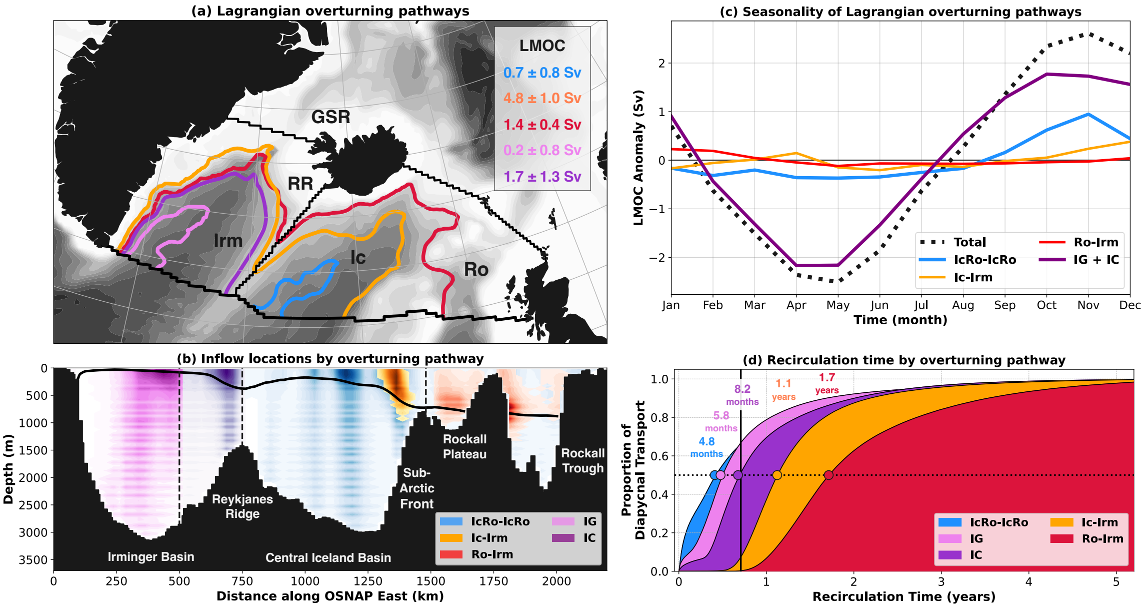

Figure 3.8: Decomposition of the seasonal cycle of Lagrangian overturning by circulation pathway north of the model-defined OSNAP East section. (a) Example water parcel trajectories illustrating each of the five circulation pathways within the eastern SPG and their respective contributions to the mean strength of Lagrangian overturning at σ_{LMOC}. (b) Inflow locations where water parcels are advected northward across OSNAP East classified by pathway. Water parcel volume transports for each pathway are averaged in discrete x - z space (Δz = 25 m, Δx = 25 km) using all 396 initialisation months before normalising by the maximum mean transport recorded across all bins (darker shading corresponds to the strongest northward transport for each pathway). (c) Seasonal cycle of the Lagrangian overturning at σ_{LMOC} decomposed by circulation pathway north of OSNAP East. For clarity, variations in the LMOC are presented as anomalies about the time-mean overturning determined from monthly composites of each pathway. (d) The proportion of the total diapycnal transport ($|\Delta\sigma| > 0.01$ kg m^{-3}, where $\Delta\sigma$ is the net change in potential density between northward and southward crossing of OSNAP East) to have successfully recirculated back to OSNAP East as a function of the time elapsed following northward flow across the section. Coloured circles correspond to the median recirculation time of each circulation pathway.

and those governing its mean state. We find that the two pathways crossing the Reykjanes Ridge north of OSNAP East account for 70% of the mean strength of the Lagrangian overturning within the eastern SPG (Fig. 3.8a) yet exhibit negligible variability on seasonal timescales (Fig. 3.8c). This is because the recirculation times of water parcels advected across the ridge north of OSNAP East consistently exceed the critical 8.5 month threshold required to be transferred into the lower limb. Water parcels advected along the ***Ic-Irm*** pathway typically experience 1.1

years (Fig. 3.8d) of along-stream surface buoyancy loss in order to transfer 4.8 ± 1.0 Sv of water into the lower limb. As shown in Chapter 2, the slower ***Ro-Irm*** pathway ($\bar{\tau}$ = 1.7 years) forms 1.4 ± 0.4 Sv of dense Icelandic Slope Water (Read, 2000; Van Aken & De Boer, 1995) by entraining Iceland Scotland Overflow Water (ISOW) in the vicinity of the Faroe Bank Channel (Fig. 3.8a).

Figure 3.8c shows that the seasonal cycle of Lagrangian overturning at OSNAP East is dominated by water parcels recirculating exclusively within the Irminger basin (***IG*** + ***IC***). We find that the northward inflows to the ***IG*** ($\leq$ 500 km from Cape Farewell) make a disproportionately large contribution to the seasonality of the LMOC (26%) compared with their limited contribution to its time-mean strength (3% in Fig. 3.7c). Water parcels advected along the path of the ***IC*** (between 500 km and 750 km from Cape Farewell in Fig. 3.7c) explain almost half (49%) of the seasonal cycle of Lagrangian overturning whilst also accounting for approximately a fifth (19%) of the mean volume flux into the lower limb. The larger contribution of the ***IC*** pathway to the mean Lagrangian overturning is explained by Figure 3.8d, which shows that water parcels typically spend 8.2 months recirculating within the ***IC*** compared with only 5.8 months within the ***IG***. Since the median recirculation time of the ***IC*** pathway is comparable to the 8.5-month threshold required to avoid intense wintertime surface buoyancy loss, it follows that approximately half of all water parcels advected along the boundary current of the Irminger Sea will be transferred into the lower limb north of OSNAP East.

Although diapycnal transformation along the ***IcRo-IcRo*** pathway accounts for only a quarter of the seasonal cycle of Lagrangian overturning at OSNAP East, Figure 3.8c highlights its critical role in establishing the timing of the seasonal maximum of the LMOC. Notably, it is the rapid recirculation of water parcels from the northern NAC branch to the ERRC within 4.8 months that dominates seasonal overturning variability along this pathway. Figure 3.8c shows that the largest volume flux into the lower limb occurs for water flowing north in November because then ***IcRo-IcRo*** water parcels experience the greatest surface buoyancy loss throughout the ensuing winter spent north of OSNAP East. This is consistent with the results of de Boisséson et al. (2010), who found the strongest net heat loss over the Iceland basin between November and February.

3.3.4 Transformation along seasonal overturning pathways

To understand how seasonal Lagrangian overturning variability results from diapycnal transformation along water parcel trajectories, we next calculate the net potential density change of water parcels between northward and southward crossings of OSNAP East, $\Delta\sigma_\theta$, as a function of their inflow location along the section. Figure 3.9a-b highlights the striking disparity between the net diapycnal transformation of water parcels flowing northward in the upper 250 m of the Irminger and Central Iceland basins during May (lightening) and November (densification). We find that large negative diapycnal transformations occur along water parcel trajectories sourced from the upper 100m of the ***IG*** and the Central Iceland Basin (***IcRo-IcRo***) in May, consistent with the pronounced region of negative Lagrangian overturning in Figure 3.6c. In contrast, water parcels flowing northward into the upper Irminger and Central Iceland basins in November undergo strong positive diapycnal transformation north of OSNAP East, and hence are responsible for the largest seasonal volume flux into the lower limb.

Since water parcels recirculating cyclonically along the boundary current of the Irminger Sea typically spend an additional 2.4 months north of OSNAP East compared with those circulating in the interior of the Irminger and Central Iceland basins (Fig. 3.8), we next explore how the character of seasonal water mass transformation differs along boundary and interior pathways within the eastern SPG. We focus our analysis on the water parcels circulating in the upper 250 m of the Irminger Sea (pink and purple boxes in Figs. 3.9a-b), since these collectively account for three quarters of the seasonal cycle of Lagrangian overturning at OSNAP East (Fig. 3.7c). To determine the relative importance of temperature and salinity changes along boundary and interior pathways, we further decompose the net diapycnal transformation ($\Delta\sigma_\theta$) north of OSNAP East into diathermal

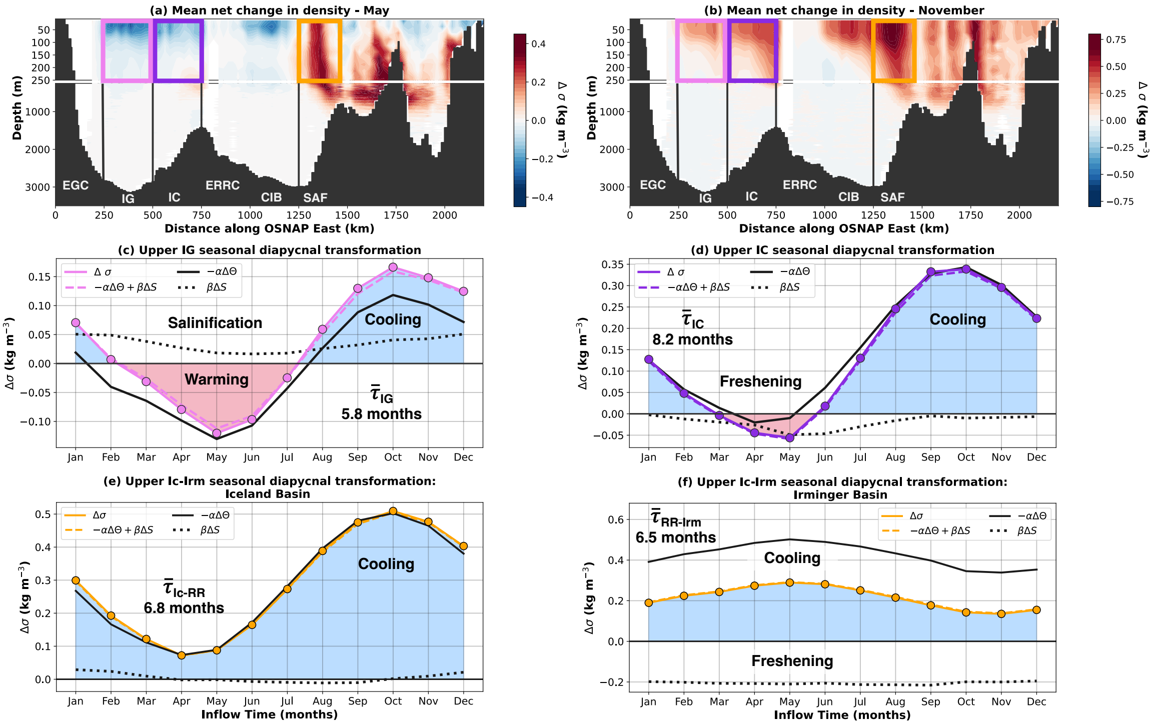

Figure 3.9: (a) Mean net change in potential density of water parcels flowing northward across OSNAP East in May as a function of their inflow location along OSNAP East. The net change in potential density, $\Delta\sigma_\theta$ (kg m^{-3}), between northward and southward crossings of OSNAP East is computed for each recirculating water parcel before averaging in discrete $x - z$ space (Δz = 25 m, x = 25 km). (b) Same as (a) for water parcels flowing northward in November. Vertical solid lines correspond to the geographical limits of the major currents intercepted along the section. Boxes included in the upper 250 m define the upper ***IG*** (pink), ***IC*** (purple) and ***Ic-Irm*** (orange) pathways. (c, d) Mean seasonal cycle of transport-weighted mean net change in potential density and contributions from diathermal ($\Delta\theta$, black solid line) and diahaline (ΔS, black dotted line) components for the upper (c) ***IG*** and (d) ***IC*** pathways. (e, f) Same as (c, d) for the ***Ic-Irm*** pathway once divided into two successive diapycnal transformations in the Iceland (e, Ic-RR) and Irminger basins (f, RR-Irm) using water parcel properties on crossing the Reykjanes Ridge (RR) north of OSNAP East.

and diahaline components. We approximate $\Delta\sigma_\theta$ using a linearised form of the equation of state following the integral approach of Tamsitt et al. (2018):

$$\Delta\sigma_\theta \approx -\alpha(\bar{\theta}, \bar{S})\Delta\theta + \beta(\bar{\theta}, \bar{S})\Delta S, \tag{3.3}$$

where θ denotes potential temperature, S denotes salinity, α represents the thermal expansion coefficient, and β represents the haline contraction coefficient. The values of $\bar{\theta}$ and $\bar{S}$ correspond to the average potential temperature and salinity of a water parcel on its northward and southward crossings of OSNAP East. To validate our approximation, Figures 3.9c-d show strong agreement between the seasonal cycles of net diapycnal transformation (pink/purple solid line) along the upper ***IG*/*IC*** pathways and its reconstruction, given by the sum of diathermal ($-\alpha\Delta\theta$) and diahaline ($\beta\Delta S$) components (pink/purple dashed line).

Consistent with the strong seasonality of surface heat fluxes over the Irminger Basin (de Jong & de Steur, 2016; Piron et al., 2016), we find that the seasonal cycle of diapycnal transformation along both boundary and interior pathways is dominated by diathermal transformation along water parcel trajectories initialised in the upper 250 m. Yet, despite a similar seasonality in their mean potential density on northward inflow, upper ***IG*** water parcels exhibit a broader potential density range (27.52 - 27.68 kg m^{-3}; Fig. 3.10b) on southward outflow compared with those recirculating along the upper ***IC*** pathway (27.48 - 27.59 kg m^{-3}; Fig. 3.10c). This is because the longer recirculation time of the upper ***IC*** pathway ($\bar{\tau}_{out}$ = 6.2 months) allows water parcels to experience a greater surface-forced diathermal transformation along the boundary current (Fig. 3.9d), thereby damping the seasonality of their water mass properties on inflow. The additional time upper ***IC*** water parcels spend north of OSNAP East is also reflected by the shorter 2-month window (April-May in Fig. 3.9d) during which water parcels flowing north subsequently experience negative diapycnal transformation, compared with the 5-month window (March-July in Fig. 3.9c) for the rapidly recirculating upper ***IG*** pathway ($\bar{\tau}_{out}$ = 3.8 months).

Figures 3.9c-d highlight the opposing roles of along-stream diahaline transformation along boundary and interior pathways in the upper Irminger Sea. We find that upper ***IG*** water parcels rapidly recirculating in the interior of the Irminger basin experience year-round salinification north of OSNAP East (Fig. 3.9c). Salinification is strongest when water parcels flow north across the section during winter, suggesting that lateral mixing between the warmer and saltier boundary current and cold, fresh interior waters, formed via open-ocean convection (Chafik et al., 2022; Lavender et al., 2000), is enhanced during the ensuing months. This proposition is supported by the recent observations of de Jong et al. (2020), who found that eddy kinetic energy is largest near the surface of the Irminger Current between January and April.

Diahaline transformation along the upper ***IC*** pathway is characterised by the freshening of water parcels flowing northward across OSNAP East between February-August. Interestingly, Figure 3.9d shows that it is this substantial freshening, rather than summertime heating, which is responsible for the negative diapycnal transformation along water parcel trajectories flowing north in late spring - early summer. The largest freshening along the boundary current is associated with water parcels which flow northward in the ***IC*** during May-June and return southward across OSNAP East via the EGC in November-December. This is consistent with observations, which show that the largest freshwater transport of the East Greenland Coastal Current (EGCC) occurs during autumn (Daniault et al., 2011b; Le Bras et al., 2018) following the summertime accumulation of meltwater on the shelf. Moreover, observations indicate that the strongest mixing between cold, fresh EGCC water and comparatively warmer and saltier EGC water occurs in winter (Le Bras et al., 2018), concurrent with the return of the freshest upper ***IC*** water parcels across OSNAP East.

We next compare and contrast the boundary and interior modes of seasonal watermass transformation with that of the dominant time-mean Lagrangian overturning pathway sourced from the central branch of the NAC. Figures 3.9a-b show that water parcels sourced from the upper 250 m of the ***Ic-Irm*** pathway (orange box) experience net densification irrespective of the time of year that they flow northward across OSNAP East. Given that the ***Ic-Irm*** pathway flows from the Sub-Arctic Front to the EGC via the Reykjanes Ridge, we choose to decompose the net diapycnal transformation north of OSNAP East into two successive transformations taking place in the Iceland and Irminger basins (Fig. 3.9e-f). We find that upper ***Ic-Irm*** water parcels experience sufficient net diapycnal transformation north of OSNAP East to be transferred into the lower limb, irrespective of their water mass properties on inflow (see Fig. 3.10d). For the lightest water parcels flowing northward in autumn, diapycnal transformation is dominated by intense wintertime heat loss (equivalent to ~0.5 kg m^{-3}) during their initial 6.8 months spent within the Iceland Basin (Fig. 3.9e). In contrast, the densest water parcels arriving at OSNAP East in spring experience wintertime diathermal transformation (equivalent to ~0.5 kg m^{-3}) during their final 6.5 months spent in the Irminger basin (Fig. 3.9f). Thus, we find that wintertime surface buoyancy loss acts as an important damping mechanism of seasonal thermohaline anomalies advected northward into the eastern SPG. Meanwhile, the transit times of upper ***Ic-Irm*** water parcels through the Iceland and Irminger basins account for the 7-month phase shift in the seasonal cycles of diapycnal transformation shown in Figures 3.9e-f.

The remarkably consistent density of the upper ***Ic-Irm*** pathway on returning southward across OSNAP East in the EGC (27.55 ± 0.01 kg m^{-3}; Fig. 3.10d) additionally underscores the importance of interior mixing along water parcel trajectories. This is because mixing is associated with the convergence of water masses in T-S space, whereas transformation by surface buoyancy fluxes leads to diverging water mass properties (Groeskamp et al., 2014; Mackay et al., 2020). The strong density compensation between year-round cooling and freshening along the upper ***Ic-Irm*** pathway in the Irminger Sea (Figure 3.9f) is indicative of a constant background mixing with colder and fresher waters sourced from north of the Greenland-Scotland Ridge. A closer examination shows that this mixing along water parcel trajectories is concentrated between the Denmark Strait and the Kangerdlugssuaq Trough in the northern Irminger basin. On the one hand, this localised freshening of the boundary current is consistent with observations, which have found substantial freshwater transports directed offshore from the East Greenland Shelf (Foukal et al., 2020; Sutherland & Pickart, 2008; Sutherland et al., 2009). However, such cooling and freshening are also consistent with the excessive turbulent mixing between the dense overflows and overlying ambient Atlantic waters in this model, as documented in Chapter 2. It therefore remains an outstanding question to what extent the stable composition of the lower limb found in this simulation (see Fig. 3.6b where σ_{LMOC} = 27.51±0.02 kg m^{-3}) represents an artifact of well-established model biases (Danabasoglu et al., 2010; Wang et al., 2015) or rather underscores the importance of mixing between Atlantic, Arctic and overflow water masses along the northwestern boundary of the Irminger Sea, as highlighted in Evans et al. (2023).

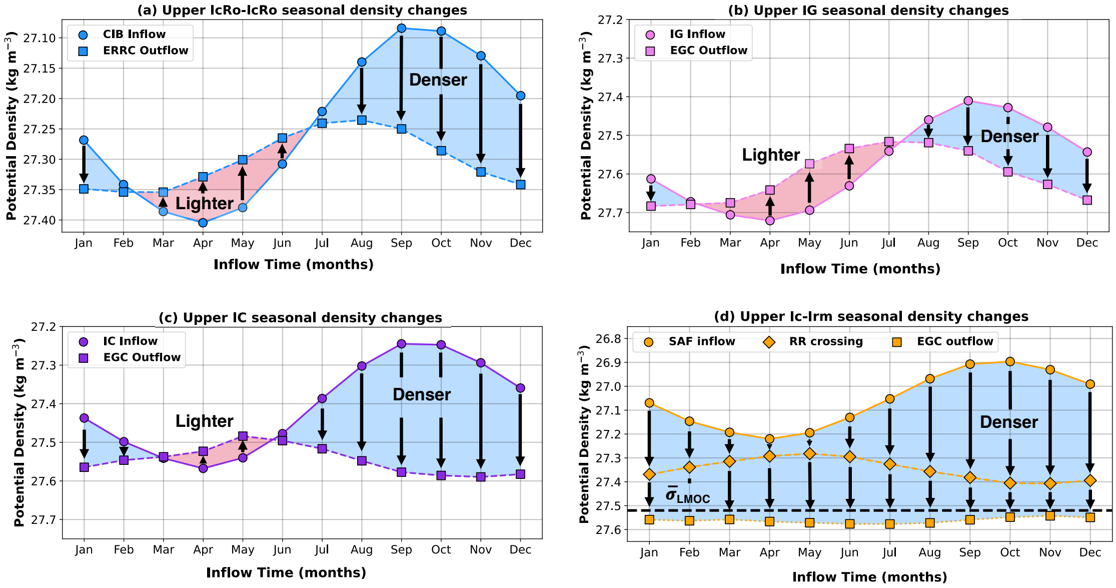

Figure 3.10: Mean seasonal cycles of the transport-weighted mean potential density on northward inflow and southward outflow crossings of the OSNAP East section for the upper 250 m of the (a) ***IcRo-IcRo***, (b) ***IG***, (c) ***IC*** pathways. (d) Same as (a-c) for Sub-Arctic Front inflow (circular markers), Reykjanes Ridge crossing (rhombus markers) and East Greenland Current outflow (square markers) for the upper 250 m of the ***Ic-Irm*** pathway. Note that transport-weighted mean potential densities on southward outflow (a-d) and crossing the Reykjanes Ridge (d) are plotted at the month when water parcels originally flowed northward across the OSNAP East section.

3.4 Discussion & Conclusions

In this Chapter, we investigate the nature of seasonal overturning variability within the eastern North Atlantic SPG using Lagrangian water parcel trajectories evaluated within an eddy-permitting ocean sea-ice hindcast simulation. To complement the traditional Eulerian overturning stream function, we employ the Lagrangian overturning stream function in density-coordinates to diagnose the total light-to-dense transformation along water parcel trajectories evaluated from the northward inflows across a model-defined OSNAP East section. Our analysis demonstrates that the advective timescales over which water masses circulate within the eastern SPG play a crucial role in shaping the simulated Eulerian and Lagrangian seasonal overturning variability at OSNAP East.

From an Eulerian perspective, we show that the net transport in the upper limb of the MOC exhibits a pronounced seasonal cycle of 4.1 Sv at OSNAP East, consistent with estimates made using both observations and ocean reanalyses (Mercier et al., 2015; Wang et al., 2021). Moreover, seasonality in the strength of Eulerian overturning is closely related to the density structure along the Irminger Sea western boundary. The weakest Eulerian overturning occurs in October when the outflowing EGC is lightest, yielding a large southward transport (-4.9 Sv) in the upper limb of the AMOC. We find the largest Eulerian overturning in April when the density structure of the EGC, closely reflecting that of the basin interior, results in the weakest southward transport (-2.1 Sv) within the density classes of the upper limb and the strongest southward transport in the lower limb. This agrees closely with the results of Holte and Straneo (2017), who used Argo profiling floats to show that the MOC seasonal cycle in the Labrador Sea peaks in spring in conjunction with the outflow of newly formed LSW in the Labrador Current.

In contrast with previous studies which attribute the seasonality of Eulerian overturning to the seasonal export of western boundary density anomalies alone (Brandt et al., 2007; Holte & Straneo, 2017; Wang et al., 2021), we also highlight the important role of seasonal wind stress forcing over the Irminger basin. In addition to the deepening of σ_{MOC} along the western boundary of the Irminger Sea, the enhanced upper limb EGC transport responsible for the MOC minimum in October is owed to a convergence of water parcels which flowed northward across OSNAP East in the upper 250 m of the Irminger basin during spring. This convergence is the result of decreasing water parcel recirculation times in the upper Irminger Sea, which is consistent with a spin-up of the eastern SPG in response to increasing wind stress curl acting over the basin during the ensuing autumn-winter (Daniault et al., 2011b; Le Bras et al., 2018; Pacini et al., 2020). We therefore propose that the seasonal cycle of Eulerian overturning at OSNAP East arises from a complex combination of seasonal dense water formation along the western boundary of the Irminger Sea and the wind-driven modulation of the upper limb EGC transport, which agrees closely with the recent study of Mercier et al. (2024).

From a Lagrangian perspective, we show that the formation of upper NADW along the cyclonic pathways of the eastern SPG is strongly dependent upon the time of year water parcels flow northward across OSNAP East. The lightest water parcels, arriving at the section in autumn, experience the greatest positive diapycnal transformation due to intense wintertime heat loss along-stream and constitute the strongest seasonal volume flux into the lower limb. Meanwhile, the weakest volume flux into the lower limb is associated with the densest water parcels arriving at OSNAP East in spring and results from summertime heating along-stream.

Given the asymmetry between stronger wintertime surface buoyancy loss and weaker summertime buoyancy gain over the Iceland and Irminger Basins (Brambilla et al., 2008; de Boisséson et al., 2010; Xu et al., 2018a), it is interesting to frame seasonal Lagrangian overturning variability somewhat analogously to "Stommel's Demon" (Stommel, 1979; Williams et al., 1995). That is to say, water parcels advected northward across OSNAP East in the upper limb of the AMOC are participating in a recirculation race against time to avoid wintertime diapycnal transformation into the lower limb. The majority of upper limb water parcels, sourced from the central and southern NAC branches, are unsuccessful and hence determine the mean strength of Lagrangian overturning within the eastern SPG. In contrast, the seasonal cyle of Lagrangian overturning originates from rapidly recirculating ($\leq$ 8.5 months) water parcels in the upper Irminger and Central Iceland basins, whose along-stream diapycnal transformation is dependent on their time of arrival at OSNAP East. As such, the proximity of the OSNAP East array to regions of dense water formation constrains the amplitude of seasonal Lagrangian overturning variability recorded at the section. For example, if we calculated the LMOC seasonal cycle across a trans-basin section located further south, we would likely find a weaker amplitude of seasonality since a larger fraction of upper limb water parcels would experience wintertime diapycnal transformation into the lower limb owing to their longer recirculation.

The recent study of MacGilchrist et al. (2021) extended the concept of a seasonal "Demon" by demonstrating that the subduction of water parcels into the interior of the SPNA is additionally modulated by interannual variations in atmospheric forcing, such as the NAO (Hurrell, 1995). Although it is beyond the scope of this Chapter, it would be interesting to establish whether Lagrangian overturning exhibits a similar sensitivity to interannual variations in surface buoyancy forcing over the Iceland and Irminger basins. It may alternatively be the case that enhanced surface heat loss, such as that associated with strong positive phases of the NAO (Bersch et al., 2007; Visbeck et al., 2003), would be of secondary importance to changes in the distribution and transport of upper limb waters flowing northward across OSNAP East owing to the concordant intensification and contraction of the SPG circulation (Curry & McCartney, 2001; Flatau et al., 2003; Pollard et al., 2004). Thus, we might anticipate an increase in the amplitude of seasonal Lagrangian overturning variability following positive phases of the NAO since the westward retreat of the Subarctic Front (Bersch et al., 1999; Pollard et al., 2004) favours greater inflow to the Irminger and Central Iceland basins, which dominate the seasonality of Lagrangian overturning at OSNAP East.

Through a detailed investigation of the overturning pathways recirculating north of OSNAP East, we identify two dominant modes of seasonal Lagrangian overturning variability operating in the upper 250 m of the eastern SPG. Approximately half of the seasonal cycle of Lagrangian overturning at OSNAP East is sourced from water parcels rapidly recirculating in the interior of the Central Iceland and Irminger basins ($\bar{\tau}_{out} \approx 4$ months), while the remainder originates from the longer boundary current encircling the Irminger Sea ($\bar{\tau}_{out}$ ≈ 6 months). Although seasonal diapycnal transformation along both boundary and interior pathways is dominated by the surface-forced diathermal component, diahaline transformations highlight the important and contrasting roles of lateral mixing between water masses along-stream. In the upper Irminger Gyre, the year-round salinification of water parcels owing to boundary-interior exchange acts to reinforce their wintertime densification. Meanwhile, water parcels advected northward across OSNAP East in the Irminger Current during spring experience substantial freshening downstream, consistent with the greater mixing observed between boundary current and Arctic-origin waters along the shelfbreak during winter (Le Bras et al., 2018). Our proposition that the contrasting diahaline changes along the boundary current (freshening) and within the basin interior (salinification) result from mixing is supported by Xu et al. (2018b), who found that, on average, the mixing-induced diapycnal transformation is negative (lightening) on the inshore side of the boundary current and positive (densification) between the boundary current and the interior. While we have only sought to infer the contributions of air-sea interaction and mixing to the net densification along water parcel trajectories in this Chapter, it would prove valuable for a future study to formally diagnose their respective contributions to the diathermal and diahaline transformations governing the densification of water masses within the eastern SPG.

The Lagrangian analysis presented in this Chapter also demonstrates how the longest circulation pathways within the eastern SPG maintain the consistent water mass properties of the AMOC lower limb flowing southward across OSNAP East. By decomposing the seasonal cycle of diapycnal transformation along the dominant ***Ic-Irm*** overturning pathway, we show that, provided water parcels spend at least one winter north of OSNAP East, they will experience sufficient surface-forced diathermal transformation to form upper NADW, irrespective of their properties on inflow. We therefore suggest that wintertime surface buoyancy loss over the Iceland and Irminger basins constitutes an important damping mechanism for seasonal thermohaline variability imported northward across OSNAP East. Meanwhile, the stable year-round composition of lower limb waters flowing southward in the EGC results from a constant background mixing with both overflow and Arctic-origin waters along the northwestern boundary of the Irminger Sea.

It is important to recognise that the conclusions of this Chapter are drawn from a single ocean sea-ice hindcast simulation and thus several limitations should be acknowledged. Firstly, the water parcel recirculation timescales identified within the eastern SPG will be sensitive to our choice of model horizontal resolution, since this governs the representation of submesoscale and mesoscale dynamics. In particular, the study of Blanke et al. (2012) shows that the inclusion of finer-scale structures in the velocity fields simulated by eddy-rich models reduces water parcel transit times despite also increasing the complexity of trajectories (Gary et al., 2011). This is further compounded by the stronger SPG circulation simulated in eddy-rich models compared with those configured at eddy-permitting resolution (Hirschi et al., 2020; Jackson & Wood, 2020), which favours shorter recirculation times and hence a larger seasonal Lagrangian overturning signal at OSNAP East.

Secondly, the mixing-induced diapycnal transformations along water parcel trajectories will be dependent upon both model resolution and the chosen parameterisations of lateral eddy mixing and turbulent entrainment in the bottom boundary layer. Although not included in this ORCA025 configuration, previous studies have shown that implementing a modified form of the mesoscale eddy mixing scheme of Gent and Mcwilliams (1990) at eddy-permitting resolution can significantly improve model hydrography in the SPNA by reducing spurious diapycnal mixing between boundary and interior water masses (Deacu & Myers, 2005a, 2005b). Given their ability to explicitly resolve the effects of mesoscale eddies, we would also expect eddy-rich models (e.g., Biastoch et al., 2021; Böning et al., 2016; Hirschi et al., 2020; Marzocchi et al., 2015) to simulate more realistic mixing along water parcel trajectories. However, this is partly undermined by the well-documented warming and salinification trends in the Labrador and Irminger Seas at eddy-rich resolution (Jackson et al., 2023b; Marzocchi et al., 2015; Treguier et al., 2005), which yield significantly larger than observed diapycnal transformation and hence overturning within the SPNA (Hirschi et al., 2020).

Establishing whether the mechanisms governing overturning seasonality are consistent across numerical models should therefore be considered an ongoing priority, especially given that the accurate assessment of long-term trends in the strength of the subpolar MOC is predicated on adequately resolving the variability simulated on seasonal-interannual timescales.

In this Chapter, we have investigated the nature of seasonal overturning variability in the eastern SPG using water parcel trajectories calculated within an eddy-permitting ocean sea-ice hindcast. We showed that the seasonal cycle of Eulerian overturning at OSNAP East reflects a complex combination of seasonal dense water formation along the western boundary of the Irminger Sea and the wind-driven modulation of water parcel recirculation times. We also explored seasonal overturning variability from a Lagrangian perspective, highlighting that the seasonality of dense water formation along the cyclonic pathways of the eastern SPG is explained by a small collection of water parcels, circulating rapidly ($\leq$ 8.5 months) in the upper Irminger and Central Iceland Basins. In the next Chapter, we will explore the factors controlling dense water formation variability along the pathways of the SPG on longer, decadal timescales.

4

Controls on dense water formation along the path of the North Atlantic subpolar gyre

In Chapters 2 & 3, we saw how the Lagrangian overturning framework can be used to identify the circulation pathways responsible for the time-mean strength and seasonality of the AMOC in the eastern SPNA. In this Chapter, we extend our Lagrangian analysis to explore the controls on dense water formation along the path of the SPG, from arrival across OSNAP East in the NAC to returning southward across OSNAP West in the Labrador Sea.

4.1 Introduction

Observations and ocean reanalyses indicate that the upper subpolar North Atlantic Ocean exhibits pronounced thermohaline variability on decadal timescales (Bersch, 2002; Bersch et al., 2007; Curry et al., 1998; Fu et al., 2020; Holliday et al., 2018; Holliday et al., 2020; Lozier et al., 2008), with significant implications for both regional and global climate. On a regional scale, the northward propagation of upper ocean thermohaline anomalies from the subpolar North Atlantic into the Nordic Seas yields predictable climate impacts on surface air temperatures over northwest Europe (Årthun et al., 2017; Collins & Sinha, 2003; Keenlyside et al., 2008; Li et al., 2013), Arctic sea ice extent (Yeager et al., 2015; Zhang & Zhang, 2015) and the rates of Greenland ice melt (Straneo & Heimbach, 2013). Low-frequency variability in subpolar ocean dynamics is believed to be the source of skillful decadal climate prediction through the modulation of North Atlantic sea surface temperatures (SST) (Årthun & Eldevik, 2016; Chepurin & Carton, 2012; Delworth & Mann, 2000; Furevik, 2001; Knight et al., 2006; Sutton & Allen, 1997; Sutton & Hodson, 2005). The impacts of North Atlantic multi-decadal SST variability also extend far beyond the regional scale (Zhang et al., 2019), including through hemispheric teleconnections which contribute to multidecadal changes in the West African and Indian monsoons (Feng & Hu, 2008; Goswami et al., 2006; Luo et al., 2011; Martin & Thorncroft, 2014; Martin et al., 2014) and Pacific decadal climate variability (d'Orgeville & Peltier, 2007; Zhang et al., 2007). Given the significant socioeconomic implications of the climate impacts outlined above, better understanding the physical mechanisms underpinning both the generation and persistence of thermohaline anomalies in the SPNA is essential to improving the skill of decadal climate predictions.

Since Bjerknes (1964) first hypothesised that low-frequency overturning variability drives decadal fluctuations in the surface climate of the North Atlantic sector, numerical modelling studies have repeatedly identified decadal changes in dense water formation as the principal source of subpolar upper ocean thermohaline variability (Desbruyères et al., 2015; Grist et al., 2010; Robson et al., 2016; Yeager & Robson, 2017). Low-frequency fluctuations in the AMOC are excited by shifts in the state of the NAO, which is the dominant mode of atmospheric variability governing wind and surface buoyancy forcing over the North Atlantic sector (Hurrell, 1995; Marshall et al., 2001). During positive phases of the NAO, anomalously strong westerly winds yield an intensification of surface heat loss over the Labrador and Irminger Seas, which favours enhanced NADW formation (Kim et al., 2020; Yeager & Danabasoglu, 2014). The resulting densification of the AMOC lower limb induces a geostrophic intensification of both the subpolar overturning and gyre circulations (Kim et al., 2024; Yeager et al., 2021), thereby increasing the northward transport of warm and saline subtropical waters into the eastern SPG (Desbruyères et al., 2013; Jacobs et al., 2019). This manifests as a delayed warming and salinification of the eastern SPNA (Chafik et al., 2023; Desbruyères et al., 2021; Khatri et al., 2022) which continues to propagate downstream into the Nordic Seas (Fan et al., 2023; Passos et al., 2024).

Although our mechanistic understanding of the generation of thermohaline anomalies has progressed significantly in recent decades (Robson et al., 2012; Zhang, 2017), few studies have investigated the extent to which the arrival of such anomalies impacts the downstream formation of dense water masses and hence feeds back on the strength of the subpolar ocean circulation (Passos et al., 2024). On the one hand, we might anticipate that upper limb thermohaline (buoyancy) anomalies will feed back on the AMOC strength by impacting the efficiency of diapycnal water mass transformation and, therefore, the production of NADW downstream. Indeed, this view forms the basis of the salt-advection feedback, in which a weakened AMOC transports less salt into the SPNA, thereby reducing NADW formation by increasing stratification, which further weakens the AMOC (de Vries & Weber, 2005; Rahmstorf, 1996; Stommel, 1961). However, this is at odds with the recent observational analysis of Fu et al. (2020), which showed that subpolar overturning has remained stable in spite of the large-scale thermohaline variability observed during the past three decades. This implies that only a weak coupling exists between upper limb thermohaline anomalies and the magnitude of dense water formation downstream on multi-decadal timescales (Fu et al., 2020). Thus, determining precisely what controls the amount of dense water formed along the path of the SPG and its relationship to subpolar overturning variability on multi-decadal timescales represents an important open question.

When exploring the downstream evolution of upper ocean thermohaline anomalies in the SPNA, studies adopting the traditional Eulerian frame of reference typically use lagged correlation analysis (Årthun & Eldevik, 2016; Årthun et al., 2017; Fan et al., 2023; Holliday et al., 2008), which relies upon the coherent propagation of signals downstream. In reality, however, thermohaline anomalies are communicated over a diverse range of advective timescales owing to the dispersive nature of subpolar circulation pathways (e.g., Yashayaev & Seidov, 2015), which often convolve water masses from many different sources. In this Chapter, we overcome this challenge by adopting a Lagrangian frame of reference to investigate the controls on dense water formation along the path of the SPG. By evaluating Lagrangian water parcel trajectories in an eddy-rich ocean sea-ice hindcast, we are able to trace the evolution of upper limb thermohaline anomalies arriving into the eastern SPNA and directly assess their influence on the formation of NADW downstream.

This Chapter is organised as follows. In Section 4.2, we introduce the eddy-rich ocean sea-ice hindcast, Lagrangian particle tracking experiments and both the Eulerian and Lagrangian diagnostics used in our analysis. Section 4.3.1 explores the nature of dense water formation along the path of the SPG, including validation against OSNAP observations. We investigate the sources of variability in along-stream dense water formation in Section 4.3.2. In Section 4.3.3, we introduce a linear model to skilfully predict along-stream dense water formation. Section 4.3.4 explores the two dense water pathways circulating cyclonically around the SPG. Section 4.3.5 offers a theoretical perspective on the relationship between upper limb thermohaline (buoyancy) anomalies and SPG dense water formation. Finally, in Section 4.3.6, we assess the role of remote buoyancy forcing in driving decadal variations in dense water formation along the path of the SPG. The study concludes with a summary of our main findings and a critical discussion of their wider significance in Section 4.4, including the implications for observing subpolar AMOC variability.

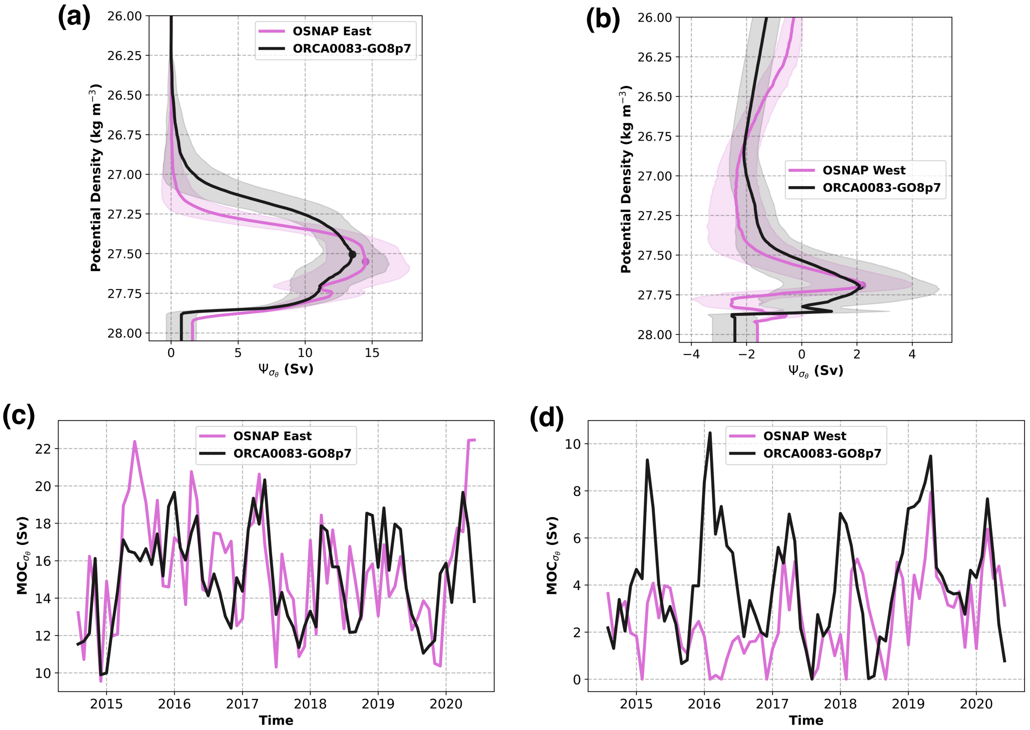

Figure 4.1: Time-mean (2014-2020) Eulerian diapycnal overturning stream functions at (a) OSNAP East and (b) OSNAP West calculated using the ORCA0083-GO8p7 hindcast (black) and OSNAP observations (purple). The shaded regions represent ±1 (monthly) standard deviation in the Eulerian overturning stream function. Time series of maximum Eulerian diapycnal overturning at (c) OSNAP East and (d) OSNAP West calculated using the ORCA0083-GO8p hindcast (black) and OSNAP observations (purple).

4.2 Methods

4.2.1 Ocean General Circulation Model

To investigate the variability of dense water formation along the path of the subpolar gyre, we use output from a higher resolution ocean sea-ice hindcast than that employed in earlier Chapters, the eddy-rich, global ORCA0083-GO8p7 integration (see Table 1.1; Megann et al., 2022). The integration uses the Nucleus for European Modelling of the Ocean (NEMO) ocean circulation model version 4.0.4 (Madec et al., 2019) implemented in the UK Global Ocean (GO) version 8 configuration.

The NEMO ocean model is discretised on an Arakawa C-grid with a nominal 1/12° resolution (equivalent to ∼8 km in the subtropical North Atlantic and ∼4 km in the Arctic). The extended version of the quasi-uniform ORCA12 orthogonal tripolar grid (eORCA12) with poles located on land in Canada, Siberia and Antarctica is used, enabling the explicit representation of the ocean circulation beneath ice cavities in Antarctica. In the vertical, the model uses 75 unevenly spaced z-partial-step coordinate levels with depth increments ranging from 1 m to 250 m. Notably, the volume of the grid cells at each vertical level varies through time due to the implementation of a non-linear free surface (Madec et al., 2019). The vertical mixing of tracers is parameterised using an improved version of the Turbulent Kinetic Energy (TKE) scheme (Gaspar et al., 1990). Within the NEMO framework, the ocean general circulation model OPA (Ocean Parallélisé) is coupled to the Community Ice CodE (CICE) dynamic-thermodynamic sea-ice model version 4 (Hunke & Lipscomb, 2010), which includes the effects of surface melt ponds.

The ORCA0083-GO8p7 integration is initialised from a 1995-2014 average climatology of the EN4 objective ocean analysis (Good et al., 2013). The model is forced by the Japanese 55-year atmospheric reanalysis (JRA55-do; Tsujino et al., 2018) for the period 1958-2021. We disregard the initial 18 years of the integration when model adjustment is largest and make use of the monthly-mean velocity and tracer fields, output between 1975-2021.

To assess the fidelity of the subpolar ocean circulation in the ORCA0083-GO8p7 hindcast, we compare the simulated diapycnal overturning to OSNAP observations between 2014-2020. This comparison is possible due to the extended length of the JRA55-do atmospheric forcing used in the ORCA0083-GO8p7 simulation (1958-2021) and is one of the key reasons for using a different hindcast in this Chapter. Figures 4.1a-b show the time-mean Eulerian diapycnal overturning stream functions at the OSNAP East and OSNAP West sections calculated using both the model and observations. Overall, we find close agreement between the modelled and observed overturning stream functions in density space at the OSNAP array. At OSNAP East, the maximum of the time-mean diapycnal overturning stream function in the model (13.5 Sv at 27.51 kg m^{-3}) is slightly weaker than observed (14.5 Sv at 27.55 kg m^{-3}). However, this is primarily due to the weaker time-mean net throughflow across the section in the model (0.8 Sv) compared to the 1.6 Sv imposed in OSNAP observations. Figure 4.1b shows that there is also strong agreement between both the magnitude and isopycnal of maximum diapycnal overturning in the model (2.1 Sv at 27.70 kg m^{-3} and observations (2.2 Sv at 27.69 kg m^{-3}) at OSNAP West. This is particularly encouraging, given that many eddy-rich models considerably overestimate the time-mean strength of diapycnal overturning in the Labrador Sea (e.g., Markina et al., 2024; Petit et al., 2023b). Note that, once we account for the larger net southward flow across the OSNAP West section in the model (-2.4 Sv) compared with that imposed in OSNAP observations (-1.6 Sv), we do find that the modelled diapycnal overturning is stronger than observed, although this difference is not statistically significant.

Figures 4.1c-d show the time series of diapycnal overturning strength at OSNAP East and OSNAP West determined by calculating the maximum of each monthly overturning stream function. Although we find a significant correlation ($r = 0.55$, $p < 0.01$) between the modelled and observed diapycnal overturning strength at OSNAP East, it is clear that the model (monthly SD = ± 2.6 Sv) underestimates the monthly overturning variability captured in observations (monthly SD = ± 3.0 Sv). In contrast, at OSNAP West, we find a much weaker correlation ($r = 0.27$, $p < 0.05$) since the observed diapycnal overturning strength is less variable than found in the model, especially on seasonal timescales. Further investigation reveals that the stronger overturning seasonality in the model is due to the presence of warm (∼0.14°C) and saline (∼0.1 g kg^{-1}) biases in the western Labrador Sea (47.5° - 46°W) compared with OSNAP observations. This is because warmer and saltier waters experience less density compensation between wintertime cooling and year-round freshening (Bebieva & Lozier, 2023; Zou et al., 2020b) and thus experience greater diapycnal transformation during their recirculation in the Labrador Sea.

In addition to reproducing much of the observed strength and monthly variability of overturning along the OSNAP array, we also find good agreement between the modelled (6.5 ± 1.0 Sv) and observed (5.8 ± 0.7 Sv; Østerhus et al., 2019) overturning strength at the Greenland-Scotland Ridge (1995-2015). Furthermore, given our strong focus on the formation of dense water along the boundary currents of the SPG in this Chapter, we also note the close agreement between the time-mean top-to-bottom strength of the East Greenland Current (-33.8 ± 2.7 Sv) in the model and that observed by Daniault et al. (2016) (-33.1 ± 2.6 Sv) between 2002-2012 along the OVIDE section. However, in the Labrador Sea, the model (-27.4 ± 5.8 Sv) slightly underestimates the time-mean (1997-2014) strength of the DWBC at 53°N as reported by Zantopp et al. (2017) (-30.2 ± 6.6 Sv where $\sigma_\theta \geq 27.68$ kg m^{-3}). In spite of these differences, we consider the broad overall agreement between the strength of both the SPG and diapycnal overturning circulations simulated in the ORCA0083-GO8p7 hindcast and that observed along trans-basin arrays as sufficient justification for using this model to investigate the nature of dense water formation along the path of the SPG.

4.2.2 Lagrangian Particle Tracking

We evaluate the Lagrangian trajectories of virtual water parcels advected by the time-evolving velocity fields of the ORCA0083-GO8p7 hindcast using TRACMASS version 7.1 (Aldama-Campino et al., 2020). We use the stepwise stationary scheme, which divides the duration between successive monthly-mean velocity fields into 100 intermediate time-steps. In contrast to Chapters 2 & 3, we calculate purely advective water parcel trajectories without attempting to parameterise any sub-grid scale diffusive processes in the surface mixed layer. This is because, in Chapter 3, we showed that the strength and variability of along-stream diapycnal transformation was not influenced by our parameterisation of vertical convective mixing along water parcel trajectories.

The Lagrangian experiment used in this study evaluates the trajectories of water parcels sampling the full-depth northward transport across a subsection of the OSNAP East array extending from the Reykjanes Ridge (RR, 30°W) to the Scottish Shelf (SS). We chose this subsection of the array to focus our Lagrangian analysis on the waters which flow northward across OSNAP East in the northern, central and southern branches of the NAC and to avoid oversampling the recirculating upper limb waters which return northward in the Irminger Current (see Fig. 4.2). Water parcels are initialised at the beginning of each month for 456 consecutive months between 1975-2012. The number of water parcels assigned to each model grid cell along the model-defined OSNAP East array (RR-SS) is determined using Eq. 2.2.2. We chose $V_{max} = 2.5$ mSv per parcel to ensure that a sufficiently large number of water parcels are initialised to calculate robust Lagrangian diagnostics (Jones et al., 2016).

In total, more than 12.5 million water parcels are advected forwards-in-time using monthly mean velocity fields for a maximum of 9-years to determine their future trajectories. Water parcel trajectories are terminated on reaching the maximum advection time (τ_{max}) or upon meeting any one of the following geographical criteria (Fig. 4.2a): (i) crossing (southward) a subsection of the OSNAP West array (53°N) (ii) crossing the Greenland-Scotland Ridge, (iii) crossing the Davis or Hudson Straits or (iv) crossing 50°N. Figures 4.3a-c show that the 9-year maximum advection time is sufficient to capture the SPG circulation because the accumulated volume transport reaching OSNAP West and the Greenland-Scotland Ridge have stabilised within this period. The location, conservative temperature and absolute salinity along each water parcel trajectory are calculated through linear interpolation using the monthly mean model tracer fields. The potential density referenced to the sea surface (σ_θ) is calculated along each trajectory using the TEOS-10 equation of state (McDougall et al., 2012) as implemented in the ORCA0083-GO8p7 hindcast (Megann et al., 2022).

4.2.3 Lagrangian Diagnostics

To quantify the amount of dense water formed along the path of the North Atlantic SPG, we calculate Lagrangian overturning stream function, $F(\sigma_\theta^*, t)$ in density-coordinates using only the subset of water parcel trajectories initialised at time t

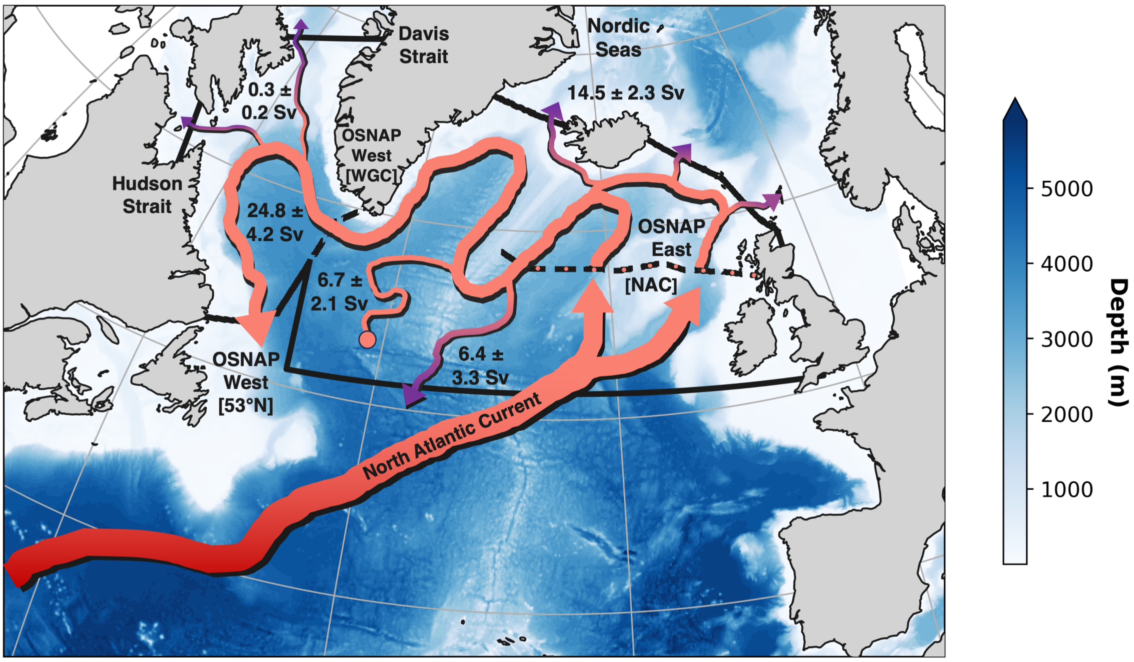

Figure 4.2: Schematic of the North Atlantic Subpolar Gyre (SPG) circulation and Lagrangian experiment domain (solid black lines). Water parcels are initialised northward across the subsection of the OSNAP East array extending from the Reykjanes Ridge (~31°W) to the Scottish Shelf (NAC, black dashed line with orange markers). The SPG pathway (orange) contains all water parcels which flow southward across the OSNAP West array between the Labrador Coast and the basin interior (53°N, solid black line) once initialised across OSNAP East and within the 9-year maximum advection period. Purple arrows represent the pathways of water parcels which are terminated on reaching the boundaries of the Lagrangian experiment domain. Water parcels remaining in the Lagrangian experiment domain are represented by the pathway terminating with an orange circle. The time-mean (1975-2012) volume transports conveyed by each pathway are shown in bold.

which transit from OSNAP East (NAC) to OSNAP West (53°N) within the $\tau_{max} = 9$-year maximum advection period (i.e., $0 < \tau_{out} \leq \tau_{max}$ where τ_{out} is the termination time for each water parcel). We focus on this particular subset of water parcels since the overwhelming majority of water parcels which exit via the southern boundary at 50°N or remain inside the domain following 9 years of advection are already contained within the lower limb on flowing northward across the OSNAP East section. The Lagrangian diapycnal overturning stream function for each monthly ensemble of $N(t)$ water parcels initialised across the OSNAP East section at time t is calculated following Chapter 3:

$$F(\sigma_\theta^*, t) = \sum_{\sigma_\theta=\sigma_{min}}^{\sigma_\theta^*} V_{NAC,\sigma_\theta}(t) - V_{53^\circ N,\sigma_\theta}(t + \tau_{out}) \tag{4.1}$$

where V_{NAC} and $V_{53^\circ N}$ represent the absolute volume transport distributions of SPG water parcels in density-coordinates on their initial northward (NAC) and final southward (53°N) crossings of the OSNAP array.

In order to investigate the downstream evolution of thermohaline anomalies, we additionally define the volume-weighted mean of a specified quantity q of a collection of $N(t)$ water parcels at some time τ following initialisation as:

$$\overline{q}(\tau) = \frac{\sum_{n\in N(t)} V_n q_n(\tau)}{\sum_{n\in N(t)} V_n} \tag{4.2}$$

where V_n is the constant volume transport conveyed by an individual water parcel with index n and $q_n(\tau)$ represents the value of q recorded at time τ following initialisation, where $t \leq \tau \leq t + \tau_{out}$.

4.2.4 Eulerian Diagnostics

4.2.4.1 Surface-Forced Water Mass Transformation

As discussed in Section 1.2, decadal variations in the strength of the subpolar overturning circulation can be related to changes in water mass transformation due to surface buoyancy exchanges and diapycnal mixing. To quantify the amount of dense water formed by surface buoyancy loss over our Lagrangian experiment domain, we begin by computing the surface density flux due to the fluxes of heat (Q_H, W m^{-2}) and freshwater (Q_{FW}, kg m^{-2} s^{-1}) at the sea surface following Speer and Tziperman (1992):

$$f(x, y, t) = -\frac{\alpha}{C_p} Q_H(x, y, t) + \beta \frac{S(x, y, t)}{1 - S(x, y, t)} Q_{FW}(x, y, t) \tag{4.3}$$

where α is the thermal expansion coefficient, β is the haline contraction coefficient, C_p is the specific heat capacity of seawater and S is the sea surface salinity. Note that a positive surface density flux (i.e., $f(x, y, t) > 0$ kg m^{-2} s^{-1}) represents an increase in sea surface density. To calculate the surface-forced diapycnal water mass transformation $H(\sigma_2^*, t)$ across an outcropping isopycnal surface, we then integrate the surface density flux over the area of each surface density outcrop σ_2^*:

$$H(\sigma_2^*, t) = \frac{1}{\Delta\sigma_2} \int \int f(x, y, t)\, \Pi(\sigma_2^*(x, y, t))\, dx\, dy \tag{4.4}$$

where

$$\Pi(\sigma_2^*(x, y, t)) = \begin{cases} 1 & \text{for } |\sigma_2^*(x, y, t) - \sigma_2| \leq \frac{\Delta\sigma_2}{2} \\ 0 & \text{elsewhere} \end{cases}$$

The sea surface potential density σ_2 referenced to 2000 m is computed using model monthly-mean sea surface temperature and salinity fields. The density bin size is given by $\Delta\sigma_2 = 0.02$ kg m^{-3} following Yeager et al. (2021).

4.2.4.2 Definition of Labrador Sea Water

We define Labrador Sea Water (LSW) from the long-term average surface-forced diapycnal water mass transformation calculated over our Lagrangian experiment domain following the methodology of Yeager et al. (2021). The potential density range of LSW at OSNAP West is determined as the interval over which positive annual mean formation of LSW occurs in the 1975-2012 climatology of $H(\sigma_2^*, t)$ over the region north of OSNAP West in our Lagrangian experiment domain. In this study, LSW is defined by the density range $\sigma_2 =$ 37.01 - 37.11 kg m^{-3}. To account for the lighter composition of LSW in the eastern SPG, we use a modified potential density range $\sigma_2 =$ 36.95 - 37.11 kg m^{-3} to define LSW in the Irminger Sea. We quantify the interior LSW thickness, Δz_{LSW}, in the Labrador and Irminger Seas by calculating the average layer thickness of LSW defined by the potential density ranges above along both OSNAP West and OSNAP East where the ocean depth exceeds 2000 m.

4.3 Results

4.3.1 Characterising dense water formation along the path of the subpolar gyre

To characterise the nature of dense water formation along the path of the SPG, we begin by describing the circulation pathways of water parcels flowing northward into the eastern SPG between 1975-2012 (Fig. 4.2).

On average, water parcels represent 52.7 ± 9.0 Sv flowing northward across the OSNAP East array between the Reykjanes Ridge and the Scottish Shelf via the branches of the NAC. Of this total northward transport, 24.8 ± 4.2 Sv (47.0 ± 3.1%; Fig. 4.2) circulates around the SPG before flowing southwards across the OSNAP West array at 53°N (extending from the Labrador coast to the basin interior), which we shall herein refer to as the SPG pathway. The remaining northward transport across OSNAP East is distributed between pathways crossing the Greenland-Scotland Ridge (27.0 ± 4.5%), the Davis and Hudson Straits (0.5 ± 0.4%) and 50°N (12.4 ± 4.2%), with a small fraction remaining within the SPG interior following 9-years of advection (11.4 ± 2.0%).

Figure 4.3 shows that the 14.5 ± 2.3 Sv flowing northward into the Nordic Seas is dominated by shallow water parcels, sourced almost equally from the upper 500 m of the central and southern NAC branches, which typically reach the Greenland-Scotland Ridge in less than a year. Interestingly, although this Nordic Seas inflow is larger than observed (Chafik & Rossby, 2019; Østerhus et al., 2019), we find close agreement between the modelled (6.5 ± 1.0 Sv) and observed (5.8 ± 0.7 Sv; Østerhus et al., 2019) overturning strength at the Greenland-Scotland Ridge (1995-2015), suggesting that a substantial fraction of northward transport across the ridge is recirculated within the upper limb in the model.

As a typical water parcel flows cyclonically around the SPG (Fig. 4.4a), it will form dense NADW by cooling ($\Delta\theta_{SPG}$ = -4.0 ± 0.2 °C) and freshening (ΔS_{SPG} = -0.36 ± 0.03 g kg^{-1}) along-stream. Figure 4.4b shows that, on average, the total light-to-dense transformation of SPG water parcels peaks across the $\sigma_\theta = 27.66$ kg m^{-3} isopycnal, which we herein refer to as $\bar{\sigma}_{DWF}$. We hence define the along-stream Dense Water Formation (DWF) as the total volume flux of water parcels across this constant isopycnal between their initial arrival at OSNAP East and final southward crossing of OSNAP West (i.e., DWF$_{SPG}(t) = F(\bar{\sigma}_{DWF}, t)$). Notably, $\bar{\sigma}_{DWF}$ agrees closely with the isopycnal of maximum overturning recorded in OSNAP observations ($\bar{\sigma}_{MOC} = 27.63$ kg m^{-3} during 2014-2020 in Fu et al. (2023)), although

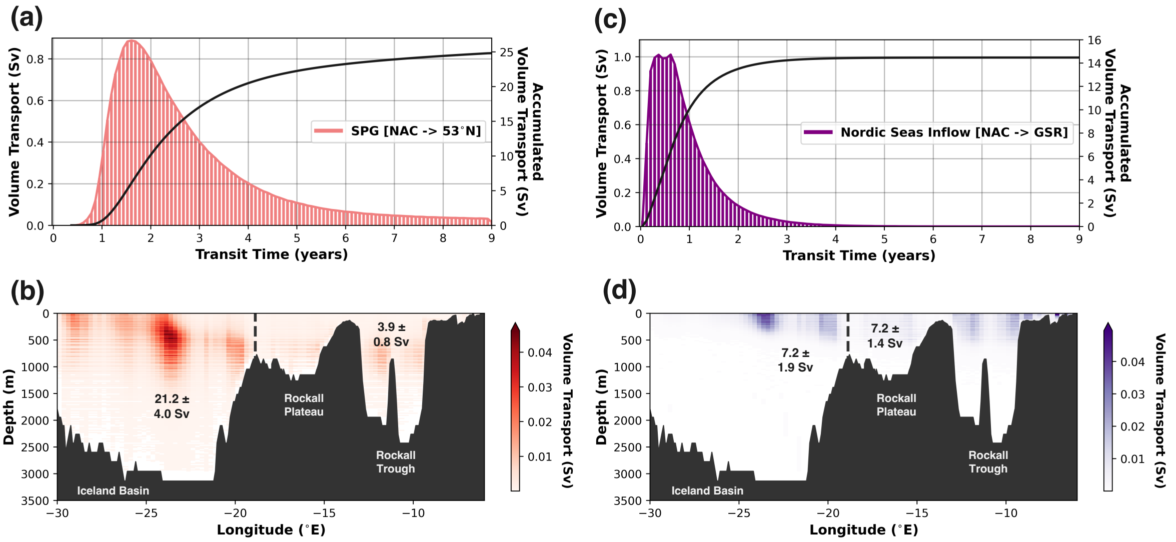

Figure 4.3: (a,b) Volume transport distributions of (a) SPG and (b) Nordic Seas inflow water parcels as a function of the time taken to reach either (a) OSNAP West at 53°N or (b) the Greenland-Scotland following initialisation across OSNAP East in the NAC. The solid black lines represents the accumulated volume transport as a function of water parcel transit time. (c,d) Water parcel release locations in the NAC along OSNAP East between the Reykjanes Ridge and the Scottish Shelf for the SPG pathway (c, red) and the inflows to the Nordic Seas (d, purple). The black dashed line at -18.875 °E is used to distinguish between the northward volume transport arriving in the Iceland Basin and the Rockall Trough and Plateau along OSNAP East. The time-mean volume transport distributions for each pathway are calculated by summing the absolute volume transports conveyed by water parcels in discrete longitude-depth bins, where the bin widths are defined as $\Delta x = 0.25°$E and $\Delta z = 20$ m.

we acknowledge that this lies outside of our study period. We herein refer to water parcels with a potential density less than or greater than $\bar{\sigma}_{DWF}$ as being found in the upper or lower limb of the AMOC, respectively. Furthermore, we refer to lower limb water parcels collectively as NADW throughout the study since $\bar{\sigma}_{DWF}$ constitutes the time-mean upper isopycnal limit of NADW.

Figure 4.4b shows that, of the 24.8 ± 4.2 Sv circulating around the SPG, 12.7 ± 1.9 Sv forms dense NADW in the lower limb (i.e., $\sigma_{53^\circ N} >= \bar{\sigma}_{DWF}$). However, not all of the water circulating around the SPG is eligible to form NADW along-stream, given that 5.6 ± 1.4 Sv already arrives across OSNAP East in the lower limb. Therefore, on average, we find that 12.7 ± 1.9 Sv of the 19.2 ± 3.0 Sv flowing northward across OSNAP East in the upper limb forms NADW along-stream.

We additionally decompose the total DWF along-stream into the separate

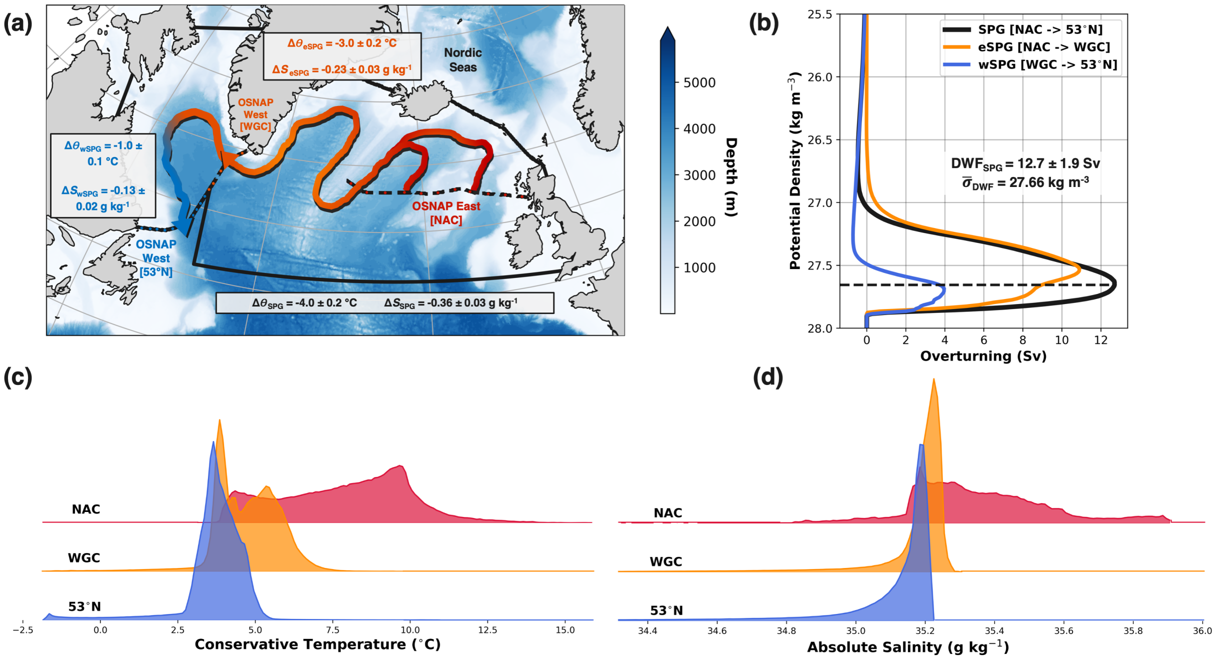

Figure 4.4: Water mass transformation along the path of the North Atlantic SPG. (a) Schematic of the SPG pathway transiting from the NAC inflows across OSNAP East to 53°N along the OSNAP West array. The volume-weighted average changes in conservative temperature and absolute salinity experienced by water parcels in the eastern SPG (NAC to WGC), the western SPG (WGC to 53°N) and along the full SPG pathway (NAC to 53°N) are shown in boxes. (b) Time-mean (1975-2012) Lagrangian overturning stream functions in density-coordinates for the SPG pathway. The total diapycnal overturning along the full path of the SPG (black) is decomposed into the contributions of water mass transformation in the eastern (orange) and western SPG (blue). The black dashed line indicates the isopycnal of the maximum of the time-mean Lagrangian overturning stream function denoted as $\overline{\sigma}_{DWF}$. (c, d) Time-mean (1975-2012) volume transport distributions of water parcels along the path of the SPG in conservative temperature and absolute salinity coordinates. The three distributions shown in each panel correspond to the water parcel properties at their initial location along OSNAP East (NAC, red), their subsequent northward crossing of OSNAP West (WGC, orange) and their final southward crossing of OSNAP West (53°N, blue)

contributions made in the eastern and western SPG by calculating partial Lagrangian overturning stream functions using the properties of water parcels on their northward crossing of the OSNAP West array via the West Greenland Current (WGC; Fig. 4.4a). In agreement with OSNAP observations, we find that DWF_{SPG} is dominated by cooling-driven diapycnal transformation in the eastern SPG (9.0 ± 1.7 Sv). In contrast, DWF is much weaker in the Labrador Sea (3.7 ± 0.9 Sv) since there is greater density compensation between cooling and freshening along-stream (Fig. 4.4c-d). The mean strength of along-stream DWF in the Labrador Sea agrees well with the magnitude of diapycnal overturning observed along OSNAP West (3.0 ± 1.5 Sv during 2014-2020 in Fu et al. (2023)). An equivalent comparison of DWF with observations in the eastern SPG is impeded by the contribution of the Nordic Seas overflows in the Eulerian diapycnal overturning stream function calculated at OSNAP East. However, we note that our finding that the eastern SPG accounts for 9.0 ± 1.7 Sv of the total along-stream DWF agrees closely with both the results presented in Chapters 2 & 3 and previous estimates from observations and ocean reanalyses, which suggest that between 9-10 Sv of diapycnal transformation takes place in the Iceland and Irminger Basins (e.g., Buckley et al., 2023; Chafik & Rossby, 2019; Koman et al., 2022; Sarafanov et al., 2012).

4.3.2 What governs dense water formation along the path of the subpolar gyre?

Figure 4.5a shows that the amount of dense NADW formed along the path of the SPG varies substantially across seasonal to decadal timescales. Given that we quantify DWF using the Lagrangian water parcels circulating around the SPG, we next explore whether the initial properties of an upper limb water parcel on arrival at OSNAP East have any influence on their likelihood of forming dense NADW downstream.

Consistent with Chapter 3, we find that variability in the composition of the upper limb at OSNAP East is dominated by seasonality (Fig. 4.5b); upper limb water parcels are, on average, lighter on arrival during autumn and denser during spring. However, Figure 4.5b shows that DWF_{SPG} is not significantly correlated ($p > 0.05$) with the volume-weighted average potential density of water parcels arriving at OSNAP East in the upper limb. Furthermore, we find no statistically significant relationship between annual-means of DWF_{SPG} and upper limb potential density (buoyancy), suggesting that along-stream DWF is not influenced by the arrival of upper limb buoyancy anomalies into the eastern SPG on either seasonal or interannual timescales. In contrast, we find a strong

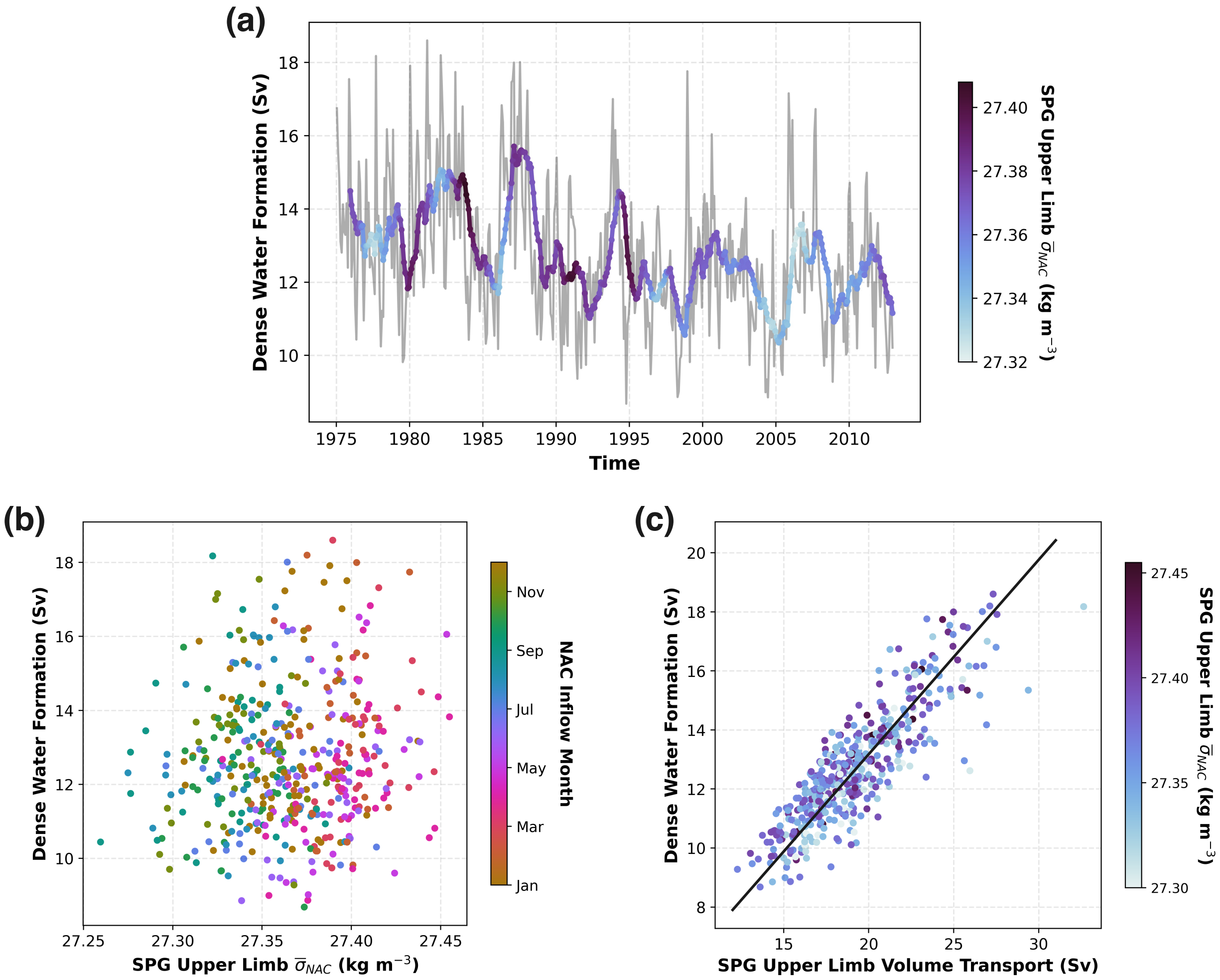

Figure 4.5: Controls on dense water formation along the path of the North Atlantic SPG. (a) Dense water formation (i.e., total volume flux of water parcels across $\overline{\sigma}_{DWF}$) along the path of the SPG (NAC to 53°N) plotted according to the common inflow time when water parcels are released across OSNAP East. The bold line is obtained by applying a 12-month running mean filter to the monthly dense water formation (light grey line) coloured by the volume-weighted mean potential density of the SPG upper limb (i.e., $\sigma_{NAC} \leq \overline{\sigma}_{DWF}$) water parcels. (b) Monthly dense water formation and the volume-weighted mean potential density of SPG upper limb water parcels coloured by their month of release across OSNAP East in the NAC. (c) Monthly dense water formation and the total volume transport of SPG upper limb water parcels coloured by their volume-weighted mean potential density on release across OSNAP East.

positive correlation ($r = 0.86$, $p < 0.01$) between DWF$_{SPG}$ and the total northward transport of the upper limb (i.e., $\sigma_{NAC} < \overline{\sigma}_{DWF}$) across OSNAP East, such that a larger volume transport of upper limb waters into the eastern SPG results in greater NADW formation downstream (Fig. 4.5c).

To better understand the relationship between upper limb volume transport and along-stream diapycnal transformation, we can express the total DWF along the path of the SPG as:

$$DWF_{SPG}(t) = \kappa(t) V_{SPG[UL]}(t) \tag{4.5}$$

where $V_{SPG[UL]}(t)$ represents the SPG upper limb volume transport arriving at OSNAP East at a time t and $\kappa(t)$ represents the fraction of this upper limb volume transport that will form dense NADW downstream. Furthermore, by decomposing each term into its steady and fluctuating components (i.e., $\kappa(t) = \bar{\kappa} + \kappa'(t)$ and $V_{SPG[UL]}(t) = \bar{V}_{SPG[UL]} + V'_{SPG[UL]}(t)$), we can clearly see that variations in DWF$_{SPG}$ are potentially determined by a complex combination of changes in the amount of upper limb water imported into the eastern SPG ($V'_{SPG[UL]}(t)$) and changes in the efficiency by which water parcels are transferred from the upper to the lower limb along-stream ($\kappa'(t)$):

$$DWF'_{SPG}(t) = \bar{\kappa} V'_{SPG[UL]}(t) + \kappa'(t) \bar{V}_{SPG[UL]} + \kappa'(t) V'_{SPG[UL]}(t) \tag{4.6}$$

Surprisingly, Figure 4.5c suggests that the efficiency of along-stream diapycnal transformation (κ') is not the rate-limiting factor governing DWF along the path of the SPG. Instead, variations in DWF$_{SPG}$ are proportional to the amount of upper limb water imported into the eastern SPG via the branches of the NAC (i.e., $DWF'_{SPG}(t) \propto V'_{SPG[UL]}(t)$). This implies that along-stream diapycnal transformation is sufficient to transfer a steady fraction ($\bar{\kappa}$) of upper limb water parcels into the lower limb, irrespective of their initial thermohaline properties on arrival across OSNAP East. Furthermore, the SPG upper limb volume transport is also strongly correlated with the total volume transport along the path of the SPG ($r = 0.97$, $p < 0.01$), indicating that DWF$_{SPG}$ is closely related to the overall strength of the SPG circulation.

4.3.3 How predictable is subpolar gyre dense water formation?

Since we have shown that DWF along the path of the SPG is proportional to the upper limb volume transport imported into the eastern SPNA, we next develop a simple linear model to predict the amount of dense NADW formed along-stream. By assuming that the efficiency of water mass transformation from the upper to the lower limb is time-independent (i.e., $\kappa = \bar{\kappa}$), we can formulate a linear model for DWF$_{SPG}$ as follows:

$$DWF_{SPG}(t) = \bar{\kappa} V_{SPG[UL]}(t) + \epsilon(t) \tag{4.7}$$

where $\bar{\kappa}$ is the constant fraction of the upper limb volume transport which forms NADW along-stream and $\epsilon(t)$ represents the residual error, which is given by $\epsilon(t) = \kappa'(t)\bar{V}_{SPG[UL]} + \kappa'(t)V'_{SPG[UL]}(t)$, following Equation 4.7.

To determine $\bar{\kappa}$, we use ordinary-least-squares linear regression without an intercept term since it would be unphysical to suggest that any amount of dense NADW would be formed if no upper limb water arrived across OSNAP East (i.e., $V_{SPG[UL]} = 0$ Sv). We find that $\bar{\kappa} = 0.66$, implying that, on average, 66% of upper limb waters arriving at OSNAP East are transferred into the lower limb prior to their southward crossing of OSNAP West (53°N). Figure 4.6a shows the strong predictive skill of our linear model on both monthly (RMSE = 1.1 Sv) and interannual (RMSE = 0.8 Sv) timescales, accounting for 74% and 68% of the variance in monthly and interannual (12-month running mean filtered) DWF, respectively.

To better understand the sources of error in our linear model, we decompose the residual DWF ($\epsilon(t)$) into its two components in Figure 4.6b. We find that the residual DWF is almost exclusively explained by fluctuations in the efficiency of along-stream diapycnal transformation from the upper to the lower limb acting on the time-mean volume transport of the SPG upper limb. In particular, our linear model overestimates the amount of dense NADW formed during the late 1970's and mid-1980's, indicating that the time-independent efficiency of diapycnal transformation of our model is too large during these periods (i.e., $\bar{\kappa} > \kappa(t)$). In contrast, during the early and late 2000's, the efficiency of transformation is slightly underestimated (i.e., $\bar{\kappa} < \kappa(t)$) resulting in an underestimation of the DWF downstream. Despite these differences, the high predictive skill of our linear model, especially on interannual to decadal timescales, suggests that changes in diapycnal transformation play a secondary role in governing variations in DWF$_{SPG}$ when compared to variability in the upper limb transport imported into the eastern SPG.

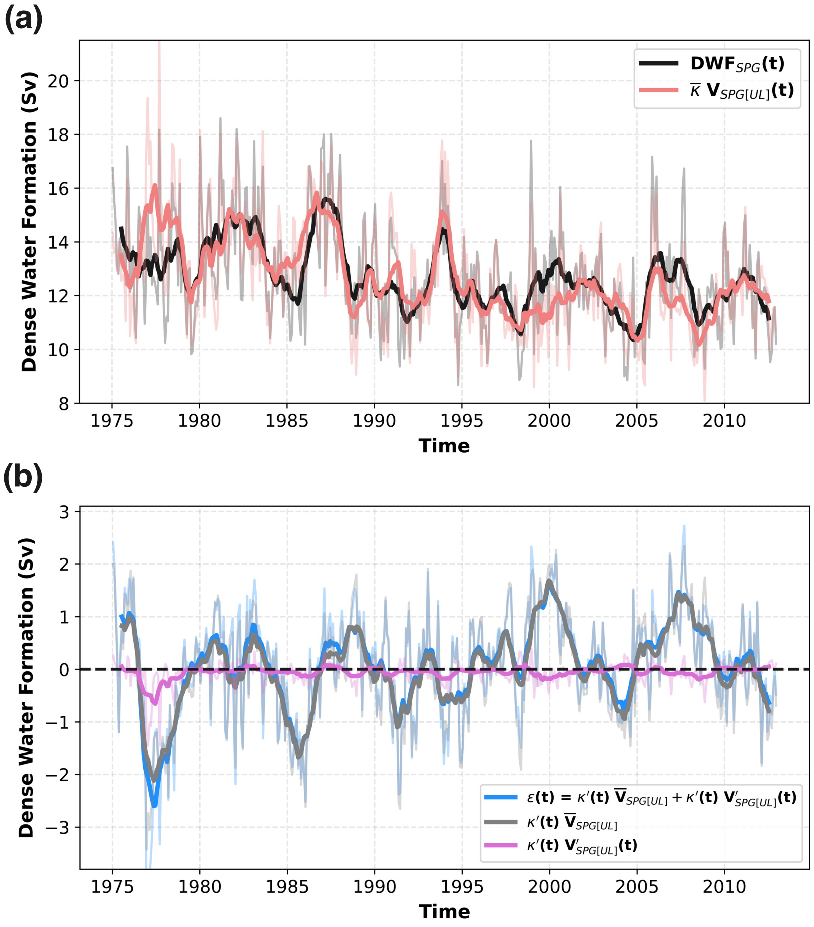

Figure 4.6: A linear model for Dense Water Formation (DWF) along the path of the North Atlantic SPG. (a) Monthly DWF along the path of the SPG (NAC to 53°N, black) and estimated DWF using a simple linear model $\kappa V_{SPG[UL]}(t)$ (pink). (b) The residual DWF $\epsilon(t)$ which is not included in the simple linear model is decomposed into the contributions made by the fluctuations in the efficiency of diapycnal transformation from the upper to the lower limb acting on the time-mean transport of the upper limb and a non-linear term representing the correlation between fluctuations in the efficiency of diapycnal transformation and in the upper limb volume transport. The bold lines are obtained by applying a 12-month running mean filter to the monthly values.

Given that $\bar{\kappa} = 66\%$ of the upper limb waters arriving across OSNAP form dense NADW along the path of the SPG, we next consider what happens to the remaining (1 - $\bar{\kappa}$) = 34% of upper limb waters which do not form dense NADW before crossing OSNAP West at 53°N. Of the 6.4 ± 1.7 Sv of upper limb water parcels which do not form dense NADW along the path of the SPG, we find that 1.5 ± 0.5 Sv of water parcels become lighter through entrainment into the fresh Labrador Coastal Current. Meanwhile, the majority (5.0 ± 1.4 Sv) become denser but not dense enough to be transferred into the lower limb on crossing OSNAP West via the Labrador Current. To determine the fate of these denser water parcels remaining in the upper limb at 53°N, we extend our original Lagrangian experiment by continuing to track upper limb water parcels once they cross the OSNAP West section. We find that almost all of the denser upper limb water parcels (94%) are either transformed into dense NADW south of the OSNAP West section or return to OSNAP East via the NAC to continue circulating around the SPG. Thus, of the total upper limb transport imported into the eastern SPG, we would expect that, on average, almost 92.5% will form dense NADW during one or more circuits of the SPG, whereas 7.5% will join the fresh, estuarine circulation confined to the shelves of the SPNA.

4.3.4 Two dense water formation pathways around the subpolar gyre

We have demonstrated that the total DWF along the path of the SPG can be skilfully predicted with knowledge of only the northward upper limb transport arriving across OSNAP East and a time-independent parameter $\bar{\kappa}$, representing the efficiency of diapycnal transformation along-stream. However, in Chapters 2 and 3, we showed that a wide range of circulation pathways are responsible for the diapycnal transformation of upper limb waters arriving across OSNAP East. Hence, in this Section, we investigate how DWF along the path of the SPG and its variability are partitioned amongst the the NAC branches flowing northward across OSNAP East, and explore how this relates to the nature of diapycnal water mass transformation along-stream.

Figure 4.7 reveals that there are, in-fact, two distinct pathways by which dense water is formed along the path of the SPG. By decomposing the total

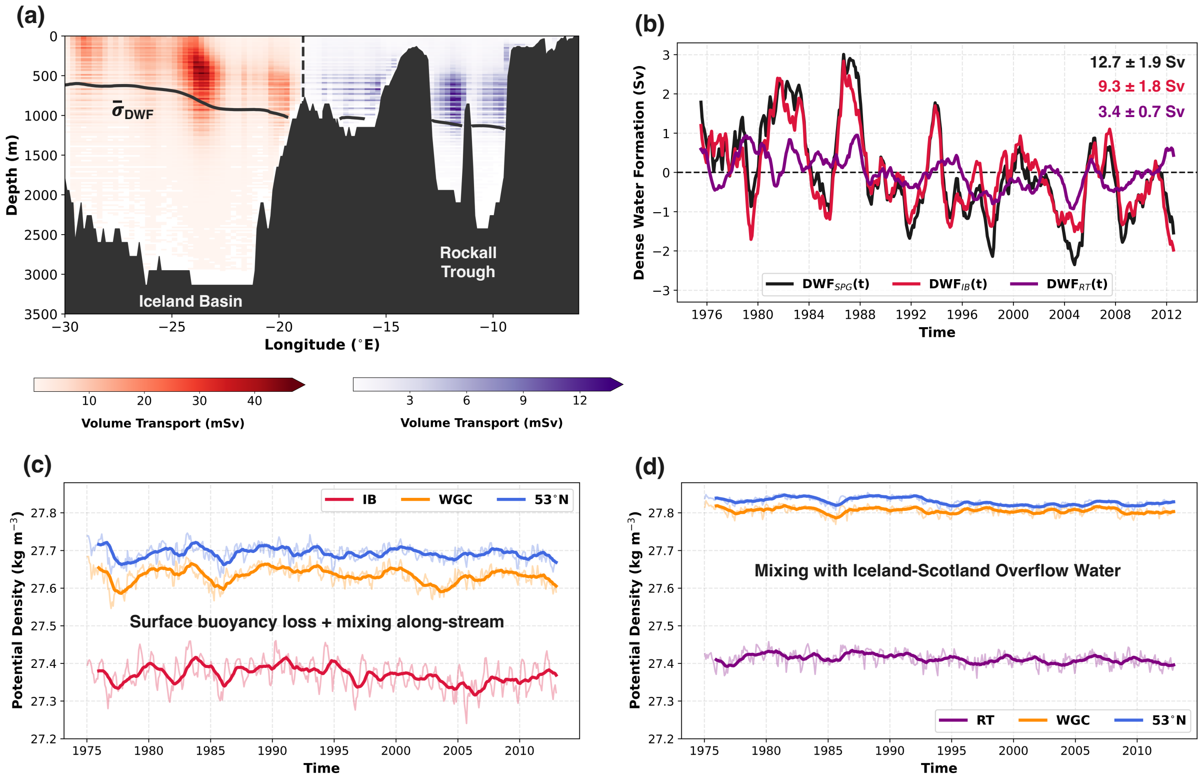

Figure 4.7: Dense water formation along the two circulation pathways of the North Atlantic SPG. (a) Time-mean (1975-2012) volume transport of SPG water parcels originating from the Iceland Basin (**IB**, red) and the Rockall Trough (**RT**, purple) across OSNAP East. Water parcel volume transports are binned in discrete longitude-depth space ($\Delta x = 0.25$°E, $\Delta z = 20$ m) according to their initial release locations along OSNAP East. The black solid line shows the time-mean (1975-2012) position of the $\bar{\sigma}_{DWF}$ isopycnal used to define along-stream dense water formation and hence delimits the upper and lower limbs of the AMOC in this study. (b) Variations in the total DWF along the path of the SPG (DWF'_{SPG}, black) decomposed into the contributions made by upper limb water parcels sourced from the Iceland Basin (DWF'_{IB}, red) and the Rockall Trough (DWF'_{RT}, purple). We apply a 12-month running mean filter to the monthly DWF values in order to highlight interannual to decadal variability. (c,d) Volume-weighted mean potential density evolution of upper limb water parcels, sourced from the **IB** (c) and the **RT** (d), which experience a net positive diapycnal transformation along-stream ($\Delta\sigma > 0$ kg m^{-3}). The bold lines are obtained by applying a 12-month running mean filter to the monthly mean potential density values recorded on arrival at OSNAP East (**IB** / **RT**) and on crossing OSNAP West via both the West Greenland Current (WGC) and the Labrador Current (53°N).

DWF along the path of the SPG into the contributions made by NAC branches flowing northward in the Iceland Basin and Rockall Trough (Figure 4.7a), we find that upper limb water parcels sourced from the Iceland Basin (DWF_{IB}) account for almost three quarters (9.3 ± 1.8 Sv) of the time-mean DWF_{SPG} and 88% of its variance on interannual timescales (Fig. 4.7b). This is contrasted by the weaker 3.4

± 0.7 Sv of along-stream DWF due to upper limb water parcels flowing northward in the Rockall Trough (DWF_{RT}), which explain around 31% of the interannual variability in DWF_{SPG}. On the one hand, these differences in along-stream DWF are partly owed to the much larger northward transport entering the Iceland Basin across OSNAP East (21.2 ± 4.0 Sv) compared with the Rockall Trough (3.9 ± 0.8 Sv in Fig. 4.3b). However, this is far from the complete picture, given that these two dense water pathways also exhibit distinct modes of diapycnal transformation downstream (Figures 4.7c-d), which result in markedly different efficiencies in the transformation of water parcels from the upper to the lower limb.

We find that 59% ($\bar{\kappa}_{IB} = 0.59$, Fig. 4.8a) of upper limb waters entering the Iceland Basin via the northern and central branches of the NAC form upper NADW downstream ($\bar{\sigma}_{DWF} < \sigma_{53^{\circ}N} < 27.80$ kg m^{-3}). Consistent with dominant Lagrangian overturning pathway identified in Chapters 2 & 3, we find that upper limb water parcels undergo continuous transformation by surface buoyancy loss and diapycnal mixing along-stream (Fig. 4.7c). In contrast, practically all ($\bar{\kappa}_{RT} = 0.97$, Fig. 4.8a) of upper limb waters arriving in the subsurface of the Rockall Trough form dense lower NADW ($\sigma_{53N} > 27.80$ kg m^{-3}) by intense diapycnal mixing with Iceland-Scotland Overflow Waters (ISOW) at the exit of the Faroe-Bank Channel (Fig. 4.7c). This finding is consistent with both Chapter 2 and previous studies (e.g., Chafik & Holliday, 2022; Devana et al., 2021; Sarafanov et al., 2012), which identify a 'short-cut' pathway for subtropical-origin waters to penetrate the deep ocean on sub-decadal timescales by mixing with overflow waters south of the Iceland-Faroes Ridge. The clear distinction between the character of diapycnal transformation along these two dense water pathways is further highlighted by the two peaks in the conservative temperature distribution of SPG water parcels on their northward crossing of OSNAP West via the WGC in Figure 4.4c.

Concordant with our earlier analysis in Section 4.3.2, Figures 4.7c-d show that buoyancy anomalies conveyed by upper limb water parcels arriving in both the Iceland Basin and the Rockall Trough are strongly damped downstream. This is particularly evident in the Iceland Basin (Fig. 4.7c), where we find that variations in the average potential density (buoyancy) of upper limb water parcels can only explain around 30% of their downstream variability at 53°N (i.e., $r(\sigma_{IB}, \sigma_{53^{\circ}N}) = 0.56, p < 0.01$). The increasing homogeneity of the two dense water pathways on reaching the exit of the Labrador Sea (53°N) is further highlighted in Figures 4.8b-c, which present the relationship between the initial potential density (buoyancy) of upper limb water parcels (excluding those entrained into the fresh estuarine circulation) and their average densification along the path of the SPG. Here, we find that upper limb water parcels sourced from both the Iceland Basin and the Rockall Trough experience a net densification along-stream which is inversely proportional to their initial potential density (buoyancy) on arrival at OSNAP East (Figs. 4.8b-c). This supports the view that diapycnal transformation is not the rate-limiting factor governing DWF along the path of the SPG, given that along-stream densification is sufficient to transform upper limb water parcels into near-homogeneous NADW varieties, irrespective of their initial properties on arrival at OSNAP East.

4.3.5 The relationship between upper limb buoyancy anomalies and subpolar gyre dense water formation.

We have seen that upper limb buoyancy anomalies arriving in the Iceland Basin and the Rockall Trough on seasonal to interannual timescales are strongly damped by diapycnal transformation downstream (Fig. 4.7b-c). However, Figure 4.7d suggests that this is no longer the case on multi-decadal timescales since upper limb buoyancy anomalies arriving in the Rockall Trough persist downstream, imprinting onto the low-frequency potential density variability recorded at 53°N. For example, Figure 4.8c shows that lighter upper limb water parcels flowing northward in the Rockall Trough between 2000-2010 undergo less densification and hence form a lighter variety of lower NADW on mixing with ISOW downstream, owing to ISOW's relatively stable source properties. In contrast, Figure 4.8b explains why the final properties of upper limb water parcels flowing northward in the Iceland Basin remain largely consistent, even on decadal timescales (see Fig.

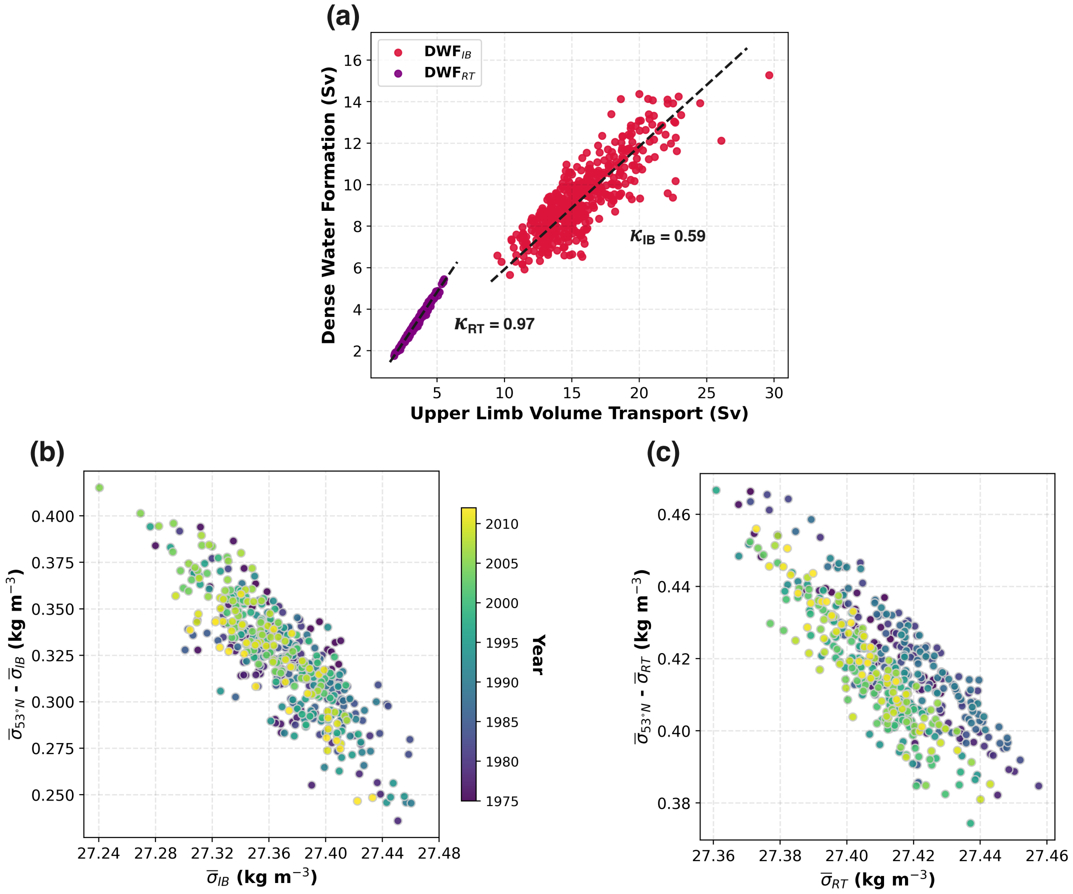

Figure 4.8: Variability in dense water formation along the two circulation pathways of the North Atlantic SPG. (a) Dense water formation and the total volume transport of SPG upper limb water parcels sourced from the Iceland Basin (**IB**, red) and the Rockall Trough (**RT**, purple) inflows across OSNAP East. The values of $\bar{\kappa}$ overlaid represent the fraction of upper limb waters sourced from the **IB** and **RT** which form dense NADW before reaching 53°N at OSNAP West. (c, d) Volume-weighted mean potential density of SPG upper limb water parcels ($\bar{\sigma}_{IB}$, $\bar{\sigma}_{RT}$) and their volume-weighted mean net densification along-stream ($\bar{\sigma}_{53^\circ N}$ - $\bar{\sigma}_{IB}$, $\bar{\sigma}_{RT}$) coloured by their year of arrival across OSNAP East. We include only the SPG upper limb water parcels experiencing a net positive diapycnal transformation (i.e, $\Delta\sigma > 0$ kg m^{-3}) along-stream to exclude those entrained into the fresh estuarine circulation in the Labrador Sea.

4.7b), given that their along-stream densification remains inversely proportional to their initial potential density (buoyancy) on crossing OSNAP East. This disparity reflects the fact that the SPG pathway sourced from the Iceland Basin behaves more like an idealised boundary current in a marginal sea (Buckley et al., 2023; Spall, 2004; Straneo, 2006), which exchanges buoyancy with both the overlying atmosphere and the basin interior. Thus, in this Section, we more closely examine the disconnect between upper limb buoyancy anomalies arriving in the Iceland Basin and the strength of DWF downstream.

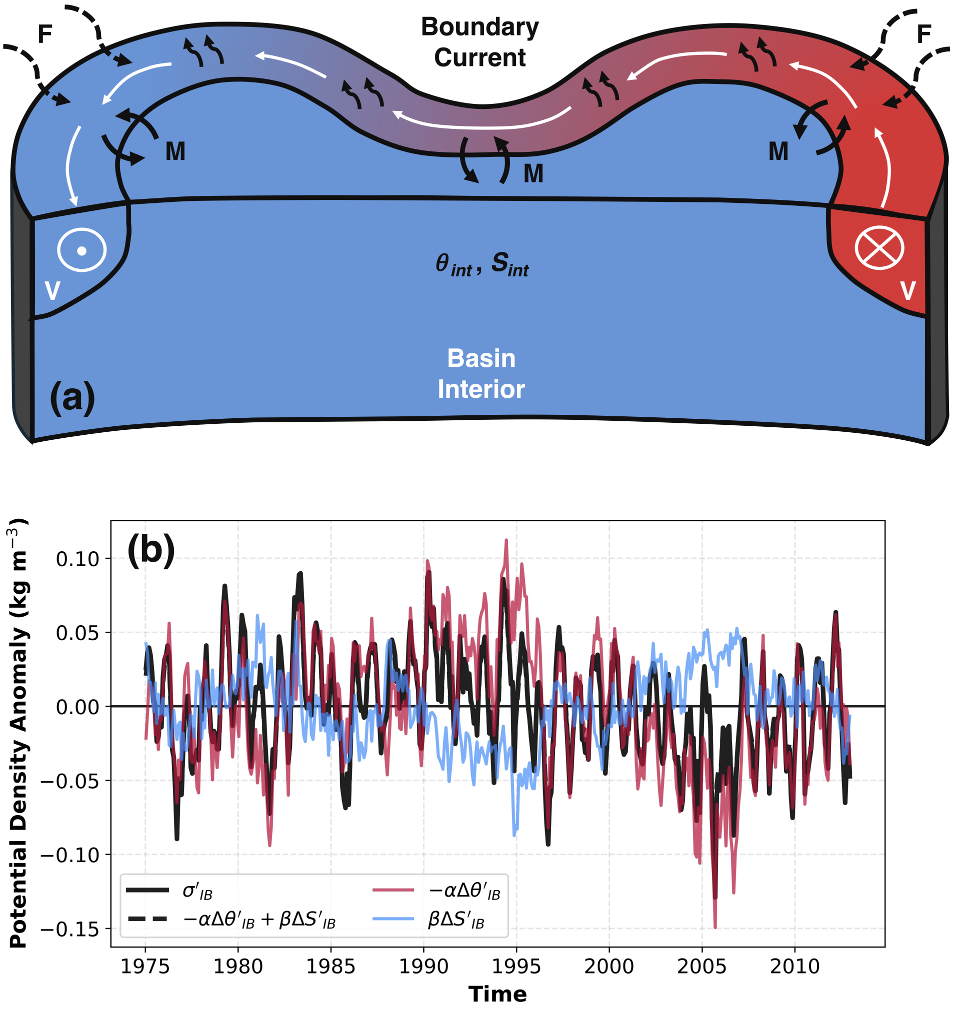

Figure 4.9: (a) Schematic of an idealised boundary current with a constant volume transport V circulating cylonically around a subpolar basin. (b) Decomposition of the volume-weighted mean potential density anomaly of upper limb waters released in the Iceland Basin. Potential density anomalies from the time-mean (σ'_{IB}, black) are decomposed into their respective diathermal ($-\alpha\Delta\theta'_{IB}$, red) and diahaline ($\beta\Delta S'_{IB}$, blue) components using a linearised equation of state for seawater. Note that the potential density anomaly (solid black line) of upper limb waters is entirely reconstructed by the sum of diathermal ($-\alpha\Delta\theta'_{IB}$) and diahaline ($\beta\Delta S'_{IB}$) components (underlying dashed black line).

We adopt the theoretical framework of Wåhlin and Johnson (2009), which describes the temperature θ and salinity S evolution along an idealised, well-mixed boundary current flowing cyclonically around a subpolar basin (Fig. 4.9a). The heat and freshwater budgets of the idealised boundary current are given by:

$$V\frac{d\theta}{dy} = -\frac{\gamma R}{\rho c_p}(\theta - \theta_{atm}) - M(\theta - \theta_{int}) \tag{4.8}$$

$$V\frac{dS}{dy} = -FS - M(S - S_{int}) \tag{4.9}$$

where V and R are the volume transport and width of the boundary current, respectively, and y is the along-stream coordinate. The surface heat flux along the boundary current is assumed to be proportional to the temperature difference between the sea surface ($\theta(y)$) and the overlying atmosphere (θ_{atm}, which is assumed to be constant) and is modulated by a temperature relaxation coefficient γ (Haney, 1971). The freshwater flux F represents the combined net rate at which freshwater is added to the boundary current by precipitation minus evaporation, coastal runoff and exchange with fresh coastal currents at the shelf break. The boundary current also exchanges heat and salt with the basin interior through a combination of eddy ($M_{_{Eddy}}$) and wind-driven ($M_{_{EK}}$) exchange, where $M = M_{Eddy} + M_{EK}$. The constant temperature and salinity of the basin interior are given by θ_{int} and S_{int}, respectively.

The solutions of the above equations, describing the exponential adjustment of temperature $\theta(y)$ and salinity $S(y)$ along the path of the boundary current towards the equilibrium values θ_{eq} and S_{eq}, are given by:

$$(\theta(y) - \theta_{eq}) = (\theta_0 - \theta_{eq})e^{-y/L_\theta} \tag{4.10}$$

$$(S(y) - S_{eq}) = (S_0 - S_{eq})e^{-y/L_S} \tag{4.11}$$

where θ_0 and S_0 represent the initial values of temperature and salinity at $y = 0$ and L_θ and L_S are the adjustment length scales of the boundary current with respect to temperature and salinity. We can, therefore, interpret (θ_{eq}, S_{eq}) as the temperature and salinity the boundary current would acquire if fully adjusted to the forcing (i.e, at $\theta(y) \rightarrow \theta_{eq}$ and $S(y) \rightarrow S_{eq}$ given a sufficiently long y). In general, it is assumed that heat loss to the overlying atmosphere is much larger than the heat flux due to exchange between the boundary current and the basin interior (i.e., $\frac{\gamma R}{\rho c_p}(\theta - \theta_{atm}) \gg M(\theta - \theta_{int})$), such that the the basin interior is in equilibrium with the atmosphere (i.e., $\theta_{int} = \theta_{atm}$ following Lambert et al., 2018; Straneo, 2006; Wåhlin & Johnson, 2009). As a result, the downstream temperature $\theta(y)$ will approach the shared equilibrium temperature of both the atmosphere and the basin interior (i.e., $\theta(L) \rightarrow \theta_{int} \approx \theta_{atm}$). Moreover, under this assumption, the boundary current will converge towards an equilibrium density $\sigma(\theta_{int}, S_{eq})$ provided that the ratios L/L_θ and $L/L_S \gg 1$, where L is the boundary current length.

The simple theoretical model above is particularly insightful when applied to the evolution of upper limb buoyancy anomalies arriving in the Iceland Basin via the NAC. This is because we can show that, provided the path length $L_{IB} \gg L_\theta, L_S$, surface buoyancy loss and diapycnal mixing along-stream will damp upper limb buoyancy anomalies to form upper NADW with a time-independent density $\sigma(\theta_{eq}, S_{eq})$ on reaching 53°N. To assess the extent to which upper limb water parcels arriving in the Iceland Basin adjust to the forcing downstream, we return to our Lagrangian water parcel trajectories. By calculating the typical path length of upper limb water parcel trajectories which circulate cyclonically from the Iceland Basin to OSNAP West at 53°N, we estimate that $L_{IB} \approx 6000$ km. Following Wåhlin and Johnson (2009), the adjustment length scales with respect to temperature and salinity are given by:

$$L_\theta = \frac{V}{M + R\frac{\gamma}{\rho c_p}} \tag{4.12}$$

$$L_S = \frac{V}{F + M} \tag{4.13}$$

To estimate the value of L_θ and L_S for the upper limb water parcels sourced from the Iceland Basin, we model the SPG pathway as an idealised boundary current using the parameters given in Table 4.1. We find that $L_\theta \approx$ 2400 km and hence the pathway is almost fully adjusted in terms of temperature ($L_{IB}/L_\theta \approx 2.5$), such that its final temperature on reaching 53°N is virtually independent of both the volume transport and initial temperature of upper limb waters arriving across

OSNAP East (Wåhlin & Johnson, 2009). In order to obtain a rough estimate of L_S, we assume that the along-stream addition of freshwater is small compared with the freshwater flux due to exchange with the basin interior (i.e., $F \ll M$), such that $L_S \approx V/M$. This estimate yields an upper limit for the length scale with respect to salinity $L_S \approx 7100$ km, which informs us that the SPG pathway is not fully adjusted in terms of salinity ($L_{IB}/L_S \approx 0.84$) and thus salinity anomalies arriving in the Iceland Basin will persist downstream. Interestingly, Figure 4.9b shows that upper limb buoyancy (potential density) anomalies arriving in the Iceland Basin are dominated by temperature rather than salinity fluctuations on monthly to decadal timescales (i.e., $r(-\alpha\theta'_{IB}, \sigma'_{IB}) = 0.82$, $p < 0.01$). The dominance of thermal anomalies in the upper limb, combined with their efficient damping by air-sea fluxes and mixing downstream, hence explains the strong decoupling between decadal changes in upper-ocean properties and DWF in the SPG (e.g., Fu et al., 2020).

4.3.6 What drives decadal variability in subpolar gyre dense water formation?

We have seen that the amount of dense water formed along the path of the SPG exhibits substantial variations on decadal timescales (Fig. 4.5a), which principally result from changes in the transport of upper limb water arriving across OSNAP East via the branches of the NAC. More specifically, we find that DWF$_{SPG}$ transitions from a relatively strong period between 1975-1987 (13.7 ± 2.0 Sv) to a weaker, less variable period extending from 2000-2012 (12.1 ± 1.5 Sv; see Fig. 4.7b). Since we have also shown that the amount of upper limb water flowing northward in the NAC is closely correlated with the total volume transport along the path of the SPG, we next investigate the mechanisms responsible for generating variability in the strength of the SPG and hence DWF on decadal to multi-decadal timescales.

Previous numerical modelling studies have highlighted the important role of localised surface buoyancy forcing, driven by low-frequency changes in the NAO, in modulating decadal variability in the subpolar ocean circulation (Böning et al.,

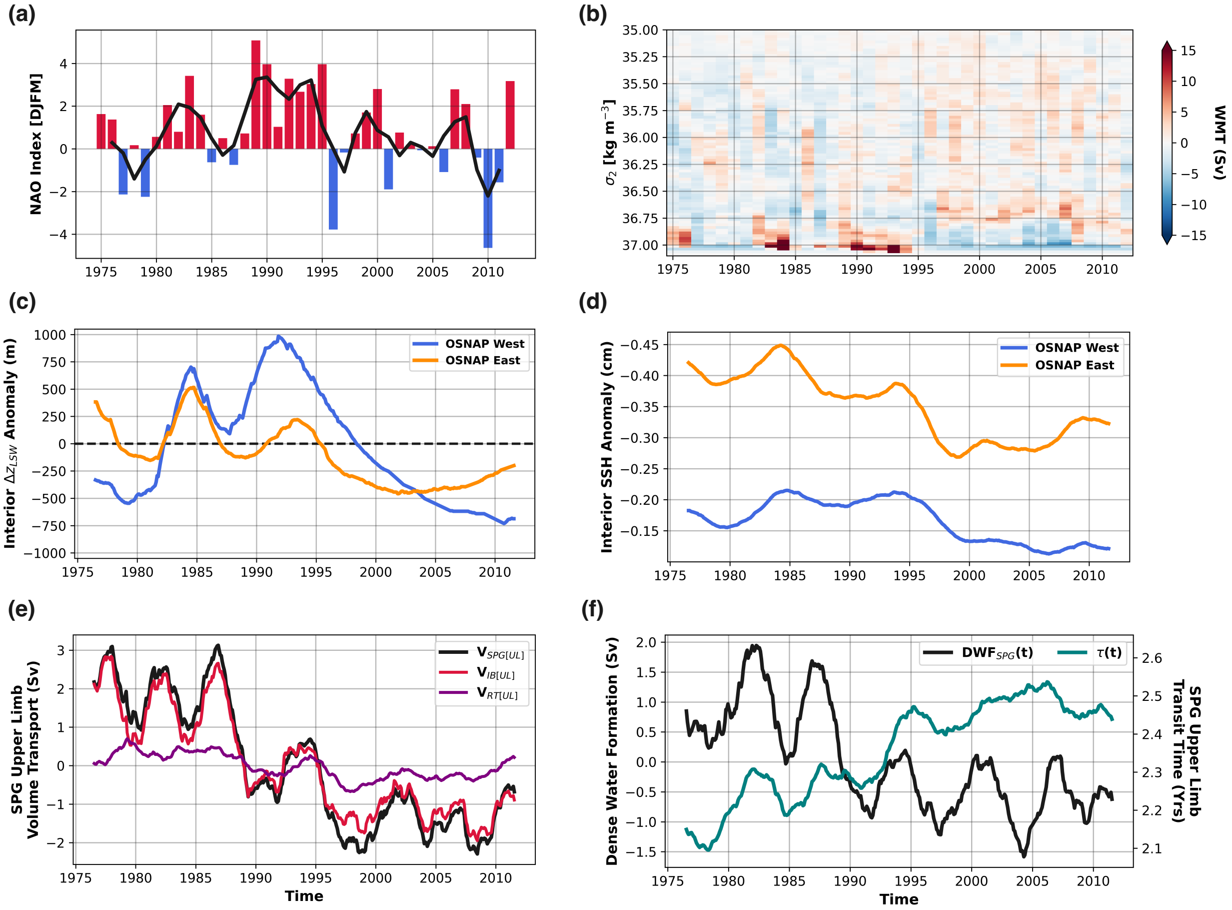

Figure 4.10: Mechanisms governing decadal variability in dense water formation along the path of the North Atlantic SPG. (a) Winter [DJFM] station-based North Atlantic Oscillation (NAO) index. (b) Surface forced Water Mass Transformation (WMT) anomalies calculated over the Lagrangian experiment domain (see Fig. 4.1a) in σ_2 potential density coordinates (referenced to 2000 m). (c) Layer thickness anomalies of Labrador Sea Water (Δz_{LSW}) in the basin interior (where bathymetry exceeds 2000 m) along the OSNAP West (blue) and OSNAP East (orange) arrays. (d) Basin interior (where bathymetry exceeds 2000 m) Sea Surface Height (SSH) anomaly relative to the section-wide mean SSH along the OSNAP West (blue) and OSNAP East (orange) arrays. (e) Total volume transport of SPG upper limb water parcels ($V_{SPG[UL]}$, black) decomposed into contributions from water parcels sourced from the Iceland Basin ($V_{IB[UL]}$, red) and the Rockall Trough ($V_{RT[UL]}$, purple). (f) Dense water formation along the path of the SPG (black) and the volume-weighted mean transit time of upper limb water parcels circulating around the SPG (teal). All anomalies are determined by removing the long-term time-mean (1975-2012) from monthly values before applying a 36-month running mean filter.

Parameter	**Iceland Basin Value**	**Description**
$V_{IB[UL]}$	14.3 Sv	Upper limb volume transport sourced from the Iceland Basin (excluding the fresh estuarine circulation component)
R_{IB}	200 km	Typical width of upper limb inflow arriving in the Iceland Basin
ρ	1027 kg m^{-3}	Reference density
c_p	3994 J kg^{-1}C^{-1}	Specific heat capacity of seawater
γ	80 W m^{-2}	Temperature relaxation coefficient (upper estimate used in Wåhlin & Johnson, 2009)
M	2.0 m^{2}s^{-1}	Exchange rate between the boundary current and the basin interior (Furevik & Nilsen, 2005; Spall, 2004; Wåhlin & Johnson, 2009, upper estimate of)

Table 4.1: Definitions of parameters used to estimate the adjustment length scales with respect to temperature L_θ and salinity L_S along the SPG pathway sourced from the Iceland Basin.

2006; Delworth & Zeng, 2016; Jackson et al., 2022; Khatri et al., 2022; Kim et al., 2018a; Robson et al., 2012; Yeager, 2020; Yeager & Danabasoglu, 2014; Yeager et al., 2015). Consistent with the mechanisms proposed in these studies, we find that the generation of subsurface density anomalies and the densification of the AMOC lower limb are both important precursors to sustained positive anomalies in DWF along the path of the SPG. In particular, Figures 4.10a-b show that persistent positive phases of the NAO during the mid-1980s and early 1990s were responsible for enhanced surface heat loss and, therefore, an intensification in deep convection in the SPG interior. This resulted in anomalously strong surface-forced water mass transformation in the LSW density range (i.e., $\sigma_2 > 37.0$ kg m^{-3} in Fig. 4.10b), which increased the thickness of the LSW layer in the central Labrador and western Irminger Seas (Fig. 4.10c). The densification of the SPG interior also manifests at the surface through a depression in the sea-surface height (SSH) field (see Fig. 4.10d), which induces a delayed spin-up of the SPG circulation by steepening the SSH gradient across the basin (Eden & Willebrand, 2001; Häkkinen & Rhines, 2004; Kostov et al., 2023). In agreement with recent studies (Chafik et al., 2022; Mercier et al., 2024; Roussenov et al., 2022), we find that SSH (density) anomalies in the Irminger Sea interior play an important role in determining the northward geostrophic transport of the upper limb by modulating the pressure gradient across the NAC. Specifically, Figure 4.10e shows that the stronger upper limb transport arriving in the Iceland Basin between 1975-1987 is associated with a period of anomalously low sea-surface heights in the Irminger Sea interior, whereas elevated sea-surface heights are concomitant with the weaker upper limb transport recorded during the 2000s (Fig. 4.10d).

To further demonstrate that multi-decadal variations in the upper limb transport entering the Iceland Basin are concordant with low-frequency changes in SPG dynamics, Figure 4.10f shows the average transit times taken for upper limb water parcels to circulate around the SPG. We can clearly see that the greater upper limb volume transport across OSNAP East during the 1970s and 1980s coincides with a faster, stronger SPG circulation. Meanwhile, in the 2000s, the slower SPG circulation is responsible for the weaker upper limb transport arriving in the NAC. Finally, since we have already shown that DWF along the path of the SPG depends linearly on the upper limb transport arriving across OSNAP East, Figure 4.10f shows that multi-decadal changes in SPG DWF are largely determined by the delayed response of the gyre circulation to remote (i.e., Labrador Sea) surface buoyancy forcing. The strong interannual variability superimposed on this multi-decadal trend in DWF likely reflects the faster wind-driven response of the SPG circulation to changes in the NAO. For example, Wang et al. (2021) show that wind-stress curl induced variations in the transport of the NAC branches arriving in the Iceland Basin and Rockall Trough play an important role in driving interannual variability in the upper limb transport across OSNAP East.

In summary, we have shown that decadal surface buoyancy forcing anomalies in the central Labrador and Irminger Seas can remotely influence NADW formation taking place along the path of the SPG by modifying the strength of the SPG circulation and hence the amount of upper limb water arriving across OSNAP East.

4.4 Discussion & Conclusions

Despite the success of the Overturning in the Subpolar North Atlantic Program (OSNAP) in revealing the complex nature of DWF in the SPNA, the extent to which large-scale changes in upper-ocean properties impact the downstream formation of NADW remains unclear. In this Chapter, we take a Lagrangian approach to determining how much dense NADW is formed along the path of the SPG in an eddy-rich ocean sea-ice hindcast. By evaluating the Lagrangian trajectories of water parcels flowing northward in the NAC, we investigate the physical mechanisms governing DWF along the path of the SPG, including addressing the role of upper limb buoyancy anomalies advected along-stream.

Our Lagrangian analysis demonstrates that DWF along the path of the SPG principally depends on the amount of upper limb waters arriving in the eastern SPG via the NAC rather than the efficiency of diapycnal transformation. We thus show that along-stream DWF can be skilfully predicted using a simple linear model, which assumes that a constant fraction $\bar{\kappa} = 66\%$ of upper limb volume transport is transformed into NADW during each circuit of the SPG. The efficiency of diapycnal transformation from the upper to the lower limb $\bar{\kappa}$ can also be conceptualised as a measure of the relative alignment between the gyre and the overturning circulations at subpolar latitudes. To illustrate this, we can consider the idealised case in which the SPG and overturning circulations are perfectly aligned (i.e., $\bar{\kappa} = 100\%$), with the upper limb waters flowing northward in the NAC separated horizontally from lower limb waters returning southward in the Labrador Current. Here, the volume transport flowing around the SPG would be equivalent to the diapycnal overturning downstream and we could quantify DWF by simply measuring the volume transport arriving into the eastern SPG via the branches of the NAC. In reality, we know from observations that $\bar{\kappa} < 1$ since the density surface delimiting upper NADW does not continuously outcrop at the sea surface along the western boundary of the Labrador Sea (see Fig. 4 in Zantopp et al., 2017) and hence the SPG circulation projects onto a diapycnal overturning cell (and thus the formation of NADW) with a time-evolving efficiency characterised by $\kappa(t)$.

It is also interesting to compare the character of DWF along the path of the SPG to that taking place within the Nordic Seas. Previous studies have framed the circulation of the Nordic Seas as a double estuary, comprising of a fresh estuarine and a thermohaline circulation (e.g., Eldevik & Nilsen, 2013; Rudels, 2010). According to Østerhus et al. (2019), 70% of the Atlantic Water inflow across the Greenland-Scotland Ridge participates in the thermohaline circulation to form dense lower NADW, whereas the remaining 30% joins the freshwater sourced from the Arctic in the estuarine circulation. On the one hand this implies a similar efficiency of diapycnal transformation along the boundary currents of both the SPG and the Nordic Seas. However, this conceals the fact that a much smaller fraction of the upper limb water circulating around the SPG (8% or 1.5 ± 0.5 Sv) participates in the estuarine circulation compared with the Nordic Seas. Instead, we find that the overwhelming majority of the $(1 - \bar{\kappa})$ water parcels which remain in the upper limb after completing one circuit of the SPG participate in the thermohaline circulation either by forming NADW further downstream or returning to the eastern SPG with a greater density. It would be interesting to apply the Lagrangian methodology introduced in this study to see if a similar linear relationship can be found between the northward transport of Atlantic Waters imported across the Greenland-Scotland Ridge and the downstream formation of lower NADW in the Nordic Seas (i.e., DWF$_{NS} = \bar{\kappa}_{NS} V_{AW}$, where $\bar{\kappa}_{NS} \approx 0.7$).

The likelihood of downstream transformation into the lower limb is also strongly dependent on where upper limb waters arrive into the eastern SPG. In particular, we find that upper limb waters arriving in the subsurface of the Rockall Trough are almost guaranteed ($\bar{\kappa}_{RT} = 97\%$) to form dense lower NADW via vigorous mixing with ISOW, whereas only $\bar{\kappa}_{IB} = 59\%$ of upper limb waters arriving in the Iceland Basin form upper NADW. In spite of their different efficiencies of diapycnal transformation, we show that the amount of dense water formed along both pathways is independent of the initial properties of water parcels arriving in the NAC on seasonal to interannual timescales, implying that upper limb buoyancy anomalies do not feed back onto the strength of DWF downstream. This is consistent with the conclusion of Fu et al. (2020) that diapycnal overturning is strongly decoupled from upper-ocean properties in the SPNA. To better understand this decoupling, we further examine the evolution of diapycnal transformation along the SPG pathway sourced from the Iceland Basin using the simple theoretical model of Wåhlin and Johnson (2009). Our analysis indicates that the Iceland Basin pathway has almost reached an equilibrium density on reaching 53°N, and thus along-stream buoyancy loss due to air-sea fluxes and diapycnal mixing acts to damp upper limb buoyancy anomalies arriving from upstream.

There are two important implications of the strong decoupling between the composition of upper limb waters arriving in the eastern SPG and the strength of DWF downstream. Firstly, it accounts for the consistent properties of upper NADW flowing southward across 53°N, which is typically defined by the narrow potential density range of 27.68 - 27.74 kg m^{-3} (e.g., Kieke et al., 2007; Rhein et al., 2011). Secondly, this result suggests that buoyancy anomalies advected along the path of the SPG do not play an active role in driving variability in DWF on seasonal to decadal timescales since they are unable to persist downstream. This supports the conclusion of Buckley et al. (2012) that although AMOC variability can generate upper-ocean thermohaline anomalies, these anomalies are not themselves responsible for generating subpolar overturning variability. Instead, we find that decadal variations in the amount of dense water formed along the path of the SPG are determined by surface buoyancy forcing localised in the central Labrador and Irminger Seas.

Concordant with recent studies (e.g., Kostov et al., 2024; Roussenov et al., 2022), we show that enhanced surface buoyancy loss during persistent positive phases of the NAO drives a geostrophic increase in the northward upper limb transport into the Iceland Basin, which is consistent with an intensification of the cyclonic SPG circulation in response to the densification of the Irminger Sea interior. Since along-stream DWF is proportional to the amount of upper limb water arriving across OSNAP East, we might anticipate that this spin-up of the SPG circulation would directly translate into an increase in the strength of the basin-scale overturning. However, in order for DWF to imprint onto the diapycnal overturning circulation, lower limb waters must also be exported out of the SPG and into the subtropical North Atlantic (Buckley et al., 2023). An outstanding question from this study is, therefore, what fraction of the NADW formed along the path of the SPG is subsequently exported to the subtropics compared with that which recirculates in the SPG? By comparing the long-term mean subpolar AMOC strength ($\sim$16 Sv) to the typical southward transport of NADW across 53°N ($\sim$30 Sv; Fröhle et al., 2022; Zantopp et al., 2017), Buckley et al. (2023) suggest that only around half of all NADW is exported from the SPG. While it is beyond the scope of this study, it would be interesting to investigate whether decadal changes in DWF can influence the rate at which NADW is exported to the subtropical North Atlantic and, hence, act to modulate the advective propagation of overturning anomalies downstream.

It is important to acknowledge the limitations of this study. Firstly, our use of monthly-mean model velocity and tracer fields will result in an underestimation of the dispersive nature of Lagrangian trajectories. This is particularly relevant for representing the exchanges between the SPG boundary and interior of the Labrador and Irminger Seas. Thus, we would expect shorter circulation times and greater boundary-interior exchange along the path of the SPG if daily or 5-day mean velocity and tracer fields were used. Similarly, by calculating purely advective Lagrangian trajectories within the surface mixed layer, we will inevitably underestimate the influence of unresolved vertical convective mixing on water parcel trajectories. However, the effects of such turbulent mixing are implicitly included in the tracer fields sampled by water parcels (Chenillat et al., 2015).

Secondly, our Lagrangian analysis solely focuses on the water parcels which transit directly from OSNAP East to OSNAP West and thus, by definition, excludes water parcels which exit the domain to the south (primarily sourced from the central Iceland Basin) and those which do not reach any of the boundaries of the domain following 9-years of advection. Further investigation of the volume transport reaching the southern boundary of the Lagrangian experiment domain at $\sim$52°N indicates that more than 95% of these water parcels are already found in the lower limb when initialised across OSNAP East. Similarly, of the 6.7 ± 2.1 Sv of volume transport which remains inside the Lagrangian experiment domain following 9-years of advection, only $\sim$10.6% originate from the upper limb on crossing OSNAP East. This quantity may be underestimated, however, given our use of temporally smoothed monthly mean velocity fields in this study.

The central finding of this study, that the amount of dense water formed along the path of the SPG is principally determined by changes in the transport of upper limb waters circulating around the SPG, suggests that large-scale changes in subpolar overturning must also manifest in the SPG circulation. This underscores the importance of monitoring the SPG for both decadal and longer-term climate predictions as previously highlighted by Curry and McCartney (2001), Hawkins and Sutton (2009), and Bingham et al. (2007). Furthermore, our Lagrangian analysis suggests that the projected decline of the AMOC over the course of the 21stcentury may be closely related to the evolution of the SPG circulation and its representation in coupled climate models (Hirschi et al., 2020). On the one hand, coupled climate models show a robust weakening and contraction of the SPG circulation in response to external anthropogenic forcing (Born & Stocker, 2014; Sgubin et al., 2017; Swingedouw et al., 2020, 2021), which is entirely consistent with a reduction in DWF along-stream. However, we also know that the low horizontal resolution of the ocean components of current generation coupled climate models favour NADW formation through deep convection in the basin interior rather than via continuous diapycnal transformation along the encircling boundary currents (Heuzé, 2017, 2021). Moreover, the large diversity of mean ocean states of coupled climate models has been highlighted as a critical source of uncertainty in both historical and future projections of the AMOC (e.g., Jackson et al., 2023b; Reintges et al., 2024).

In this Chapter, we have investigated the mechanisms governing DWF along the path of the SPG by tracking water parcels flowing northward in the NAC until their southward crossing of the OSNAP West array in the Labrador Sea. We have shown that neither the diapycnal transformation of water parcels, nor their initial properties on arrival at OSNAP East, are the rate limiting factor governing DWF downstream. Instead, the amount of dense water formed along-stream can be skilfully predicted based solely on the volume transport of upper limb waters circulating cyclonically around the SPG, which is modulated by surface buoyancy forcing in the basin interior on decadal timescales.

5

Lagrangian decomposition of the meridional heat transport in the subtropical North Atlantic

We saw in Chapter 4 how variability in subpolar dense water formation is intrinsically related to changes in the strength of the SPG circulation. In this Chapter, we turn our attention to the subtropical North Atlantic, where we use our Lagrangian overturning framework to diagnose the role of the STG circulation in the meridional overturning and heat transport recorded at 26.5°N.

5.1 Introduction

Throughout the coming century, the AMOC will play a critical role in shaping the response of the global climate system to anthropogenic activity through the redistribution of excess heat, freshwater and carbon. Since 2004, the Rapid Climate Change-Meridional Overturning Circulation and Heatflux Array (RAPID-MOCHA, herein referred to as RAPID) trans-basin observing system has made continuous measurements of the strength of the AMOC and the associated meridional transports of heat and freshwater across 26.5°N (Cunningham et al., 2007). Here, the subtropical North Atlantic Ocean transports $\sim$1.2 PW of heat northwards

(Hall & Bryden, 1982; Johns et al., 2011; McCarthy et al., 2015b), accounting for 30% of the total ocean-atmosphere Meridional Heat Transport (MHT) (Ganachaud & Wunsch, 2000; Trenberth & Fasullo, 2017).

Traditionally, the total ocean heat transport across 26.5°N has been partitioned into zonally-averaged vertical and residual horizontal circulation components (Böning & Herrmann, 1994; Bryan, 1982; Johns et al., 2011), typically referred to as overturning and gyre heat transports, respectively. However, the degree to which these 2-dimensional geometric components represent the actual contributions made by the 3-dimensional flow structures of the AMOC and STG to the total MHT at 26.5°N has been widely debated (e.g., Johns et al., 2023b; Talley, 2003). Previous studies have criticised this interpretation of the horizontal gyre circulation because the waters flowing northward within the western boundary current of the STG do not recirculate horizontally along constant depth surfaces, but rather spiral downwards to form Subtropical Mode Water (STMW) in a shallow local overturning cell (Berglund et al., 2022; Burkholder & Lozier, 2014; Spall, 1992; Talley, 2003). According to Talley (2003), this wind-driven STMW cell within the STG could account for up to 0.4 PW of the total MHT observed at 24°N, much larger than the traditionally defined horizontal gyre heat transport. In contrast, the modelling study of Xu et al. (2016) concludes that the STG makes a negligible contribution to the total heat transport at 26.5°N since the authors argue that the near-surface waters of the Florida Current participate directly in the basin-scale AMOC rather than circulating around the STG.

The long-standing uncertainty regarding the relative contributions of the AMOC and the STG flow structures to the total MHT at 26.5°N ultimately reflects the subjective nature of approaching this problem within the confines of the traditional Eulerian framework (Johns et al., 2023b). To overcome this challenge, in this Chapter, we present the first Lagrangian decomposition of the MHT and overturning across the RAPID 26.5°N array using water parcel trajectories evaluated within an eddy-rich ocean sea-ice hindcast simulation.

The Chapter is organised as follows. We begin by introducing the eddy-rich ocean sea-ice hindcast simulation, Lagrangian particle tracking experiments and Eulerian and Lagrangian diagnostics used in this study in Section 5.2. In Section 5.3.1, we compare the Eulerian meridional overturning and heat transport simulated by the model to RAPID observations at 26.5°N. We then partition the time-mean meridional overturning and heat transport at 26.5°N between the STG and basin-scale overturning circulation in Section 5.3.2. Finally, Section 5.4 concludes this Chapter with a discussion of our principal findings, including their wider significance for our understanding of the role of the STG within the basin-scale overturning circulation.

5.2 Methods

5.2.1 Ocean General Circulation Model

To investigate the meridional overturning and heat transport at 26.5°N, we use the output from the ORCA0083-N06 ocean sea-ice hindcast, documented in Table 1.1. We choose to use a different eddy-rich simulation to Chapter 4 since the mean velocity and tracer fields output by the ORCA0083-N06 hindcast are available at 5-day rather than monthly resolution and because this simulation has already been validated against RAPID observations by Moat et al. (2016). The simulation uses a global implementation of the Nucleus for European Modelling of the Ocean (NEMO) ocean circulation model version 3.6 (Madec et al., 2017) coupled to the thermodynamic Louvain-la-Neuve Ice Model version 2 (LIM2) sea-ice model (Fichefet & Maqueda, 1999). The ocean component is configured with a nominal horizontal resolution of 1/12° (equivalent to 8.3 km at 26.5°N) and with 75 unevenly spaced z-partial-step coordinate levels ranging from 1 m to 250 m depth increments. The hindcast simulation is integrated for the historical period from 1958-2015 using the Drakkar Forcing Set 5.2 (Dussin et al., 2016). Here, we make use of the 5-day mean velocity and tracer fields output for the period 1980-2015.

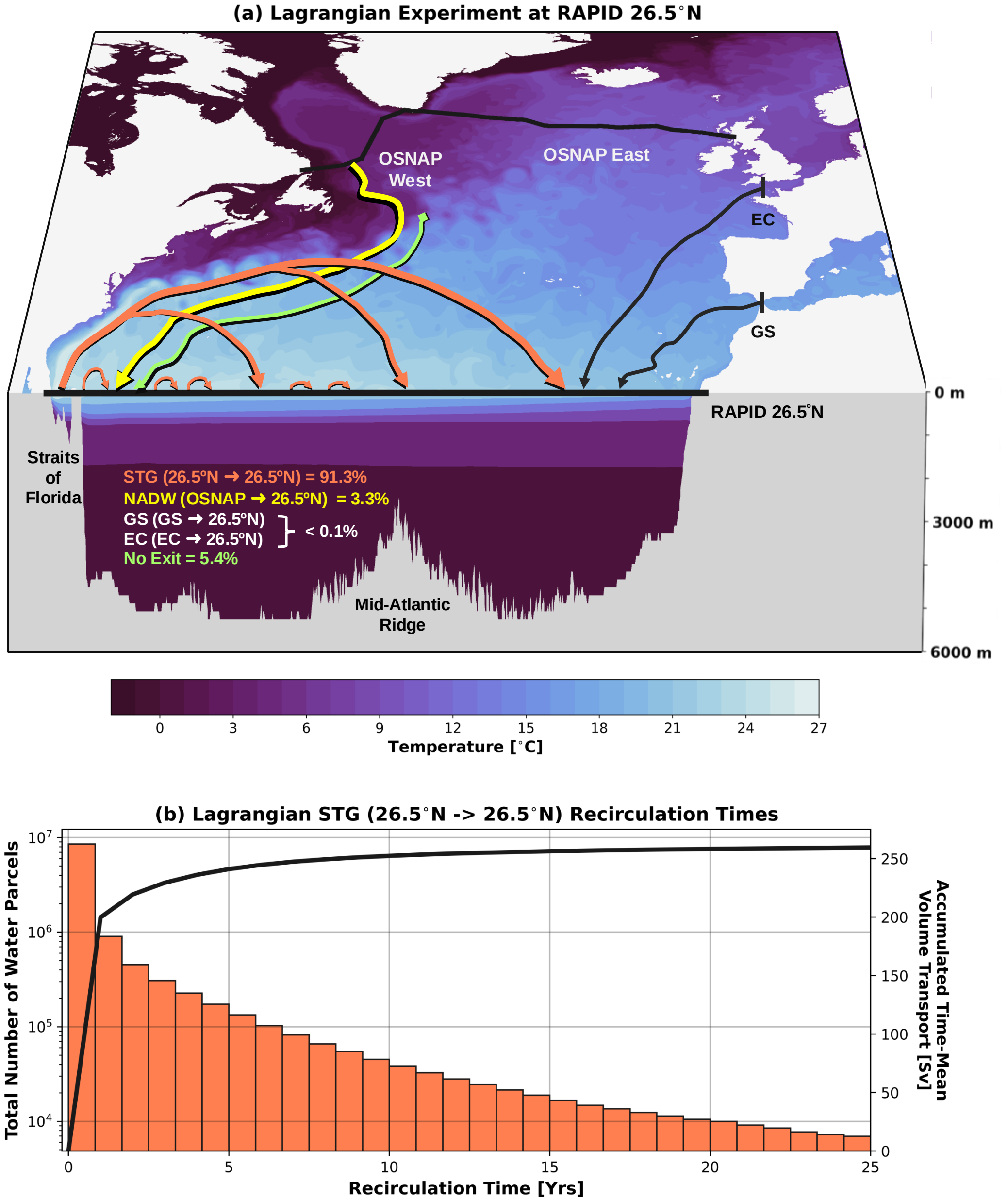

(a) Lagrangian Experiment at RAPID 26.5°N

(b) Lagrangian STG (26.5°N -> 26.5°N) Recirculation Times

Figure 5.1: (a) Schematic representation of the Lagrangian pathways north of the RAPID array at 26.5°N. Pathways originating from the English Channel (EC) and the Gibraltar Strait (GS) are shown in black. (b) Distribution of recirculation times for STG water parcels returning to 26.5°N within the 25-year maximum advection period. The solid black line overlaid shows the accumulation of the time-mean volume transport (Sv) of the STG pathway as a function of water parcel recirculation time.

Throughout this Chapter, we compare the results derived from the ORCA0083-N06 simulation to observations made along the RAPID array at 26.5°N for the overlapping period 2004-2015 (Johns et al., 2023a). To ensure consistency between model and observational diagnostics, we implement a zero net volume transport constraint across 26.5°N, equivalent to that imposed by the RAPID program (e.g., Kanzow et al., 2010), in all Eulerian meridional overturning and heat transport calculations.

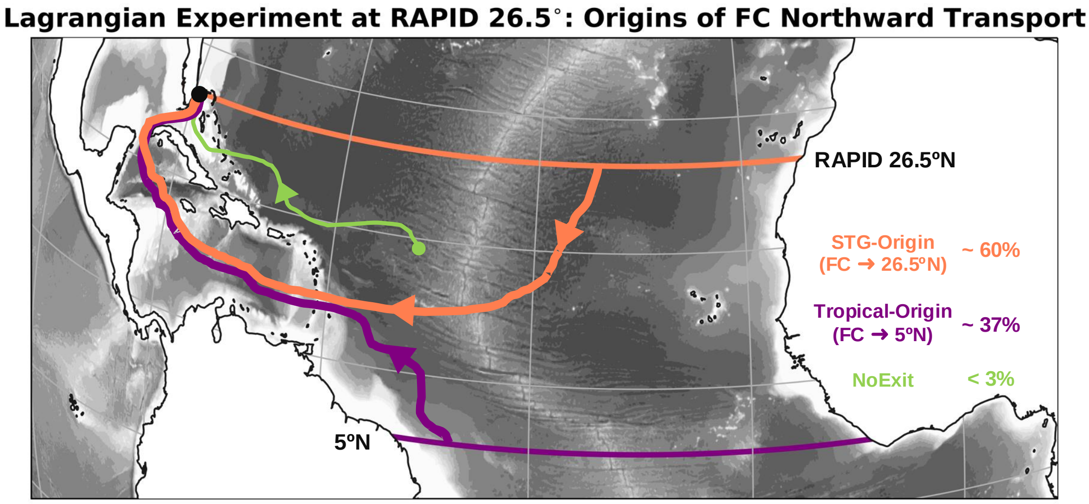

Figure 5.2: Schematic representation of the Lagrangian experiment used to determine the origins of water parcels flowing northward in the Florida Current (FC, indicated by the black dot along RAPID 26.5°N). Water parcel trajectories, sampling the full-depth northward transport of the FC, are advected backwards-in-time for a maximum of 25 years or upon returning to the RAPID 26.5°N array within the Subtropical Gyre (STG-origin, orange) or transiting to the trans-basin section along 5°N (Tropical North Atlantic-origin, purple). Note that less than 3% of all water parcels initialised within the FC remain within the experiment domain following their 25-year maximum advection time (NoExit, green).

5.2.2 Lagrangian Particle Tracking

To determine the contributions of the STG and the basin-scale overturning circulation to the total MHT at 26.5°N, we calculate the Lagrangian trajectories of virtual water parcels advected by the time-evolving velocity fields of the ORCA0083-N06 hindcast using TRACMASS version 7.1 (Aldama-Campino et al., 2020).

To compare the results of our Lagrangian experiment with observations made along 26.5°N, we track water parcels flowing southward across the RAPID section backwards-in-time to determine their origin. In total, we initialise more than 12.3 million water parcels sampling the full-depth southward transport across 26.5°N over 144 months between 2004-2015. At the beginning of each month, the number of water parcels to be distributed evenly across each grid cell face

(N_{gc}) is determined using Eq. 2.2.2. To ensure that we initialise a sufficiently large number of water parcels to obtain robust Lagrangian statistics (Jones et al., 2016), we compare the results of a subset of our primary Lagrangian experiment (Jan-Dec 2004) to a repeat of this experiment, in which we used a considerably smaller maximum volume transport of 1 mSv per parcel. We find that the time-mean MHT and overturning associated with the STG circulation is unchanged by increasing the number of water parcels initialised along 26.5°N and, hence, the conclusions of this Chapter are insensitive to the chosen "Lagrangian resolution" (Döös et al., 2008) of our primary experiment.

Water parcels are advected backwards-in-time using 5-day mean velocity fields for a maximum of 25 years to trace their origins. Water parcel trajectories are terminated on reaching this maximum advection time or when they meet any one of the following criteria (Fig. 5.1a): (i) returning to the RAPID 26.5°N section, (ii) reaching the OSNAP array in the SPNA, or (iii) reaching either the Gibraltar Strait (GS) or English Channel (EC). The overwhelming majority of trajectories initialised across 26.5°N also originate from 26.5°N (91.3%), indicating a robust recirculation of waters at this latitude. This large recirculating transport is dominated by short-lived trajectories capturing eddy recirculations in the ocean interior (197.3 ± 22.0 Sv), whereas only 20.6 ± 3.0 Sv is sourced directly from the Florida Current at 26.5°N. Importantly, Figure 5.1b shows that the 25-year maximum advection time is sufficient to fully resolve the STG circulation because the accumulated volume transport originating from 26.5°N has stabilised within this period.

We perform an additional Lagrangian experiment to determine the origins of the northward Florida Current transport by tracking trajectories backwards-in-time from the Florida Straits (see Fig. 5.2). We use the same water parcel initialisation and advection strategy outlined above for consistency. In this experiment, we terminate water parcel trajectories on crossing one of two geographic boundaries (5°N or 26.5°N in Fig. 5.2) or upon reaching the 25-year maximum advection time ($<$ 3% of the northward Florida Current transport).

5.2.3 Diagnosing Meridional Overturning and Heat Transport at 26.5°N

We quantify the strength of the Eulerian overturning at 26.5°N by calculating meridional overturning stream functions in both depth (ψ_z) and density (ψ_{σ_θ}) coordinates as shown in Section 1.4.1:

$$\psi_z(z,t) = \int_z^{\eta} \int_{x_w}^{x_e} v(x,z',t)\; dx\; dz' \tag{5.1}$$

$$\psi_{\sigma_\theta}(\sigma_\theta,t) = \int_{x_w}^{x_e} \int_{z(x,\sigma_\theta,t)}^{\eta} v(x,z',t)\; dz'\; dx, \tag{5.2}$$

where $v(x,z,t)$ is the meridional velocity and $z(x,\sigma_\theta,t)$ is the time-evolving depth of the isopycnal σ_θ across the trans-basin section between the eastern (x_e) and western (x_w) boundaries. We account for the time-evolving net volume transport across the section using a spatially uniform compensating meridional velocity (Kanzow et al., 2010).

The northward MHT across 26.5°N is calculated following Moat et al. (2016) by integrating the product of the meridional velocity $v(x,z,t)$ and potential temperature (θ) from the sea surface η to the sea floor $H(x)$:

$$Q_{Total}(t) = \int_{-H(x)}^{\eta} \int_{x_w}^{x_e} \rho_o c_p\; v(x,z,t)\; \theta(x,z,t)\; dx\; dz \tag{5.3}$$

where the product of the seawater density and the specific heat capacity of seawater is given by $\rho_o c_p = 4.1\text{x}10^6$ J m^{-3} °C^{-1} following Johns et al. (2011). We further partition the total MHT across the RAPID section (Q_{Total}) into horizontal (Q_{horz}) and vertical (Q_{vert}) components (Bryden & Imawaki, 2001; Johns et al., 2011) as introduced in Section 1.4.1:

$$Q_{vert}(t) = \int_{-H}^{0} \int_{x_w}^{x_e} \rho_o c_p\; \langle v \rangle \langle \theta \rangle\; dx\; dz \tag{5.4}$$

$$Q_{horz}(t) = \int_{-H}^{0} \int_{x_w}^{x_e} \rho_o c_p\; v'(x,z,t)\; \theta'(x,z,t)\; dx\; dz \tag{5.5}$$

where $\langle v \rangle$ and $\langle \theta \rangle$ represent the zonally averaged velocity and potential temperature profiles (both functions of depth), and v' and θ' represent deviations from these zonally averaged profiles.

To complement the Eulerian diagnostics outlined above, we additionally quantify the strength of overturning and MHT across 26.5°N from the Lagrangian water parcel trajectories initialised between 2004-2015. To determine the vertical and diapycnal overturning taking place within the STG, we consider only the subset of water parcels which return to 26.5°N within the $\tau_{max} =$ 25-year maximum advection period. For each monthly ensemble containing $N(t)$ water parcels, which flow northward across 26.5°N at time $t - \tau_{out}$ (where τ_{out} is the water parcel termination time) and return southward across the section at the later time t, we calculate partial Lagrangian overturning stream functions following Section 3.2.3:

$$F_z(z^*, t) = \sum_{z=z_{min}}^{z^*} V_{North,z}(t - \tau_{out}) - V_{South,z}(t) \tag{5.6}$$

$$F_{\sigma_\theta}(\sigma_\theta^*, t) = \sum_{\sigma_\theta=\sigma_{min}}^{\sigma_\theta^*} V_{North,\sigma_\theta}(t - \tau_{out}) - V_{South,\sigma_\theta}(t) \tag{5.7}$$

where V_{North} and V_{South} represent the absolute volume transport distributions of all recirculating STG water parcels on their northward and southward crossings of the RAPID 26.5°N.

Since Döös et al. (2008) showed that, provided a sufficiently large number of water parcels are initialised, the total Lagrangian overturning stream function will converge towards the time-mean Eulerian stream function, it follows that the time-mean overturning of the NADW and AABW cells can be estimated by calculating the residual between the time-mean total Eulerian overturning stream function and the Lagrangian overturning stream function of the the STG (i.e., $\overline{\psi_{\sigma_\theta}} - \overline{F_{\sigma_\theta}}$). An important consideration when using Lagrangian water parcel trajectories to decompose the Eulerian overturning is the choice of time-averaging window to use when calculating the time-mean Eulerian overturning stream function ($\overline{\psi_{\sigma_\theta}}$). Here we seek a time window that optimises the sampling of the meridional velocity and potential density field along 26.5°N by water parcels recirculating in the STG. Given that more than 90% of STG water parcels return to 26.5°N within 4 years of their initialisation (Fig. 5.1b), we use the time-mean Eulerian overturning averaged over 2000-2015 in our Lagrangian decomposition.

We additionally define a Lagrangian measure of the heat transport due to the $N(t)$ water parcels recirculating within the STG using their potential temperatures on their northward ($\theta_{North,n}$) and southward ($\theta_{South,n}$) crossings of the RAPID section at 26.5°N:

$$Q_{STG}(t) = \rho c_p \sum_{n \in N} V_n \left(\theta_{North,n}(t - \tau) - \theta_{South,n}(t)\right) \tag{5.8}$$

where V_n is the volume transport conveyed by an individual water parcel with index n returning to 26.5°N, which is conserved along its entire trajectory.

5.3 Results

5.3.1 Evaluating Eulerian Meridional Overturning and Heat Transport at 26.5°N

We begin by adopting the traditional Eulerian frame of reference to compare the meridional overturning and heat transport simulated in ORCA0083-N06 to RAPID observations between 2004-2015. Although there is strong agreement between the modelled and observed time-mean vertical overturning stream functions at 26.5°N (see Fig. 5.3), Figure 5.3b shows that the simulated 15.1 ± 2.8 Sv of vertical overturning is around 2 Sv weaker than observed (17.0 ± 3.6 Sv).

Figures 5.4a-b present equivalent decompositions of the Eulerian heat transport across 26.5°N in both RAPID observations and the ORCA0083-N06 hindcast. Concordant with its weaker than observed overturning, the model time-mean MHT is 0.98 ± 0.21 PW compared with 1.2 ± 0.28 PW in observations. The model does, however, reproduce many features of the overturning and heat transport variability recorded in observations (Moat et al., 2016), including the reduction in overturning between 2009-2010 (McCarthy et al., 2012). Observations show that both the magnitude and variability of the MHT at 26.5°N is dominated ($>$ 90%) by the vertical component, while $<$ 10% is associated with the horizontal circulation (Johns et al., 2011; Johns et al., 2023b; McCarthy et al., 2015b). Figure 5.4b shows a similar vertical-horizontal partition in ORCA0083-N06; the vertical

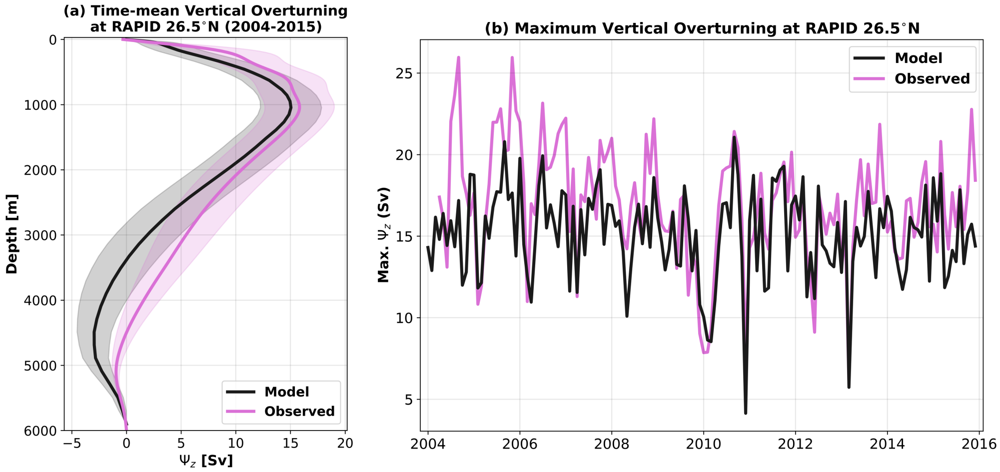

Figure 5.3: (a) Model (black) and observed (pink) time-mean (2004-2015) Eulerian vertical overturning streamfunctions calculated at RAPID 26.5°N. Shading denotes the (monthly) standard deviation of the modelled and observed time-mean vertical overturning stream functions. (b) Monthly-mean modelled (black) and observed (pink) maximum Eulerian vertical overturning at 26.5°N.

cell accounts for 85% (0.84 ± 0.21 PW), and the horizontal cell for the remaining 15% of the total MHT.

A closer examination of the simulated hydrography along 26.5°N shows that both the volume transport (31.3 ± 1.8 Sv) and temperature transport (2.56 ± 0.14 PW) of the Florida Current are well represented in the model compared with observed estimates reported in Meinen et al. (2010) and Johns et al. (2023b). However, Moat et al. (2016) highlighted the larger than observed southward Mid-Ocean (WB2 mooring to Africa) heat transport component in ORCA0083-N06 as a likely source of the model's underestimation of the observed total MHT. Further investigation indicates that, in the model, more of the warm and shallow waters transported northwards in the Florida Current are returned in the upper 100 m of the Mid-Ocean region along the RAPID array compared with observations (Fig. 5.4c). This is in contrast to previous studies, which have attributed the widespread underestimation of subtropical MHT in numerical models (e.g., Liu et al., 2022) to the overly diffusive thermocline simulated in z-coordinates (Msadek et al., 2013; Roberts et al., 2020), which results in a warmer than observed AMOC lower limb. Notably, there is good agreement between the basin-wide average potential

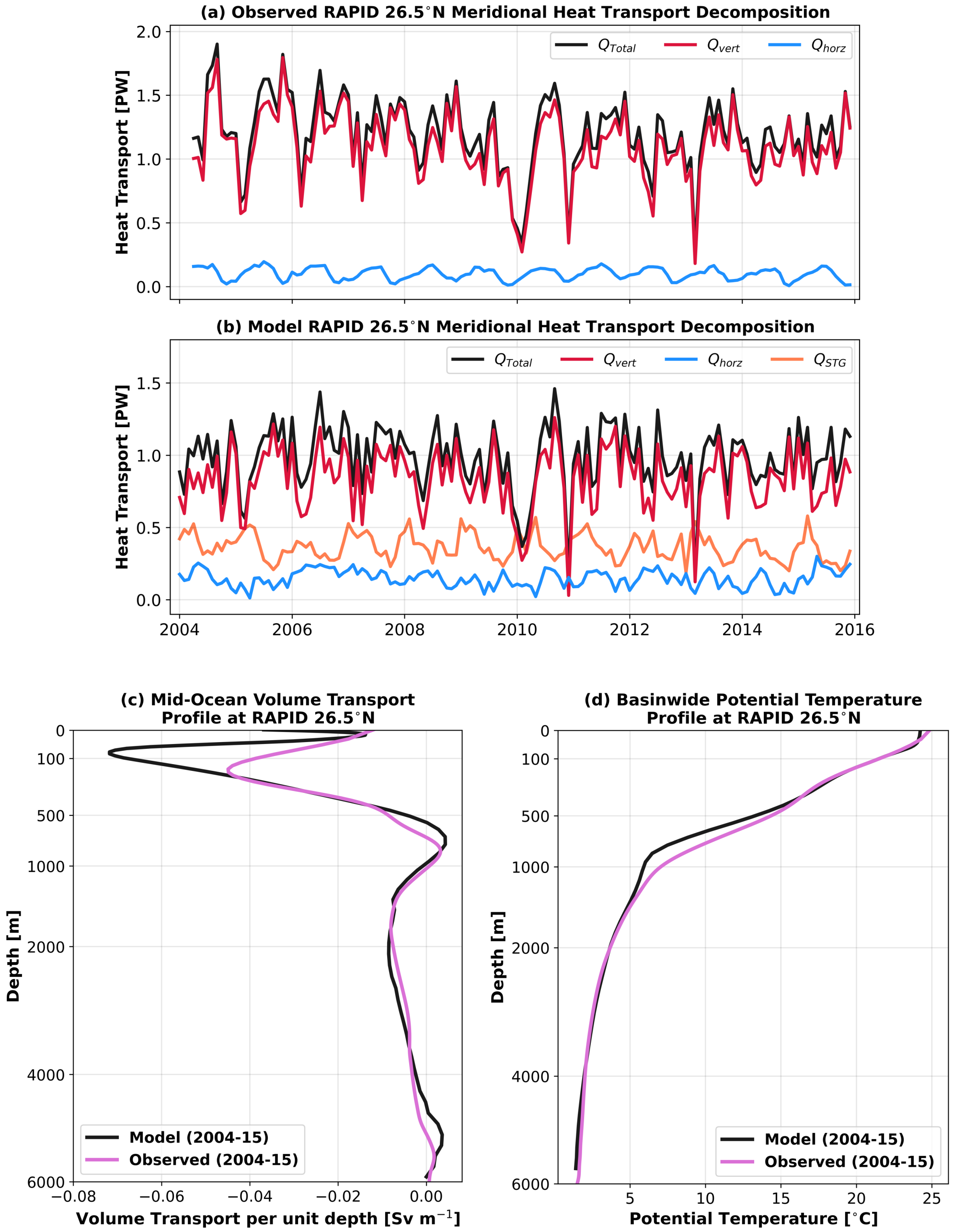

Figure 5.4: (a) Total observed MHT (black) at 26.5°N decomposed into a zonally-averaged vertical cell (Q_{vert}, red) and a residual horizontal cell (Q_{horz}, blue). (b) As in (a) but calculated using model Eulerian meridional velocity and potential temperature fields at 26.5°N. The STG heat transport calculated using recirculating trajectories (Q_{STG}, orange) is plotted according to the month water parcels flow southward across 26.5°N. (c) Model (black) and observed (pink) time-mean (2004-2015) meridional volume transport per unit depth (Sv m^{-1}) in the Mid-Ocean region (Bahamas to Africa). (d) Time-mean (2004-2015) potential temperature profiles (°C) for the entire basin (Straits of Florida to Africa) in the model (black) and RAPID observations (pink). Note that we use non-linear vertical axes in (c) and (d) to highlight the upper 500 m.

temperature profiles simulated in ORCA0083-N06 and observed along the RAPID array (Fig. 5.4d), with even a slightly sharper main thermocline (between depths of 400-800m) in the model than in observations.

Since we propose that the excess shallow return flow in the STG accounts for the model's underestimation of MHT compared with RAPID observations, we next consider how this bias might influence the relative contribution of the STG circulation to total MHT across 26.5°N. By examining the Lagrangian trajectories sourced from the upper Florida Current, we determine that rapidly recirculated water parcels return southward in the upper 100 m of the Mid-Ocean region between 75.5°W and 72°W (Fig. 5.5a) where potential temperatures typically exceed 23°C. We will later show that STG water parcels flowing southward across 26.5°N in this potential temperature range contribute negligibly to the time-mean MHT when averaged on longer than seasonal timescales (see Fig. 5.5d). As such, we do not expect the underestimation of MHT in ORCA0083-N06 to impact the relative heat transport contributions of the STG and basin-scale overturning circulations identified in this study.

Overall, we find sufficient agreement between the structure and variability of both the vertical overturning and MHT simulated by ORCA0083-N06 and observations to justify our use of the model to better understand the contributions made by the STG and basin-scale overturning circulation to the MHT at RAPID 26.5°N.

5.3.2 Lagrangian Decomposition of Meridional Overturning and Heat Transport at 26.5°N

To complement the traditional Eulerian vertical-horizontal decomposition, we use our Lagrangian trajectories to quantify the contribution made by water parcels which recirculate in the STG to the time-mean MHT at 26.5°N. We find that the STG circulation accounts for 0.36 ± 0.09 PW or 37 ± 9% of the total MHT across 26.5°N in the model (Fig. 5.4b). This implies that the heat transport of the STG is more than twice that of the horizontal gyre heat transport component and is in closer agreement with the observed estimate of 0.4 PW at 24°N (Talley, 2003). Figure

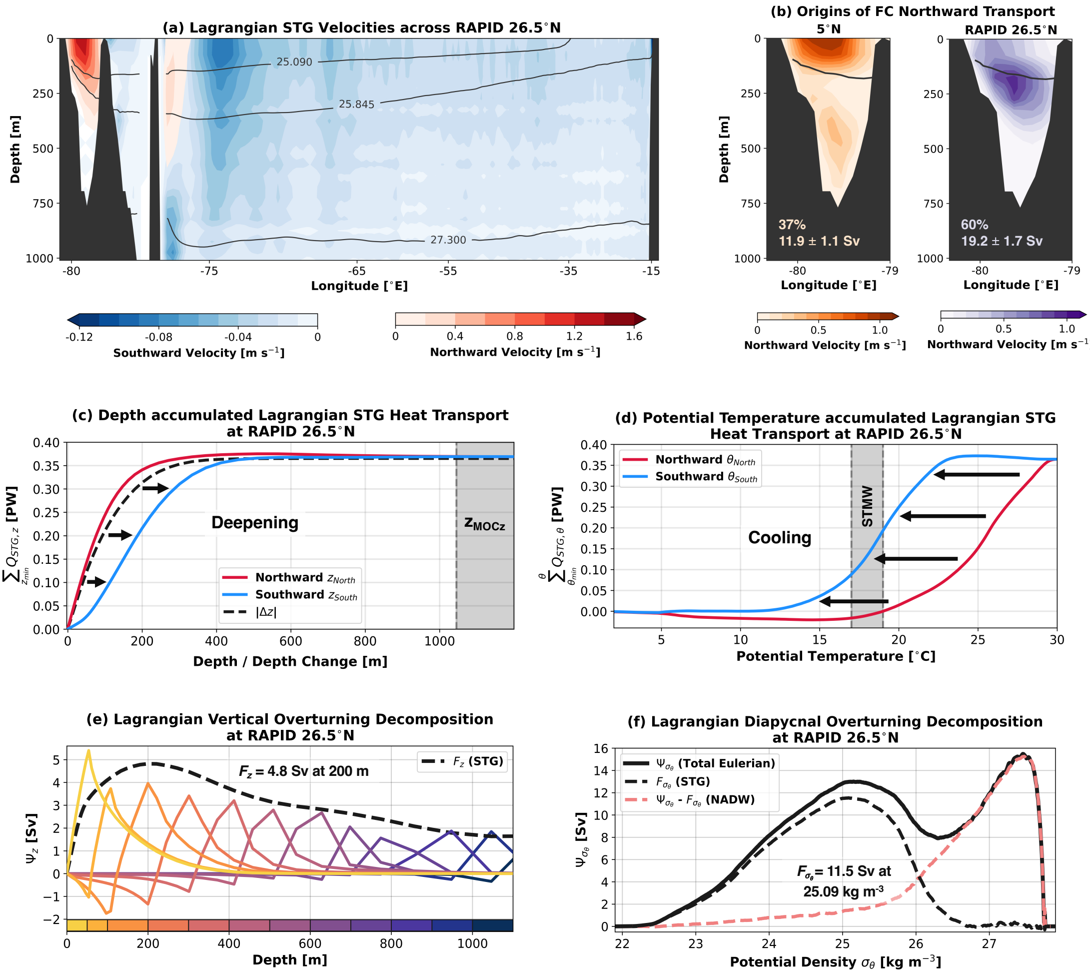

Figure 5.5: (a) Distribution of STG water parcel northward (red contours) and southward (blue contours) crossings of the RAPID 26.5°N section shown as the velocity of water parcels in m s^{-1}. Note that the longitude axis is stretched to highlight the Florida Current. (b) Origins of the Florida Current (FC) northward transport shown as the velocity (m s^{-1}) of waters parcels sourced from the tropical North Atlantic (5°N) and the STG recirculation (RAPID 26.5°N). The σ_θ = 25.09 kg m^{-3} time-mean isopycnal surface is overlaid. Heat transport of the STG circulation accumulated as a function of the (c) depth and (d) potential temperature of recirculating water parcels on their northward (red) and southward (blue) crossings of 26.5°N. The black dashed line in (c) represents the STG heat transport accumulated as a function of the absolute depth change between crossings of 26.5°N. The depth of maximum Eulerian overturning in depth-space, z_{MOC} = 1045 m is indicated by the grey dashed line in (c). The shaded region in (d) defines STMW (17-19°C) following Kwon and Riser (2004). (e) Time-mean (2004-2015) vertical overturning stream function of the STG circulation (F_z, black dashed) decomposed according to the depth of water parcels on their northward crossing of 26.5°N. Water parcels are grouped into discrete depth layers defined in the lower colorbar. (f) Lagrangian decomposition of the time-mean (2004-2015) diapycnal overturning stream function at 26.5°N ($\bar{\psi}_{\sigma_\theta}$, black solid) into a STG component ($\bar{F}_{\sigma_\theta}$, black dashed), determined from recirculating water parcels, and a residual NADW component ($\bar{\psi}_{\sigma_\theta}$ - $\bar{F}_{\sigma_\theta}$, pink dashed).

5.5a additionally confirms the assumption of Talley (2003) that the lightest waters flowing northward in the upper Florida Current ($\sigma_\theta < 25.875$) are returned across 26.5°N via the broad southward interior flow ($\sigma_\theta < 27.3$) between the Bahamas and Africa. In total, we find that 72% of STG heat transport is sourced from water parcels flowing northward in the upper 150 m of the Florida Current, which overwhelmingly originate from the tropical North Atlantic (5°N in Fig. 5.5b). Further, Figure 5.5b clearly shows that the thermocline waters flowing northward in the Florida Current are predominantly sourced from the STG along 26.5°N.

Figures 5.5c-d show how the time-mean MHT of the STG is accumulated as a function of the depth and potential temperature of water parcels on their northward (red) and southward (blue) crossings of the RAPID 26.5°N array. For example, we produce the red curve in Figure 5.5c by binning the MHT of all recirculating water parcels according to their depth on flowing northward across RAPID 26.5°N before calculating the cumulative sum with increasing depth. We find that STG heat transport is dominated by water which participate in a shallow vertical overturning cell north of 26.5°N (Fig. 5.5c). More specifically, Figures 5.5c-d show that the entire MHT of the STG can be explained by trajectories which follow a downwards cooling spiral within the upper 500 m of the AMOC upper limb ($z_{MOC} \leq$ 1045 m). Interestingly, although STG heat transport depends strongly on along-stream diapycnal (diathermal) transformation, STMW formation can only account for 29% of the total MHT of the STG (17°C $\leq \theta_{South} \leq$ 19°C in Fig. 5.5d). Diapycnal transformation within the STG instead peaks at lighter density classes ($\theta \approx$ 22.7°C or $\sigma_\theta =$ 25.09 kg m^{-3} in Fig. 5.5f), including Subtropical Underwater (STUW; O'Connor et al., 2005), which accounts for 47% of the STG heat transport ($\theta_{South} >$ 19°C in Fig. 5.5d).

A particularly surprising finding is the large 6.7 Sv discrepancy between the strength of vertical (4.8 Sv in Fig. 5.5e) and diapycnal (11.5 Sv in Fig. 5.5f) overturning in the STG. Previous studies in the subpolar North Atlantic have interpreted the similar discrepancy there as evidence for a substantial horizontal circulation across sloping isopycnals (Zhang & Thomas, 2021). However, Figure 5.5e reveals that here in the subtropical North Atlantic, this discrepancy is, in fact, due to the underestimation of STG vertical overturning, which results from compensation between the northward and southward flowing limbs of the downward spiral when accumulated along constant depth levels. This is analogous to the large, compensating depth-space transports within the Deacon cell in the Southern Ocean (Döös & Webb, 1994) and illustrates how the downward spiralling behaviour of the STG circulation (Berglund et al., 2022) is concealed by the superposition of many shallow overturning cells in the vertical overturning stream function (Fig. 5.5e; Döös et al., 2008).

By subtracting the diapycnal overturning associated with STG water parcels from the time-mean Eulerian overturning stream functions in Figures 5.5f and 5.6a, we obtain an estimate for the contribution of the NADW cell to the total overturning in density-space at 26.5°N. The residual diapycnal overturning stream functions, in combination with Figure 5.5b (RAPID 26.5°N), confirm the earlier propositions of Burkholder and Lozier (2014) and Qu et al. (2013) that the mode waters returned in the southward limb of the shallow STG overturning cell are the principal source waters for the northward, subsurface limb of the NADW cell. Meanwhile, the remainder of the NADW cell is sourced directly from denser waters ($\sigma_\theta > 26.5$ kg m^{-3}) originating in the tropical North Atlantic, which flow northward across 26.5°N at depth in the Florida Current (Fig. 5.5b).

5.4 Discussion & Conclusions

In this Chapter, we present the first Lagrangian decomposition of the meridional overturning and heat transport at 26.5°N using an eddy-rich ocean hindcast. We show that water parcels circulating around the STG account for 37% (0.36 PW) of the total MHT across 26.5°N, more than twice that of the classical horizontal gyre component (15%). This underestimation of STG heat transport is attributable to the downward spiralling nature of the STG recirculation (Berglund et al., 2022; Spall, 1992), which imprints onto a shallow vertical overturning cell rather than the horizontal circulation across 26.5°N.

Our Lagrangian analysis demonstrates that the MHT of the STG overturning cell is analogous to a subtropical mode water cascade (Blanke et al., 2002) in which water parcels arriving in the upper Florida Current are successively transformed towards intermediate densities via a downwards cooling spiral (Spall, 1992). The spiral begins with the convective formation and lateral subduction of STUW varieties (O'Connor et al., 2005; Qu et al., 2016), which account for 47% of STG heat transport. The subsequent transformation of recirculating STUW into STMW via intense wintertime cooling along the path of the Gulf Stream (e.g., Joyce et al., 2013) surprisingly explains less than a third of STG heat transport. The downwards cooling spiral, which typically spans several decades (Berglund et al., 2022), concludes when STG water parcels reach the required depth ($z > 200$ m) and density ($\sigma_\theta > 25.5$ kg m^{-3}) to be exported northward in the subsurface limb of the NADW cell (Fig. 5.5f).

In contrast to the STG overturning cell, the NADW cell spans both subtropical and subpolar latitudes (Fig. 5.6a), because the weaker potential vorticity gradient across the Gulf Stream at depth permits water parcels to be advected north-eastward via the subsurface pathways of the NAC (Bower & Lozier, 1994; Burkholder & Lozier, 2011b; Gary et al., 2014; Jacobs et al., 2019). The northward subsurface branch of the NADW cell was arguably first identified as a 'nutrient stream' from the biogeochemical observations of Pelegrí and Csanady (1991). This nutrient stream plays a fundamental role in maintaining biological productivity at high latitudes by transporting large concentrations of nutrients along shoaling isopycnals which outcrop within the eastern SPG (Williams et al., 2011). There are two important implications of this subsurface subtropical to surface subpolar connectivity (Burkholder & Lozier, 2014). Firstly, water parcels flowing northward in the NADW cell experience negligible heat loss prior to reaching the southern limit of the SPG (~47°N in Fig. 5.6b) and hence the heat transport divergence between 26.5°N and the inter-gyre boundary is equivalent to the STG heat transport (0.36 PW). Secondly, no inter-gyre pathway exists for sea surface temperature anomalies originating in the Gulf Stream to propagate advectively towards the eastern SPG (Foukal & Lozier, 2016). Instead, upper ocean thermohaline anomalies advected by the large-scale circulation in the SPNA are likely to originate from variations in the strength of the sub-surface to surface connectivity between the subtropical and subpolar gyres (e.g., Bryden et al., 2020; Chafik et al., 2023; Desbruyères et al., 2021), which manifest via predominantly geostrophic changes in MHT convergence (Moat et al., 2024). This also highlights the central challenge of inferring large-scale circulation from Eulerian overturning stream functions since the streamlines presented in Figure 5.6a misleadingly suggest a continuous meridional pathway from the lightest to the densest water masses in the North Atlantic while, in fact, there are two overlapping diapycnal cells, which are, themselves, the superposition of many smaller overturning cells.

Although the strength of our conclusions is limited by the use of a single eddy-rich ocean hindcast, we note the strong agreement between our findings and those of Ferrari and Ferreira (2011), who used model sensitivity experiments to show that 40% of North Atlantic MHT is associated with the wind-driven STG circulation, whereas the remaining 60% is due to high latitude convection. Moreover, when our estimate of STG heat transport (37%) is applied to observations along 26.5°N, this translates to 0.44 PW of the total 1.2 PW due to the STG circulation, which is in remarkable agreement with the 0.42 PW (35%) estimated by Johns et al. (2023b) when applying the approach of Talley (2003) to RAPID observations. The remaining 0.76 PW (63%) of the total observed MHT across 26.5°N is due to the formation of NADW within the SPG and the Nordic Seas. These two regions exhibit complex overturning geometries, with a substantial fraction of dense water formation owed to horizontal circulation across sloping isopycnals (Hirschi et al., 2020; Xu et al., 2018b; Zhang & Thomas, 2021).

In contrast to the traditional conveyor-belt view of North Atlantic overturning, our Lagrangian analysis demonstrates that both vertical and horizontal circulation cells are fundamental components of the AMOC and thus basin-scale overturning cannot be meaningfully distinguished from the gyre circulations of the North Atlantic (Fig. 5.6c). A more natural decomposition of the AMOC is between the STG and NADW diapycnal overturning cells shown in Figure 5.6a since these capture the successive transformations required to form dense NADW from the lightest waters flowing northward in the Florida Current. Extending the Lagrangian analysis presented here to reveal the phenomenology of overturning variability within each of these circulation cells and their interconnectivity across timescales is the subject of future research.

In this Chapter, we have shown that water parcels recirculating in the STG in an eddy-rich ocean model account for 37% (0.36 PW) of the total MHT across 26.5°N, more than twice that of the classical horizontal gyre component. This disparity reflects the fact that the heat transport of the STG is associated with shallow vertical overturning rather than the horizontal circulation north of 26.5°N. Our findings indicate that the STG plays a critical role in the basin-scale overturning circulation since the water parcels preconditioned within the gyre subsequently feed regions of dense water formation at high-latitudes.

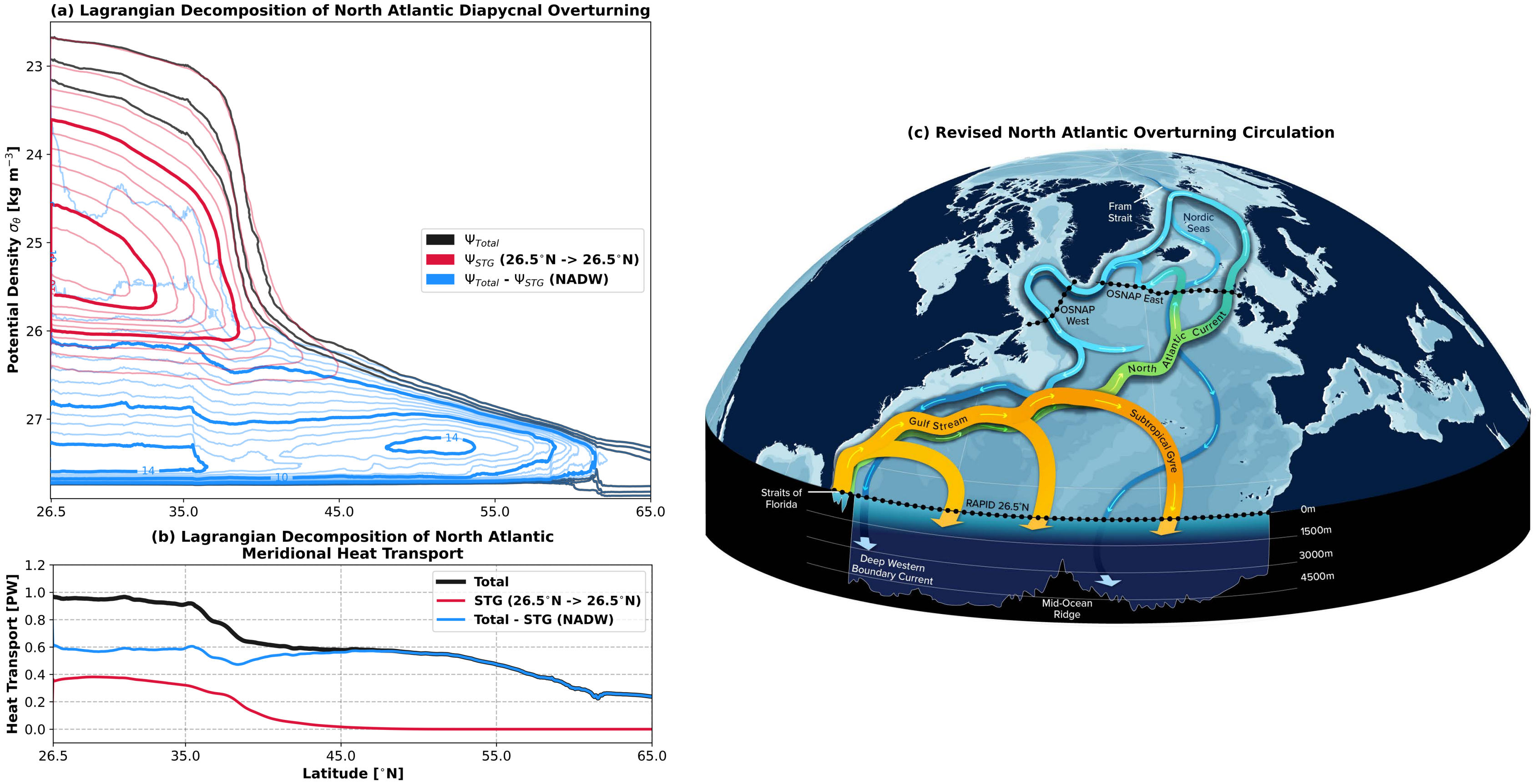

Figure 5.6: (a) Lagrangian decomposition of the time-mean (2000-2015) North Atlantic Ocean diapycnal overturning stream function north of RAPID 26.5°N into a STG component (red), derived from recirculating water parcel trajectories, and a residual component (NADW cell, blue). Selected streamlines (1-3 Sv) of the total Eulerian overturning stream function are overlaid in black. (b) Lagrangian decomposition of the latitudinal distribution of the time-mean North Atlantic Ocean MHT (black) into the contributions of the STG cell (red) and residual NADW cell (blue). (c) Schematic depicting the principal circulation components of the Atlantic Meridional Overturning Circulation (AMOC) north of the RAPID 26.5°N section.

6
Conclusions

6.1 Summary

In this thesis, we set out to generate new insights into the nature of the meridional overturning circulation in the North Atlantic Ocean by introducing a novel Lagrangian framework to analyse numerical model simulations. Our objectives were to: quantify the principal pathways and advective timescales of the subpolar overturning circulation, identify the physical mechanisms responsible for subpolar overturning variability on seasonal to multi-decadal timescales, assess the predictability of dense water formation along the path of the SPG and diagnose the contribution of the STG circulation to the meridional overturning and heat transport at 26.5°N.

We began in Chapter 2 by exploring how the time-mean strength of the AMOC in the eastern subpolar North Atlantic is partitioned amongst the individual circulation pathways of the SPG and the Nordic Seas overflows. To do this, we evaluated the Lagrangian trajectories of water parcels sampling the full-depth northward transport across the OSNAP East section in an eddy-permitting ocean sea-ice hindcast. By calculating the time-mean Lagrangian diapycnal overturning stream function (Blanke et al., 1999; Döös et al., 2008) at OSNAP East, we showed that dense water formation along the pathways of the eastern SPG accounts for

55% of the time-mean strength of the eastern subpolar AMOC. We found that water parcels following the dominant SPG pathway, sourced from the Sub-Arctic Front, form upper NADW by circulating horizontally across sloping isopycnals in less than 2 years. Meanwhile, a slower SPG route, entrained by overflow waters south of the Iceland-Faroes Ridge, was identified as a crucial conduit for subtropical-origin water masses to penetrate the deep ocean on subdecadal timescales.

On reproducing our findings using time-averaged velocity and tracer fields, we further showed that the Nordic Seas overflow pathways integrate multiple decades of water mass transformation before returning southward across the Greenland-Scotland Ridge. We therefore proposed that the strong disparity between the typical advective timescales of the SPG (seasonal-interannual) and the Nordic Seas overflows (multi-decadal) has important implications for the propagation of density anomalies within the eastern subpolar North Atlantic and hence the sources of AMOC variability.

In Chapter 3, we extended the Lagrangian overturning framework to explore, for the first time, the circulation pathways responsible for seasonal diapycnal overturning variability in the eastern subpolar North Atlantic in both the Eulerian and Lagrangian frames of reference. Using the Lagrangian trajectories evaluated in Chapter 2, we showed that the seasonal cycle of Eulerian diapycnal overturning at OSNAP East reflects a complex combination of seasonal dense water formation along the western boundary of the Irminger Sea and the wind-driven modulation of water parcel recirculation times. In particular, we highlighted that the seasonal minimum of the Eulerian diapycnal overturning in autumn results from both enhanced stratification and a greater convergence of southward transport within the upper East Greenland Current, consistent with a gyre-scale response to seasonal wind forcing.

To account for the diversity of recirculation times within the eastern subpolar gyre, we also examined seasonal diapycnal overturning variability from a Lagrangian perspective by quantifying the total dense water formation along water parcel trajectories. We found that the majority of water parcels, sourced from the central and southern branches of the NAC, fail to return to OSNAP East prior to experiencing wintertime diapycnal transformation into the lower limb, and thus determine the time-mean strength of the Lagrangian diapycnal overturning within the eastern subpolar gyre (8.9 ± 2.2 Sv). In contrast, the strong seasonality of Lagrangian diapycnal overturning is explained by a small collection of upper limb water parcels, circulating rapidly ($\leq$ 8.5 months) in the upper Irminger and Central Iceland Basins, whose along-stream transformation is determined by their month of arrival flowing northward across OSNAP East.

Looking beyond seasonal timescales, Chapter 4 explored the mechanisms responsible for interannual to multi-decadal subpolar overturning variability by taking a Lagrangian perspective to determining how much dense water is formed as water parcels circulate around the SPG. To do this, we evaluated the trajectories of water parcels flowing northward across OSNAP East in the NAC until their final southward crossing of OSNAP West at 53°N in an eddy-rich ocean model. We showed that neither the transformation of water parcels across density surfaces, nor their initial properties on arrival into the eastern SPG, are the rate-limiting factor governing dense water formation. Instead, the amount of dense water formed along-stream can be skilfully predicted, based solely on the volume transport of light, upper limb waters arriving at OSNAP East via the branches of the NAC. More specifically, we found that 66% of upper limb water flowing northward is transformed into dense NADW on its first circuit around the SPG, with most of the remainder returning to OSNAP East to be transferred into the lower limb during subsequent circuits.

Using the simple theoretical model of Wåhlin and Johnson (2009), we demonstrated that the linear relationship between dense water formation and upper limb volume transport emerges since the SPG boundary current is long enough to be fully adjusted with respect to temperature, meaning that upper limb buoyancy anomalies (principally driven by temperature fluctuations) do not feed back onto the rate of dense water formation and hence the strength of subpolar overturning downstream. As a consequence, multi-decadal changes in subpolar overturning are closely related to the state of the SPG, such that a stronger SPG circulation results in a greater northward transport of upper limb waters and hence an increase in NADW formation along-stream.

Finally, in Chapter 5, we shifted our focus to the subtropical North Atlantic, where continuous measurements of meridional heat and volume transports have been made along the RAPID-MOCHA observing array at 26.5°N since 2004. Here, the meridional heat transport has traditionally been partitioned geometrically into vertical and horizontal circulation cells, which are attributed to the overturning and STG circulations, respectively. However, the assumption that the STG flows horizontally along constant depth levels remains widely debated, raising doubts over the utility of 2-dimensional geometric components to quantify the contributions made by the AMOC and the STG circulation to the total heat transport across 26.5°N. Using water parcel trajectories evaluated within an eddy-rich ocean hindcast, we presented the first Lagrangian decomposition of the time-mean meridional heat transport and overturning across 26.5°N. We showed that water parcels recirculating within the STG account for 37% (0.36 PW) of the total heat transport across 26.5°N, more than twice that of the classical horizontal gyre component (15%). This is because STG water parcels spiral downwards across depth levels. Moreover, we argued that the STG heat transport cannot be meaningfully distinguished from that of the large-scale overturning circulation since water parcels cooled within the gyre subsequently flow northward in the subsurface limb of the AMOC to form dense NADW at the subpolar latitudes.

6.2 Overarching Themes & Outstanding Questions

In this penultimate Section, we synthesise the findings of this thesis into four overarching themes and highlight several outstanding questions presenting opportunities for further research.

6.2.1 Challenges of Diagnosing the Atlantic Meridional Overturning Circulation.

Translating the complex, 3-dimensional circulation of the AMOC into a single diagnostic is a considerable challenge, particularly given that both observations and numerical models are typically defined in the Eulerian frame of reference. Since the development of the first ocean general circulation models (e.g., Bryan, 1986; Manabe & Stouffer, 1988), it has been standard practice to zonally integrate over the many complex flow structures comprising the AMOC by means of the Eulerian overturning stream function (Buckley & Marshall, 2016). However, this decision to condense the rich structure of the overturning circulation into a much simpler 2-dimensional representation comes at a significant cost.

The most notable cost comes from the loss of geographical information inherent in the construction of the Eulerian overturning stream function. For example, in Chapter 5, we showed that the streamlines of both vertical and diapycnal Eulerian overturning stream functions cannot be interpreted as circulation pathways, given that they suggest a continuous route for light, near-surface subtropical waters to form NADW at subpolar latitudes while, in-fact, waters must first be preconditioned via a downward cooling spiral within the STG (Berglund et al., 2022; Burkholder & Lozier, 2014; Gary et al., 2014). Additionally, when describing the Eulerian overturning, we should avoid conflating the upper and lower limbs diagnosed in depth and potential density coordinates (Foukal & Chafik, 2024), given that the coupling between vertical and diapycnal overturning cells is neither localised nor instantaneous at subpolar latitudes (Fraser et al., 2024).

A further challenge is how to interpret the extent to which the Eulerian overturning behaves like the meridionally coherent conveyor belt envisioned by Broecker (1991) versus a "stochastic collection of regional processes" (Frajka-Williams et al., 2023). An important innovation in this thesis has been to adopt a complementary Lagrangian perspective to diagnosing AMOC variability, in which we preserve the identity of water parcels following the flow. As such, the Eulerian and Lagrangian overturning diagnosed at a given time t represent two fundamentally different quantities. The Eulerian overturning represents the total northward transport in the upper limb, which is balanced by a compensating southward return flow in the instantaneous velocity field. Meanwhile, the Lagrangian overturning represents the total transformation along recirculating water parcel trajectories, which flow northward at some shared time t before returning southward at a range of later times $t + \tau_{out}$.

In spite of their differences, we have seen in Chapters 2 and 5 that the Eulerian and Lagrangian overturning stream functions converge when averaged over a sufficiently long timescale. This is because, on timescales typical of the advective circulation, the net northward transport in the upper limb at a given latitude must be balanced by the total transformation by air-sea fluxes and mixing along recirculating water parcel trajectories, north of that latitude. In other words, the timescale at which the Eulerian and Lagrangian overturning converge represents the timescale beyond which the AMOC behaves like a conveyor belt, and overturning variability can reflect coherent changes in the advective circulation. One important implication of this, is that the timescale of AMOC coherence is strongly dependent on the latitude at which the overturning is diagnosed, since this governs the typical advective timescale of recirculating water parcel trajectories.

On timescales shorter than the typical recirculation timescale, the Eulerian overturning no longer reflects coherent changes in the advective circulation, but rather locally and remotely forced imbalances between the inflows and outflows of light and dense water masses. For example, in a recent study led by Alejandra Sanchez-Franks, we found that high-frequency variability in the Eulerian diapycnal overturning observed at OSNAP East is closely related to the recirculation of existing lower limb water within the Irminger Gyre. In particular, we showed that weak diapycnal overturning results from a strengthening of the northward branch of the Irminger Gyre, which acts to reduce the net southward flow in the lower limb (Sanchez-Franks et al., 2024). Interestingly, numerical modelling studies utilising ensemble approaches have demonstrated that the OSNAP array is located close to a local maximum in the chaotic (initial-condition dependent) variability of the AMOC on sub-annual timescales (Germe et al., 2022; Hirschi et al., 2013), suggesting that observed high-frequency overturning variability may be much more stochastic than previously thought.

One approach to better understand the large, often compensating Eulerian overturning variability recorded on monthly to interannual timescales would be to identify the contributions of individual circulation pathways to the instantaneous northward and southward transports of the upper and lower limbs. Future studies could draw inspiration from the work of Desbruyères et al. (2013), who combined partial Lagrangian overturning stream functions calculated from forward and backward trajectories to investigate how decadal variability in the upper limb transport arriving into the eastern SPG is related to changes in the contributions of subpolar and subtropical-origin waters. It would be informative to extend this methodology to explore how seasonal to multi-decadal Eulerian overturning variability recorded along the OSNAP array is partitioned between the circulation pathways of the SPG and the Nordic Seas overflows.

6.2.2 Importance of Overturning Geometry

Throughout this thesis, we have seen that the complex geometry of the North Atlantic Ocean circulation plays a fundamental role in shaping the strength and variability of the overturning circulation captured in both the Eulerian and Lagrangian frames of reference.

From a Lagrangian perspective, we have shown that, since temperature and salinity adjust to air-sea fluxes and mixing on different length (time) scales (Wåhlin & Johnson, 2009), the propagation of buoyancy anomalies and hence the magnitude of dense water formation is closely related to the length and time scales of advection along a given circulation pathway. In the subpolar North Atlantic, we have seen that the boundary currents of the SPG and the Nordic Seas are long enough to be fully adjusted with respect to temperature, since there is sufficient time for temperature anomalies to be damped by air-sea heat fluxes downstream. However, neither boundary current is long enough to be fully adjusted with respect to salinity, meaning that salinity anomalies can persist to influence dense water formation downstream. This is consistent with observations, which suggest that salinity anomalies can propagate advectively around the SPG and the Nordic Seas (Belkin, 2004; Biló et al., 2022; Holliday et al., 2020), whereas temperature anomalies tend to be quickly damped by surface heat loss (Fan et al., 2023). By allowing for the persistence of salinity anomalies, the geometry of the subpolar overturning circulation is also directly implicated in the existence of the salt advection feedback (Rahmstorf, 1996; Stommel, 1961), which would not exist if the boundary currents of the subpolar North Atlantic were fully adjusted with respect to salinity.

The positioning of ocean observing systems relative to the local geometry of overturning also constrains the AMOC variability captured in the Eulerian frame of reference. For example, Fu et al. (2023) highlighted that the greater length of the OSNAP East array alongside its almost zonal orientation means that seasonal meridional Ekman transports have a much larger influence on seasonal overturning variability recorded at the section compared with that across OSNAP West. The proximity of ocean observing arrays to regions of dense water formation is also an important constraint on estimates of seasonal Eulerian overturning variability since this determines the export timescales of newly ventilated water masses (Fu et al., 2023; Holte & Straneo, 2017; Le Bras et al., 2020). However, in an upcoming study led by Gwyn Evans, we use the water mass transformation framework to challenge this proposition, demonstrating that, whilst the seasonal cycle of surface buoyancy-driven transformation is largely compensated by changes in the volume of dense water masses, overturning seasonality reflects local seasonal variations in the observed velocity and density fields along the OSNAP array.

A broader implication of the complex geometry of the North Atlantic circulation is that zonally-integrated decompositions of Eulerian heat and freshwater transports (e.g., Jones et al., 2024) cannot accurately reflect the contributions made by components of the large-scale circulation. This was clearly demonstrated in

Chapter 5, where we showed that the long-standing, geometric decomposition of the meridional heat transport at 26.5°N into a zonally-averaged vertical cell and residual horizontal cell does not meaningfully distinguish between the overturning and gyre circulations in the subtropical North Atlantic.

The typical approach of separating Eulerian property transports into horizontal and vertical components also extends far beyond the subtropics. For example, the vertical component of freshwater transport (F_{ov}) in the South Atlantic is widely considered to be an indicator of overturning stability (e.g., de Vries & Weber, 2005; Rahmstorf, 1996; Weber & Drijfhout, 2007), where a negative F_{ov} is indicative of a bistable AMOC. Previous studies have questioned the validity of the F_{ov} criterion (Buckley & Marshall, 2016; Gent, 2018), highlighting that changes in the horizontal component of freshwater transport, attributed to the wind-driven gyre circulation, often equal, if not exceed, that of the vertical component in hosing experiments (Mecking et al., 2016; Van Westen et al., 2024). However, we would further question whether identifying long-term trends in a diagnostic derived from simple box models (see review by Weijer et al., 2019) can tell us anything meaningful about the future stability of the AMOC, given the complex and interwoven nature of the gyre and overturning circulations highlighted throughout this thesis.

The geometry of the overturning circulation is arguably most complex at subpolar latitudes, where, in Chapter 4, we showed that the SPG circulation projects strongly onto the diapycnal overturning cell at eddy-rich resolution. A particularly intriguing question emerging from this thesis is: to what extent does this alignment between the SPG and diapycnal overturning circulations depend on numerical model resolution? Previous studies suggest that subpolar overturning geometry changes markedly from eddy-parameterised ($\sim$1°) to eddy-rich ($\sim$1/12°) resolution (e.g., Hirschi et al., 2020). In particular, a greater fraction of vertical overturning takes place at subpolar latitudes in eddy-parameterised compared with eddy-rich simulations (Marsh et al., 2009; Treguier et al., 2006), consistent with their dominant mode of dense water formation via unrealistically deep convective mixing (Heuzé, 2017, 2021). In contrast, at eddy-rich resolution, a substantial fraction of NADW formation occurs via the horizontal component of the SPG circulation across sloping isopycnals (Marsh et al., 2009; Xu et al., 2018b; Zhang & Thomas, 2021). In the future, it would prove fruitful to use the Lagrangian overturning framework developed in this thesis to undertake a comprehensive model inter-comparison exercise to better quantify how the pathways and advective timescales of the overturning circulation differ from eddy-parameterised to eddy-rich resolution.

6.2.3 Unresolved Scales in the North Atlantic Overturning Circulation.

One of the reasons that the geometry of overturning varies so greatly across OGCMs is that the AMOC is the net result of integrating ocean processes ranging from the submesoscale to the basin-scale (Jackson et al., 2023b). As a result, a consistent theme throughout this thesis has been the importance of unresolved scales in shaping the North Atlantic overturning circulation viewed from the Lagrangian frame of reference.

Within each Chapter, we have seen that one of the inevitable limitations of the Lagrangian overturning framework is its reliance on the fidelity of the model velocity and tracer fields used to generate water parcel trajectories. We can therefore distinguish between two major sources of error impacting Lagrangian overturning analyses. The first source of error results from the method used to evaluate water parcel trajectories (methodological error). Meanwhile, the second source of error results from the inability of OGCMs to perfectly represent the dynamics and flow structures of the real ocean (model error).

The primary source of methodological error impacting the Lagrangian overturning analyses presented in this thesis is the time-averaging period at which the model velocity and tracer fields are archived (Blanke et al., 2012). Even in the idealised case of having a perfect OGCM, the Lagrangian trajectories generated would be strongly dependent on the frequency at which we archive the mean model velocity and tracer fields, given that this would omit any variability occurring on timescales shorter than the chosen time-averaging period (MacGilchrist et al., 2020). Interestingly, previous studies suggest that the water parcel transit times and inter-connectivity between large-scale flow structures may be highly sensitive to the choice of time-averaging period (Blanke et al., 2012; Roach & Speer, 2019), with coarser time-averages found to produce slower and less chaotic trajectories.

Even in the absence of methodological errors resulting from Lagrangian particle tracking, many features of the flow field would still not be captured by water parcel trajectories because they are not resolved by our chosen OGCM. The ocean hindcasts used throughout this thesis fall within the eddy-permitting to eddy-rich regime of OGCMs, meaning that their horizontal resolution is adequate to fully resolve mesoscale features on the order of the first baroclinic deformation radius in the subtropics, but not in weakly stratified subpolar latitudes (Hallberg, 2013). As a result, mesoscale and submesoscale features are not globally resolved in eddy-permitting to eddy-rich models and, hence, are not explicitly captured in the velocity fields used to evaluate water parcel trajectories. However, the effects of unresolved turbulent mixing are implicitly included in the tracer fields sampled by water parcels through sub-grid scale diffusion (Chenillat et al., 2015).

Recent studies have found a significant improvement in the representation of many of the major flow structures comprising the AMOC upon reaching submesoscale-resolving resolution ($\sim$1.5 km at mid-latitudes) (e.g., Chassignet & Xu, 2017; Lévy et al., 2010; Pennelly & Myers, 2020; Talandier et al., 2014). Here, we would like to briefly highlight three important advances especially relevant to the findings of this thesis.

6.2.3.1 Gulf Stream Dynamics

In the subtropical North Atlantic, Chassignet and Xu (2017) and Chassignet et al. (2020) showed that the eastward penetration of both the Gulf Stream and its associated eddy kinetic energy is dramatically improved compared with observations in a submesoscale-resolving configuration of HYCOM with high-resolution bathymetry. It would be interesting to establish if this improved representation of

Gulf Stream dynamics would also address the underestimation of the meridional heat transport at 26.5°N (see Chapter 5) commonly encountered at eddy-rich resolution and below. Furthermore, it would be intriguing to assess how, if at all, explicitly resolving submesoscale features impacts the subtropical to subpolar connectivity of the northward branch of the NADW cell, given that increasing horizontal resolution has not previously been found to improve the overly-zonal representation of the NAC at the North West Corner (Chassignet & Xu, 2021; Jackson et al., 2023b).

6.2.3.2 Boundary-Interior Exchange

In the subpolar North Atlantic, submesoscale-resolving simulations have also been shown to dramatically improve the representation of deep convection by enhancing the eddy-driven exchange between the SPG interior and encircling boundary currents (Li et al., 2023; Pennelly & Myers, 2022; Tagklis et al., 2020). This is because submesoscale instabilities play a fundamental role in modulating the stratification and convective mixing within both the basin interior (Lilly et al., 1999, 2003) and western boundary currents (Goldsworth et al., 2024; Le Bras et al., 2022). Recently, Tagklis et al. (2020) showed that the greater eddy-induced buoyancy flux into the central Labrador Sea at submesoscale-resolving resolution results in a significant reduction in the convective volume of LSW compared with eddy-permitting simulations owing to the more realistic restratification of the interior (Clément et al., 2023; Frajka-Williams et al., 2014).

Interestingly, although the dynamics of boundary-interior exchange have previously been explored using Lagrangian trajectories in the Labrador Sea (Georgiou et al., 2020, 2021), few studies have explored how such exchanges might also modulate convective activity in the eastern SPG. Thus, in an upcoming study led by Nora Fried, we are investigating the role of the Irminger Current in restratifying the Irminger Sea interior using Lagrangian trajectories evaluated within a $\sim$2 km resolution regional simulation of the MITgcm (Almansi et al., 2017, 2019). Our preliminary results suggest that up to 30% of the relatively warm and saline waters flowing northward in the Irminger Current enter regions of deep convection during their recirculation and, hence, actively contribute to seasonal restratification in the Irminger Sea interior.

6.2.3.3 Nordic Seas Overflows

It is also important to emphasise that increasing horizontal resolution alone does not yield universal bias reductions in the representation of the North Atlantic overturning circulation (Chassignet et al., 2020; Jackson et al., 2023b). For example, to faithfully simulate the overflows of lower NADW sourced from the Nordic Seas, we must also resolve dynamical processes occurring on vertical length scales on the order tens of metres or less (Girton & Sanford, 2003; Riemenschneider & Legg, 2007). Given that hydrostatic, $z-$coordinate models cannot resolve such small vertical scales, the sinking of dense overflow waters is synonymous with spurious diapycnal mixing, which results in the unrealistic dilution of the overflows via turbulent entrainment downstream (Roberts et al., 1996; Wang et al., 2015; Winton et al., 1998). We saw the consequences of this in Chapter 2, where the excessive diapycnal mixing south of the Greenland-Scotland Ridge at eddy-permitting resolution produced overflow water trajectories which were far too light and shallow compared with observations, consistent with previous Lagrangian analyses (Fröhle et al., 2022; MacGilchrist et al., 2020). Encouragingly, when hybrid vertical coordinates (e.g., Bruciaferri et al., 2024; Xu et al., 2010) or explicit overflow parameterisations have been implemented in OGCMs (e.g., Danabasoglu et al., 2010; Yeager & Danabasoglu, 2012), overflow waters are much better preserved downstream, yielding a deeper penetration depth of lower NADW.

Although there have been a large number of Lagrangian studies investigating the sources of the Nordic Seas overflows (e.g., Chafik et al., 2020; Saberi et al., 2020; Ypma et al., 2019), the challenges outlined above have meant that very few Lagrangian analyses have focused on the downstream evolution of the overflows south of the Greenland-Scotland Ridge (Koszalka et al., 2013). However, owing to the adoption of the AGRIF two-way grid refinement software (Debreu et al., 2008), OGCMs are now able to embed eddy-resolving nests in the vicinity of the Greenland-Scotland Ridge within existing global simulations (e.g., Colombo et al., 2020), yielding a much more realistic overflow dilution and downstream properties, even in $z-$coordinate models. Inspired by the previous work of Ypma et al. (2016), future studies could utilise such simulations to extend Lagrangian analyses beyond kinematics by considering how potential vorticity evolves along overflow water trajectories. This focus on overflow dynamics is particularly motivated by the recent study of Fraser et al. (2024), who highlight the importance of relative vorticity advection for the sinking of overflow waters and, hence, for establishing the strength of vertical overturning in the subpolar North Atlantic.

6.2.4 Connectivity of the North Atlantic Overturning Circulation.

We have seen throughout this thesis that the Lagrangian overturning framework is a valuable addition to existing Eulerian measures of the overturning circulation, owing to its unique ability to connect water mass transformation integrated at the basin scale to individual circulation pathways. As a result, we can unambiguously interpret variations in the strength of Lagrangian overturning at a given latitude in terms of three successive phases, which together constitute the overturning circulation (Fig. 6.1). In the North Atlantic, the overturning circulation begins with the northward flow of light upper limb waters from subtropical to subpolar latitudes (import phase). This is followed by the transformation phase, in which water is transferred from the upper to the lower limb by diapycnal transformation due to air-sea fluxes and mixing in the SPG and the Nordic Seas. Finally, the overturning circulation concludes when dense water masses are exported southwards in the lower limb from subpolar to subtropical latitudes (export phase). Thus, given that the upper and lower limbs must be connected across latitudes and interconnected through dense water formation to produce a closed overturning cell, changes in meridional connectivity and water mass transformation are synonymous with overturning variability in the Lagrangian frame of reference.

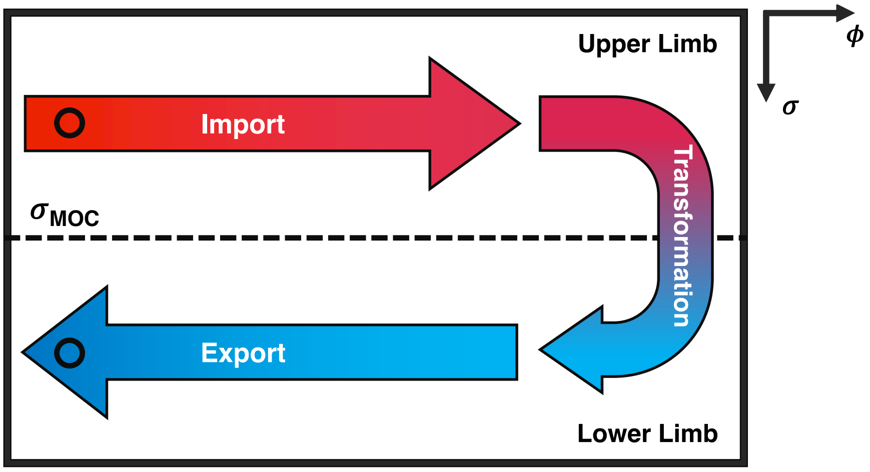

Figure 6.1: Schematic depicting the three phases constituting the Lagrangian / advective diapycnal overturning circulation north of a given latitude in the North Atlantic. The import phase represents the northward flow of light waters in the upper limb. The transformation phase represents the diapycnal transformation of waters from the upper to the lower limb at subpolar latitudes. Lagrangian overturning concludes with the export phase, in which dense waters are returned southward to the chosen latitude in the lower limb.

The first way to generate Lagrangian overturning variability is through changes in the amount of light upper limb waters imported into regions of dense water formation at subpolar latitudes. Since we demonstrated in Chapter 5 that upper limb waters arriving in the eastern SPG must first be preconditioned within the STG (Berglund et al., 2022; Burkholder & Lozier, 2014), any change in the interconnectivity of the STG and SPG circulations could conceivably project onto Lagrangian overturning variability. The importance of gyre dynamics in modulating low-frequency Lagrangian overturning variability was also highlighted in Chapter 4, where we showed that dense water formation localised in the interior of the Labrador and Irminger Seas acts as a remote control on the import of upper limb waters arriving into the eastern SPG via the branches of the NAC. The observational studies of Curry and McCartney (2001) and Kieke et al. (2007) further support this result, revealing that episodes of reduced LSW formation during negative phases of the NAO are associated with a weak baroclinic inter-gyre transport index, which closely reflects the strength of the NAC in the eastern SPG (Desbruyères et al., 2013). In contrast, NAC transport is strengthened following sustained positive phases of the NAO (Desbruyères et al., 2013; Mercier et al., 2024; Wett et al., 2023), resulting in the greater penetration of subtropical-origin waters into the eastern SPG (Desbruyères et al., 2019; Jacobs et al., 2019).

In addition to variations in the import of upper limb waters to regions of dense water formation, changes in the efficiency of diapycnal transformation from the upper to the lower limb can also drive Lagrangian overturning variability. For example, we have seen that the likelihood of being transferred into the lower limb strongly depends on where upper limb waters arrive into the eastern SPG. Thus, a positive overturning anomaly could also be generated by redistributing upper limb waters in favour of a more efficient overturning pathway. The redistribution of upper limb waters has previously been documented in the numerical modelling study of Desbruyères et al. (2013), who found that a stronger upper limb transport arriving into the eastern SPG generally coincides with a greater northward inflow into the Iceland Basin and a weaker inflow into the Rockall Trough.

The final way to generate Lagrangian overturning variability is through changes in the rate by which dense NADW formed at subpolar latitudes is exported to the subtropics. This can be achieved by increasing the fraction of dense water formation occurring within the western boundary currents of the Labrador and Irminger Seas, given that this upper NADW is rapidly exported towards the inter-gyre boundary in less than a year (Deshayes et al., 2007; Le Bras et al., 2020). In contrast, since the majority of newly ventilated NADW in the SPG interior is recirculated within the basin (Lavender et al., 2005; Rhein et al., 2002; Sy et al., 1997) on decadal timescales (Zou & Lozier, 2016), an enhanced rate of interior dense water formation is most likely to manifest in local changes in the volume of NADW rather than its export (Mauritzen & Häkkinen, 1999).

To date, almost all Lagrangian studies exploring the subpolar to subtropical connectivity of the lower limb have focused on describing the time-mean pathways and advective timescales of NADW exported in the DWBC (Gary et al., 2011; Lozier et al., 2013; Petit et al., 2023a). However, very few studies have explored the extent to which the connectivity of the lower limb is modulated by the strength of subpolar dense water formation versus a purely stochastic phenomenon (Zou & Lozier, 2016). In an ongoing study led by Olivia Atkins, we are exploring this question in detail by analysing the Lagrangian trajectories of lower limb waters transiting from OSNAP West to the RAPID array at 26.5°N in the ORCA0083-GO8p7 hindcast documented in Chapter 4. Our preliminary findings suggest that during episodes of intense deep convection associated with strong positive phases of the NAO, there is an intensification of the Labrador Current at depth which favours the direct export of NADW towards the subtropics rather than via recirculation pathways within the SPG.

The connectivity of the North Atlantic overturning circulation will also play a fundamental role in shaping the projected future decline of the AMOC over the course of the 21$^{\text{st}}$century. Traditionally, both theoretical and numerical modelling studies have attributed the projected AMOC weakening in response to anthropogenic forcing to the reduction in NADW formation (transformation phase) as a result of the large-scale warming and freshening of the subpolar North Atlantic (Levang & Schmitt, 2020; Rahmstorf, 1999; Wood et al., 1999). However, this long-standing paradigm, that future AMOC weakening is synonymous with the cessation of high-latitude deep convection (Brodeau & Koenigk, 2016; Cheng et al., 2013; Sévellec et al., 2017; Stouffer et al., 2006), has recently been challenged by Madan et al. (2024), who argue that Arctic-origin freshwater first acts to reduce the geostrophic transport of upper limb waters into the eastern SPG (import phase) by decreasing the density gradient across the NAC. A future study could seek to reconcile these two competing hypotheses by investigating the role that subtropical to subpolar connectivity in the upper limb plays in driving future AMOC weakening from a Lagrangian perspective. This could be achieved by evaluating the backwards-in-time trajectories of the full-depth northward transport arriving in the eastern SPG in a CMIP6 (Eyring et al., 2016) coupled climate model simulation forced using a Shared Socio-Economic Pathway scenario (O'Neill et al., 2014). In addition to quantifying how the throughput of subtropical water into the eastern SPG is related to the projected AMOC and MHT decline in the coming century, such an experiment would also allow us to establish the direction of causality between future changes in subpolar dense water formation and the meridional connectivity of the upper limb in the North Atlantic.

6.3 Concluding remarks

We began this thesis by highlighting in Chapter 1 the formidable challenge posed by defining a diagnostic measure of the AMOC that accurately reflects the 3-dimensional time-varying phenomenon of overturning. In truth, physical oceanographers have long evaded this challenge by simply reconceiving the AMOC to be synonymous with the zonally integrated diagnostics used to measure it rather than the physical phenomenon it represents. As a result, the behaviour of the overturning circulation diagnosed in observations and numerical models depends strongly on how, where and for how long we measure it. To progress, we should focus on better understanding the dynamics of the individual flow structures comprising the AMOC (e.g., western boundary currents) rather than attempting to over-interpret their zonal integral (Wunsch & Heimbach, 2013).

A broader challenge facing the AMOC community is how we should synthesise the increasingly disconnected literature in order to better identify emerging questions and avoid excessive replication of existing results. Recent reviews have done an outstanding job of highlighting the major contributions of theory (e.g., Johnson et al., 2019), observations (e.g., Frajka-Williams et al., 2023; Frajka-Williams et al., 2019) and numerical models (e.g., Buckley & Marshall, 2016; Hirschi et al., 2020) to our understanding of the structure and variability of the overturning circulation, but this could be greatly facilitated by encouraging standard practices when communicating new findings. At a minimum, paleoclimate, process-based and future climate focused AMOC studies should clearly communicate (i) the latitude at which they calculate their chosen overturning diagnostic, (ii) the vertical coordinate system used to calculate the overturning stream function, and (iii) include the timeseries of the isosurface corresponding to the maximum overturning strength. Better still, studies should present the full overturning stream function in the form of a timeseries plot, especially when diagnosing the AMOC in tracer coordinates in the context of future climate change. Moving forward, it would also be valuable for the AMOC community to progress beyond referring to "overturning" in isolation, given that this could equally describe the shallow-to-deep or light-to-dense conversion of water masses. In the absence of a universally accepted definition of the AMOC as proposed by Foukal and Chafik (2024), we should at least distinguish between vertical, diapycnal, diahaline and diathermal varieties of overturning variability.

From an observational perspective, there is little doubt that AMOC monitoring should continue throughout the coming decades (Frajka-Williams et al., 2023), but the fundamental question is how and where should this take place? Over the past 20-years, since the first deployment of the RAPID array at 26.5°N, we have seen a proliferation of continuous ocean observing arrays throughout the Atlantic Ocean, yet its remains unclear if we are any better placed to detect long-term changes in the state of the AMOC. One of the fundamental lessons of the OSNAP era has been that the regions responsible for establishing the mean strength of the overturning circulation need not coincide with those responsible for driving its variability (Li et al., 2021a; Lozier et al., 2019), especially on decadal timescales and longer (Böning et al., 2023; Yeager et al., 2021). Hence, given the growing concern regarding the long-term sustainability of continuous AMOC observing-systems, oceanographers must prioritise which of our existing observations are best placed to identify externally-forced trends in the AMOC over the course of the 21stcentury. In the long-term, observing precursor quantities of low-frequency overturning variability, such as Labrador Sea subsurface density (Ortega et al., 2017, 2021) or inter-gyre transport indices (Curry & McCartney, 2001), may prove to be a more effective means of diagnosing future AMOC weakening than attempting to monitor the state of the circulation itself.

From an ocean modelling perspective, the faithful simulation of the AMOC continues to present a number of significant challenges, many of which cannot be overcome by simply pursuing ever-increasing horizontal resolution (Jackson et al., 2023b). Furthermore, these challenges have been exacerbated by the growing disparity between the eddy-rich OGCMs used in process-based analyses (Chassignet et al., 2020), and operational forecasting (e.g., Verezemskaya et al., 2021) and the predominantly eddy-parameterised ocean components of CMIP-class coupled climate models (Griffies et al., 2016). Given the unfeasibly high computational costs required to reach submesoscale-resolving coupled climate model simulations, an achievable compromise would be to implement hybrid vertical coordinate systems (Bruciaferri et al., 2024) and substantially increase horizontal resolution (Ringler et al., 2013) in limited geographical regions (e.g., the region south of the Greenland-Scotland Ridge).

Overall, balancing the long-standing pursuit of a more complete understanding of overturning dynamics with the urgent need to deliver robust projections of the future state of our climate will be the defining challenge for the AMOC community in the decades to come.

Appendices

A

Supplementary Figures for Chapter 3

(a) Seasonality of maximum Eulerian overturning

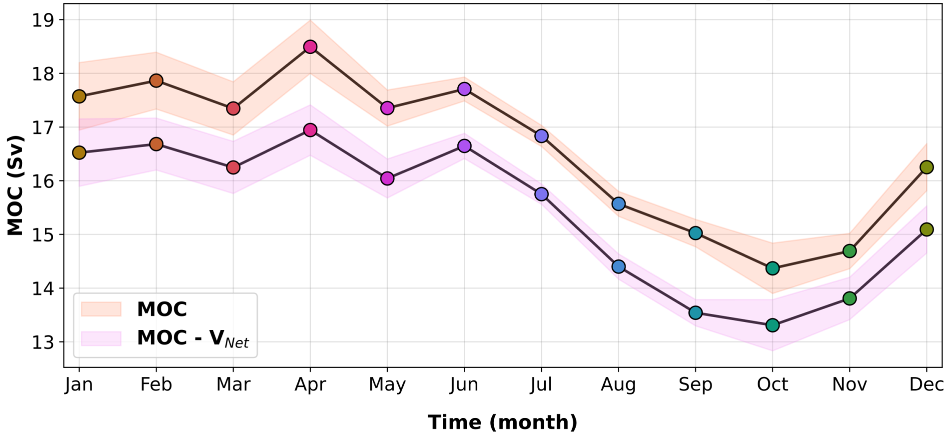

(b) Difference in seasonality of maximum Eulerian overturning

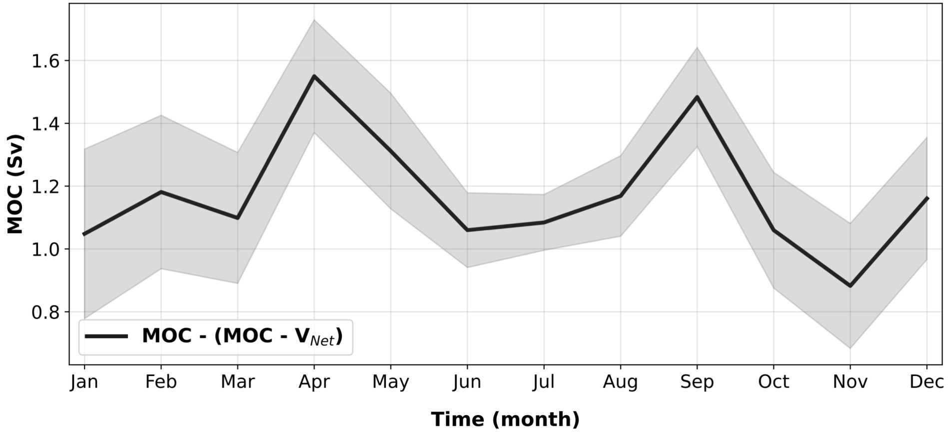

Figure A.1: Eulerian overturning variability at the model-defined OSNAP East section excluding the net throughflow to the Arctic. (a) Mean seasonal cycles of the maximum of the Eulerian overturning computed from monthly composites including (orange shading) and excluding (pink shading) the net throughflow across the OSNAP East section. Shading represents ±1 standard error of the monthly estimates (i.e., monthly standard deviation divided by $\sqrt{n}$ where n is the number of independent samples - equivalent to the number of years in this case). (b) Difference between the mean seasonal cycles of the maximum of the Eulerian overturning computed from monthly composites including and excluding the net throughflow across the OSNAP East section. Shading represents ±1 standard error of the monthly estimates.

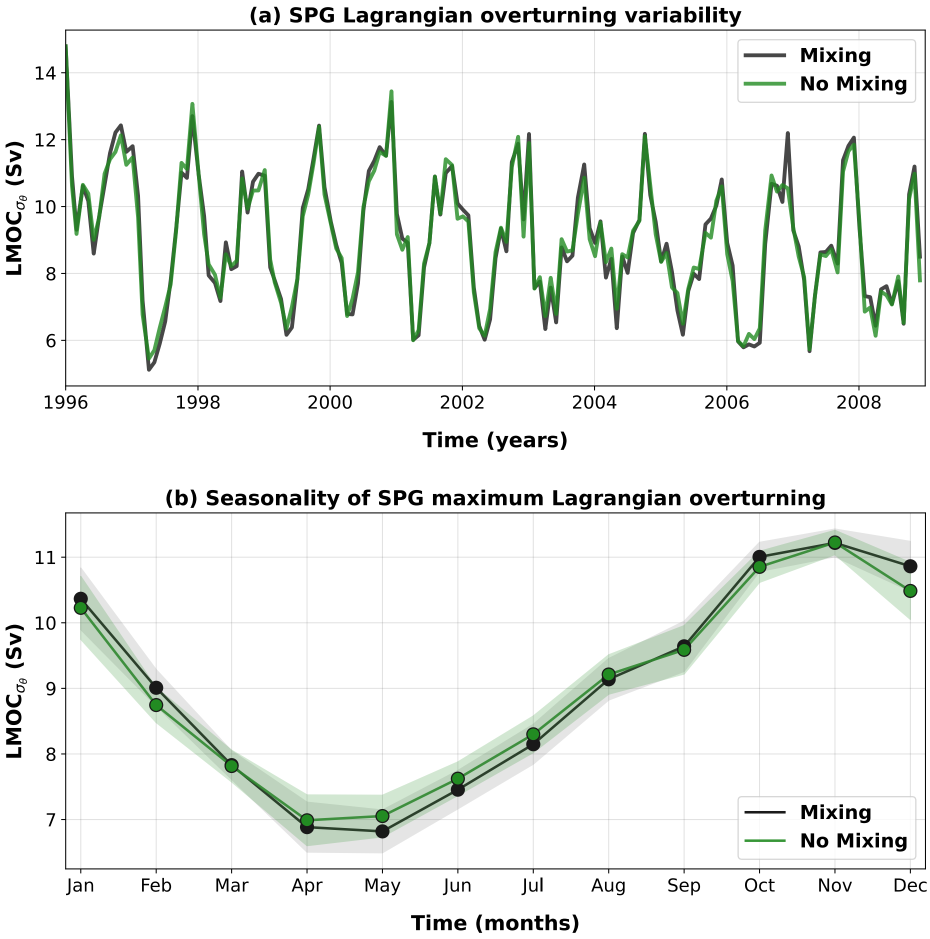

Figure A.2: Lagrangian overturning variability in the eastern SPG at the model-defined OSNAP East section excluding vertical convective mixing along water parcel trajectories in the surface mixed layer. (a) Monthly maximum Lagrangian diapycnal overturning with (black line) and without (green line) vertical convective mixing in the surface mixed layer between 1996-2008. (b) Mean seasonal cycles of the maximum Lagrangian overturning within the eastern SPG calculated from monthly composites with (grey shading) and without (green shading) vertical convective mixing in the surface mixed layer. Shading represents ±1 standard error of the monthly estimates (i.e., monthly standard deviation divided by $\sqrt{n}$ where n is the number of independent samples - equivalent to the number of years in this case).

References

Aldama-Campino, A., Döös, K., Kjellsson, J., & Jönsson, B. (2020, December). TRACMASS: Formal release of version 7.0.

Alley, R. B., Clark, P. U., Keigwin, L. D., & Webb, R. S. (1999). Making sense of millennial-scale climate change. In U. Clark, S. Webb, & D. Keigwin (Eds.), *Geophysical Monograph Series* (pp. 385–394, Vol. 112). American Geophysical Union.

Alley, R. B. (2007). Wally Was Right: Predictive Ability of the North Atlantic "Conveyor Belt" Hypothesis for Abrupt Climate Change. *Annual Review of Earth and Planetary Sciences*, *35*(1), 241–272.

Alley, R. B., & Clark, P. U. (1999). The Deglaciation of the Northern Hemisphere: A Global Perspective. *Annual Review of Earth and Planetary Sciences*, *27*(1), 149–182.

Almansi, M., Gelderloos, R., Haine, T., Saberi, A., & Siddiqui, A. (2019). OceanSpy: A Python package to facilitate ocean model data analysis and visualization. *Journal of Open Source Software*, *4*(39), 1506.

Almansi, M., Haine, T. W. N., Pickart, R. S., Magaldi, M. G., Gelderloos, R., & Mastropole, D. (2017). High-Frequency Variability in the Circulation and Hydrography of the Denmark Strait Overflow from a High-Resolution Numerical Model. *Journal of Physical Oceanography*, *47*(12), 2999–3013.

Andersen, K. K., Azuma, N., Barnola, J.-M., Bigler, M., Biscaye, P., Caillon, N., Chappellaz, J., Clausen, H. B., Dahl-Jensen, D., Fischer, H., Flückiger, J., Fritzsche, D., Fujii, Y., Goto-Azuma, K., Grønvold, K., Gundestrup, N. S., Hansson, M., Huber, C., Hvidberg, C. S., . . . North Greenland Ice Core Project members. (2004). High-resolution record of Northern Hemisphere climate extending into the last interglacial period. *Nature*, *431*(7005), 147–151.

Andrews, J. T. (1998). Abrupt changes (Heinrich events) in late Quaternary North Atlantic marine environments: A history and review of data and concepts. *Journal of Quaternary Science*, *13*(1), 3–16.

Årthun, M., Eldevik, T., Smedsrud, L. H., Skagseth, Ø., & Ingvaldsen, R. B. (2012). Quantifying the Influence of Atlantic Heat on Barents Sea Ice Variability and Retreat. *Journal of Climate*, *25*(13), 4736–4743.

Årthun, M. (2023). Surface-Forced Variability in the Nordic Seas Overturning Circulation and Overflows. *Geophysical Research Letters*, *50*(15), e2023GL104158.

Årthun, M., & Eldevik, T. (2016). On Anomalous Ocean Heat Transport toward the Arctic and Associated Climate Predictability. *Journal of Climate*, *29*(2), 689–704.

Årthun, M., Eldevik, T., Viste, E., Drange, H., Furevik, T., Johnson, H. L., & Keenlyside, N. S. (2017). Skillful prediction of northern climate provided by the ocean. *Nature Communications*, *8*(1), 15875.

Årthun, M., Wills, R. C. J., Johnson, H. L., Chafik, L., & Langehaug, H. R. (2021). Mechanisms of Decadal North Atlantic Climate Variability and Implications for the Recent Cold Anomaly. *Journal of Climate*, *34*(9), 3421–3439.

Asbjørnsen, H., Johnson, H. L., & Årthun, M. (2021). Variable Nordic Seas inflow linked to shifts in North Atlantic circulation. *Journal of Climate*, 1–50.

Atamanchuk, D., Koelling, J., Send, U., & Wallace, D. W. R. (2020). Rapid transfer of oxygen to the deep ocean mediated by bubbles. *Nature Geoscience*, *13*(3), 232–237.

Bacon, S., Reverdin, G., Rigor, I. G., & Snaith, H. M. (2002). A freshwater jet on the east Greenland shelf. *Journal of Geophysical Research: Oceans*, *107*(C7).

Baehr, J., Hirschi, J., Beismann, J.-O., & Marotzke, J. (2004). Monitoring the meridional overturning circulation in the North Atlantic: A model-based array design study. *Journal of Marine Research*, *62*(3), 283–312.

Balan Sarojini, B., Gregory, J. M., Tailleux, R., Bigg, G. R., Blaker, A. T., Cameron, D. R., Edwards, N. R., Megann, A. P., Shaffrey, L. C., & Sinha, B. (2011). High frequency variability of the Atlantic meridional overturning circulation. *Ocean Science*, *7*(4), 471–486.

Beaird, N. L., Rhines, P. B., & Eriksen, C. C. (2013). Overflow Waters at the Iceland–Faroe Ridge Observed in Multiyear Seaglider Surveys. *Journal of Physical Oceanography*, *43*(11), 2334–2351.

Bebieva, Y., & Lozier, M. S. (2023). Fresh Water and Atmospheric Cooling Control on Density-Compensated Overturning in the Labrador Sea. *Journal of Physical Oceanography*, *53*(11), 2575–2589.

Behrens, E., Våge, K., Harden, B., Biastoch, A., & Böning, C. W. (2017). Composition and variability of the Denmark Strait Overflow Water in a high-resolution numerical model hindcast simulation. *Journal of Geophysical Research: Oceans*, *122*(4), 2830–2846.

Belkin, I. M. (2004). Propagation of the "Great Salinity Anomaly" of the 1990s around the northern North Atlantic. *Geophysical Research Letters*, *31*(8), 2003GL019334.

Bellomo, K., Angeloni, M., Corti, S., & Von Hardenberg, J. (2021). Future climate change shaped by inter-model differences in Atlantic meridional overturning circulation response. *Nature Communications*, *12*(1), 3659.

Bellomo, K., Meccia, V. L., D'Agostino, R., Fabiano, F., Larson, S. M., Von Hardenberg, J., & Corti, S. (2023). Impacts of a weakened AMOC on precipitation over the Euro-Atlantic region in the EC-Earth3 climate model. *Climate Dynamics*, *61*(7-8), 3397–3416.

Bellomo, K., Murphy, L. N., Cane, M. A., Clement, A. C., & Polvani, L. M. (2018). Historical forcings as main drivers of the Atlantic multidecadal variability in the CESM large ensemble. *Climate Dynamics*, *50*(9-10), 3687–3698.

Berglund, S., Döös, K., Campino, A. A., & Nycander, J. (2021). The Water Mass Transformation in the Upper Limb of the Overturning Circulation in the Southern Hemisphere. *Journal of Geophysical Research: Oceans*, *126*(8).

Berglund, S., Döös, K., Groeskamp, S., & McDougall, T. (2023). North Atlantic Ocean Circulation and Related Exchange of Heat and Salt Between Water Masses. *Geophysical Research Letters*, *50*(13), e2022GL100989.

Berglund, S., Döös, K., Groeskamp, S., & McDougall, T. J. (2022). The downward spiralling nature of the North Atlantic Subtropical Gyre. *Nature Communications*, *13*(1), 2000.

Berglund, S., Döös, K., & Nycander, J. (2017). Lagrangian tracing of the water–mass transformations in the Atlantic Ocean. *Tellus A: Dynamic Meteorology and Oceanography*, *69*(1), 1306311.

Bernard, B., Madec, G., Penduff, T., Molines, J.-M., Treguier, A.-M., Le Sommer, J., Beckmann, A., Biastoch, A., Böning, C., Dengg, J., Derval, C., Durand, E., Gulev, S., Remy, E., Talandier, C., Theetten, S., Maltrud, M., McClean, J., & De Cuevas, B. (2006). Impact of partial steps and momentum advection schemes in a global ocean circulation model at eddy-permitting resolution. *Ocean Dynamics*, *56*(5-6), 543–567.

Bersch, M. (2002). North Atlantic Oscillation–induced changes of the upper layer circulation in the northern North Atlantic Ocean. *Journal of Geophysical Research: Oceans*, *107*(C10).

Bersch, M., Meincke, J., & Sy, A. (1999). Interannual thermohaline changes in the northern North Atlantic 1991–1996. *Deep Sea Research Part II: Topical Studies in Oceanography*, *46*(1-2), 55–75.

Bersch, M., Yashayaev, I., & Koltermann, K. P. (2007). Recent changes of the thermohaline circulation in the subpolar North Atlantic. *Ocean Dynamics*, *57*(3), 223–235.

Biastoch, A., Böning, C. W., & Lutjeharms, J. R. E. (2008). Agulhas leakage dynamics affects decadal variability in Atlantic overturning circulation. *Nature*, *456*(7221), 489–492.

Biastoch, A., Schwarzkopf, F. U., Getzlaff, K., Rühs, S., Martin, T., Scheinert, M., Schulzki, T., Handmann, P., Hummels, R., & Böning, C. W. (2021). Regional imprints of changes in the Atlantic Meridional Overturning Circulation in the eddy-rich ocean model VIKING20X. *Ocean Science*, *17*(5), 1177–1211.

Biló, T. C., Straneo, F., Holte, J., & Le Bras, I. A.-A. (2022). Arrival of New Great Salinity Anomaly Weakens Convection in the Irminger Sea. *Geophysical Research Letters*, *49*(11).

Bingham, R. J., Hughes, C. W., Roussenov, V., & Williams, R. G. (2007). Meridional coherence of the North Atlantic meridional overturning circulation. *Geophysical Research Letters*, *34*(23), 2007GL031731.

Bjerknes, J. (1964). Atlantic Air-Sea Interaction. In *Advances in Geophysics* (pp. 1–82, Vol. 10). Elsevier.

Blaker, A. T., Hirschi, J. J.-M., McCarthy, G., Sinha, B., Taws, S., Marsh, R., Coward, A., & De Cuevas, B. (2015). Historical analogues of the recent extreme minima observed in the Atlantic meridional overturning circulation at 26°N. *Climate Dynamics*, *44*(1-2), 457–473.

Blanke, B., Arhan, M., Lazar, A., & Prévost, G. (2002). A Lagrangian numerical investigation of the origins and fates of the salinity maximum water in the Atlantic. *Journal of Geophysical Research: Oceans*, *107*(C10).

Blanke, B., Arhan, M., Madec, G., & Roche, S. (1999). Warm Water Paths in the Equatorial Atlantic as Diagnosed with a General Circulation Model. *Journal of Physical Oceanography*, *29*(11), 2753–2768.

Blanke, B., Bonhommeau, S., Grima, N., & Drillet, Y. (2012). Sensitivity of advective transfer times across the North Atlantic Ocean to the temporal and spatial resolution of model velocity data: Implication for European eel larval transport. *Dynamics of Atmospheres and Oceans*, *55–56*, 22–44.

Blanke, B., & Delecluse, P. (1993). Variability of the Tropical Atlantic Ocean Simulated by a General Circulation Model with Two Different Mixed-Layer Physics. *Journal of Physical Oceanography*, *23*(7), 1363–1388.

Blanke, B., & Raynaud, S. (1997). Kinematics of the Pacific Equatorial Undercurrent: An Eulerian and Lagrangian Approach from GCM Results. *Journal of Physical Oceanography*, *27*(6), 1038–1053.

Boccaletti, G., Ferrari, R., Adcroft, A., Ferreira, D., & Marshall, J. (2005). The vertical structure of ocean heat transport. *Geophysical Research Letters*, *32*(10), 2005GL022474.

Boé, J., Hall, A., & Qu, X. (2009). Deep ocean heat uptake as a major source of spread in transient climate change simulations. *Geophysical Research Letters*, *36*(22), 2009GL040845.

Bond, G., Heinrich, H., Broecker, W., Labeyrie, L., McManus, J., Andrews, J., Huon, S., Jantschik, R., Clasen, S., Simet, C., Tedesco, K., Klas, M., Bonani, G., & Ivy, S. (1992). Evidence for massive discharges of icebergs into the North Atlantic ocean during the last glacial period. *Nature*, *360*(6401), 245–249.

Böning, C. W., Scheinert, M., Dengg, J., Biastoch, A., & Funk, A. (2006). Decadal variability of subpolar gyre transport and its reverberation in the North Atlantic overturning. *Geophysical Research Letters*, *33*(21), 2006GL026906.

Böning, C. W., Wagner, P., Handmann, P., Schwarzkopf, F. U., Getzlaff, K., & Biastoch, A. (2023). Decadal changes in Atlantic overturning due to the excessive 1990s Labrador Sea convection. *Nature Communications*, *14*(1), 4635.

Böning, C. W., Behrens, E., Biastoch, A., Getzlaff, K., & Bamber, J. L. (2016). Emerging impact of Greenland meltwater on deepwater formation in the North Atlantic Ocean. *Nature Geoscience*, *9*(7), 523–527.

Böning, C. W., & Herrmann, P. (1994). Annual Cycle of Poleward Heat Transport in the Ocean: Results from High-Resolution Modeling of the North and Equatorial Atlantic. *Journal of Physical Oceanography*, *24*(1), 91–107.

Booth, B. B. B., Dunstone, N. J., Halloran, P. R., Andrews, T., & Bellouin, N. (2012). Aerosols implicated as a prime driver of twentieth-century North Atlantic climate variability. *Nature*, *484*(7393), 228–232.

Born, A., & Stocker, T. F. (2014). Two Stable Equilibria of the Atlantic Subpolar Gyre. *Journal of Physical Oceanography*, *44*(1), 246–264.

Bower, A., Lozier, S., Biastoch, A., Drouin, K., Foukal, N., Furey, H., Lankhorst, M., Rühs, S., & Zou, S. (2019). Lagrangian Views of the Pathways of the Atlantic Meridional Overturning Circulation. *Journal of Geophysical Research: Oceans*, *124*(8), 5313–5335.

Bower, A. S., Le Cann, B., Rossby, T., Zenk, W., Gould, J., Speer, K., Richardson, P. L., Prater, M. D., & Zhang, H.-M. (2002). Directly measured mid-depth circulation in the northeastern North Atlantic Ocean. *Nature*, *419*(6907), 603–607.

Bower, A. S., Rossby, H. T., & Lillibridge, J. L. (1985). The Gulf Stream—Barrier or Blender? *Journal of Physical Oceanography*, *15*(1), 24–32.

Bower, A., Lozier, S., & Gary, S. (2011). Export of Labrador Sea Water from the subpolar North Atlantic: A Lagrangian perspective. *Deep Sea Research Part II: Topical Studies in Oceanography*, *58*(17-18), 1798–1818.

Bower, A. S., & Lozier, M. S. (1994). A Closer Look at Particle Exchange in the Gulf Stream. *Journal of Physical Oceanography*, *24*(6), 1399–1418.

Bower, A. S., Lozier, M. S., Gary, S. F., & Böning, C. W. (2009). Interior pathways of the North Atlantic meridional overturning circulation. *Nature*, *459*(7244), 243–247.

Bower, A. S., & Von Appen, W.-J. (2008). Interannual Variability in the Pathways of the North Atlantic Current over the Mid-Atlantic Ridge and the Impact of Topography. *Journal of Physical Oceanography*, *38*(1), 104–120.

Brakstad, A., Gebbie, G., Våge, K., Jeansson, E., & Ólafsdóttir, S. R. (2023). Formation and pathways of dense water in the Nordic Seas based on a regional inversion. *Progress in Oceanography*, *212*, 102981.

Brambilla, E., & Talley, L. D. (2006). Surface drifter exchange between the North Atlantic subtropical and subpolar gyres. *Journal of Geophysical Research: Oceans*, *111*(C7), 2005JC003146.

Brambilla, E., & Talley, L. D. (2008). Subpolar Mode Water in the northeastern Atlantic: 1. Averaged properties and mean circulation. *Journal of Geophysical Research*, *113*(C4), C04025.

Brambilla, E., Talley, L. D., & Robbins, P. E. (2008). Subpolar Mode Water in the northeastern Atlantic: 2. Origin and transformation. *Journal of Geophysical Research*, *113*(C4), C04026.

Brandt, P., Funk, A., Czeschel, L., Eden, C., & Böning, C. W. (2007). Ventilation and Transformation of Labrador Sea Water and Its Rapid Export in the Deep Labrador Current. *Journal of Physical Oceanography*, *37*(4), 946–961.

Brayshaw, D. J., Woollings, T., & Vellinga, M. (2009). Tropical and Extratropical Responses of the North Atlantic Atmospheric Circulation to a Sustained Weakening of the MOC. *Journal of Climate*, *22*(11), 3146–3155.

Breckenfelder, T., Rhein, M., Roessler, A., Böning, C. W., Biastoch, A., Behrens, E., & Mertens, C. (2017). Flow paths and variability of the N orth A tlantic C urrent: A comparison of observations and a high-resolution model. *Journal of Geophysical Research: Oceans*, *122*(4), 2686–2708.

Brennecke, W. (1921). *Die ozeanographischen Arbeiten der Deutschen Antarktischen Expedition 1911-1912.* (1st ed., Vol. 39). Hammerich and Lesser.

Bringedal, C., Eldevik, T., Skagseth, Ø., Spall, M. A., & Østerhus, S. (2018). Structure and Forcing of Observed Exchanges across the Greenland–Scotland Ridge. *Journal of Climate*, *31*(24), 9881–9901.

Brodeau, L., & Koenigk, T. (2016). Extinction of the northern oceanic deep convection in an ensemble of climate model simulations of the 20th and 21st centuries. *Climate Dynamics*, *46*(9-10), 2863–2882.

Broecker, W. S. (1997). Thermohaline Circulation, the Achilles Heel of Our Climate System: Will Man-Made CO $_2$ Upset the Current Balance? *Science*, *278*(5343), 1582–1588.

Broecker, W. S. (1998). Paleocean circulation during the Last Deglaciation: A bipolar seesaw? *Paleoceanography*, *13*(2), 119–121.

Broecker, W. S., Peteet, D. M., & Rind, D. (1985). Does the ocean–atmosphere system have more than one stable mode of operation? *Nature*, *315*(6014), 21–26.

Broecker, W. (1991). The Great Ocean Conveyor. *Oceanography*, *4*(2), 79–89.

Broecker, W., & Peng, T. (1982). *Tracers in the Sea* (Vol. 24). Sea Eldigio Press.

Bruciaferri, D., Guiavarc'h, C., Hewitt, H. T., Harle, J., Almansi, M., Mathiot, P., & Colombo, P. (2024). Localized General Vertical Coordinates for Quasi-Eulerian Ocean Models: The Nordic Overflows Test-Case. *Journal of Advances in Modeling Earth Systems*, *16*(3), e2023MS003893.

Brüggemann, N., & Katsman, C. A. (2019). Dynamics of Downwelling in an Eddying Marginal Sea: Contrasting the Eulerian and the Isopycnal Perspective. *Journal of Physical Oceanography*, *49*(11), 3017–3035.

Bryan, F. (1986). High-latitude salinity effects and interhemispheric thermohaline circulations. *Nature*, *323*(6086), 301–304.

Bryan, K. (1982). Seasonal variation in meridional overturning and poleward heat transport in the Atlantic and Pacific Oceans: A model study. *Journal of Marine Research*, *40*.

Bryan, K., & Cox, M. D. (1968). A Nonlinear Model of an Ocean Driven by Wind and Differential Heating: Part I. Description of the Three-Dimensional Velocity and Density Fields. *Journal of the Atmospheric Sciences*, *25*(6), 945–967.

Bryden, H., & Imawaki, S. (2001). Chapter 6.1 Ocean heat transport. In *International Geophysics* (pp. 455–474, Vol. 77). Elsevier.

Bryden, H. L. (2021). Wind-driven and buoyancy-driven circulation in the subtropical North Atlantic Ocean. *Proceedings of the Royal Society A: Mathematical, Physical and Engineering Sciences*, *477*(2256), 20210172.

Bryden, H. L., & Hall, M. M. (1980). Heat Transport by Currents Across 25°N Latitude in the Atlantic Ocean. *Science*, *207*(4433), 884–886.

Bryden, H. L., Johns, W. E., King, B. A., McCarthy, G., McDonagh, E. L., Moat, B. I., & Smeed, D. A. (2020). Reduction in Ocean Heat Transport at 26°N since 2008 Cools the Eastern Subpolar Gyre of the North Atlantic Ocean. *Journal of Climate*, *33*(5), 1677–1689.

Buckley, M. W., Ferreira, D., Campin, J.-M., Marshall, J., & Tulloch, R. (2012). On the Relationship between Decadal Buoyancy Anomalies and Variability of the Atlantic Meridional Overturning Circulation. *Journal of Climate*, *25*(23), 8009–8030.

Buckley, M. W., Lozier, M. S., Desbruyères, D., & Evans, D. G. (2023). Buoyancy forcing and the subpolar Atlantic meridional overturning circulation. *Philosophical Transactions of the Royal Society A: Mathematical, Physical and Engineering Sciences*, *381*(2262), 20220181.

Buckley, M. W., & Marshall, J. (2016). Observations, inferences, and mechanisms of the Atlantic Meridional Overturning Circulation: A review. *Reviews of Geophysics*, *54*(1), 5–63.

Buizert, C., & Schmittner, A. (2015). Southern Ocean control of glacial AMOC stability and Dansgaard-Oeschger interstadial duration. *Paleoceanography*, *30*(12), 1595–1612.

Burkholder, K. C., & Lozier, M. S. (2011a). Mid-depth Lagrangian pathways in the North Atlantic and their impact on the salinity of the eastern subpolar gyre. *Deep Sea Research Part I: Oceanographic Research Papers*, *58*(12), 1196–1204.

Burkholder, K. C., & Lozier, M. S. (2011b). Subtropical to subpolar pathways in the North Atlantic: Deductions from Lagrangian trajectories. *Journal of Geophysical Research: Oceans*, *116*(C7).

Burkholder, K. C., & Lozier, M. S. (2014). Tracing the pathways of the upper limb of the North Atlantic Meridional Overturning Circulation. *Geophysical Research Letters*, *41*(12), 4254–4260.

Cabanes, C., Lee, T., & Fu, L.-L. (2008). Mechanisms of Interannual Variations of the Meridional Overturning Circulation of the North Atlantic Ocean. *Journal of Physical Oceanography*, *38*(2), 467–480.

Caesar, L., McCarthy, G. D., Thornalley, D. J. R., Cahill, N., & Rahmstorf, S. (2021). Current Atlantic Meridional Overturning Circulation weakest in last millennium. *Nature Geoscience*, *14*(3), 118–120.

Caesar, L., Rahmstorf, S., Robinson, A., Feulner, G., & Saba, V. (2018). Observed fingerprint of a weakening Atlantic Ocean overturning circulation. *Nature*, *556*(7700), 191–196.

Candela, J., Tanahara, S., Crepon, M., Barnier, B., & Sheinbaum, J. (2003). Yucatan Channel flow: Observations versus CLIPPER ATL6 and MERCATOR PAM models. *Journal of Geophysical Research: Oceans*, *108*(C12), 2003JC001961.

Cane, M. A., Clement, A. C., Murphy, L. N., & Bellomo, K. (2017). Low-Pass Filtering, Heat Flux, and Atlantic Multidecadal Variability. *Journal of Climate*, *30*(18), 7529–7553.

Chafik, L., Holliday, N. P., Bacon, S., & Rossby, T. (2022). Irminger Sea Is the Center of Action for Subpolar AMOC Variability. *Geophysical Research Letters*, *49*(17).

Chafik, L., Rossby, T., & Schrum, C. (2014). On the spatial structure and temporal variability of poleward transport between Scotland and Greenland. *Journal of Geophysical Research: Oceans*, *119*(2), 824–841.

Chafik, L., Hátún, H., Kjellsson, J., Larsen, K. M. H., Rossby, T., & Berx, B. (2020). Discovery of an unrecognized pathway carrying overflow waters toward the Faroe Bank Channel. *Nature Communications*, *11*(1), 3721.

Chafik, L., & Holliday, N. P. (2022). Rapid Communication of Upper-Ocean Salinity Anomaly to Deep Waters of the Iceland Basin Indicates an AMOC Short-Cut. *Geophysical Research Letters*, *49*(3).

Chafik, L., Penny Holliday, N., Bacon, S., Baker, J. A., Desbruyères, D., Frajka-Williams, E., & Jackson, L. C. (2023). Observed mechanisms activating the recent subpolar North Atlantic Warming since 2016. *Philosophical Transactions of the Royal Society A: Mathematical, Physical and Engineering Sciences*, *381*(2262), 20220183.

Chafik, L., & Rossby, T. (2019). Volume, Heat, and Freshwater Divergences in the Subpolar North Atlantic Suggest the Nordic Seas as Key to the State of the Meridional Overturning Circulation. *Geophysical Research Letters*, *46*(9), 4799–4808.

Chassignet, E. P., & Xu, X. (2017). Impact of Horizontal Resolution (1/12° to 1/50°) on Gulf Stream Separation, Penetration, and Variability. *Journal of Physical Oceanography*, *47*(8), 1999–2021.

Chassignet, E. P., & Xu, X. (2021). On the Importance of High-Resolution in Large-Scale Ocean Models. *Advances in Atmospheric Sciences*, *38*(10), 1621–1634.

Chassignet, E. P., Yeager, S. G., Fox-Kemper, B., Bozec, A., Castruccio, F., Danabasoglu, G., Horvat, C., Kim, W. M., Koldunov, N., Li, Y., Lin, P., Liu, H., Sein, D. V., Sidorenko, D., Wang, Q., & Xu, X. (2020). Impact of horizontal resolution on global ocean–sea ice model simulations based on the experimental protocols of the Ocean Model Intercomparison Project phase 2 (OMIP-2). *Geoscientific Model Development*, *13*(9), 4595–4637.

Chen, C., Liu, W., & Wang, G. (2019). Understanding the Uncertainty in the 21st Century Dynamic Sea Level Projections: The Role of the AMOC. *Geophysical Research Letters*, *46*(1), 210–217.

Cheng, W., Chiang, J. C. H., & Zhang, D. (2013). Atlantic Meridional Overturning Circulation (AMOC) in CMIP5 Models: RCP and Historical Simulations. *Journal of Climate*, *26*(18), 7187–7197.

Chenillat, F., Blanke, B., Grima, N., Franks, P. J. S., Capet, X., & Rivière, P. (2015). Quantifying tracer dynamics in moving fluids: A combined Eulerian-Lagrangian approach. *Frontiers in Environmental Science*, *3*.

Chepurin, G. A., & Carton, J. A. (2012). Subarctic and Arctic sea surface temperature and its relation to ocean heat content 1982–2010. *Journal of Geophysical Research: Oceans*, *117*(C6), 2011JC007770.

Chidichimo, M. P., Kanzow, T., Cunningham, S. A., Johns, W. E., & Marotzke, J. (2010). The contribution of eastern-boundary density variations to the Atlantic meridional overturning circulation at 26.5° N. *Ocean Science*, *6*(2), 475–490.

Clarke, R. A., Hill, H. W., Reiniger, R. F., & Warren, B. A. (1980). Current System South and East of the Grand Banks of Newfoundland. *Journal of Physical Oceanography*, *10*(1), 25–65.

Clement, A., Bellomo, K., Murphy, L. N., Cane, M. A., Mauritsen, T., Rädel, G., & Stevens, B. (2015). The Atlantic Multidecadal Oscillation without a role for ocean circulation. *Science*, *350*(6258), 320–324.

Clément, L., Frajka-Williams, E., Von Oppeln-Bronikowski, N., Goszczko, I., & De Young, B. (2023). Cessation of Labrador Sea Convection Triggered by Distinct Fresh and Warm (Sub)Mesoscale Flows. *Journal of Physical Oceanography*, *53*(8), 1959–1977.

Collins, M., & Sinha, B. (2003). Predictability of decadal variations in the thermohaline circulation and climate. *Geophysical Research Letters*, *30*(6), 2002GL016504.

Colombo, P., Barnier, B., Penduff, T., Chanut, J., Deshayes, J., Molines, J.-M., Le Sommer, J., Verezemskaya, P., Gulev, S., & Treguier, A.-M. (2020). Representation of the Denmark Strait overflow in a z-coordinate eddying configuration of the NEMO (v3.6) ocean model: Resolution and parameter impacts. *Geoscientific Model Development*, *13*(7), 3347–3371.

Cronin, M., & Sprintall, J. (2001). Wind And Buoyancy-forced Upper Ocean. In *Encyclopedia of Ocean Sciences* (pp. 3219–3226). Elsevier.

Cunningham, S. A., Kanzow, T., Rayner, D., Baringer, M. O., Johns, W. E., Marotzke, J., Longworth, H. R., Grant, E. M., Hirschi, J. J.-M., Beal, L. M., Meinen, C. S., & Bryden, H. L. (2007). Temporal Variability of the Atlantic Meridional Overturning Circulation at 26.5°N. *Science*, *317*(5840), 935–938.

Cuny, J., Rhines, P. B., Niiler, P. P., & Bacon, S. (2002). Labrador Sea Boundary Currents and the Fate of the Irminger Sea Water. *Journal of Physical Oceanography*, *32*(2), 627–647.

Cuny, J., Rhines, P. B., Schott, F., & Lazier, J. (2005). Convection above the Labrador Continental Slope. *Journal of Physical Oceanography*, *35*(4), 489–511.

Curry, R. G., & McCartney, M. S. (2001). Ocean Gyre Circulation Changes Associated with the North Atlantic Oscillation*. *Journal of Physical Oceanography*, *31*(12), 3374–3400.

Curry, R. G., McCartney, M. S., & Joyce, T. M. (1998). Oceanic transport of subpolar climate signals to mid-depth subtropical waters. *Nature*, *391*(6667), 575–577.

Czaja, A., & Marshall, J. (2006). The Partitioning of Poleward Heat Transport between the Atmosphere and Ocean. *Journal of the Atmospheric Sciences*, *63*(5), 1498–1511.

Danabasoglu, G., Large, W. G., & Briegleb, B. P. (2010). Climate impacts of parameterized Nordic Sea overflows. *Journal of Geophysical Research*, *115*(C11), C11005.

Danabasoglu, G., Yeager, S. G., Bailey, D., Behrens, E., Bentsen, M., Bi, D., Biastoch, A., Böning, C., Bozec, A., Canuto, V. M., Cassou, C., Chassignet, E., Coward, A. C., Danilov, S., Diansky, N., Drange, H., Farneti, R., Fernandez, E., Fogli, P. G., … Wang, Q. (2014). North Atlantic simulations in Coordinated Ocean-ice Reference Experiments phase II (CORE-II). Part I: Mean states. *Ocean Modelling*, *73*, 76–107.

Danabasoglu, G., Yeager, S. G., Kim, W. M., Behrens, E., Bentsen, M., Bi, D., Biastoch, A., Bleck, R., Böning, C., Bozec, A., Canuto, V. M., Cassou, C., Chassignet, E., Coward, A. C., Danilov, S., Diansky, N., Drange, H., Farneti, R., Fernandez, E., … Yashayaev, I. (2016). North Atlantic simulations in Coordinated Ocean-ice Reference Experiments phase II (CORE-II). Part II: Inter-annual to decadal variability. *Ocean Modelling*, *97*, 65–90.

Daniault, N., Mercier, H., & Lherminier, P. (2011a). The 1992-2009 transport variability of the East Greenland-Irminger Current at 60°N: EGIC TRANSPORT VARIABILITY. *Geophysical Research Letters*, *38*(7), n/a–n/a.

Daniault, N., Lherminier, P., & Mercier, H. (2011b). Circulation and Transport at the Southeast Tip of Greenland. *Journal of Physical Oceanography*, *41*(3), 437–457.

Daniault, N., Mercier, H., Lherminier, P., Sarafanov, A., Falina, A., Zunino, P., Pérez, F. F., Ríos, A. F., Ferron, B., Huck, T., Thierry, V., & Gladyshev, S. (2016). The northern North Atlantic Ocean mean circulation in the early 21st century. *Progress in Oceanography*, *146*, 142–158.

de Boisséson, E., Thierry, V., Mercier, H., & Caniaux, G. (2010). Mixed layer heat budget in the Iceland Basin from Argo. *Journal of Geophysical Research: Oceans*, *115*(C10), 2010JC006283.

de Boisséson, E., Thierry, V., Mercier, H., Caniaux, G., & Desbruyères, D. (2012). Origin, formation and variability of the Subpolar Mode Water located over the Reykjanes Ridge. *Journal of Geophysical Research: Oceans*, *117*(C12), n/a–n/a.

de Jong, M. F., Bower, A. S., & Furey, H. H. (2014). Two Years of Observations of Warm-Core Anticyclones in the Labrador Sea and Their Seasonal Cycle in Heat and Salt Stratification. *Journal of Physical Oceanography*, *44*(2), 427–444.

de Jong, M. F., Steur, L., Fried, N., Bol, R., & Kritsotalakis, S. (2020). Year-Round Measurements of the Irminger Current: Variability of a Two-Core Current System Observed in 2014–2016. *Journal of Geophysical Research: Oceans*, *125*(10).

de Jong, M. F., van Aken, H. M., Våge, K., & Pickart, R. S. (2012). Convective mixing in the central Irminger Sea: 2002–2010. *Deep Sea Research Part I: Oceanographic Research Papers*, *63*, 36–51.

de Jong, M. F., & de Steur, L. (2016). Strong winter cooling over the Irminger Sea in winter 2014–2015, exceptional deep convection, and the emergence of anomalously low SST. *Geophysical Research Letters*, *43*(13), 7106–7113.

de Vries, P., & Weber, S. L. (2005). The Atlantic freshwater budget as a diagnostic for the existence of a stable shut down of the meridional overturning circulation. *Geophysical Research Letters*, *32*(9), 2004GL021450.

de Vries, T., Primeau, F., & Deutsch, C. (2012). The sequestration efficiency of the biological pump. *Geophysical Research Letters*, *39*(13), 2012GL051963.

Deacu, D., & Myers, P. G. (2005a). Analysis of an 80-Year Integration of a 1/3-Degree Ocean Model of the Subpolar North Atlantic. *Journal of Oceanography*, *61*(3), 549–555.

Deacu, D., & Myers, P. G. (2005b). Effect of a Variable Eddy Transfer Coefficient in an Eddy-Permitting Model of the Subpolar North Atlantic Ocean. *Journal of Physical Oceanography*, *35*(3), 289–307.

Debreu, L., Vouland, C., & Blayo, E. (2008). AGRIF: Adaptive grid refinement in Fortran. *Computers & Geosciences*, *34*(1), 8–13.

Dee, D. P., Uppala, S. M., Simmons, A. J., Berrisford, P., Poli, P., Kobayashi, S., Andrae, U., Balmaseda, M. A., Balsamo, G., Bauer, P., Bechtold, P., Beljaars, A. C. M., van de Berg, L., Bidlot, J., Bormann, N., Delsol, C., Dragani, R., Fuentes, M., Geer, A. J., … Vitart, F. (2011). The ERA-Interim reanalysis: Configuration and performance of the data assimilation system. *Quarterly Journal of the Royal Meteorological Society*, *137*(656), 553–597.

Defant, A. (1941). Die absolute Topographie des physikalischen Meeresniveaus und der Drückflachen sowie die Wasserbewegungen im Raum des Atlantischen Ozeans. In *Wissenschaftliche Ergebnisse der Deutschen Atlantischen Expedition auf dem Forschungs—und Vermessungsschiff "Meteor" 1925–1927* (1st ed., pp. 191–260, Vol. 6).

Delandmeter, P., & Van Sebille, E. (2019). The Parcels v2.0 Lagrangian framework: New field interpolation schemes. *Geoscientific Model Development*, *12*(8), 3571–3584.

Delworth, T., Manabe, S., & Stouffer, R. J. (1993). Interdecadal Variations of the Thermohaline Circulation in a Coupled Ocean-Atmosphere Model. *Journal of Climate*, *6*(11), 1993–2011.

Delworth, T. L., & Mann, M. E. (2000). Observed and simulated multidecadal variability in the Northern Hemisphere. *Climate Dynamics*, *16*(9), 661–676.

Delworth, T. L., & Zeng, F. (2012). Multicentennial variability of the Atlantic meridional overturning circulation and its climatic influence in a 4000 year simulation of the GFDL CM2.1 climate model. *Geophysical Research Letters*, *39*(13), 2012GL052107.

Delworth, T. L., & Zeng, F. (2016). The Impact of the North Atlantic Oscillation on Climate through Its Influence on the Atlantic Meridional Overturning Circulation. *Journal of Climate*, *29*(3), 941–962.

Dengler, M., Fischer, J., Schott, F. A., & Zantopp, R. (2006). Deep Labrador Current and its variability in 1996–2005. *Geophysical Research Letters*, *33*(21), 2006GL026702.

Desbruyères, D., Chafik, L., & Maze, G. (2021). A shift in the ocean circulation has warmed the subpolar North Atlantic Ocean since 2016. *Communications Earth & Environment*, *2*(1), 48.

Desbruyères, D., Mercier, H., & Thierry, V. (2015). On the mechanisms behind decadal heat content changes in the eastern subpolar gyre. *Progress in Oceanography*, *132*, 262–272.

Desbruyères, D., Thierry, V., & Mercier, H. (2013). Simulated decadal variability of the meridional overturning circulation across the A25-Ovide section. *Journal of Geophysical Research: Oceans*, *118*(1), 462–475.

Desbruyères, D. G., Mercier, H., Maze, G., & Daniault, N. (2019). Surface predictor of overturning circulation and heat content change in the subpolar North Atlantic. *Ocean Science*, *15*(3), 809–817.

Deser, C., Phillips, A. S., Tomas, R. A., Okumura, Y. M., Alexander, M. A., Capotondi, A., Scott, J. D., Kwon, Y.-O., & Ohba, M. (2012). ENSO and Pacific Decadal Variability in the Community Climate System Model Version 4. *Journal of Climate*, *25*(8), 2622–2651.

Deshayes, J., Frankignoul, C., & Drange, H. (2007). Formation and export of deep water in the Labrador and Irminger Seas in a GCM. *Deep Sea Research Part I: Oceanographic Research Papers*, *54*(4), 510–532.

Devana, M. S., Johns, W. E., Houk, A., & Zou, S. (2021). Rapid Freshening of Iceland Scotland Overflow Water Driven by Entrainment of a Major Upper Ocean Salinity Anomaly. *Geophysical Research Letters*, *48*(22).

Dickson, B., Dye, S., Jónsson, S., Köhl, A., Macrander, A., Marnela, M., Meincke, J., Olsen, S., Rudels, B., Valdimarsson, H., & Voet, G. (2008). The Overflow Flux West of Iceland: Variability, Origins and Forcing. In R. R. Dickson, J. Meincke, & P. Rhines (Eds.), *Arctic–Subarctic Ocean Fluxes* (pp. 443–474). Springer Netherlands.

Dickson, B., Yashayaev, I., Meincke, J., Turrell, B., Dye, S., & Holfort, J. (2002). Rapid freshening of the deep North Atlantic Ocean over the past four decades. *Nature*, *416*(6883), 832–837.

Dickson, R. R., & Brown, J. (1994). The production of North Atlantic Deep Water: Sources, rates, and pathways. *Journal of Geophysical Research: Oceans*, *99*(C6), 12319–12341.

Dong, B., & Sutton, R. T. (2005). Mechanism of Interdecadal Thermohaline Circulation Variability in a Coupled Ocean–Atmosphere GCM. *Journal of Climate*, *18*(8), 1117–1135.

Döös, K., Nycander, J., & Coward, A. C. (2008). Lagrangian decomposition of the Deacon Cell. *Journal of Geophysical Research: Oceans*, *113*(C7).

Döös, K. (1995). Interocean exchange of water masses. *Journal of Geophysical Research: Oceans*, *100*(C7), 13499–13514.

Döös, K., Jönsson, B., & Kjellsson, J. (2017). Evaluation of oceanic and atmospheric trajectory schemes in the TRACMASS trajectory model v6.0. *Geoscientific Model Development*, *10*(4), 1733–1749.

Döös, K., Kjellsson, J., & Jönsson, B. (2013). TRACMASS—A Lagrangian Trajectory Model. In T. Soomere & E. Quak (Eds.), *Preventive Methods for Coastal Protection* (pp. 225–249). Springer International Publishing.

Döös, K., Nilsson, J., Nycander, J., Brodeau, L., & Ballarotta, M. (2012). The World Ocean Thermohaline Circulation. *Journal of Physical Oceanography*, *42*(9), 1445–1460.

Döös, K., & Webb, D. J. (1994). The Deacon Cell and the Other Meridional Cells of the Southern Ocean. *Journal of Physical Oceanography*, *24*(2), 429–442.

d'Orgeville, M., & Peltier, W. R. (2007). On the Pacific Decadal Oscillation and the Atlantic Multidecadal Oscillation: Might they be related? *Geophysical Research Letters*, *34*(23), 2007GL031584.

Drijfhout, S. S., de Vries, P., Döös, K., & Coward, A. C. (2003). Impact of Eddy-Induced Transport on the Lagrangian Structure of the Upper Branch of the Thermohaline Circulation. *Journal of Physical Oceanography*, *33*(10), 2141–2155.

Drijfhout, S. S., Maier-Reimer, E., & Mikolajewicz, U. (1996). Tracing the conveyor belt in the Hamburg large-scale geostrophic ocean general circulation model. *Journal of Geophysical Research: Oceans*, *101*(C10), 22563–22575.

Duchez, A., Courtois, P., Harris, E., Josey, S. A., Kanzow, T., Marsh, R., Smeed, D. A., & Hirschi, J. J.-M. (2016). Potential for seasonal prediction of Atlantic sea surface temperatures using the RAPID array at 26 $$^{\circ }$$ ∘ N. *Climate Dynamics*, *46*(9-10), 3351–3370.

Dunstone, N. J., Smith, D. M., & Eade, R. (2011). Multi-year predictability of the tropical Atlantic atmosphere driven by the high latitude North Atlantic Ocean. *Geophysical Research Letters*, *38*(14), n/a–n/a.

Durgadoo, J. V., Loveday, B. R., Reason, C. J. C., Penven, P., & Biastoch, A. (2013). Agulhas Leakage Predominantly Responds to the Southern Hemisphere Westerlies. *Journal of Physical Oceanography*, *43*(10), 2113–2131.

Durgadoo, J. V., Rühs, S., Biastoch, A., & Böning, C. W. B. (2017). Indian Ocean sources of Agulhas leakage. *Journal of Geophysical Research: Oceans*, *122*(4), 3481–3499.

Dussin, R., Barnier, B., Brodeau, L., & Molines, J. (2016). *The making of the DRAKKAR forcing set DFS5* (Technical Report). Laboratoire de Glaciologie et G{\'{e}}ophysique de l'Environnement.

Eden, C., & Jung, T. (2001). North Atlantic Interdecadal Variability: Oceanic Response to the North Atlantic Oscillation (1865–1997). *Journal of Climate*, *14*(5), 676–691.

Eden, C., & Willebrand, J. (2001). Mechanism of Interannual to Decadal Variability of the North Atlantic Circulation. *Journal of Climate*, *14*(10), 2266–2280.

Eldevik, T., & Nilsen, J. E. Ø. (2013). The Arctic–Atlantic Thermohaline Circulation*. *Journal of Climate*, *26*(21), 8698–8705.

Eldevik, T., Nilsen, J. E. Ø., Iovino, D., Anders Olsson, K., Sandø, A. B., & Drange, H. (2009). Observed sources and variability of Nordic seas overflow. *Nature Geoscience*, *2*(6), 406–410.

Elliot, M., Labeyrie, L., & Duplessy, J.-C. (2002). Changes in North Atlantic deep-water formation associated with the Dansgaard–Oeschger temperature oscillations (60–10ka). *Quaternary Science Reviews*, *21*(10), 1153–1165.

Enfield, D. B., Mestas-Nuñez, A. M., & Trimble, P. J. (2001). The Atlantic Multidecadal Oscillation and its relation to rainfall and river flows in the continental U.S. *Geophysical Research Letters*, *28*(10), 2077–2080.

Evans, D. G., Holliday, N. P., Bacon, S., & Le Bras, I. (2023). Mixing and air–sea buoyancy fluxes set the time-mean overturning circulation in the subpolar North Atlantic and Nordic Seas. *Ocean Science*, *19*(3), 745–768.

Eyring, V., Bony, S., Meehl, G. A., Senior, C. A., Stevens, B., Stouffer, R. J., & Taylor, K. E. (2016). Overview of the Coupled Model Intercomparison Project Phase 6 (CMIP6) experimental design and organization. *Geoscientific Model Development*, *9*(5), 1937–1958.

Ezer, T., & Atkinson, L. P. (2014). Accelerated flooding along the U.S. East Coast: On the impact of sea-level rise, tides, storms, the Gulf Stream, and the North Atlantic Oscillations. *Earth's Future*, *2*(8), 362–382.

Fan, H., Borchert, L. F., Brune, S., Koul, V., & Baehr, J. (2023). North Atlantic subpolar gyre provides downstream ocean predictability. *npj Climate and Atmospheric Science*, *6*(1), 145.

Faure, V., & Speer, K. (2005). Labrador Sea Water circulation in the Northern North Atlantic Ocean. *Deep Sea Research Part II: Topical Studies in Oceanography*, *52*(3-4), 565–581.

Feng, S., & Hu, Q. (2008). How the North Atlantic Multidecadal Oscillation may have influenced the Indian summer monsoon during the past two millennia. *Geophysical Research Letters*, *35*(1), 2007GL032484.

Ferrari, R., & Ferreira, D. (2011). What processes drive the ocean heat transport? *Ocean Modelling*, *38*(3-4), 171–186.

Ferrari, R., & Wunsch, C. (2009). Ocean Circulation Kinetic Energy: Reservoirs, Sources, and Sinks. *Annual Review of Fluid Mechanics*, *41*(1), 253–282.

Feucher, C., Garcia-Quintana, Y., Yashayaev, I., Hu, X., & Myers, P. G. (2019). Labrador Sea Water Formation Rate and Its Impact on the Local Meridional Overturning Circulation. *Journal of Geophysical Research: Oceans*, *124*(8), 5654–5670.

Feulner, G., Rahmstorf, S., Levermann, A., & Volkwardt, S. (2013). On the Origin of the Surface Air Temperature Difference between the Hemispheres in Earth's Present-Day Climate. *Journal of Climate*, *26*(18), 7136–7150.

Fichefet, T., & Maqueda, M. A. M. (1999). Modelling the influence of snow accumulation and snow-ice formation on the seasonal cycle of the Antarctic sea-ice cover. *Climate Dynamics*, *15*(4), 251–268.

Fischer, J., & Schott, F. A. (2002). Labrador Sea Water Tracked by Profiling Floats—From the Boundary Current into the Open North Atlantic. *Journal of Physical Oceanography*, *32*(2), 573–584.

Flatau, M. K., Talley, L., & Niiler, P. P. (2003). The North Atlantic Oscillation, Surface Current Velocities, and SST Changes in the Subpolar North Atlantic. *Journal of Climate*, *16*(14), 2355–2369.

Florindo-López, C., Bacon, S., Aksenov, Y., Chafik, L., Colbourne, E., & Holliday, N. P. (2020). Arctic Ocean and Hudson Bay Freshwater Exports: New Estimates from Seven Decades of Hydrographic Surveys on the Labrador Shelf. *Journal of Climate*, *33*(20), 8849–8868.

Fofonoff, N., & Millard Jr., R. (1983). *Algorithms for the computation of fundamental properties of seawater.* (tech. rep.). [object Object].

Folland, C. K., Palmer, T. N., & Parker, D. E. (1986). Sahel rainfall and worldwide sea temperatures, 1901–85. *Nature*, *320*(6063), 602–607.

Folland, C. K., Colman, A. W., Rowell, D. P., & Davey, M. K. (2001). Predictability of Northeast Brazil Rainfall and Real-Time Forecast Skill, 1987–98. *Journal of Climate*, *14*(9), 1937–1958.

Foukal, N., & Chafik, L. (2024). Consensus Around a Common Definition of Atlantic Overturning Will Promote Progress. *Oceanography*.

Foukal, N. P., Gelderloos, R., & Pickart, R. S. (2020). A continuous pathway for fresh water along the East Greenland shelf. *Science Advances*, *6*(43), eabc4254.

Foukal, N. P., & Lozier, M. S. (2016). No inter-gyre pathway for sea-surface temperature anomalies in the North Atlantic. *Nature Communications*, *7*(1), 11333.

Foukal, N. P., & Lozier, M. S. (2018). Examining the Origins of Ocean Heat Content Variability in the Eastern North Atlantic Subpolar Gyre. *Geophysical Research Letters*, *45*(20).

Fox, A. D., Biastoch, A., Cunningham, S. A., Fraser, N., Handmann, P., Holliday, N. P., Johnson, C., Martin, T., Oltmanns, M., Rath, W., Rühs, S., Sanchez-Franks, A., & Schmidt, C. (2022, April). *Exceptional freshening and cooling in the eastern subpolar North Atlantic caused by reduced Labrador Sea surface heat loss* (Preprint). All Depths/Numerical Models/Deep Seas: North Atlantic/Gyres/Oceans and climate.

Fox-Kemper, B., Hewitt, H., Xiao, C., Aðalgeirsdóttir, G., Drijfhout, S., Edwards, T., Golledge, N., Hemer, N., Kopp, G., Mix, A., Notz, D., Nowicki, S., Nurhati, I., Ruiz, L., Sallée, J., Slangen, A., & Yu, Y. (2021). Ocean, Cryosphere and Sea Level Change. In V. Masson-Delmotte, P. Zhai, A. Pirani, S. Connors, C. Péan, S. Berger, N. Caud, Y. Chen, L. Goldfarb, Gomis, M. Huang, K. Leitzell, E. Lonnoy, J. Matthews, T. Maycock, T. Waterfield, O. Yelekçi, R. Yu, & B. Zhou (Eds.), *Climate Change 2021 – The Physical Science Basis: Working Group I Contribution to the Sixth Assessment Report of the Intergovernmental Panel on Climate Change* (1st ed.). Cambridge University Press.

Frajka-Williams, E., Foukal, N., & Danabasoglu, G. (2023). Should AMOC observations continue: How and why? *Philosophical Transactions of the Royal Society A: Mathematical, Physical and Engineering Sciences*, *381*(2262), 20220195.

Frajka-Williams, E., Lankhorst, M., Koelling, J., & Send, U. (2018). Coherent Circulation Changes in the Deep North Atlantic From 16°N and 26°N Transport Arrays. *Journal of Geophysical Research: Oceans*, *123*(5), 3427–3443.

Frajka-Williams, E., Ansorge, I. J., Baehr, J., Bryden, H. L., Chidichimo, M. P., Cunningham, S. A., Danabasoglu, G., Dong, S., Donohue, K. A., Elipot, S., Heimbach, P., Holliday, N. P., Hummels, R., Jackson, L. C., Karstensen, J., Lankhorst, M., Le Bras, I. A., Lozier, M. S., McDonagh, E. L., … Wilson, C. (2019). Atlantic Meridional Overturning Circulation: Observed Transport and Variability. *Frontiers in Marine Science*, *6*, 260.

Frajka-Williams, E., Rhines, P. B., & Eriksen, C. C. (2014). Horizontal Stratification during Deep Convection in the Labrador Sea. *Journal of Physical Oceanography*, *44*(1), 220–228.

Fraser, N. J., Fox, A. D., Cunningham, S. A., Rath, W., Schwarzkopf, F. U., & Biastoch, A. (2024). Vertical Velocity Dynamics in the North Atlantic and Implications for AMOC. *Journal of Physical Oceanography*.

Fratantoni, D. M. (2001). North Atlantic surface circulation during the 1990's observed with satellite-tracked drifters. *Journal of Geophysical Research: Oceans*, *106*(C10), 22067–22093.

Fratantoni, D. M., Johns, W. E., Townsend, T. L., & Hurlburt, H. E. (2000). Low-Latitude Circulation and Mass Transport Pathways in a Model of the Tropical Atlantic Ocean. *Journal of Physical Oceanography*, *30*(8), 1944–1966.

Fratantoni, D. M., Kwon, Y.-O., & Hodges, B. A. (2013). Direct observation of subtropical mode water circulation in the western North Atlantic Ocean. *Deep Sea Research Part II: Topical Studies in Oceanography*, *91*, 35–56.

Fratantoni, P. S., & Pickart, R. S. (2007). The Western North Atlantic Shelfbreak Current System in Summer. *Journal of Physical Oceanography*, *37*(10), 2509–2533.

Fried, N., & de Jong, M. F. (2022). The Role of the Irminger Current in the Irminger Sea Northward Transport Variability. *Journal of Geophysical Research: Oceans*, *127*(3), e2021JC018188.

Fried, N., Katsman, C. A., & de Jong, M. F. D. (2023, November). Where do the two cores of the Irminger Current come from? A Lagrangian study using a 1/10 degree ocean model simulation.

Frierson, D. M. W., Hwang, Y.-T., Fučkar, N. S., Seager, R., Kang, S. M., Donohoe, A., Maroon, E. A., Liu, X., & Battisti, D. S. (2013). Contribution of ocean overturning circulation to tropical rainfall peak in the Northern Hemisphere. *Nature Geoscience*, *6*(11), 940–944.

Fröhle, J., Handmann, P. V. K., & Biastoch, A. (2022). Major sources of North Atlantic Deep Water in the subpolar North Atlantic from Lagrangian analyses in an eddy-rich ocean model. *Ocean Science*, *18*(5), 1431–1450.

Fu, Y., Li, F., Karstensen, J., & Wang, C. (2020). A stable Atlantic Meridional Overturning Circulation in a changing North Atlantic Ocean since the 1990s. *Science Advances*, *6*(48), eabc7836.

Fu, Y., Lozier, M. S., Biló, T. C., Bower, A. S., Cunningham, S. A., Cyr, F., de Jong, M. F., de Young, B., Drysdale, L., Fraser, N., Fried, N., Furey, H. H., Han, G., Handmann, P., Holliday, N. P., Holte, J., Inall, M. E., Johns, W. E., Jones, S., . . . Yashayaev, I. (2023). Seasonality of the Meridional Overturning Circulation in the subpolar North Atlantic. *Communications Earth & Environment*, *4*(1), 181.

Furevik, T. (2001). Annual and interannual variability of Atlantic Water temperatures in the Norwegian and Barents Seas: 1980–1996. *Deep Sea Research Part I: Oceanographic Research Papers*, *48*(2), 383–404.

Furevik, T., & Nilsen, J. E. Ø. (2005). Large-scale atmospheric circulation variability and its impacts on the Nordic seas ocean climate: A review. In H. Drange, T. Dokken, T. Furevik, R. Gerdes, & W. Berger (Eds.), *Geophysical Monograph Series* (pp. 105–136, Vol. 158). American Geophysical Union.

Ganachaud, A., & Wunsch, C. (2000). Improved estimates of global ocean circulation, heat transport and mixing from hydrographic data. *Nature*, *408*(6811), 453–457.

Gary, S. F., Lozier, M. S., Kwon, Y.-O., & Park, J. J. (2014). The Fate of North Atlantic Subtropical Mode Water in the FLAME Model. *Journal of Physical Oceanography*, *44*(5), 1354–1371.

Gary, S. F., Lozier, M. S., Böning, C. W., & Biastoch, A. (2011). Deciphering the pathways for the deep limb of the Meridional Overturning Circulation. *Deep Sea Research Part II: Topical Studies in Oceanography*, *58*(17), 1781–1797.

Gaspar, P., Grégoris, Y., & Lefevre, J.-M. (1990). A simple eddy kinetic energy model for simulations of the oceanic vertical mixing: Tests at station Papa and long-term upper ocean study site. *Journal of Geophysical Research: Oceans*, *95*(C9), 16179–16193.

Gent, P. R. (2018). A commentary on the Atlantic meridional overturning circulation stability in climate models. *Ocean Modelling*, *122*, 57–66.

Gent, P. R., & Mcwilliams, J. C. (1990). Isopycnal Mixing in Ocean Circulation Models. *Journal of Physical Oceanography*, *20*(1), 150–155.

Georgiou, S., Van Der Boog, C. G., Brüggemann, N., Ypma, S. L., Pietrzak, J. D., & Katsman, C. A. (2019). On the interplay between downwelling, deep convection and mesoscale eddies in the Labrador Sea. *Ocean Modelling*, *135*, 56–70.

Georgiou, S., Ypma, S. L., Brüggemann, N., Sayol, J.-M., Pietrzak, J. D., & Katsman, C. A. (2020). Pathways of the water masses exiting the Labrador Sea: The importance of boundary–interior exchanges. *Ocean Modelling*, *150*, 101623.

Georgiou, S., Ypma, S. L., Brüggemann, N., Sayol, J.-M., Van Der Boog, C. G., Spence, P., Pietrzak, J. D., & Katsman, C. A. (2021). Direct and Indirect Pathways of Convected Water Masses and Their impacts on the Overturning Dynamics of the Labrador Sea. *Journal of Geophysical Research: Oceans*, *126*(1), e2020JC016654.

Germe, A., Hirschi, J. J.-M., Blaker, A. T., & Sinha, B. (2022). Chaotic Variability of the Atlantic Meridional Overturning Circulation at Subannual Time Scales. *Journal of Physical Oceanography*, *52*(5), 929–949.

Getzlaff, J., Böning, C. W., Eden, C., & Biastoch, A. (2005). Signal propagation related to the North Atlantic overturning. *Geophysical Research Letters*, *32*(9), 2004GL021002.

Girton, J. B., & Sanford, T. B. (2003). Descent and Modification of the Overflow Plume in the Denmark Strait*. *Journal of Physical Oceanography*, *33*(7), 1351–1364.

Glessmer, M. S., Eldevik, T., Våge, K., Øie Nilsen, J. E., & Behrens, E. (2014). Atlantic origin of observed and modelled freshwater anomalies in the Nordic Seas. *Nature Geoscience*, *7*(11), 801–805.

Gnanadesikan, A. (1999). A Simple Predictive Model for the Structure of the Oceanic Pycnocline. *Science*, *283*(5410), 2077–2079.

Goldsworth, F. W., Johnson, H. L., Marshall, D. P., & Le Bras, I. A. (2024). Destratifying and Restratifying Instabilities During Down-Front Wind Events: A Case Study in the Irminger Sea. *Journal of Geophysical Research: Oceans*, *129*(2), e2023JC020365.

Good, S. A., Martin, M. J., & Rayner, N. A. (2013). EN4: Quality controlled ocean temperature and salinity profiles and monthly objective analyses with uncertainty estimates. *Journal of Geophysical Research: Oceans*, *118*(12), 6704–6716.

Gordon, A. L. (1986). Interocean exchange of thermocline water. *Journal of Geophysical Research: Oceans*, *91*(C4), 5037–5046.

Gordon, A. L. (1991). The Role of Thermohaline Circulation in Global Climate Change.

Goswami, B. N., Madhusoodanan, M. S., Neema, C. P., & Sengupta, D. (2006). A physical mechanism for North Atlantic SST influence on the Indian summer monsoon. *Geophysical Research Letters*, *33*(2), 2005GL024803.

Grégorio, S., Penduff, T., Sérazin, G., Molines, J.-M., Barnier, B., & Hirschi, J. (2015). Intrinsic Variability of the Atlantic Meridional Overturning Circulation at Interannual-to-Multidecadal Time Scales. *Journal of Physical Oceanography*, *45*(7), 1929–1946.

Griffies, S. M., Danabasoglu, G., Durack, P. J., Adcroft, A. J., Balaji, V., Böning, C. W., Chassignet, E. P., Curchitser, E., Deshayes, J., Drange, H., Fox-Kemper, B., Gleckler, P. J., Gregory, J. M., Haak, H., Hallberg, R. W., Heimbach, P., Hewitt, H. T., Holland, D. M., Ilyina, T., . . . Yeager, S. G. (2016). OMIP contribution to CMIP6: Experimental and diagnostic protocol for the physical component of the Ocean Model Intercomparison Project. *Geoscientific Model Development*, *9*(9), 3231–3296.

Griffies, S. M., & Tziperman, E. (1995). A Linear Thermohaline Oscillator Driven by Stochastic Atmospheric Forcing. *Journal of Climate*, *8*(10), 2440–2453.

Grist, J. P., Josey, S. A., Jacobs, Z. L., Marsh, R., Sinha, B., & Van Sebille, E. (2016). Extreme air–sea interaction over the North Atlantic subpolar gyre during the winter of 2013–2014 and its sub-surface legacy. *Climate Dynamics*, *46*(11-12), 4027–4045.

Grist, J. P., Josey, S. A., Marsh, R., Good, S. A., Coward, A. C., De Cuevas, B. A., Alderson, S. G., New, A. L., & Madec, G. (2010). The roles of surface heat flux and ocean heat transport convergence in determining Atlantic Ocean temperature variability. *Ocean Dynamics*, *60*(4), 771–790.

Grist, J. P., Marsh, R., & Josey, S. A. (2009). On the Relationship between the North Atlantic Meridional Overturning Circulation and the Surface-Forced Overturning Streamfunction. *Journal of Climate*, *22*(19), 4989–5002.

Groeskamp, S., Zika, J. D., Sloyan, B. M., McDougall, T. J., & McIntosh, P. C. (2014). A Thermohaline Inverse Method for Estimating Diathermohaline Circulation and Mixing. *Journal of Physical Oceanography*, *44*(10), 2681–2697.

Grootes, P. M., Stuiver, M., White, J. W. C., Johnsen, S., & Jouzel, J. (1993). Comparison of oxygen isotope records from the GISP2 and GRIP Greenland ice cores. *Nature*, *366*(6455), 552–554.

Gulev, S., Thorne, P., Ahn, J., Dentener, F., Domingues, C., Gerland, S., Gong, D., Kaufman, D., Nnamchi, H., Quaas, J., Rivera, J., Sathyendranath, S., Smith, S., Trewin, B., von Schuckmann, K., & Vose, R. (2021). Changing State of the Climate System. In V. Masson-Delmotte, P. Zhai, A. Pirani, S. Connors, C. Péan, S. Berger, N. Caud, Y. Chen, L. Goldfarb, Gomis, M. Huang, K. Leitzell, E. Lonnoy, J. Matthews, T. Maycock, T. Waterfield, O. Yelekçi, R. Yu, & B. Zhou (Eds.), *Climate Change 2021 – The Physical Science Basis: Working Group I Contribution to the Sixth Assessment Report of the Intergovernmental Panel on Climate Change* (1st ed.). Cambridge University Press.

Hakkinen, S., & Rhines, P. B. (2009). Shifting surface currents in the northern North Atlantic Ocean. *Journal of Geophysical Research: Oceans*, *114*(C4), 2008JC004883.

Häkkinen, S. (1999). A Simulation of Thermohaline Effects of a Great Salinity Anomaly. *Journal of Climate*, *12*(6), 1781–1795.

Häkkinen, S., & Rhines, P. B. (2004). Decline of Subpolar North Atlantic Circulation During the 1990s. *Science*, *304*(5670), 555–559.

Häkkinen, S., Rhines, P. B., & Worthen, D. L. (2011). Warm and saline events embedded in the meridional circulation of the northern North Atlantic. *Journal of Geophysical Research*, *116*(C3), C03006.

Hall, M. M., Torres, D. J., & Yashayaev, I. (2013). Absolute velocity along the AR7W section in the Labrador Sea. *Deep Sea Research Part I: Oceanographic Research Papers*, *72*, 72–87.

Hall, M. M., & Bryden, H. L. (1982). Direct estimates and mechanisms of ocean heat transport. *Deep Sea Research Part A. Oceanographic Research Papers*, *29*(3), 339–359.

Hallberg, R. (2013). Using a resolution function to regulate parameterizations of oceanic mesoscale eddy effects. *Ocean Modelling*, *72*, 92–103.

Halliwell, G., Weisberg, R., & Mayer, D. (2003). A synthetic float analysis of upper-limb meridional overturning circulation interior ocean pathways in the tropical/subtropical Atlantic. In *Elsevier Oceanography Series* (pp. 93–136, Vol. 68). Elsevier.

Hanawa, K., & Talley, L. D. (2001). Chapter 5.4 Mode waters. In *International Geophysics* (pp. 373–386, Vol. 77). Elsevier.

Haney, R. (1971). Surface thermal boundary condition for ocean circulation models. *Journal of Physical Oceanography*, *1*, 241–248.

Hansell, D., Carlson, C., Repeta, D., & Schlitzer, R. (2009). Dissolved Organic Matter in the Ocean: A Controversy Stimulates New Insights. *Oceanography*, *22*(4), 202–211.

Hansen, B., & Østerhus, S. (2000). North Atlantic–Nordic Seas exchanges. *Progress in Oceanography*, *45*(2), 109–208.

Hansen, B., Østerhus, S., Turrell, W. R., Jónsson, S., Valdimarsson, H., Hátún, H., & Olsen, S. M. (2008). The Inflow of Atlantic Water, Heat, and Salt to the Nordic Seas Across the Greenland–Scotland Ridge. In R. R. Dickson, J. Meincke, & P. Rhines (Eds.), *Arctic–Subarctic Ocean Fluxes* (pp. 15–43). Springer Netherlands.

Hassan, T., Allen, R. J., Liu, W., & Randles, C. A. (2021). Anthropogenic aerosol forcing of the Atlantic meridional overturning circulation and the associated mechanisms in CMIP6 models. *Atmospheric Chemistry and Physics*, *21*(8), 5821–5846.

Hátún, H., Sandø, A. B., Drange, H., Hansen, B., & Valdimarsson, H. (2005). Influence of the Atlantic Subpolar Gyre on the Thermohaline Circulation. *Science*, *309*(5742), 1841–1844.

Hawkins, E., & Sutton, R. (2009). Decadal Predictability of the Atlantic Ocean in a Coupled GCM: Forecast Skill and Optimal Perturbations Using Linear Inverse Modeling. *Journal of Climate*, *22*(14), 3960–3978.

Held, I. M. (2001). The Partitioning of the Poleward Energy Transport between the Tropical Ocean and Atmosphere. *Journal of the Atmospheric Sciences*, *58*(8), 943–948.

Henry, L. G., McManus, J. F., Curry, W. B., Roberts, N. L., Piotrowski, A. M., & Keigwin, L. D. (2016). North Atlantic ocean circulation and abrupt climate change during the last glaciation. *Science*, *353*(6298), 470–474.

Hermanson, L., Dunstone, N., Haines, K., Robson, J., Smith, D., & Sutton, R. (2014). A novel transport assimilation method for the Atlantic meridional overturning circulation at 26°N. *Quarterly Journal of the Royal Meteorological Society*, *140*(685), 2563–2572.

Herrford, J., Brandt, P., Kanzow, T., Hummels, R., Araujo, M., & Durgadoo, J. V. (2021). Seasonal variability of the Atlantic Meridional Overturning Circulation at 11° S inferred from bottom pressure measurements. *Ocean Science*, *17*(1), 265–284.

Heuzé, C. (2017). North Atlantic deep water formation and AMOC in CMIP5 models. *Ocean Science*, *13*(4), 609–622.

Heuzé, C. (2021). Antarctic Bottom Water and North Atlantic Deep Water in CMIP6 models. *Ocean Science*, *17*(1), 59–90.

Hirschi, J., Baehr, J., Marotzke, J., Stark, J., Cunningham, S., & Beismann, J.-O. (2003). A monitoring design for the Atlantic meridional overturning circulation. *Geophysical Research Letters*, *30*(7), 2002GL016776.

Hirschi, J., & Marotzke, J. (2007). Reconstructing the Meridional Overturning Circulation from Boundary Densities and the Zonal Wind Stress. *Journal of Physical Oceanography*, *37*(3), 743–763.

Hirschi, J. J.-M., Blaker, A. T., Sinha, B., Coward, A., De Cuevas, B., Alderson, S., & Madec, G. (2013). Chaotic variability of the meridional overturning circulation on subannual to interannual timescales. *Ocean Science*, *9*(5), 805–823.

Hirschi, J. J.-M., Barnier, B., Böning, C., Biastoch, A., Blaker, A. T., Coward, A., Danilov, S., Drijfhout, S., Getzlaff, K., Griffies, S. M., Hasumi, H., Hewitt, H., Iovino, D., Kawasaki, T., Kiss, A. E., Koldunov, N., Marzocchi, A., Mecking, J. V., Moat, B., . . . Xu, X. (2020). The Atlantic Meridional Overturning Circulation in High-Resolution Models. *Journal of Geophysical Research: Oceans*, *125*(4).

Hogg, N. G. (1992). On the transport of the gulf stream between cape hatteras and the grand banks. *Deep Sea Research Part A. Oceanographic Research Papers*, *39*(7-8), 1231–1246.

Hogg, N. G., & Johns, W. E. (1995). Western boundary currents. *Reviews of Geophysics*, *33*(S2), 1311–1334.

Hogg, N. G., Pickart, R. S., Hendry, R. M., & Smethie, W. J. (1986). The northern recirculation gyre of the gulf Stream. *Deep Sea Research Part A. Oceanographic Research Papers*, *33*(9), 1139–1165.

Holliday, N. P. (2003). Air-sea interaction and circulation changes in the northeast Atlantic. *Journal of Geophysical Research: Oceans*, *108*(C8), 2002JC001344.

Holliday, N. P., Bacon, S., Allen, J., & McDonagh, E. L. (2009). Circulation and Transport in the Western Boundary Currents at Cape Farewell, Greenland. *Journal of Physical Oceanography*, *39*(8), 1854–1870.

Holliday, N. P., Bacon, S., Cunningham, S. A., Gary, S. F., Karstensen, J., King, B. A., Li, F., & Mcdonagh, E. L. (2018). Subpolar North Atlantic Overturning and Gyre-Scale Circulation in the Summers of 2014 and 2016. *Journal of Geophysical Research: Oceans*, *123*(7), 4538–4559.

Holliday, N. P., Bersch, M., Berx, B., Chafik, L., Cunningham, S., Florindo-López, C., Hátún, H., Johns, W., Josey, S. A., Larsen, K. M. H., Mulet, S., Oltmanns, M., Reverdin, G., Rossby, T., Thierry, V., Valdimarsson, H., & Yashayaev, I. (2020). Ocean circulation causes the largest freshening event for 120 years in eastern subpolar North Atlantic. *Nature Communications*, *11*(1), 585.

Holliday, N. P., Hughes, S. L., Bacon, S., Beszczynska-Möller, A., Hansen, B., Lavín, A., Loeng, H., Mork, K. A., Østerhus, S., Sherwin, T., & Walczowski, W. (2008). Reversal of the 1960s to 1990s freshening trend in the northeast North Atlantic and Nordic Seas. *Geophysical Research Letters*, *35*(3), 2007GL032675.

Holte, J., & Straneo, F. (2017). Seasonal Overturning of the Labrador Sea as Observed by Argo Floats. *Journal of Physical Oceanography*, *47*(10), 2531–2543.

Houpert, L., Cunningham, S., Fraser, N., Johnson, C., Holliday, N. P., Jones, S., Moat, B., & Rayner, D. (2020). Observed Variability of the North Atlantic Current in the Rockall Trough From 4 Years of Mooring Measurements. *Journal of Geophysical Research: Oceans*, *125*(10).

Houpert, L., Inall, M. E., Dumont, E., Gary, S., Johnson, C., Porter, M., Johns, W. E., & Cunningham, S. A. (2018). Structure and Transport of the North Atlantic Current in the Eastern Subpolar Gyre From Sustained Glider Observations. *Journal of Geophysical Research: Oceans*, *123*(8), 6019–6038.

Hu, A., Meehl, G. A., Han, W., & Yin, J. (2009). Transient response of the MOC and climate to potential melting of the Greenland Ice Sheet in the 21st century. *Geophysical Research Letters*, *36*(10), 2009GL037998.

Hunke, E. C., & Lipscomb, W. H. (2010). *CICE: The Los Alamos Sea Ice Model Documentation and Software User's Manual Version 4.* (tech. rep. No. LA-CC-06-012). Los Alamos National Laboratory.

Hurrell, J. W. (1995). Decadal Trends in the North Atlantic Oscillation: Regional Temperatures and Precipitation. *Science*, *269*(5224), 676–679.

Isachsen, P. E., Mauritzen, C., & Svendsen, H. (2007). Dense water formation in the Nordic Seas diagnosed from sea surface buoyancy fluxes. *Deep Sea Research Part I: Oceanographic Research Papers*, *54*(1), 22–41.

Jackson, L. C., Kahana, R., Graham, T., Ringer, M. A., Woollings, T., Mecking, J. V., & Wood, R. A. (2015). Global and European climate impacts of a slowdown of the AMOC in a high resolution GCM. *Climate Dynamics*, *45*(11-12), 3299–3316.

Jackson, L. C., & Petit, T. (2023). North Atlantic overturning and water mass transformation in CMIP6 models. *Climate Dynamics*, *60*(9-10), 2871–2891.

Jackson, L. C., & Wood, R. A. (2020). Fingerprints for Early Detection of Changes in the AMOC. *Journal of Climate*, *33*(16), 7027–7044.

Jackson, L. C., Alastrué De Asenjo, E., Bellomo, K., Danabasoglu, G., Haak, H., Hu, A., Jungclaus, J., Lee, W., Meccia, V. L., Saenko, O., Shao, A., & Swingedouw, D. (2023a). Understanding AMOC stability: The North Atlantic Hosing Model Intercomparison Project. *Geoscientific Model Development*, *16*(7), 1975–1995.

Jackson, L. C., Biastoch, A., Buckley, M. W., Desbruyères, D. G., Frajka-Williams, E., Moat, B., & Robson, J. (2022). The evolution of the North Atlantic Meridional Overturning Circulation since 1980. *Nature Reviews Earth & Environment*, *3*(4), 241–254.

Jackson, L. C., Hewitt, H. T., Bruciaferri, D., Calvert, D., Graham, T., Guiavarc'h, C., Menary, M. B., New, A. L., Roberts, M., & Storkey, D. (2023b). Challenges simulating the AMOC in climate models. *Philosophical Transactions of the Royal Society A: Mathematical, Physical and Engineering Sciences*, *381*(2262), 20220187.

Jackson, L. C., Peterson, K. A., Roberts, C. D., & Wood, R. A. (2016). Recent slowing of Atlantic overturning circulation as a recovery from earlier strengthening. *Nature Geoscience*, *9*(7), 518–522.

Jacobs, Z. L., Grist, J. P., Marsh, R., & Josey, S. A. (2019). A Subannual Subsurface Pathway From the Gulf Stream to the Subpolar Gyre and Its Role in Warming and Salinification in the 1990s. *Geophysical Research Letters*, *46*(13), 7518–7526.

Jayne, S. R., & Marotzke, J. (2001). The dynamics of ocean heat transport variability. *Reviews of Geophysics*, *39*(3), 385–411.

Jean-Marc Molines. (2021, March). Meom-configurations/ORCA025.L75-GJM189.

Jochumsen, K., Quadfasel, D., Valdimarsson, H., & Jónsson, S. (2012). Variability of the Denmark Strait overflow: Moored time series from 1996–2011. *Journal of Geophysical Research: Oceans*, *117*(C12), 2012JC008244.

Johns, W. E., Baringer, M. O., Beal, L. M., Cunningham, S. A., Kanzow, T., Bryden, H. L., Hirschi, J. J. M., Marotzke, J., Meinen, C. S., Shaw, B., & Curry, R. (2011). Continuous, Array-Based Estimates of Atlantic Ocean Heat Transport at 26.5°N. *Journal of Climate*, *24*(10), 2429–2449.

Johns, W. E., Devana, M., Houk, A., & Zou, S. (2021). Moored Observations of the Iceland-Scotland Overflow Plume Along the Eastern Flank of the Reykjanes Ridge. *Journal of Geophysical Research: Oceans*, *126*(8), e2021JC017524.

Johns, W. E., Shay, T. J., Bane, J. M., & Watts, D. R. (1995). Gulf Stream structure, transport, and recirculation near 68°W. *Journal of Geophysical Research: Oceans*, *100*(C1), 817–838.

Johns, W., Elipot, S., Smeed, D., Moat, B., KING, B., Volkov, D., & Smith, R. (2023a). Atlantic Meridional Overturning Circulation (AMOC) Heat Transport Time Series between April 2004 and December 2020 at 26.5°N.

Johns, W. E., Elipot, S., Smeed, D. A., Moat, B., King, B., Volkov, D. L., & Smith, R. H. (2023b). Towards two decades of Atlantic Ocean mass and heat transports at 26.5° N. *Philosophical Transactions of the Royal Society A: Mathematical, Physical and Engineering Sciences*, *381*(2262), 20220188.

Johns, W. E., Townsend, T. L., Fratantoni, D. M., & Wilson, W. (2002). On the Atlantic inflow to the Caribbean Sea. *Deep Sea Research Part I: Oceanographic Research Papers*, *49*(2), 211–243.

Johnson, H. L., Cessi, P., Marshall, D. P., Schloesser, F., & Spall, M. A. (2019). Recent Contributions of Theory to Our Understanding of the Atlantic Meridional Overturning Circulation. *Journal of Geophysical Research: Oceans*, *124*(8), 5376–5399.

Johnson, H. L., & Marshall, D. P. (2002). A Theory for the Surface Atlantic Response to Thermohaline Variability. *Journal of Physical Oceanography*, *32*(4), 1121–1132.

Johnson, H. L., Marshall, D. P., & Sproson, D. A. J. (2007). Reconciling theories of a mechanically driven meridional overturning circulation with thermohaline forcing and multiple equilibria. *Climate Dynamics*, *29*(7-8), 821–836.

Jones, B. T., Solow, A., & Ji, R. (2016). Resource Allocation for Lagrangian Tracking. *Journal of Atmospheric and Oceanic Technology*, *33*(6), 1225–1235.

Jones, C. S., Jiang, S., & Abernathey, R. P. (2024). A Comparison of Diagnostics for AMOC Heat Transport Applied to the CESM Large Ensemble. *Journal of Advances in Modeling Earth Systems*, *16*(8), e2023MS003978.

Jones, S. C., Fraser, N. J., Cunningham, S. A., Fox, A. D., & Inall, M. E. (2023). Observation-based estimates of volume, heat, and freshwater exchanges between the subpolar North Atlantic interior, its boundary currents, and the atmosphere. *Ocean Science*, *19*(1), 169–192.

Jónsson, S., & Valdimarsson, H. (2005). The flow of Atlantic water to the North Icelandic Shelf and its relation to the drift of cod larvae. *ICES Journal of Marine Science*, *62*(7), 1350–1359.

Jónsson, S., & Valdimarsson, H. (2012). Water mass transport variability to the North Icelandic shelf, 1994–2010. *ICES Journal of Marine Science*, *69*(5), 809–815.

Josey, S. A., Grist, J. P., & Marsh, R. (2009). Estimates of meridional overturning circulation variability in the North Atlantic from surface density flux fields. *Journal of Geophysical Research: Oceans*, *114*(C9), 2008JC005230.

Jourdan, D., Balopoulos, E., Garcia-Fernandez, M.-J., & Maillard, C. (1998). Objective analysis of temperature and salinity historical data set over the Mediterranean basin. *IEEE Oceanic Engineering Society. OCEANS'98. Conference Proceedings (Cat. No.98CH36259)*, *1*, 82–87.

Joyce, T. M., Thomas, L. N., Dewar, W. K., & Girton, J. B. (2013). Eighteen Degree Water formation within the Gulf Stream during CLIMODE. *Deep Sea Research Part II: Topical Studies in Oceanography*, *91*, 1–10.

Jutras, M., Dufour, C. O., Mucci, A., & Talbot, L. C. (2023). Large-scale control of the retroflection of the Labrador Current. *Nature Communications*, *14*(1), 2623.

Kang, I.-S., No, H.-h., & Kucharski, F. (2014). ENSO Amplitude Modulation Associated with the Mean SST Changes in the Tropical Central Pacific Induced by Atlantic Multidecadal Oscillation. *Journal of Climate*, *27*(20), 7911–7920.

Kang, S. M., Held, I. M., Frierson, D. M. W., & Zhao, M. (2008). The Response of the ITCZ to Extratropical Thermal Forcing: Idealized Slab-Ocean Experiments with a GCM. *Journal of Climate*, *21*(14), 3521–3532.

Kanzow, T., Cunningham, S. A., Johns, W. E., Hirschi, J. J.-M., Marotzke, J., Baringer, M. O., Meinen, C. S., Chidichimo, M. P., Atkinson, C., Beal, L. M., Bryden, H. L., & Collins, J. (2010). Seasonal Variability of the Atlantic Meridional Overturning Circulation at 26.5°N. *Journal of Climate*, *23*(21), 5678–5698.

Kanzow, T., Cunningham, S. A., Rayner, D., Hirschi, J. J.-M., Johns, W. E., Baringer, M. O., Bryden, H. L., Beal, L. M., Meinen, C. S., & Marotzke, J. (2007). Observed Flow Compensation Associated with the MOC at 26.5°N in the Atlantic. *Science*, *317*(5840), 938–941.

Kanzow, T., Send, U., Zenk, W., Chave, A. D., & Rhein, M. (2006). Monitoring the integrated deep meridional flow in the tropical North Atlantic: Long-term performance of a geostrophic array. *Deep Sea Research Part I: Oceanographic Research Papers*, *53*(3), 528–546.

Kanzow, T., & Zenk, W. (2014). Structure and transport of the Iceland Scotland Overflow plume along the Reykjanes Ridge in the Iceland Basin. *Deep Sea Research Part I: Oceanographic Research Papers*, *86*, 82–93.

Katsman, C. A., Spall, M. A., & Pickart, R. S. (2004). Boundary Current Eddies and Their Role in the Restratification of the Labrador Sea*. *Journal of Physical Oceanography*, *34*(9), 1967–1983.

Keenlyside, N. S., Latif, M., Jungclaus, J., Kornblueh, L., & Roeckner, E. (2008). Advancing decadal-scale climate prediction in the North Atlantic sector. *Nature*, *453*(7191), 84–88.

Keigwin, L. D., & Lehman, S. J. (1994). Deep circulation change linked to HEINRICH Event 1 and Younger Dryas in a middepth North Atlantic Core. *Paleoceanography*, *9*(2), 185–194.

Kerr, R. A. (2000). A North Atlantic Climate Pacemaker for the Centuries. *Science*, *288*(5473), 1984–1985.

Kersalé, M., Meinen, C. S., Perez, R. C., Le Hénaff, M., Valla, D., Lamont, T., Sato, O. T., Dong, S., Terre, T., Van Caspel, M., Chidichimo, M. P., Van Den Berg, M., Speich, S., Piola, A. R., Campos, E. J. D., Ansorge, I., Volkov, D. L., Lumpkin, R., & Garzoli, S. L. (2020). Highly variable upper and abyssal overturning cells in the South Atlantic. *Science Advances*, *6*(32), eaba7573.

Khatri, H., Williams, R. G., Woollings, T., & Smith, D. M. (2022). Fast and Slow Subpolar Ocean Responses to the North Atlantic Oscillation: Thermal and Dynamical Changes. *Geophysical Research Letters*, *49*(24), e2022GL101480.

Kieke, D., Rhein, M., Stramma, L., Smethie, W. M., Bullister, J. L., & LeBel, D. A. (2007). Changes in the pool of Labrador Sea Water in the subpolar North Atlantic. *Geophysical Research Letters*, *34*(6), L06605.

Kim, W. M., Ruprich-Robert, Y., Zhao, A., Yeager, S., & Robson, J. (2024). North Atlantic Response to Observed North Atlantic Oscillation Surface Heat Flux in Three Climate Models. *Journal of Climate*, *37*(5), 1777–1796.

Kim, W. M., Yeager, S., Chang, P., & Danabasoglu, G. (2018a). Low-Frequency North Atlantic Climate Variability in the Community Earth System Model Large Ensemble. *Journal of Climate*, *31*(2), 787–813.

Kim, W. M., Yeager, S., & Danabasoglu, G. (2020). Atlantic Multidecadal Variability and Associated Climate Impacts Initiated by Ocean Thermohaline Dynamics. *Journal of Climate*, *33*(4), 1317–1334.

Kim, W. M., Yeager, S. G., & Danabasoglu, G. (2018b). Key Role of Internal Ocean Dynamics in Atlantic Multidecadal Variability During the Last Half Century. *Geophysical Research Letters*, *45*(24).

Kjellsson, J., & Döös, K. (2012). Lagrangian decomposition of the Hadley and Ferrel cells. *Geophysical Research Letters*, *39*(15), 2012GL052420.

Knight, J. R., Allan, R. J., Folland, C. K., Vellinga, M., & Mann, M. E. (2005). A signature of persistent natural thermohaline circulation cycles in observed climate. *Geophysical Research Letters*, *32*(20), 2005GL024233.

Knight, J. R., Folland, C. K., & Scaife, A. A. (2006). Climate impacts of the Atlantic Multidecadal Oscillation. *Geophysical Research Letters*, *33*(17), 2006GL026242.

Koelling, J., Atamanchuk, D., Karstensen, J., Handmann, P., & Wallace, D. W. R. (2022). Oxygen export to the deep ocean following Labrador Sea Water formation. *Biogeosciences*, *19*(2), 437–454.

Koelling, J., Wallace, D. W. R., Send, U., & Karstensen, J. (2017). Intense oceanic uptake of oxygen during 2014–2015 winter convection in the Labrador Sea. *Geophysical Research Letters*, *44*(15), 7855–7864.

Köhl, A. (2005). Anomalies of Meridional Overturning: Mechanisms in the North Atlantic. *Journal of Physical Oceanography*, *35*(8), 1455–1472.

Koman, G., Johns, W. E., & Houk, A. (2020). Transport and Evolution of the East Reykjanes Ridge Current. *Journal of Geophysical Research: Oceans*, *125*(10).

Koman, G., Johns, W., Houk, A., Houpert, L., & Li, F. (2022). Circulation and overturning in the eastern North Atlantic subpolar gyre. *Progress in Oceanography*, *208*, 102884.

Kostov, Y., Armour, K. C., & Marshall, J. (2014). Impact of the Atlantic meridional overturning circulation on ocean heat storage and transient climate change. *Geophysical Research Letters*, *41*(6), 2108–2116.

Kostov, Y., Messias, M.-J., Mercier, H., Johnson, H. L., & Marshall, D. P. (2023). Fast mechanisms linking the Labrador Sea with subtropical Atlantic overturning. *Climate Dynamics*, *60*(9-10), 2687–2712.

Kostov, Y., Messias, M.-J., Mercier, H., Marshall, D. P., & Johnson, H. L. (2024). Surface factors controlling the volume of accumulated Labrador Sea Water. *Ocean Science*, *20*(2), 521–547.

Koszalka, I. M., Haine, T. W. N., & Magaldi, M. G. (2013). Fates and Travel Times of Denmark Strait Overflow Water in the Irminger Basin. *Journal of Physical Oceanography*, *43*(12), 2611–2628.

Krauss, W. (1986). The North Atlantic Current. *Journal of Geophysical Research: Oceans*, *91*(C4), 5061–5074.

Krauss, W. (1995). Currents and mixing in the Irminger Sea and in the Iceland Basin. *Journal of Geophysical Research: Oceans*, *100*(C6), 10851–10871.

Kuhlbrodt, T., Griesel, A., Montoya, M., Levermann, A., Hofmann, M., & Rahmstorf, S. (2007). On the driving processes of the Atlantic meridional overturning circulation. *Reviews of Geophysics*, *45*(2), RG2001.

Kushnir, Y. (1994). Interdecadal Variations in North Atlantic Sea Surface Temperature and Associated Atmospheric Conditions. *Journal of Climate*, *7*(1), 141–157.

Kushnir, Y., Seager, R., Ting, M., Naik, N., & Nakamura, J. (2010). Mechanisms of Tropical Atlantic SST Influence on North American Precipitation Variability*. *Journal of Climate*, *23*(21), 5610–5628.

Kwon, Y.-O., Park, J.-J., Gary, S. F., & Lozier, M. S. (2015). Year-to-Year Reoutcropping of Eighteen Degree Water in an Eddy-Resolving Ocean Simulation. *Journal of Physical Oceanography*, *45*(4), 1189–1204.

Kwon, Y.-O., & Riser, S. C. (2004). North Atlantic Subtropical Mode Water: A history of ocean-atmosphere interaction 1961–2000. *Geophysical Research Letters*, *31*(19), 2004GL021116.

Kwon, Y.-O., & Riser, S. C. (2005). General circulation of the western subtropical North Atlantic observed using profiling floats. *Journal of Geophysical Research: Oceans*, *110*(C10), 2005JC002909.

Lambert, E., Eldevik, T., & Spall, M. A. (2018). On the Dynamics and Water Mass Transformation of a Boundary Current Connecting Alpha and Beta Oceans. *Journal of Physical Oceanography*, *48*(10), 2457–2475.

Lampitt, R., Salter, I., De Cuevas, B., Hartman, S., Larkin, K., & Pebody, C. (2010). Long-term variability of downward particle flux in the deep northeast Atlantic: Causes and trends. *Deep Sea Research Part II: Topical Studies in Oceanography*, *57*(15), 1346–1361.

Lankhorst, M., & Zenk, W. (2006). Lagrangian Observations of the Middepth and Deep Velocity Fields of the Northeastern Atlantic Ocean. *Journal of Physical Oceanography*, *36*(1), 43–63.

Large, W. G., McWilliams, J. C., & Doney, S. C. (1994). Oceanic vertical mixing: A review and a model with a nonlocal boundary layer parameterization. *Reviews of Geophysics*, *32*(4), 363.

Large, W., & Yeager, S. (2004). *Diurnal to decadal global forcing for ocean and sea-ice models: The data sets and flux climatologies.* (NCAR Technical Note No. NCAR/TN-460+STR). CGD Division of the National Center for Atmospheric Research.

Larson, S. M., Buckley, M. W., & Clement, A. C. (2020). Extracting the Buoyancy-Driven Atlantic Meridional Overturning Circulation. *Journal of Climate*, *33*(11), 4697–4714.

Latif, M., Böning, C. W., Willebrand, J., Biastoch, A., Alvarez-Garcia, F., Keenlyside, N., & Pohlmann, H. (2007). Decadal to multidecadal variability of the Atlantic MOC: Mechanisms and predictability. In A. Schmittner, J. C. H. Chiang, & S. R. Hemming (Eds.), *Geophysical Monograph Series* (pp. 149–166, Vol. 173). American Geophysical Union.

Lavender, K. L., Brechner Owens, W., & Davis, R. E. (2005). The mid-depth circulation of the subpolar North Atlantic Ocean as measured by subsurface floats. *Deep Sea Research Part I: Oceanographic Research Papers*, *52*(5), 767–785.

Lavender, K. L., Davis, R. E., & Owens, W. B. (2000). Mid-depth recirculation observed in the interior Labrador and Irminger seas by direct velocity measurements. *Nature*, *407*(6800), 66–69.

Lazier, J. R. N., & Wright, D. G. (1993). Annual Velocity Variations in the Labrador Current. *Journal of Physical Oceanography*, *23*(4), 659–678.

Lazier, J. R. (1980). Oceanographic conditions at Ocean Weather Ship *Bravo* , 1964–1974. *Atmosphere-Ocean*, *18*(3), 227–238.

Le Bras, I. A.-A., Callies, J., Straneo, F., Biló, T. C., Holte, J., & Johnson, H. L. (2022). Slantwise Convection in the Irminger Sea. *Journal of Geophysical Research: Oceans*, *127*(10), e2022JC019071.

Le Bras, I. A.-A., Straneo, F., Holte, J., de Jong, M. F., & Holliday, N. P. (2020). Rapid Export of Waters Formed by Convection Near the Irminger Sea's Western Boundary. *Geophysical Research Letters*, *47*(3), e2019GL085989.

Le Bras, I. A.-A., Straneo, F., Holte, J., & Holliday, N. P. (2018). Seasonality of Freshwater in the East Greenland Current System From 2014 to 2016. *Journal of Geophysical Research: Oceans*, *123*(12), 8828–8848.

Lenz, E. (1845). Bemerkungen über die Temperatur des Weltmeers in verschiedenen Tiefen. *Annalen der Physik und Chemie*, *149*(S4), 615–626.

Levang, S. J., & Schmitt, R. W. (2020). What Causes the AMOC to Weaken in CMIP5? *Journal of Climate*, *33*(4), 1535–1545.

Levine, A. F. Z., McPhaden, M. J., & Frierson, D. M. W. (2017). The impact of the AMO on multidecadal ENSO variability. *Geophysical Research Letters*, *44*(8), 3877–3886.

Levitus, S., Boyer, T. P., Conkright, M. E., O'Brien, T., Antonov, J., Stephens, C., Stathoplos, L., Johnson, D., & Gelfield, R. (1998). *World Ocean Database 1998* (NOAA Atlas NESDIS 18.).

Lévy, M., Klein, P., Tréguier, A.-M., Iovino, D., Madec, G., Masson, S., & Takahashi, K. (2010). Modifications of gyre circulation by sub-mesoscale physics. *Ocean Modelling*, *34*(1-2), 1–15.

Lherminier, P., Mercier, H., Gourcuff, C., Alvarez, M., Bacon, S., & Kermabon, C. (2007). Transports across the 2002 Greenland-Portugal Ovide section and comparison with 1997. *Journal of Geophysical Research: Oceans*, *112*(C7), 2006JC003716.

Lherminier, P., Mercier, H., Huck, T., Gourcuff, C., Perez, F. F., Morin, P., Sarafanov, A., & Falina, A. (2010). The Atlantic Meridional Overturning Circulation and the subpolar gyre observed at the A25-OVIDE section in June 2002 and 2004. *Deep Sea Research Part I: Oceanographic Research Papers*, *57*(11), 1374–1391.

Li, F., Lozier, M. S., Bacon, S., Bower, A. S., Cunningham, S. A., de Jong, M. F., de Young, B., Fraser, N., Fried, N., Han, G., Holliday, N. P., Holte, J., Houpert, L., Inall, M. E., Johns, W. E., Jones, S., Johnson, C., Karstensen, J., Le Bras, I. A., … Zhou, C. (2021a). Subpolar North Atlantic western boundary density anomalies and the Meridional Overturning Circulation. *Nature Communications*, *12*(1), 3002.

Li, F., & Lozier, M. S. (2018). On the Linkage between Labrador Sea Water Volume and Overturning Circulation in the Labrador Sea: A Case Study on Proxies. *Journal of Climate*, *31*(13), 5225–5241.

Li, F., Lozier, M. S., Holliday, N. P., Johns, W. E., Le Bras, I. A., Moat, B. I., Cunningham, S. A., & de Jong, M. F. (2021b). Observation-based estimates of heat and freshwater exchanges from the subtropical North Atlantic to the Arctic. *Progress in Oceanography*, *197*, 102640.

Li, F., Lozier, M. S., & Johns, W. E. (2017). Calculating the Meridional Volume, Heat, and Freshwater Transports from an Observing System in the Subpolar North Atlantic: Observing System Simulation Experiment. *Journal of Atmospheric and Oceanic Technology*, *34*(7), 1483–1500.

Li, J., Sun, C., & Jin, F.-F. (2013). NAO implicated as a predictor of Northern Hemisphere mean temperature multidecadal variability. *Geophysical Research Letters*, *40*(20), 5497–5502.

Li, P., Chen, R., Gou, R., Pennelly, C., Luo, Y., & Myers, P. G. (2023). Winter Mixed Layer Restratification Induced by Vertical Eddy Buoyancy Flux in the Labrador Sea. *Geophysical Research Letters*, *50*(17), e2023GL103341.

Lillibridge, J. L., & Mariano, A. J. (2013). A statistical analysis of Gulf Stream variability from 18+ years of altimetry data. *Deep Sea Research Part II: Topical Studies in Oceanography*, *85*, 127–146.

Lilly, J. M., Rhines, P. B., Schott, F., Lavender, K., Lazier, J., Send, U., & D'Asaro, E. (2003). Observations of the Labrador Sea eddy field. *Progress in Oceanography*, *59*(1), 75–176.

Lilly, J. M., Rhines, P. B., Visbeck, M., Davis, R., Lazier, J. R. N., Schott, F., & Farmer, D. (1999). Observing Deep Convection in the Labrador Sea during Winter 1994/95. *Journal of Physical Oceanography*, *29*(8), 2065–2098.

Lique, C., & Thomas, M. D. (2018). Latitudinal shift of the Atlantic Meridional Overturning Circulation source regions under a warming climate. *Nature Climate Change*, *8*(11), 1013–1020.

Liu, C., Yang, Y., Liao, X., Cao, N., Liu, J., Ou, N., Allan, R. P., Jin, L., Chen, N., & Zheng, R. (2022). Discrepancies in Simulated Ocean Net Surface Heat Fluxes over the North Atlantic. *Advances in Atmospheric Sciences*, *39*(11), 1941–1955.

Liu, Z., Gu, S., Zou, S., Zhang, S., Yu, Y., & He, C. (2024). Wind-steered Eastern Pathway of the Atlantic Meridional Overturning Circulation. *Nature Geoscience*, *17*(4), 353–360.

Lockyer, W. J. S. (1906). Studies of Temperature and Pressure Observations. *Nature*, *73*(1903), 594–595.

Lohmann, K., Drange, H., & Bentsen, M. (2009). Response of the North Atlantic subpolar gyre to persistent North Atlantic oscillation like forcing. *Climate Dynamics*, *32*(2-3), 273–285.

Lozier, M. S., Bacon, S., Bower, A. S., Cunningham, S. A., de Jong, F. M., De Steur, L., deYoung, B., Fischer, J., Gary, S. F., Greenan, B. J. W., Heimbach, P., Holliday, N. P., Houpert, L., Inall, M. E., Johns, W. E., Johnson, H. L., Karstensen, J., Li, F., Lin, X., … Zika, J. D. (2017). Overturning in the Subpolar North Atlantic Program: A New International Ocean Observing System. *Bulletin of the American Meteorological Society*, *98*(4), 737–752.

Lozier, M. S., Bower, A. S., Furey, H. H., Drouin, K. L., Xu, X., & Zou, S. (2022). Overflow water pathways in the North Atlantic. *Progress in Oceanography*, *208*, 102874.

Lozier, M. S., Li, F., Bacon, S., Bahr, F., Bower, A. S., Cunningham, S. A., de Jong, M. F., de Steur, L., deYoung, B., Fischer, J., Gary, S. F., Greenan, B. J. W., Holliday, N. P., Houk, A., Houpert, L., Inall, M. E., Johns, W. E., Johnson, H. L., Johnson, C., … Zhao, J. (2019). A sea change in our view of overturning in the subpolar North Atlantic. *Science*, *363*(6426), 516–521.

Lozier, M. S. (1999). The impact of mid-depth recirculations on the distribution of tracers in the North Atlantic. *Geophysical Research Letters*, *26*(2), 219–222.

Lozier, M. S. (2023). Overturning in the subpolar North Atlantic: A review. *Philosophical Transactions of the Royal Society A: Mathematical, Physical and Engineering Sciences*, *381*(2262), 20220191.

Lozier, M. S., Gary, S. F., & Bower, A. S. (2013). Simulated pathways of the overflow waters in the North Atlantic: Subpolar to subtropical export. *Deep Sea Research Part II: Topical Studies in Oceanography*, *85*, 147–153.

Lozier, M. S., Leadbetter, S., Williams, R. G., Roussenov, V., Reed, M. S. C., & Moore, N. J. (2008). The Spatial Pattern and Mechanisms of Heat-Content Change in the North Atlantic. *Science*, *319*(5864), 800–803.

Lozier, M. S., Pratt, L. J., Rogerson, A. M., & Miller, P. D. (1997). Exchange Geometry Revealed by Float Trajectories in the Gulf Stream*. *Journal of Physical Oceanography*, *27*(11), 2327–2341.

Lumpkin, R., & Johnson, G. C. (2013). Global ocean surface velocities from drifters: Mean, variance, El Niño–Southern Oscillation response, and seasonal cycle. *Journal of Geophysical Research: Oceans*, *118*(6), 2992–3006.

Lumpkin, R., Özgökmen, T., & Centurioni, L. (2017). Advances in the Application of Surface Drifters. *Annual Review of Marine Science*, *9*(1), 59–81.

Luo, F., Li, S., & Furevik, T. (2011). The connection between the Atlantic Multidecadal Oscillation and the Indian Summer Monsoon in Bergen Climate Model Version 2.0. *Journal of Geophysical Research*, *116*(D19), D19117.

Lynch-Stieglitz, J. (2017). The Atlantic Meridional Overturning Circulation and Abrupt Climate Change. *Annual Review of Marine Science*, *9*(1), 83–104.

MacGilchrist, G. A., Johnson, H. L., Lique, C., & Marshall, D. P. (2021). Demons in the North Atlantic: Variability of Deep Ocean Ventilation. *Geophysical Research Letters*, *48*(9).

MacGilchrist, G. A., Johnson, H. L., Marshall, D. P., Lique, C., Thomas, M., Jackson, L. C., & Wood, R. A. (2020). Locations and Mechanisms of Ocean Ventilation in the High-Latitude North Atlantic in an Eddy-Permitting Ocean Model. *Journal of Climate*, *33*(23), 10113–10131.

Mackay, N., Wilson, C., Holliday, N. P., & Zika, J. D. (2020). The Observation-Based Application of a Regional Thermohaline Inverse Method to Diagnose the Formation and Transformation of Water Masses North of the OSNAP Array from 2013 to 2015. *Journal of Physical Oceanography*, *50*(6), 1533–1555.

Madan, G., Gjermundsen, A., Iversen, S. C., & LaCasce, J. H. (2024). The weakening AMOC under extreme climate change. *Climate Dynamics*, *62*(2), 1291–1309.

Madec, G., Benshila, R., Bricaud, C., Coward, A., Dobricic, S., Furner, R., & Oddo, P. (2013). NEMO ocean engine.

Madec, G., Bourdallé-Badie, R., Chanut, J., Clementi, E., Coward, A., Ethé, C., Iovino, D., Lea, D., Lévy, C., Lovato, T., Martin, N., Masson, S., Mocavero, S., Rousset, C., Storkey, D., Vancoppenolle, M., Müeller, S., Nurser, G., Bell, M., & Samson, G. (2019). NEMO ocean engine.

Madec, G., Bourdallé-Badie, R., Pierre-Antoine Bouttier, Bricaud, C., Bruciaferri, D., Calvert, D., Chanut, J., Clementi, E., Coward, A., Delrosso, D., Ethé, C., Flavoni, S., Graham, T., Harle, J., Iovino, D., Lea, D., Lévy, C., Lovato, T., Martin, N., … Vancoppenolle, M. (2017). NEMO ocean engine.

Manabe, S., & Stouffer, R. J. (1988). Two Stable Equilibria of a Coupled Ocean-Atmosphere Model. *Journal of Climate*, *1*(9), 841–866.

Mann, C. (1967). The termination of the Gulf Stream and the beginning of the North Atlantic Current. *Deep Sea Research and Oceanographic Abstracts*, *14*(3), 337–359.

Markina, M. Y., Johnson, H. L., & Marshall, D. P. (2024). Response of Subpolar North Atlantic Meridional Overturning Circulation to Variability in Surface Winds on Different Timescales. *Journal of Physical Oceanography*, *54*(9), 1871–1887.

Marotzke, J., & Klinger, B. A. (2000). The Dynamics of Equatorially Asymmetric Thermohaline Circulations. *Journal of Physical Oceanography*, *30*(5), 955–970.

Marsh, R., Josey, S. A., De Nurser, A. J. G., Cuevas, B. A., & Coward, A. C. (2005). Water mass transformation in the North Atlantic over 1985-2002 simulated in an eddy-permitting model. *Ocean Science*, *1*(2), 127–144.

Marsh, R. (2000). Recent Variability of the North Atlantic Thermohaline Circulation Inferred from Surface Heat and Freshwater Fluxes. *Journal of Climate*, *13*(18), 3239–3260.

Marsh, R., De Cuevas, B. A., Coward, A. C., Jacquin, J., Hirschi, J. J.-M., Aksenov, Y., Nurser, A. G., & Josey, S. A. (2009). Recent changes in the North Atlantic circulation simulated with eddy-permitting and eddy-resolving ocean models. *Ocean Modelling*, *28*(4), 226–239.

Marsh, R., Josey, S. A., De Cuevas, B. A., Redbourn, L. J., & Quartly, G. D. (2008). Mechanisms for recent warming of the North Atlantic: Insights gained with an eddy-permitting model. *Journal of Geophysical Research: Oceans*, *113*(C4), 2007JC004096.

Marshall, J., Armour, K. C., Scott, J. R., Kostov, Y., Hausmann, U., Ferreira, D., Shepherd, T. G., & Bitz, C. M. (2014). The ocean's role in polar climate change: Asymmetric Arctic and Antarctic responses to greenhouse gas and ozone forcing. *Philosophical Transactions of the Royal Society A: Mathematical, Physical and Engineering Sciences*, *372*(2019), 20130040.

Marshall, J., Johnson, H., & Goodman, J. (2001). A Study of the Interaction of the North Atlantic Oscillation with Ocean Circulation. *Journal of Climate*, *14*(7), 1399–1421.

Marshall, J., & Schott, F. (1999). Open-ocean convection: Observations, theory, and models. *Reviews of Geophysics*, *37*(1), 1–64.

Marshall, J., & Speer, K. (2012). Closure of the meridional overturning circulation through Southern Ocean upwelling. *Nature Geoscience*, *5*(3), 171–180.

Martin, E. R., Thorncroft, C., & Booth, B. B. B. (2014). The Multidecadal Atlantic SST—Sahel Rainfall Teleconnection in CMIP5 Simulations. *Journal of Climate*, *27*(2), 784–806.

Martin, E. R., & Thorncroft, C. D. (2014). The impact of the AMO on the West African monsoon annual cycle. *Quarterly Journal of the Royal Meteorological Society*, *140*(678), 31–46.

Martin, P., Lampitt, R. S., Jane Perry, M., Sanders, R., Lee, C., & D'Asaro, E. (2011). Export and mesopelagic particle flux during a North Atlantic spring diatom bloom. *Deep Sea Research Part I: Oceanographic Research Papers*, *58*(4), 338–349.

Martin, T., Park, W., & Latif, M. (2015). Southern Ocean forcing of the North Atlantic at multi-centennial time scales in the Kiel Climate Model. *Deep Sea Research Part II: Topical Studies in Oceanography*, *114*, 39–48.

Marzocchi, A., Hirschi, J. J.-M., Holliday, N. P., Cunningham, S. A., Blaker, A. T., & Coward, A. C. (2015). The North Atlantic subpolar circulation in an eddy-resolving global ocean model. *Journal of Marine Systems*, *142*, 126–143.

Mauritzen, C., & Häkkinen, S. (1999). On the relationship between dense water formation and the "Meridional Overturning Cell" in the North Atlantic Ocean. *Deep Sea Research Part I: Oceanographic Research Papers*, *46*(5), 877–894.

Mauritzen, C. (1996). Production of dense overflow waters feeding the North Atlantic across the Greenland-Scotland Ridge. Part 1: Evidence for a revised circulation scheme. *Deep Sea Research Part I: Oceanographic Research Papers*, *43*(6), 769–806.

McCarthy, G., Frajka-Williams, E., Johns, W. E., Baringer, M. O., Meinen, C. S., Bryden, H. L., Rayner, D., Duchez, A., Roberts, C., & Cunningham, S. A. (2012). Observed interannual variability of the Atlantic meridional overturning circulation at 26.5°N. *Geophysical Research Letters*, *39*(19), 2012GL052933.

McCarthy, G., Smeed, D., Johns, W., Frajka-Williams, E., Moat, B., Rayner, D., Baringer, M., Meinen, C., Collins, J., & Bryden, H. (2015a). Measuring the Atlantic Meridional Overturning Circulation at 26°N. *Progress in Oceanography*, *130*, 91–111.

McCarthy, G. D., Haigh, I. D., Hirschi, J. J.-M., Grist, J. P., & Smeed, D. A. (2015b). Ocean impact on decadal Atlantic climate variability revealed by sea-level observations. *Nature*, *521*(7553), 508–510.

McCartney, M. S., & Talley, L. D. (1982). The Subpolar Mode Water of the North Atlantic Ocean. *Journal of Physical Oceanography*, *12*(11), 1169–1188.

McDonagh, E. L., King, B. A., Bryden, H. L., Courtois, P., Szuts, Z., Baringer, M., Cunningham, S. A., Atkinson, C., & McCarthy, G. (2015). Continuous Estimate of Atlantic Oceanic Freshwater Flux at 26.5°N. *Journal of Climate*, *28*(22), 8888–8906.

McDougall, T. J., Jackett, D. R., Millero, F. J., Pawlowicz, R., & Barker, P. M. (2012). A global algorithm for estimating Absolute Salinity. *Ocean Science*, *8*(6), 1123–1134.

McIntosh, P. C., & McDougall, T. J. (1996). Isopycnal Averaging and the Residual Mean Circulation. *Journal of Physical Oceanography*, *26*(8), 1655–1660.

Mecking, J. V., Drijfhout, S. S., Jackson, L. C., & Graham, T. (2016). Stable AMOC off state in an eddy-permitting coupled climate model. *Climate Dynamics*, *47*(7-8), 2455–2470.

Megann, A., Blaker, A., Coward, A., Guiavarc'h, C., & Storkey, D. (2022, October). Model output from 1/12° global JRA55-forced integration of GO8p7 global ocean-sea ice model from 1958 to 2021.

Megann, A., Blaker, A., Josey, S., New, A., & Sinha, B. (2021). Mechanisms for Late 20th and Early 21st Century Decadal AMOC Variability. *Journal of Geophysical Research: Oceans*, *126*(12), e2021JC017865.

Meinen, C. S., Baringer, M. O., & Garcia, R. F. (2010). Florida Current transport variability: An analysis of annual and longer-period signals. *Deep Sea Research Part I: Oceanographic Research Papers*, *57*(7), 835–846.

Meinen, C. S., Speich, S., Perez, R. C., Dong, S., Piola, A. R., Garzoli, S. L., Baringer, M. O., Gladyshev, S., & Campos, E. J. D. (2013). Temporal variability of the meridional overturning circulation at 34.5°S: Results from two pilot boundary arrays in the South Atlantic. *Journal of Geophysical Research: Oceans*, *118*(12), 6461–6478.

Menary, M. B., Hodson, D. L. R., Robson, J. I., Sutton, R. T., & Wood, R. A. (2015). A Mechanism of Internal Decadal Atlantic Ocean Variability in a High-Resolution Coupled Climate Model. *Journal of Climate*, *28*(19), 7764–7785.

Menary, M. B., Jackson, L. C., & Lozier, M. S. (2020a). Reconciling the Relationship Between the AMOC and Labrador Sea in OSNAP Observations and Climate Models. *Geophysical Research Letters*, *47*(18).

Menary, M. B., Robson, J., Allan, R. P., Booth, B. B. B., Cassou, C., Gastineau, G., Gregory, J., Hodson, D., Jones, C., Mignot, J., Ringer, M., Sutton, R., Wilcox, L., & Zhang, R. (2020b). Aerosol-Forced AMOC Changes in CMIP6 Historical Simulations. *Geophysical Research Letters*, *47*(14), e2020GL088166.

Mercier, H., Desbruyères, D., Lherminier, P., Velo, A., Carracedo, L., Fontela, M., & Pérez, F. F. (2024). New insights into the eastern subpolar North Atlantic meridional overturning circulation from OVIDE. *Ocean Science*, *20*(3), 779–797.

Mercier, H., Lherminier, P., Sarafanov, A., Gaillard, F., Daniault, N., Desbruyères, D., Falina, A., Ferron, B., Gourcuff, C., Huck, T., & Thierry, V. (2015). Variability of the meridional overturning circulation at the Greenland–Portugal OVIDE section from 1993 to 2010. *Progress in Oceanography*, *132*, 250–261.

Mertens, C., Rhein, M., Walter, M., Böning, C. W., Behrens, E., Kieke, D., Steinfeldt, R., & Stöber, U. (2014). Circulation and transports in the Newfoundland Basin, western subpolar North Atlantic. *Journal of Geophysical Research: Oceans*, *119*(11), 7772–7793.

Merz, A. (1925). *Die Deutsche Atlantische Expedition auf dem Vermessungs- und Forschungsschiff "Meteor"* (tech. rep. No. 1). Sitzungsberichte der Preussischen Akademie der Wissenschaften, Physikalische–Mathematische Klasse.

Mielke, C., Frajka-Williams, E., & Baehr, J. (2013). Observed and simulated variability of the AMOC at 26°N and 41°N. *Geophysical Research Letters*, *40*(6), 1159–1164.

Moat, B. I., Josey, S. A., Sinha, B., Blaker, A. T., Smeed, D. A., McCarthy, G. D., Johns, W. E., Hirschi, J. J.-M., Frajka-Williams, E., Rayner, D., Duchez, A., & Coward, A. C. (2016). Major variations in subtropical North Atlantic heat transport at short (5 day) timescales and their causes. *Journal of Geophysical Research: Oceans*, *121*(5), 3237–3249.

Moat, B. I., Sinha, B., Berry, D. I., Drijfhout, S. S., Fraser, N., Hermanson, L., Jones, D. C., Josey, S. A., King, B., Macintosh, C., Megann, A., Oltmanns, M., Sanders, R., & Williams, S. (2024). Ocean Heat Convergence and North Atlantic multidecadal heat content variability. *Journal of Climate*, *-1*(aop).

Moat, B. I., Sinha, B., Josey, S. A., Robson, J., Ortega, P., Sévellec, F., Holliday, N. P., McCarthy, G. D., New, A. L., & Hirschi, J. J.-M. (2019). Insights into Decadal North Atlantic Sea Surface Temperature and Ocean Heat Content Variability from an Eddy-Permitting Coupled Climate Model. *Journal of Climate*, *32*(18), 6137–6161.

Moat, B. I., Smeed, D. A., Frajka-Williams, E., Desbruyères, D. G., Beaulieu, C., Johns, W. E., Rayner, D., Sanchez-Franks, A., Baringer, M. O., Volkov, D., Jackson, L. C., & Bryden, H. L. (2020). Pending recovery in the strength of the meridional overturning circulation at 26° N. *Ocean Science*, *16*(4), 863–874.

Molinari, R. L., & Morrison, J. (1988). The separation of the Yucatan Current from the Campeche Bank and the intrusion of the Loop Current into the Gulf of Mexico. *Journal of Geophysical Research: Oceans*, *93*(C9), 10645–10654.

Moore, J. K., Fu, W., Primeau, F., Britten, G. L., Lindsay, K., Long, M., Doney, S. C., Mahowald, N., Hoffman, F., & Randerson, J. T. (2018). Sustained climate warming drives declining marine biological productivity. *Science*, *359*(6380), 1139–1143.

Msadek, R., & Frankignoul, C. (2009). Atlantic multidecadal oceanic variability and its influence on the atmosphere in a climate model. *Climate Dynamics*, *33*(1), 45–62.

Msadek, R., Johns, W. E., Yeager, S. G., Danabasoglu, G., Delworth, T. L., & Rosati, A. (2013). The Atlantic Meridional Heat Transport at 26.5°N and Its Relationship with the MOC in the RAPID Array and the GFDL and NCAR Coupled Models. *Journal of Climate*, *26*(12), 4335–4356.

O'Connor, B. M., Fine, R. A., & Olson, D. B. (2005). A global comparison of subtropical underwater formation rates. *Deep Sea Research Part I: Oceanographic Research Papers*, *52*(9), 1569–1590.

O'Neill, B. C., Kriegler, E., Riahi, K., Ebi, K. L., Hallegatte, S., Carter, T. R., Mathur, R., & Van Vuuren, D. P. (2014). A new scenario framework for climate change research: The concept of shared socioeconomic pathways. *Climatic Change*, *122*(3), 387–400.

Orihuela-Pinto, B., England, M. H., & Taschetto, A. S. (2022). Interbasin and interhemispheric impacts of a collapsed Atlantic Overturning Circulation. *Nature Climate Change*, *12*(6), 558–565.

Ortega, P., Robson, J., Sutton, R. T., & Andrews, M. B. (2017). Mechanisms of decadal variability in the Labrador Sea and the wider North Atlantic in a high-resolution climate model. *Climate Dynamics*, *49*(7-8), 2625–2647.

Ortega, P., Robson, J. I., Menary, M., Sutton, R. T., Blaker, A., Germe, A., Hirschi, J. J.-M., Sinha, B., Hermanson, L., & Yeager, S. (2021). Labrador Sea subsurface density as a precursor of multidecadal variability in the North Atlantic: A multi-model study. *Earth System Dynamics*, *12*(2), 419–438.

Østerhus, S., Sherwin, T., Quadfasel, D., & Hansen, B. (2008). The Overflow Transport East of Iceland. In R. R. Dickson, J. Meincke, & P. Rhines (Eds.), *Arctic–Subarctic Ocean Fluxes* (pp. 427–441). Springer Netherlands.

Østerhus, S., Woodgate, R., Valdimarsson, H., Turrell, B., De Steur, L., Quadfasel, D., Olsen, S. M., Moritz, M., Lee, C. M., Larsen, K. M. H., Jónsson, S., Johnson, C., Jochumsen, K., Hansen, B., Curry, B., Cunningham, S., & Berx, B. (2019). Arctic Mediterranean exchanges: A consistent volume budget and trends in transports from two decades of observations. *Ocean Science*, *15*(2), 379–399.

Pacini, A., & Pickart, R. S. (2022). Meanders of the West Greenland Current near Cape Farewell. *Deep Sea Research Part I: Oceanographic Research Papers*, *179*, 103664.

Pacini, A., Pickart, R. S., Bahr, F., Torres, D. J., Ramsey, A. L., Holte, J., Karstensen, J., Oltmanns, M., Straneo, F., Le Bras, I. A., Moore, G. W. K., & de Jong, F. M. (2020). Mean Conditions and Seasonality of the West Greenland Boundary Current System near Cape Farewell. *Journal of Physical Oceanography*, *50*(10), 2849–2871.

Palter, J. B., Lozier, M. S., & Lavender, K. L. (2008). How Does Labrador Sea Water Enter the Deep Western Boundary Current? *Journal of Physical Oceanography*, *38*(5), 968–983.

Paris, C. B., Helgers, J., van Sebille, E., & Srinivasan, A. (2013). Connectivity Modeling System: A probabilistic modeling tool for the multi-scale tracking of biotic and abiotic variability in the ocean. *Environmental Modelling & Software*, *42*, 47–54.

Passos, L., Langehaug, H. R., Årthun, M., & Straneo, F. (2024). On the relation between thermohaline anomalies and water mass transformation in the Eastern Subpolar North Atlantic. *Journal of Climate*.

Pelegrí, J. L., & Csanady, G. T. (1991). Nutrient transport and mixing in the Gulf Stream. *Journal of Geophysical Research: Oceans*, *96*(C2), 2577–2583.

Pelegrí, J. L., Vallès-Casanova, I., & Orúe-Echevarría, D. (2019, April). The Gulf Nutrient Stream. In T. Nagai, H. Saito, K. Suzuki, & M. Takahashi (Eds.), *Geophysical Monograph Series* (1st ed., pp. 23–50). Wiley.

Pennelly, C., & Myers, P. G. (2020). Introducing LAB60: A 1/60° NEMO 3.6 numerical simulation of the Labrador Sea. *Geoscientific Model Development*, *13*(10), 4959–4975.

Pennelly, C., & Myers, P. G. (2022). Tracking Irminger Rings' properties using a sub-mesoscale ocean model. *Progress in Oceanography*, *201*, 102735.

Pérez, F. F., Mercier, H., Vázquez-Rodríguez, M., Lherminier, P., Velo, A., Pardo, P. C., Rosón, G., & Ríos, A. F. (2013). Atlantic Ocean CO2 uptake reduced by weakening of the meridional overturning circulation. *Nature Geoscience*, *6*(2), 146–152.

Petit, T., Lozier, M. S., Rühs, S., Handmann, P., & Biastoch, A. (2023a). Propagation and Transformation of Upper North Atlantic Deep Water From the Subpolar Gyre to 26.5°N. *Journal of Geophysical Research: Oceans*, *128*(8), e2023JC019726.

Petit, T., Robson, J., Ferreira, D., & Jackson, L. C. (2023b). Understanding the Sensitivity of the North Atlantic Subpolar Overturning in Different Resolution Versions of HadGEM3-GC3.1. *Journal of Geophysical Research: Oceans*, *128*(10), e2023JC019672.

Petit, T., Lozier, M. S., Josey, S. A., & Cunningham, S. A. (2020). Atlantic Deep Water Formation Occurs Primarily in the Iceland Basin and Irminger Sea by Local Buoyancy Forcing. *Geophysical Research Letters*, *47*(22).

Petit, T., Lozier, M. S., Josey, S. A., & Cunningham, S. A. (2021). Role of air–sea fluxes and ocean surface density in the production of deep waters in the eastern subpolar gyre of the North Atlantic. *Ocean Science*, *17*(5), 1353–1365.

Petit, T., Mercier, H., & Thierry, V. (2018). First Direct Estimates of Volume and Water Mass Transports Across the Reykjanes Ridge. *Journal of Geophysical Research: Oceans*, *123*(9), 6703–6719.

Pickart, R. S., & Spall, M. A. (2007). Impact of Labrador Sea Convection on the North Atlantic Meridional Overturning Circulation. *Journal of Physical Oceanography*, *37*(9), 2207–2227.

Pickart, R. S., Spall, M. A., & Lazier, J. R. (1997). Mid-depth ventilation in the western boundary current system of the sub-polar gyre. *Deep Sea Research Part I: Oceanographic Research Papers*, *44*(6), 1025–1054.

Pickart, R. S., Spall, M. A., Ribergaard, M. H., Moore, G. W. K., & Milliff, R. F. (2003). Deep convection in the Irminger Sea forced by the Greenland tip jet. *Nature*, *424*(6945), 152–156.

Pickart, R. S., Torres, D. J., & Clarke, R. A. (2002). Hydrography of the Labrador Sea during Active Convection. *Journal of Physical Oceanography*, *32*(2), 428–457.

Piron, A., Thierry, V., Mercier, H., & Caniaux, G. (2016). Argo float observations of basin-scale deep convection in the Irminger sea during winter 2011–2012. *Deep Sea Research Part I: Oceanographic Research Papers*, *109*, 76–90.

Pollard, R. T., Read, J. F., Holliday, N. P., & Leach, H. (2004). Water masses and circulation pathways through the Iceland Basin during Vivaldi 1996. *Journal of Geophysical Research: Oceans*, *109*(C4), 2003JC002067.

Polo, I., Robson, J., Sutton, R., & Balmaseda, M. A. (2014). The Importance of Wind and Buoyancy Forcing for the Boundary Density Variations and the Geostrophic Component of the AMOC at 26°N. *Journal of Physical Oceanography*, *44*(9), 2387–2408.

Qu, T., Gao, S., & Fukumori, I. (2013). Formation of salinity maximum water and its contribution to the overturning circulation in the North Atlantic as revealed by a global general circulation model. *Journal of Geophysical Research: Oceans*, *118*(4), 1982–1994.

Qu, T., Zhang, L., & Schneider, N. (2016). North Atlantic Subtropical Underwater and Its Year-to-Year Variability in Annual Subduction Rate during the Argo Period. *Journal of Physical Oceanography*, *46*(6), 1901–1916.

Racapé, V., Thierry, V., Mercier, H., & Cabanes, C. (2019). ISOW Spreading and Mixing as Revealed by Deep-Argo Floats Launched in the Charlie-Gibbs Fracture Zone. *Journal of Geophysical Research: Oceans*, *124*(10), 6787–6808.

Rahmstorf, S. (1996). On the freshwater forcing and transport of the Atlantic thermohaline circulation: *Climate Dynamics*, *12*(12), 799–811.

Rahmstorf, S. (1999). Shifting seas in the greenhouse? *Nature*, *399*(6736), 523–524.

Rahmstorf, S. (2002). Ocean circulation and climate during the past 120,000 years. *Nature*, *419*(6903), 207–214.

Rahmstorf, S., & Willebrand, J. (1995). The Role of Temperature Feedback in Stabilizing the Thermohaline Circulation. *Journal of Physical Oceanography*, *25*(5), 787–805.

Read, J. (2000). CONVEX-91: Water masses and circulation of the Northeast Atlantic subpolar gyre. *Progress in Oceanography*, *48*(4), 461–510.

Reintges, A., Robson, J. I., Sutton, R., & Yeager, S. G. (2024). Subpolar North Atlantic mean state affects the response of the Atlantic Meridional Overturning Circulation to the North Atlantic Oscillation in CMIP6 models. *Journal of Climate*.

Reverdin, G., Niiler, P. P., & Valdimarsson, H. (2003). North Atlantic Ocean surface currents. *Journal of Geophysical Research: Oceans*, *108*(C1).

Rhein, M., Fischer, J., Smethie, W. M., Smythe-Wright, D., Weiss, R. F., Mertens, C., Min, D.-H., Fleischmann, U., & Putzka, A. (2002). Labrador Sea Water: Pathways, CFC Inventory, and Formation Rates. *Journal of Physical Oceanography*, *32*(2), 648–665.

Rhein, M., Kieke, D., Hüttl-Kabus, S., Roessler, A., Mertens, C., Meissner, R., Klein, B., Böning, C. W., & Yashayaev, I. (2011). Deep water formation, the subpolar gyre, and the meridional overturning circulation in the subpolar North Atlantic. *Deep Sea Research Part II: Topical Studies in Oceanography*, *58*(17-18), 1819–1832.

Rhein, M., Kieke, D., & Steinfeldt, R. (2015). Advection of North Atlantic Deep Water from the Labrador Sea to the southern hemisphere. *Journal of Geophysical Research: Oceans*, *120*(4), 2471–2487.

Rhein, M., Mertens, C., & Roessler, A. (2019). Observed Transport Decline at 47°N, Western Atlantic. *Journal of Geophysical Research: Oceans*, *124*(7), 4875–4890.

Rhein, M., Steinfeldt, R., Kieke, D., Stendardo, I., & Yashayaev, I. (2017). Ventilation variability of Labrador Sea Water and its impact on oxygen and anthropogenic carbon: A review. *Philosophical Transactions of the Royal Society A: Mathematical, Physical and Engineering Sciences*, *375*(2102), 20160321.

Richardson, P. L. (2008). On the history of meridional overturning circulation schematic diagrams. *Progress in Oceanography*, *76*(4), 466–486.

Richardson, P. (2019). Drifters and floats. In J. Cochran, H. Bokuniewicz, & P. Yager (Eds.), *Encyclopedia of Ocean Sciences* (3rd, pp. 63–70). Elsevier.

Riemenschneider, U., & Legg, S. (2007). Regional simulations of the Faroe Bank Channel overflow in a level model. *Ocean Modelling*, *17*(2), 93–122.

Ringler, T., Petersen, M., Higdon, R. L., Jacobsen, D., Jones, P. W., & Maltrud, M. (2013). A multi-resolution approach to global ocean modeling. *Ocean Modelling*, *69*, 211–232.

Ritchie, P. D. L., Smith, G. S., Davis, K. J., Fezzi, C., Halleck-Vega, S., Harper, A. B., Boulton, C. A., Binner, A. R., Day, B. H., Gallego-Sala, A. V., Mecking, J. V., Sitch, S. A., Lenton, T. M., & Bateman, I. J. (2020). Shifts in national land use and food production in Great Britain after a climate tipping point. *Nature Food*, *1*(1), 76–83.

Roach, C. J., & Speer, K. (2019). Exchange of Water Between the Ross Gyre and ACC Assessed by Lagrangian Particle Tracking. *Journal of Geophysical Research: Oceans*, *124*(7), 4631–4643.

Roberts, C. D., Waters, J., Peterson, K. A., Palmer, M. D., McCarthy, G. D., Frajka-Williams, E., Haines, K., Lea, D. J., Martin, M. J., Storkey, D., Blockley, E. W., & Zuo, H. (2013). Atmosphere drives recent interannual variability of the Atlantic meridional overturning circulation at 26.5°N. *Geophysical Research Letters*, *40*(19), 5164–5170.

Roberts, M. J., Jackson, L. C., Roberts, C. D., Meccia, V., Docquier, D., Koenigk, T., Ortega, P., Moreno-Chamarro, E., Bellucci, A., Coward, A., Drijfhout, S., Exarchou, E., Gutjahr, O., Hewitt, H., Iovino, D., Lohmann, K., Putrasahan, D., Schiemann, R., Seddon, J., … Wu, L. (2020). Sensitivity of the Atlantic Meridional Overturning Circulation to Model Resolution in CMIP6 HighResMIP Simulations and Implications for Future Changes. *Journal of Advances in Modeling Earth Systems*, *12*(8).

Roberts, M. J., Wood, R. A., Marsh, R., & New, A. L. (1996). An Intercomparison of a Bryan–Cox-Type Ocean Model and an Isopycnic Ocean Model. Part I: The Subpolar Gyre and High-Latitude Processes. *Journal of Physical Oceanography*, *26*(8), 1495–1527.

Robson, J., Menary, M. B., Sutton, R. T., Mecking, J., Gregory, J. M., Jones, C., Sinha, B., Stevens, D. P., & Wilcox, L. J. (2022). The Role of Anthropogenic Aerosol Forcing in the 1850–1985 Strengthening of the AMOC in CMIP6 Historical Simulations. *Journal of Climate*, *35*(20), 3243–3263.

Robson, J., Ortega, P., & Sutton, R. (2016). A reversal of climatic trends in the North Atlantic since 2005. *Nature Geoscience*, *9*(7), 513–517.

Robson, J., Sutton, R., Lohmann, K., Smith, D., & Palmer, M. D. (2012). Causes of the Rapid Warming of the North Atlantic Ocean in the Mid-1990s. *Journal of Climate*, *25*(12), 4116–4134.

Robson, J., Sutton, R., & Smith, D. (2014). Decadal predictions of the cooling and freshening of the North Atlantic in the 1960s and the role of ocean circulation. *Climate Dynamics*, *42*(9-10), 2353–2365.

Rodrigues, R. R., Wimbush, M., Watts, D. R., Rothstein, L. M., & Ollitrault, M. (2010). South Atlantic mass transports obtained from subsurface float and hydrographic data. *Journal of Marine Research*, *68*(6), 819–850.

Roemmich, D., & Wunsch, C. (1985). Two transatlantic sections: Meridional circulation and heat flux in the subtropical North Atlantic Ocean. *Deep Sea Research Part A. Oceanographic Research Papers*, *32*(6), 619–664.

Rossby, T. (1996). The North Atlantic Current and surrounding waters: At the crossroads. *Reviews of Geophysics*, *34*(4), 463–481.

Rossby, T. (1999). On gyre interactions. *Deep Sea Research Part II: Topical Studies in Oceanography*, *46*(1-2), 139–164.

Rousselet, L., Cessi, P., & Forget, G. (2020). Routes of the Upper Branch of the Atlantic Meridional Overturning Circulation according to an Ocean State Estimate. *Geophysical Research Letters*, *47*(18).

Rousselet, L., Cessi, P., & Forget, G. (2021). Coupling of the mid-depth and abyssal components of the global overturning circulation according to a state estimate. *Science Advances*, *7*(21), eabf5478.

Roussenov, V. M., Williams, R. G., Lozier, M. S., Holliday, N. P., & Smith, D. M. (2022). Historical Reconstruction of Subpolar North Atlantic Overturning and Its Relationship to Density. *Journal of Geophysical Research: Oceans*, *127*(6).

Rousset, C., & Beal, L. M. (2010). Observations of the Florida and Yucatan Currents from a Caribbean Cruise Ship. *Journal of Physical Oceanography*, *40*(7), 1575–1581.

Rudels, B. (2010). Constraints on exchanges in the Arctic Mediterranean—do they exist and can they be of use? *Tellus A: Dynamic Meteorology and Oceanography*, *62*(2), 109.

Rudels, B., Björk, G., Nilsson, J., Winsor, P., Lake, I., & Nohr, C. (2005). The interaction between waters from the Arctic Ocean and the Nordic Seas north of Fram Strait and along the East Greenland Current: Results from the Arctic Ocean-02 Oden expedition. *Journal of Marine Systems*, *55*(1-2), 1–30.

Rühs, S., Schwarzkopf, F. U., Speich, S., & Biastoch, A. (2019). Cold vs. warm water route – sources for the upper limb of the Atlantic Meridional Overturning Circulation revisited in a high-resolution ocean model. *Ocean Science*, *15*(3), 489–512.

Ruprich-Robert, Y., Delworth, T., Msadek, R., Castruccio, F., Yeager, S., & Danabasoglu, G. (2018). Impacts of the Atlantic Multidecadal Variability on North American Summer Climate and Heat Waves. *Journal of Climate*, *31*(9), 3679–3700.

Ruprich-Robert, Y., Msadek, R., Castruccio, F., Yeager, S., Delworth, T., & Danabasoglu, G. (2017). Assessing the Climate Impacts of the Observed Atlantic Multidecadal Variability Using the GFDL CM2.1 and NCAR CESM1 Global Coupled Models. *Journal of Climate*, *30*(8), 2785–2810.

Rypina, I. I., Pratt, L. J., & Lozier, M. S. (2011). Near-Surface Transport Pathways in the North Atlantic Ocean: Looking for Throughput from the Subtropical to the Subpolar Gyre. *Journal of Physical Oceanography*, *41*(5), 911–925.

Saberi, A., Haine, T. W. N., Gelderloos, R., De Jong, F. M., Furey, H., & Bower, A. (2020). Lagrangian Perspective on the Origins of Denmark Strait Overflow. *Journal of Physical Oceanography*, *50*(8), 2393–2414.

Sabine, C. L., Feely, R. A., Gruber, N., Key, R. M., Lee, K., Bullister, J. L., Wanninkhof, R., Wong, C. S., Wallace, D. W. R., Tilbrook, B., Millero, F. J., Peng, T.-H., Kozyr, A., Ono, T., & Rios, A. F. (2004). The Oceanic Sink for Anthropogenic CO $_2$. *Science*, *305*(5682), 367–371.

Sabine, C. L., & Tanhua, T. (2010). Estimation of Anthropogenic CO $_2$ Inventories in the Ocean. *Annual Review of Marine Science*, *2*(1), 175–198.

Sanchez-Franks, A., Holliday, N. P., Evans, D. G., Fried, N., Tooth, O., Chafik, L., Fu, Y., Li, F., de Jong, M. F., & Johnson, H. L. (2024). The Irminger Gyre as a Key Driver of the Subpolar North Atlantic Overturning. *Geophysical Research Letters*, *51*(8), e2024GL108457.

Sanders, R., Henson, S. A., Koski, M., De La Rocha, C. L., Painter, S. C., Poulton, A. J., Riley, J., Salihoglu, B., Visser, A., Yool, A., Bellerby, R., & Martin, A. P. (2014). The Biological Carbon Pump in the North Atlantic. *Progress in Oceanography*, *129*, 200–218.

Sarafanov, A. (2009). On the effect of the North Atlantic Oscillation on temperature and salinity of the subpolar North Atlantic intermediate and deep waters. *ICES Journal of Marine Science*, *66*(7), 1448–1454.

Sarafanov, A., Falina, A., Mercier, H., Sokov, A., Lherminier, P., Gourcuff, C., Gladyshev, S., Gaillard, F., & Daniault, N. (2012). Mean full-depth summer circulation and transports at the northern periphery of the Atlantic Ocean in the 2000s. *Journal of Geophysical Research: Oceans*, *117*(C1).

Sarafanov, A., Mercier, H., Falina, A., Sokov, A., & Lherminier, P. (2010). Cessation and partial reversal of deep water freshening in the northern North Atlantic: Observation-based estimates and attribution. *Tellus A: Dynamic Meteorology and Oceanography*, *62*(1), 80.

Sarmiento, J. L., Gruber, N., Brzezinski, M. A., & Dunne, J. P. (2004). High-latitude controls of thermocline nutrients and low latitude biological productivity. *Nature*, *427*(6969), 56–60.

Schauer, U., & Losch, M. (2019). "Freshwater" in the Ocean is Not a Useful Parameter in Climate Research. *Journal of Physical Oceanography*, *49*(9), 2309–2321.

Schmidt, C., Schwarzkopf, F. U., Rühs, S., & Biastoch, A. (2021). Characteristics and robustness of Agulhas leakage estimates: An inter-comparison study of Lagrangian methods. *Ocean Science*, *17*(4), 1067–1080.

Schmittner, A. (2005). Decline of the marine ecosystem caused by a reduction in the Atlantic overturning circulation. *Nature*, *434*(7033), 628–633.

Schmitz, J., William J., Luyten, J. R., & Schmitt, R. W. (1993). On the Florida Current T/S Envelope. *Bulletin of Marine Science*, *53*(3), 1048–1065.

Schmitz, W. J., & McCartney, M. S. (1993). On the North Atlantic Circulation. *Reviews of Geophysics*, *31*(1), 29–49.

Schmitz, W. J., & Richardson, P. L. (1991). On the sources of the Florida Current. *Deep Sea Research Part A. Oceanographic Research Papers*, *38*, S379–S409.

Schmitz Jr, W. J. (1996). *On the World Ocean Circulation: Volume I. Some Global Features / North Atlantic Circulation.* (Technical Report No. WHOI-96-03).

Schott, F. A., & Brandt, P. (2007). Circulation and deep water export of the subpolar North Atlantic during the 1990's. In A. Schmittner, J. C. H. Chiang, & S. R. Hemming (Eds.), *Geophysical Monograph Series* (pp. 91–118, Vol. 173). American Geophysical Union.

Schott, F. A., Zantopp, R., Stramma, L., Dengler, M., Fischer, J., & Wibaux, M. (2004). Circulation and Deep-Water Export at the Western Exit of the Subpolar North Atlantic. *Journal of Physical Oceanography*, *34*(4), 817–843.

Schott, G. (1902). Oceanographie und maritime Meteorolgie. In *Wissenschaftliche Ergebnisse der Deutschen Tiefsee-Expedition auf dem Dampfer "Valdivia" 1898–1899* (p. 403, Vol. 1).

Semper, S., Våge, K., Pickart, R. S., Jónsson, S., & Valdimarsson, H. (2022). Evolution and Transformation of the North Icelandic Irminger Current Along the North Iceland Shelf. *Journal of Geophysical Research: Oceans*, *127*(3), e2021JC017700.

Send, U., Lankhorst, M., & Kanzow, T. (2011). Observation of decadal change in the Atlantic meridional overturning circulation using 10 years of continuous transport data. *Geophysical Research Letters*, *38*(24), n/a–n/a.

Sévellec, F., Fedorov, A. V., & Liu, W. (2017). Arctic sea-ice decline weakens the Atlantic Meridional Overturning Circulation. *Nature Climate Change*, *7*(8), 604–610.

Sgubin, G., Swingedouw, D., Drijfhout, S., Mary, Y., & Bennabi, A. (2017). Abrupt cooling over the North Atlantic in modern climate models. *Nature Communications*, *8*(1), 14375.

Shoosmith, D. R., Baringer, M. O., & Johns, W. E. (2005). A continuous record of Florida Current temperature transport at 27°N. *Geophysical Research Letters*, *32*(23), 2005GL024075.

Spall, M. A. (1992). Cooling Spirals and Recirculation in the Subtropical Gyre. *Journal of Physical Oceanography*, *22*(5), 564–571.

Spall, M. A. (2004). Boundary Currents and Watermass Transformation in Marginal Seas. *Journal of Physical Oceanography*, *34*(5), 1197–1213.

Spall, M. A. (2011). On the Role of Eddies and Surface Forcing in the Heat Transport and Overturning Circulation in Marginal Seas. *Journal of Climate*, *24*(18), 4844–4858.

Spall, M. A., & Pickart, R. S. (2001). Where Does Dense Water Sink? A Subpolar Gyre Example. *Journal of Physical Oceanography*, *31*(3), 810–826.

Speer, K., & Tziperman, E. (1992). Rates of Water Mass Formation in the North Atlantic Ocean. *Journal of Physical Oceanography*, *22*(1), 93–104.

Speich, S., Blanke, B., De Vries, P., Drijfhout, S., Döös, K., Ganachaud, A., & Marsh, R. (2002). Tasman leakage: A new route in the global ocean conveyor belt. *Geophysical Research Letters*, *29*(10).

Speich, S., Blanke, B., & Madec, G. (2001). Warm and cold water routes of an O.G.C.M. thermohaline conveyor belt. *Geophysical Research Letters*, *28*(2), 311–314.

Speiss, F. (1928). *Die Meteor-Fahrt. Forschungen und Ergebnisse der Deutschen Atlantischen Expedition 1925–1927.* Dietrich Reimer.

Steele, M., Morley, R., & Ermold, W. (2001). PHC: A Global Ocean Hydrography with a High-Quality Arctic Ocean. *Journal of Climate*, *14*.

Stendardo, I., Buongiorno Nardelli, B., Durante, S., Iudicone, D., & Kieke, D. (2024). Interannual Variability of Subpolar Mode Water in the Subpolar North Atlantic. *Journal of Geophysical Research: Oceans*, *129*(3), e2023JC019937.

Stepanov, V. N., Iovino, D., Masina, S., Storto, A., & Cipollone, A. (2016). Methods of calculation of the Atlantic meridional heat and volume transports from ocean models at 26.5° N. *Journal of Geophysical Research: Oceans*, *121*(2), 1459–1475.

Stewart, A. L., Ferrari, R., & Thompson, A. F. (2014). On the Importance of Surface Forcing in Conceptual Models of the Deep Ocean. *Journal of Physical Oceanography*, *44*(3), 891–899.

Stigebrandt, A. (1981). A Model for the Thickness and Salinity of the Upper Layer in the Arctic Ocean and the Relationship between the Ice Thickness and Some External Parameters. *Journal of Physical Oceanography*, *11*(10), 1407–1422.

Stokstad, E. (2007). Ocean Research Gets a Modest Boost. *Science*, *315*(5812), 585–586.

Stommel, H. (1957). A survey of ocean current theory. *Deep Sea Research (1953)*, *4*, 149–184.

Stommel, H. (1958). The abyssal circulation. *Deep Sea Research (1953)*, *5*(1), 80–82.

Stommel, H. (1961). Thermohaline Convection with Two Stable Regimes of Flow. *Tellus*, *13*(2), 224–230.

Stommel, H. (1979). Determination of water mass properties of water pumped down from the Ekman layer to the geostrophic flow below. *Proceedings of the National Academy of Sciences*, *76*(7), 3051–3055.

Stouffer, R. J., Yin, J., Gregory, J. M., Dixon, K. W., Spelman, M. J., Hurlin, W., Weaver, A. J., Eby, M., Flato, G. M., Hasumi, H., Hu, A., Jungclaus, J. H., Kamenkovich, I. V., Levermann, A., Montoya, M., Murakami, S., Nawrath, S., Oka, A., Peltier, W. R., … Weber, S. L. (2006). Investigating the Causes of the Response of the Thermohaline Circulation to Past and Future Climate Changes. *Journal of Climate*, *19*(8), 1365–1387.

Stöven, T., Tanhua, T., Hoppema, M., & Von Appen, W.-J. (2016). Transient tracer distributions in the Fram Strait in 2012 and inferred anthropogenic carbon content and transport. *Ocean Science*, *12*(1), 319–333.

Straneo, F. (2006). On the Connection between Dense Water Formation, Overturning, and Poleward Heat Transport in a Convective Basin. *Journal of Physical Oceanography*, *36*(9), 1822–1840.

Straneo, F., & Heimbach, P. (2013). North Atlantic warming and the retreat of Greenland's outlet glaciers. *Nature*, *504*(7478), 36–43.

Strauss, B. H., Ziemlinski, R., Weiss, J. L., & Overpeck, J. T. (2012). Tidally adjusted estimates of topographic vulnerability to sea level rise and flooding for the contiguous United States. *Environmental Research Letters*, *7*(1), 014033.

Sutherland, D. A., & Pickart, R. S. (2008). The East Greenland Coastal Current: Structure, variability, and forcing. *Progress in Oceanography*, *78*(1), 58–77.

Sutherland, D. A., Pickart, R. S., Peter Jones, E., Azetsu-Scott, K., Jane Eert, A., & Ólafsson, J. (2009). Freshwater composition of the waters off southeast Greenland and their link to the Arctic Ocean. *Journal of Geophysical Research: Oceans*, *114*(C5), 2008JC004808.

Sutton, R. T., & Allen, M. R. (1997). Decadal predictability of North Atlantic sea surface temperature and climate. *Nature*, *388*(6642), 563–567.

Sutton, R. T., McCarthy, G. D., Robson, J., Sinha, B., Archibald, A. T., & Gray, L. J. (2018). Atlantic Multidecadal Variability and the U.K. ACSIS Program. *Bulletin of the American Meteorological Society*, *99*(2), 415–425.

Sutton, R. T., & Dong, B. (2012). Atlantic Ocean influence on a shift in European climate in the 1990s. *Nature Geoscience*, *5*(11), 788–792.

Sutton, R. T., & Hodson, D. L. R. (2005). Atlantic Ocean Forcing of North American and European Summer Climate. *Science*, *309*(5731), 115–118.

Sutton, R. T., & Hodson, D. L. R. (2007). Climate Response to Basin-Scale Warming and Cooling of the North Atlantic Ocean. *Journal of Climate*, *20*(5), 891–907.

Swift, J. H., & Aagaard, K. (1981). Seasonal transitions and water mass formation in the Iceland and Greenland seas. *Deep Sea Research Part A. Oceanographic Research Papers*, *28*(10), 1107–1129.

Swingedouw, D., Bily, A., Esquerdo, C., Borchert, L. F., Sgubin, G., Mignot, J., & Menary, M. (2021). On the risk of abrupt changes in the North Atlantic subpolar gyre in CMIP6 models. *Annals of the New York Academy of Sciences*, *1504*(1), 187–201.

Swingedouw, D., Ifejika Speranza, C., Bartsch, A., Durand, G., Jamet, C., Beaugrand, G., & Conversi, A. (2020). Early Warning from Space for a Few Key Tipping Points in Physical, Biological, and Social-Ecological Systems. *Surveys in Geophysics*, *41*(6), 1237–1284.

Sy, A., Rhein, M., Lazier, J. R. N., Koltermann, K. P., Meincke, J., Putzka, A., & Bersch, M. (1997). Surprisingly rapid spreading of newly formed intermediate waters across the North Atlantic Ocean. *Nature*, *386*(6626), 675–679.

Sy, A., Schauer, U., & Meincke, J. (1992). The North Atlantic current and its associated hydrographic structure above and eastwards of the mid-atlantic ridge. *Deep Sea Research Part A. Oceanographic Research Papers*, *39*(5), 825–853.

Tagklis, F., Bracco, A., Ito, T., & Castelao, R. M. (2020). Submesoscale modulation of deep water formation in the Labrador Sea. *Scientific Reports*, *10*(1), 17489.

Takahashi, T., Sutherland, S. C., Wanninkhof, R., Sweeney, C., Feely, R. A., Chipman, D. W., Hales, B., Friederich, G., Chavez, F., Sabine, C., Watson, A., Bakker, D. C., Schuster, U., Metzl, N., Yoshikawa-Inoue, H., Ishii, M., Midorikawa, T., Nojiri, Y., Körtzinger, A., ... De Baar, H. J. (2009). Climatological mean and decadal change in surface ocean pCO2, and net sea–air CO2 flux over the global oceans. *Deep Sea Research Part II: Topical Studies in Oceanography*, *56*(8-10), 554–577.

Talandier, C., Deshayes, J., Treguier, A.-M., Capet, X., Benshila, R., Debreu, L., Dussin, R., Molines, J.-M., & Madec, G. (2014). Improvements of simulated Western North Atlantic current system and impacts on the AMOC. *Ocean Modelling*, *76*, 1–19.

Talley, L. D., & McCartney, M. S. (1982). Distribution and Circulation of Labrador Sea Water. *Journal of Physical Oceanography*, *12*(11), 1189–1205.

Talley, L. (2013). Closure of the Global Overturning Circulation Through the Indian, Pacific, and Southern Oceans: Schematics and Transports. *Oceanography*, *26*(1), 80–97.

Talley, L. D. (2003). Shallow, Intermediate, and Deep Overturning Components of the Global Heat Budget. *Journal of Physical Oceanography*, *33*(3), 530–560.

Talley, L. D., Pickard, G. L., Emery, W. J., & Swift, J. H. (Eds.). (2011). *Descriptive physical oceanography: An introduction* (6. ed). Elsevier, AP.

Tamsitt, V., Abernathey, R. P., Mazloff, M. R., Wang, J., & Talley, L. D. (2018). Transformation of Deep Water Masses Along Lagrangian Upwelling Pathways in the Southern Ocean. *Journal of Geophysical Research: Oceans*, *123*(3), 1994–2017.

The Climode Group, Marshall, J., Ferrari, R., Forget, G., Maze, G., Andersson, A., Bates, N., Dewar, W., Doney, S., Fratantoni, D., Joyce, T., Straneo, F., Toole, J., Weller, R., Edson, J., Gregg, M., Kelly, K., Lozier, S., Palter, J., ... Thomas, L. (2009). The Climode Field Campaign: Observing the Cycle of Convection and Restratification over the Gulf Stream. *Bulletin of the American Meteorological Society*, *90*(9), 1337–1350.

Thierry, V., de Boisséson, E., & Mercier, H. (2008). Interannual variability of the Subpolar Mode Water properties over the Reykjanes Ridge during 1990–2006. *Journal of Geophysical Research*, *113*(C4), C04016.

Thomas, M. D., & Zhai, X. (2013). Eddy-induced variability of the meridional overturning circulation in a model of the North Atlantic. *Geophysical Research Letters*, *40*(11), 2742–2747.

Thomas, M. D., Tréguier, A.-M., Blanke, B., Deshayes, J., & Voldoire, A. (2015). A Lagrangian Method to Isolate the Impacts of Mixed Layer Subduction on the Meridional Overturning Circulation in a Numerical Model. *Journal of Climate*, *28*(19), 7503–7517.

Thornalley, D. J. R., Oppo, D. W., Ortega, P., Robson, J. I., Brierley, C. M., Davis, R., Hall, I. R., Moffa-Sanchez, P., Rose, N. L., Spooner, P. T., Yashayaev, I., & Keigwin, L. D. (2018). Anomalously weak Labrador Sea convection and Atlantic overturning during the past 150 years. *Nature*, *556*(7700), 227–230.

Toggweiler, J. R., & Samuels, B. (1995). Effect of drake passage on the global thermohaline circulation. *Deep Sea Research Part I: Oceanographic Research Papers*, *42*(4), 477–500.

Tooth, O. J., Foukal, N. P., Johns, W. E., Johnson, H. L., & Wilson, C. (2024). Lagrangian Decomposition of the Atlantic Ocean Heat Transport at 26.5°N. *Geophysical Research Letters*, *51*(14), e2023GL107399.

Tooth, O. J., Johnson, H. L., & Wilson, C. (2023a). Lagrangian Overturning Pathways in the Eastern Subpolar North Atlantic. *Journal of Climate*, *36*(3), 823–844.

Tooth, O. J., Johnson, H. L., Wilson, C., & Evans, D. G. (2023b). Seasonal overturning variability in the eastern North Atlantic subpolar gyre: A Lagrangian perspective. *Ocean Science*, *19*(3), 769–791.

Treguier, A. M., Theetten, S., Chassignet, E. P., Penduff, T., Smith, R., Talley, L., Beismann, J. O., & Böning, C. (2005). The North Atlantic Subpolar Gyre in Four High-Resolution Models. *Journal of Physical Oceanography*, *35*(5), 757–774.

Treguier, A. M., Gourcuff, C., Lherminier, P., Mercier, H., Barnier, B., Madec, G., Molines, J.-M., Penduff, T., Czeschel, L., & Böning, C. (2006). Internal and forced variability along a section between Greenland and Portugal in the CLIPPER Atlantic model. *Ocean Dynamics*, *56*(5-6), 568–580.

Trenberth, K. E., & Caron, J. M. (2001). Estimates of Meridional Atmosphere and Ocean Heat Transports. *Journal of Climate*, *14*(16), 3433–3443.

Trenberth, K. E., & Fasullo, J. T. (2017). Atlantic meridional heat transports computed from balancing Earth's energy locally. *Geophysical Research Letters*, *44*(4), 1919–1927.

Tsubouchi, T., Våge, K., Hansen, B., Larsen, K. M. H., Østerhus, S., Johnson, C., Jónsson, S., & Valdimarsson, H. (2021). Increased ocean heat transport into the Nordic Seas and Arctic Ocean over the period 1993–2016. *Nature Climate Change*, *11*(1), 21–26.

Tsujino, H., Urakawa, S., Nakano, H., Small, R. J., Kim, W. M., Yeager, S. G., Danabasoglu, G., Suzuki, T., Bamber, J. L., Bentsen, M., Böning, C. W., Bozec, A., Chassignet, E. P., Curchitser, E., Boeira Dias, F., Durack, P. J., Griffies, S. M., Harada, Y., Ilicak, M., … Yamazaki, D. (2018). JRA-55 based surface dataset for driving ocean–sea-ice models (JRA55-do). *Ocean Modelling*, *130*, 79–139.

Tuchen, F. P., Brandt, P., Lübbecke, J. F., & Hummels, R. (2022). Transports and Pathways of the Tropical AMOC Return Flow From Argo Data and Shipboard Velocity Measurements. *Journal of Geophysical Research: Oceans*, *127*(2), e2021JC018115.

Tulloch, R., & Marshall, J. (2012). Exploring Mechanisms of Variability and Predictability of Atlantic Meridional Overturning Circulation in Two Coupled Climate Models. *Journal of Climate*, *25*(12), 4067–4080.

Uppala, S. M., KÅllberg, P. W., Simmons, A. J., Andrae, U., Bechtold, V. D. C., Fiorino, M., Gibson, J. K., Haseler, J., Hernandez, A., Kelly, G. A., Li, X., Onogi, K., Saarinen, S., Sokka, N., Allan, R. P., Andersson, E., Arpe, K., Balmaseda, M. A., Beljaars, A. C. M., … Woollen, J. (2005). The ERA-40 re-analysis. *Quarterly Journal of the Royal Meteorological Society*, *131*(612), 2961–3012.

Våge, K., Pickart, R. S., Spall, M. A., Valdimarsson, H., Jónsson, S., Torres, D. J., Østerhus, S., & Eldevik, T. (2011). Significant role of the North Icelandic Jet in the formation of Denmark Strait overflow water. *Nature Geoscience*, *4*(10), 723–727.

Van Aken, H., & Becker, G. (1996). Hydrography and through-flow in the north-eastern North Atlantic Ocean: The NANSEN project. *Progress in Oceanography*, *38*(4), 297–346.

Van Aken, H., & De Boer, C. (1995). On the synoptic hydrography of intermediate and deep water masses in the Iceland Basin. *Deep Sea Research Part I: Oceanographic Research Papers*, *42*(2), 165–189.

Van Sebille, E., Baringer, M. O., Johns, W. E., Meinen, C. S., Beal, L. M., de Jong, M. F., & Van Aken, H. M. (2011). Propagation pathways of classical Labrador Sea water from its source region to 26°N. *Journal of Geophysical Research*, *116*(C12), C12027.

Van Sebille, E., Griffies, S. M., Abernathey, R., Adams, T. P., Berloff, P., Biastoch, A., Blanke, B., Chassignet, E. P., Cheng, Y., Cotter, C. J., Deleersnijder, E., Döös, K., Drake, H. F., Drijfhout, S., Gary, S. F., Heemink, A. W., Kjellsson, J., Koszalka, I. M., Lange, M., … Zika, J. D. (2018). Lagrangian ocean analysis: Fundamentals and practices. *Ocean Modelling*, *121*, 49–75.

van Sebille, E., Spence, P., Mazloff, M. R., England, M. H., Rintoul, S. R., & Saenko, O. A. (2013). Abyssal connections of Antarctic Bottom Water in a Southern Ocean State Estimate. *Geophysical Research Letters*, *40*(10), 2177–2182.

Van Westen, R. M., Kliphuis, M., & Dijkstra, H. A. (2024). Physics-based early warning signal shows that AMOC is on tipping course. *Science Advances*, *10*(6), eadk1189.

Vellinga, M., & Wood, R. A. (2002). Global Climatic Impacts of a Collapse of the Atlantic Thermohaline Circulation. *Climatic Change*, *54*(3), 251–267.

Vellinga, M., & Wood, R. A. (2008). Impacts of thermohaline circulation shutdown in the twenty-first century. *Climatic Change*, *91*(1-2), 43–63.

Verezemskaya, P., Barnier, B., Gulev, S. K., Gladyshev, S., Molines, J.-M., Gladyshev, V., Lellouche, J.-M., & Gavrikov, A. (2021). Assessing Eddying (1/12°) Ocean Reanalysis GLORYS12 Using the 14-yr Instrumental Record From 59.5°N Section in the Atlantic. *Journal of Geophysical Research: Oceans*, *126*(6), e2020JC016317.

Visbeck, M., Chassignet, E. P., Curry, R. G., Delworth, T. L., Dickson, R. R., & Krahmann, G. (2003). The ocean's response to North Atlantic Oscillation variability. In J. W. Hurrell, Y. Kushnir, G. Ottersen, & M. Visbeck (Eds.), *Geophysical Monograph Series* (pp. 113–145, Vol. 134). American Geophysical Union.

Voelker, A. H. (2002). Global distribution of centennial-scale records for Marine Isotope Stage (MIS) 3: A database. *Quaternary Science Reviews*, *21*(10), 1185–1212.

Volk, T., & Hoffert, M. I. (2013, March). Ocean Carbon Pumps: Analysis of Relative Strengths and Efficiencies in Ocean-Driven Atmospheric CO $_2$ Changes. In E. Sundquist & W. Broecker (Eds.), *Geophysical Monograph Series* (pp. 99–110). American Geophysical Union.

Volkov, D. L., Zhang, K., Johns, W. E., Willis, J. K., Hobbs, W., Goes, M., Zhang, H., & Menemenlis, D. (2023). Atlantic meridional overturning circulation increases flood risk along the United States southeast coast. *Nature Communications*, *14*(1), 5095.

Wåhlin, A. K., & Johnson, H. L. (2009). The Salinity, Heat, and Buoyancy Budgets of a Coastal Current in a Marginal Sea. *Journal of Physical Oceanography*, *39*(10), 2562–2580.

Waldman, R., Hirschi, J., Voldoire, A., Cassou, C., & Msadek, R. (2021). Clarifying the Relation between AMOC and Thermal Wind: Application to the Centennial Variability in a Coupled Climate Model. *Journal of Physical Oceanography*, *51*(2), 343–364.

Walin, G. (1982). On the relation between sea-surface heat flow and thermal circulation in the ocean. *Tellus A: Dynamic Meteorology and Oceanography*, *34*(2), 187.

Wang, H., Zhao, J., Li, F., & Lin, X. (2021). Seasonal and Interannual Variability of the Meridional Overturning Circulation in the Subpolar North Atlantic Diagnosed From a High Resolution Reanalysis Data Set. *Journal of Geophysical Research: Oceans*, *126*(6), e2020JC017130.

Wang, H., Legg, S. A., & Hallberg, R. W. (2015). Representations of the Nordic Seas overflows and their large scale climate impact in coupled models. *Ocean Modelling*, *86*, 76–92.

Waterhouse, A. F., MacKinnon, J. A., Nash, J. D., Alford, M. H., Kunze, E., Simmons, H. L., Polzin, K. L., St. Laurent, L. C., Sun, O. M., Pinkel, R., Talley, L. D., Whalen, C. B., Huussen, T. N., Carter, G. S., Fer, I., Waterman, S., Naveira Garabato, A. C., Sanford, T. B., & Lee, C. M. (2014). Global Patterns of Diapycnal Mixing from Measurements of the Turbulent Dissipation Rate. *Journal of Physical Oceanography*, *44*(7), 1854–1872.

Wdowinski, S., Bray, R., Kirtman, B. P., & Wu, Z. (2016). Increasing flooding hazard in coastal communities due to rising sea level: Case study of Miami Beach, Florida. *Ocean & Coastal Management*, *126*, 1–8.

Weber, S. L., & Drijfhout, S. S. (2007). Stability of the Atlantic Meridional Overturning Circulation in the Last Glacial Maximum climate. *Geophysical Research Letters*, *34*(22), 2007GL031437.

Wefing, A.-M., Casacuberta, N., Christl, M., Gruber, N., & Smith, J. N. (2021). Circulation timescales of Atlantic Water in the Arctic Ocean determined from anthropogenic radionuclides. *Ocean Science*, *17*(1), 111–129.

Weijer, W., Cheng, W., Drijfhout, S. S., Fedorov, A. V., Hu, A., Jackson, L. C., Liu, W., McDonagh, E. L., Mecking, J. V., & Zhang, J. (2019). Stability of the Atlantic Meridional Overturning Circulation: A Review and Synthesis. *Journal of Geophysical Research: Oceans*, *124*(8), 5336–5375.

Weijer, W., Cheng, W., Garuba, O. A., Hu, A., & Nadiga, B. T. (2020). CMIP6 Models Predict Significant 21st Century Decline of the Atlantic Meridional Overturning Circulation. *Geophysical Research Letters*, *47*(12), e2019GL086075.

Wett, S., Rhein, M., Kieke, D., Mertens, C., & Moritz, M. (2023). Meridional Connectivity of a 25-Year Observational AMOC Record at 47°N. *Geophysical Research Letters*, *50*(16), e2023GL103284.

Williams, R. G., & Follows, M. J. (2011, July). *Ocean Dynamics and the Carbon Cycle: Principles and Mechanisms* (1st ed.). Cambridge University Press.

Williams, R. G., Marshall, J. C., & Spall, M. A. (1995). Does Stommel's Mixed Layer "Demon" Work? *Journal of Physical Oceanography*, *25*(12), 3089–3102.

Williams, R. G., McDonagh, E., Roussenov, V. M., Torres-Valdes, S., King, B., Sanders, R., & Hansell, D. A. (2011). Nutrient streams in the North Atlantic: Advective pathways of inorganic and dissolved organic nutrients. *Global Biogeochemical Cycles*, *25*(4), n/a–n/a.

Williams, R. G., Roussenov, V., & Follows, M. J. (2006). Nutrient streams and their induction into the mixed layer. *Global Biogeochemical Cycles*, *20*(1), 2005GB002586.

Williams, R. G., Roussenov, V., Lozier, M. S., & Smith, D. (2015). Mechanisms of Heat Content and Thermocline Change in the Subtropical and Subpolar North Atlantic. *Journal of Climate*, *28*(24), 9803–9815.

Willis, J. K. (2010). Can in situ floats and satellite altimeters detect long-term changes in Atlantic Ocean overturning? *Geophysical Research Letters*, *37*(6), 2010GL042372.

Winton, M., Hallberg, R., & Gnanadesikan, A. (1998). Simulation of Density-Driven Frictional Downslope Flow in *Z* -Coordinate Ocean Models. *Journal of Physical Oceanography*, *28*(11), 2163–2174.

Wong, A. P. S., Wijffels, S. E., Riser, S. C., Pouliquen, S., Hosoda, S., Roemmich, D., Gilson, J., Johnson, G. C., Martini, K., Murphy, D. J., Scanderbeg, M., Bhaskar, T. V. S. U., Buck, J. J. H., Merceur, F., Carval, T., Maze, G., Cabanes, C., André, X., Poffa, N., … Park, H.-M. (2020). Argo Data 1999–2019: Two Million Temperature-Salinity Profiles and Subsurface Velocity Observations From a Global Array of Profiling Floats. *Frontiers in Marine Science*, *7*, 700.

Wood, R. A., Keen, A. B., Mitchell, J. F. B., & Gregory, J. M. (1999). Changing spatial structure of the thermohaline circulation in response to atmospheric CO2 forcing in a climate model. *Nature*, *399*(6736), 572–575.

Worthington, L. V. (1976). *On the North Atlantic circulation*. Johns Hopkins University Press.

Worthington, L. (1958). The 18° water in the Sargasso Sea. *Deep Sea Research (1953)*, *5*(2-4), 297–305.

Wunsch, C. (2005). The Total Meridional Heat Flux and Its Oceanic and Atmospheric Partition. *Journal of Climate*, *18*(21), 4374–4380.

Wunsch, C., & Heimbach, P. (2006). Estimated Decadal Changes in the North Atlantic Meridional Overturning Circulation and Heat Flux 1993–2004. *Journal of Physical Oceanography*, *36*(11), 2012–2024.

Wunsch, C., & Heimbach, P. (2009). The Global Zonally Integrated Ocean Circulation, 1992–2006: Seasonal and Decadal Variability. *Journal of Physical Oceanography*, *39*(2), 351–368.

Wunsch, C., & Heimbach, P. (2013). Two Decades of the Atlantic Meridional Overturning Circulation: Anatomy, Variations, Extremes, Prediction, and Overcoming Its Limitations. *Journal of Climate*, *26*(18), 7167–7186.

Wüst, G. (1935). Schichtung und Zirkulation des Atlantischen Ozeans. Die Stratophäre. In *Wissenschaftliche Ergebnisse der Deutschen Atlantischen Expedition auf dem Forschungs—und Vermessungsschiff "Meteor" 1925–1927* (2nd ed., p. 180, Vol. 6).

Wüst, G. (1949). *Die Kreisläufe der atlantischen Wassermassen, ein neuer Versuch räumlicher Darstellung Forschungen und Fortschritte.* (Vol. 25).

Wüst, G. (1957). Stromgeschwindigkeiten und Strommengen in den Tiefen des Atlantischen Ozeans unter besonderer Berücksichtigung des Tiefen- und Bodenwassers. In *Wissenschaftliche Ergebnisse der Deutschen Atlantischen Expedition auf dem Forschungs—und Vermessungsschiff "Meteor" 1925–1927* (2nd ed., p. 180, Vol. 6).

Xu, X., Hurlburt, H. E., Schmitz, W. J., Zantopp, R., Fischer, J., & Hogan, P. J. (2013). On the currents and transports connected with the atlantic meridional overturning circulation in the subpolar North Atlantic. *Journal of Geophysical Research: Oceans*, *118*(1), 502–516.

Xu, X., Schmitz, W. J., Hurlburt, H. E., Hogan, P. J., & Chassignet, E. P. (2010). Transport of Nordic Seas overflow water into and within the Irminger Sea: An eddy-resolving simulation and observations. *Journal of Geophysical Research: Oceans*, *115*(C12), 2010JC006351.

Xu, X., Bower, A., Furey, H., & Chassignet, E. P. (2018a). Variability of the Iceland-Scotland Overflow Water Transport Through the Charlie-Gibbs Fracture Zone: Results From an Eddying Simulation and Observations. *Journal of Geophysical Research: Oceans*, *123*(8), 5808–5823.

Xu, X., Chassignet, E. P., Johns, W. E., Schmitz, W. J., & Metzger, E. J. (2014). Intraseasonal to interannual variability of the Atlantic meridional overturning circulation from eddy-resolving simulations and observations. *Journal of Geophysical Research: Oceans*, *119*(8), 5140–5159.

Xu, X., Rhines, P. B., & Chassignet, E. P. (2016). Temperature–Salinity Structure of the North Atlantic Circulation and Associated Heat and Freshwater Transports. *Journal of Climate*, *29*(21), 7723–7742.

Xu, X., Rhines, P. B., & Chassignet, E. P. (2018b). On Mapping the Diapycnal Water Mass Transformation of the Upper North Atlantic Ocean. *Journal of Physical Oceanography*, *48*(10), 2233–2258.

Yan, X., Zhang, R., & Knutson, T. R. (2017). The role of Atlantic overturning circulation in the recent decline of Atlantic major hurricane frequency. *Nature Communications*, *8*(1), 1695.

Yashayaev, I., & Clarke, A. (2008). Evolution of North Atlantic Water Masses Inferred from Labrador Sea Salinity Series. *Oceanography*, *21*(1), 30–45.

Yashayaev, I., & Dickson, B. (2008). Transformation and Fate of Overflows in the Northern North Atlantic. In R. R. Dickson, J. Meincke, & P. Rhines (Eds.), *Arctic–Subarctic Ocean Fluxes* (pp. 505–526). Springer Netherlands.

Yashayaev, I., Holliday, N. P., Bersch, M., & Van Aken, H. M. (2008). The History of the Labrador Sea Water: Production, Spreading, Transformation and Loss. In R. R. Dickson, J. Meincke, & P. Rhines (Eds.), *Arctic–Subarctic Ocean Fluxes* (pp. 569–612). Springer Netherlands.

Yashayaev, I., & Seidov, D. (2015). The role of the Atlantic Water in multidecadal ocean variability in the Nordic and Barents Seas. *Progress in Oceanography*, *132*, 68–127.

Yeager, S. G., & Robson, J. I. (2017). Recent Progress in Understanding and Predicting Atlantic Decadal Climate Variability. *Current Climate Change Reports*, *3*(2), 112–127.

Yeager, S. (2020). The abyssal origins of North Atlantic decadal predictability. *Climate Dynamics*, *55*(7-8), 2253–2271.

Yeager, S., Castruccio, F., Chang, P., Danabasoglu, G., Maroon, E., Small, J., Wang, H., Wu, L., & Zhang, S. (2021). An outsized role for the Labrador Sea in the multidecadal variability of the Atlantic overturning circulation. *Science Advances*, *7*(41), eabh3592.

Yeager, S., & Danabasoglu, G. (2012). Sensitivity of Atlantic Meridional Overturning Circulation Variability to Parameterized Nordic Sea Overflows in CCSM4. *Journal of Climate*, *25*(6), 2077–2103.

Yeager, S., & Danabasoglu, G. (2014). The Origins of Late-Twentieth-Century Variations in the Large-Scale North Atlantic Circulation. *Journal of Climate*, *27*(9), 3222–3247.

Yeager, S. G., Karspeck, A. R., & Danabasoglu, G. (2015). Predicted slowdown in the rate of Atlantic sea ice loss. *Geophysical Research Letters*, *42*(24).

Yin, J., Griffies, S. M., & Stouffer, R. J. (2010). Spatial Variability of Sea Level Rise in Twenty-First Century Projections. *Journal of Climate*, *23*(17), 4585–4607.

Ypma, S. L., van Sebille, E., Kiss, A. E., & Spence, P. (2016). The separation of the East Australian Current: A Lagrangian approach to potential vorticity and upstream control. *Journal of Geophysical Research: Oceans*, *121*(1), 758–774.

Ypma, S., Brüggemann, N., Georgiou, S., Spence, P., Dijkstra, H., Pietrzak, J., & Katsman, C. (2019). Pathways and watermass transformation of Atlantic Water entering the Nordic Seas through Denmark Strait in two high resolution ocean models. *Deep Sea Research Part I: Oceanographic Research Papers*, *145*, 59–72.

Zantopp, R., Fischer, J., Visbeck, M., & Karstensen, J. (2017). From interannual to decadal: 17 years of boundary current transports at the exit of the L abrador S ea. *Journal of Geophysical Research: Oceans*, *122*(3), 1724–1748.

Zhai, X., Johnson, H. L., & Marshall, D. P. (2014). A Simple Model of the Response of the Atlantic to the North Atlantic Oscillation. *Journal of Climate*, *27*(11), 4052–4069.

Zhang, J., & Zhang, R. (2015). On the evolution of Atlantic Meridional Overturning Circulation Fingerprint and implications for decadal predictability in the North Atlantic. *Geophysical Research Letters*, *42*(13), 5419–5426.

Zhang, R. (2008). Coherent surface-subsurface fingerprint of the Atlantic meridional overturning circulation. *Geophysical Research Letters*, *35*(20), 2008GL035463.

Zhang, R. (2010). Latitudinal dependence of Atlantic meridional overturning circulation (AMOC) variations. *Geophysical Research Letters*, *37*(16), 2010GL044474.

Zhang, R. (2015). Mechanisms for low-frequency variability of summer Arctic sea ice extent. *Proceedings of the National Academy of Sciences*, *112*(15), 4570–4575.

Zhang, R. (2017). On the persistence and coherence of subpolar sea surface temperature and salinity anomalies associated with the Atlantic multidecadal variability. *Geophysical Research Letters*, *44*(15), 7865–7875.

Zhang, R., & Delworth, T. L. (2006). Impact of Atlantic multidecadal oscillations on India/Sahel rainfall and Atlantic hurricanes. *Geophysical Research Letters*, *33*(17), 2006GL026267.

Zhang, R., & Delworth, T. L. (2007). Impact of the Atlantic Multidecadal Oscillation on North Pacific climate variability. *Geophysical Research Letters*, *34*(23), 2007GL031601.

Zhang, R., Delworth, T. L., & Held, I. M. (2007). Can the Atlantic Ocean drive the observed multidecadal variability in Northern Hemisphere mean temperature? *Geophysical Research Letters*, *34*(2), 2006GL028683.

Zhang, R., Delworth, T. L., Sutton, R., Hodson, D. L. R., Dixon, K. W., Held, I. M., Kushnir, Y., Marshall, J., Ming, Y., Msadek, R., Robson, J., Rosati, A. J., Ting, M., & Vecchi, G. A. (2013). Have Aerosols Caused the Observed Atlantic Multidecadal Variability? *Journal of the Atmospheric Sciences*, *70*(4), 1135–1144.

Zhang, R., Sutton, R., Danabasoglu, G., Delworth, T. L., Kim, W. M., Robson, J., & Yeager, S. G. (2016). Comment on "The Atlantic Multidecadal Oscillation without a role for ocean circulation". *Science*, *352*(6293), 1527–1527.

Zhang, R., Sutton, R., Danabasoglu, G., Kwon, Y.-O., Marsh, R., Yeager, S. G., Amrhein, D. E., & Little, C. M. (2019). A Review of the Role of the Atlantic Meridional Overturning Circulation in Atlantic Multidecadal Variability and Associated Climate Impacts. *Reviews of Geophysics*, *57*(2), 316–375.

Zhang, R., & Thomas, M. (2021). Horizontal circulation across density surfaces contributes substantially to the long-term mean northern Atlantic Meridional Overturning Circulation. *Communications Earth & Environment*, *2*(1), 112.

Zhao, J., & Johns, W. (2014a). Wind-Driven Seasonal Cycle of the Atlantic Meridional Overturning Circulation. *Journal of Physical Oceanography*, *44*(6), 1541–1562.

Zhao, J., & Johns, W. (2014b). Wind-forced interannual variability of the Atlantic Meridional Overturning Circulation at 26.5°N. *Journal of Geophysical Research: Oceans*, *119*(4), 2403–2419.

Zika, J. D., England, M. H., & Sijp, W. P. (2012). The Ocean Circulation in Thermohaline Coordinates. *Journal of Physical Oceanography*, *42*(5), 708–724.

Zou, S., Bower, A., Furey, H., Susan Lozier, M., & Xu, X. (2020a). Redrawing the Iceland-Scotland Overflow Water pathways in the North Atlantic. *Nature Communications*, *11*(1), 1890.

Zou, S., & Lozier, M. S. (2016). Breaking the Linkage Between Labrador Sea Water Production and Its Advective Export to the Subtropical Gyre. *Journal of Physical Oceanography*, *46*(7), 2169–2182.

Zou, S., Lozier, M. S., Li, F., Abernathey, R., & Jackson, L. (2020b). Density-compensated overturning in the Labrador Sea. *Nature Geoscience*, *13*(2), 121–126.

Zou, S., Petit, T., Li, F., & Lozier, M. S. (2024). Observation-based estimates of water mass transformation and formation in the Labrador Sea. *Journal of Physical Oceanography*.

Zunino, P., Lherminier, P., Mercier, H., Padín, X. A., Ríos, A. F., & Pérez, F. F. (2015). Dissolved inorganic carbon budgets in the eastern subpolar North Atlantic in the 2000s from in situ data. *Geophysical Research Letters*, *42*(22), 9853–9861.